UNIVERSITY OF LIEGE

FACULTY OF APPLIED SCIENCES

UEE RESEARCH UNIT

HECE RESEARCH GROUP

Advanced porosity-based models to assess the influence of urban layouts on inundation flows and impact of urban evolution on flood damage

by

BRUWIER Martin

Thesis submitted in partial fulfilment of the requirements
for the degree of Doctor of Philosophy in Applied Sciences

Jury

DEWALS Benjamin (Advisor)	Pr. Dr. Ir., University of Liège
ARCHAMBEAU Pierre (Co-advisor)	Dr. Ir., University of Liège
DIMITRIADIS Greg (President)	Pr. Dr. Ir., University of Liège
TELLER Jacques	Pr. Dr. Ir., University of Liège
MIGNOT Emmanuel	Dr. Ir., INSA (Lyon), LMFA Laboratory
VAZQUEZ José	Pr. Dr. Ir., ENGEES (Strasbourg), Icube Laboratory

October 2017

ACKNOWLEDGMENT

This PhD thesis was funded through the ARC grant, financed by the Wallonia-Brussels Federation. I am also grateful to the University of Liège for providing the resources necessary to conduct this research.

I thank the President of the Jury committee Greg Dimitriadis and the members of the committee Jacques Teller, Emmanuel Mignot and José Vazquez for accepting to review my work. I hope they will appreciate the reading of this manuscript.

I want to thank Ahmed Mustafa for our exciting exchanges regarding the interactions between urbanization and floods.

Merci à Michel Pirotton et Sébastien Erpicum pour leur accueil au sein du service HECE.

Je remercie Pierre Archambeau, co-promoteur de ma thèse, pour ses excellents conseils, son enthousiasme et sa patience, particulièrement pour la partie numérique de ce travail.

Merci à mon promoteur, Benjamin Dewals, de m'avoir offert la possibilité de découvrir le monde de la recherche. Merci également pour le temps considérable que vous m'avez consacré tout au long de ces quatre années de thèse, pour la qualité et la pertinence de vos remarques et suggestions ainsi que pour l'enthousiasme et la rigueur scientifique que vous m'avez inculqués.

Merci également à Laurence pour son aide technique et aux autres membres de l'équipe HECE avec qui j'ai partagé de bons moments aux pauses cafés, temps de midi ou *after-works*: Maurine, Yan, Velya, Benjamin, Mohammad et Diana. Un remerciement particulier à Fred pour l'aide que tu m'as apportée en début de thèse. Je suis content d'avoir eu la chance de faire ta connaissance. Merci à Louis pour ta disponibilité, tes connaissances en informatique et, surtout, de m'avoir supporté quatre années dans notre bureau. J'ai commencé ma thèse avec un pote et je la termine avec un ami. En parlant d'amitié, merci à Ismaïl pour les bons moments passés à l'Université de Liège et en dehors.

Enfin, je remercie ma famille et mes amis pour leurs soutiens tout au long de ma thèse. En particulier, merci à mes parents pour leur présence et leur affection.

Martin Bruwier, July 2017

Articles in peer-reviewed academic journals

As a first author

1. Bruwier, M., Archambeau, P., Erpicum, S., Pirotton, M., & Dewals, B. (2017). Shallow-water models with anisotropic porosity and merging for flood modelling on Cartesian grids. Journal of Hydrology, accepted.

   http://hdl.handle.net/2268/214640
2. Bruwier, M., Erpicum, S., Pirotton, M., Archambeau, P., & Dewals, B. (2015). Assessing the operation rules of a reservoir system based on a detailed modelling chain. Natural Hazards & Earth System Sciences, 15, 365-379.

   http://hdl.handle.net/2268/171905
3. Bruwier, M., Archambeau, P., Erpicum, S., Pirotton, M., & Dewals, B. (2016). Discretization of the divergence formulation of the bed slope term in the shallow-water equations and consequences in terms of energy balance. Applied Mathematical Modelling, 40(17-18), 7532–7544.

   http://hdl.handle.net/2268/192948
4. Bruwier, M., Erpicum, S., Archambeau, P., Pirotton, M., & Dewals, B. (in press). Computing flooding of crossroads with obstacles using a 2D numerical model (Discussion). Journal of Hydraulic Research.

   http://hdl.handle.net/2268/209999

As a co-author

5. Dewals, B., Bruwier, M., Erpicum, S., Pirotton, M., & Archambeau, P. (2016). Energy conservation properties of Ritter solution for idealized dam break flow. Journal of Hydraulic Research, 54(5), 581-585.

   http://hdl.handle.net/2268/195262
6. Arrault, Finaud-Guyot, P., Archambeau, P., Bruwier, M., Erpicum, S., Pirotton, M., & Dewals, B. (2016). Hydrodynamics of long-duration urban floods: experiments and numerical modelling. Natural Hazards & Earth System Sciences, 16, 1413-1429.

   http://hdl.handle.net/2268/193294

7. Saadi, I., Bruwier, M., El Saeid Mustafa, A. M., Peltier, Y., Archambeau, P., Erpicum, S., Orban, P., Dassargues, A., Dewals, B., Pirotton, M., Teller, J., & Cools, M. (in press). Development trajectory of an integrated framework for the mitigation of future flood risk: results from the FloodLand project. Transportation Letters: The International Journal of Transportation Research.

http://hdl.handle.net/2268/208789

Scientific congresses and symposia

As a first author

8. Bruwier, M., Dewals, B., Erpicum, S., Pirotton, M., & Archambeau, P. (2014). Climate-proofing of large reservoirs in Belgium by the development of enhanced operation rules. 3rd IAHR Europe Congress.

http://hdl.handle.net/2268/163670

9. Bruwier, M., Erpicum, S., Archambeau, P., Pirotton, M., & Dewals, B. (2014). Mathematical formulations of shallow water models with porosity for urban flood modelling. ICHE 2014: 11th International Conference on Hydroscience & Engineering.

http://hdl.handle.net/2268/163671

10. Bruwier, M., Archambeau, P., Erpicum, S., Pirotton, M., & Dewals, B. (2015). A shallow-water model with depth-dependent porosity for urban flood modelling. E-proceedings of the 36th IAHR World Congress.

http://hdl.handle.net/2268/184530

11. Bruwier, M., Archambeau, P., Erpicum, S., Pirotton, M., & Dewals, B. (2015). Formulations of the bed slope term in the shallow water equations: implication for energy balance. Workshop on Advances in Numerical Modelling of Hydrodynamics.

http://hdl.handle.net/2268/178323

12. Bruwier, M., Archambeau, P., Erpicum, S., Pirotton, M., & Dewals, B. (2015). Potential damping of extreme floods in the river Meuse between Ampsin (B) and the Belgian-Dutch border. In H. J. R., Lenders, F. P. L., Collas, G. W., Geerling, & R. S. E. W., Leuven, Bridging gaps between river science, governance and management. Book of Abstracts NCR-Days 2015 (pp. 9-12).

http://hdl.handle.net/2268/186019

13. Bruwier, M., Mustafa, A., Aliaga, D., Erpicum, S., Archambeau, P., Nishida, G., Zhang, X., Pirotton, M., Teller, J., & Dewals, B. (2017). Influence of urban patterns on flooding. E-proceedings of the 37th IAHR World Congress.

    http://hdl.handle.net/2268/207587

As a co-author

14. Dewals, B., Archambeau, P., Bruwier, M., Erpicum, S., & Pirotton, M. (2014). Integrated catchment analysis in the Meuse basin for assessing water resources and future flood risk. Paper presented at Final Conference of the project "Mitigating Vulnerability of Water Resources under Climate Change" (CC-WARE), Waidhofen/Ybbs, Austria.

    http://hdl.handle.net/2268/173833

15. Dewals, B., Bruwier, M., Mohamed El Saeid Mustafa, A., Peltier, Y., Saadi, I., Archambeau, P., Erpicum, S., Orban, P., Cools, M., Dassargues, A., Teller, J., & Pirotton, M. (2015). Landuse change and future flood risk: an integrated and multi-scale approach. E-proceedings of the 36th IAHR World Congress.

    http://hdl.handle.net/2268/183058

16. Mustafa, A., Bruwier, M., Teller, J., Archambeau, P., Erpicum, S., Pirotton, M., & Dewals, B. (2016). Impacts of urban expansion on future flood damage: A case study in the River Meuse basin, Belgium. In S., Erpicum, B., Dewals, P., Archambeau, & M., Pirotton, Sustainable Hydraulics in the Era of Global Change: Advances in Water Engineering and Research. London, UK: Taylor & Francis Group.

    http://hdl.handle.net/2268/200745

17. Dewals, B., Bruwier, M., El Saeid Mustafa, A. M., Archambeau, P., Erpicum, S., Teller, J., & Pirotton, M. (2017). Urbanization and changing flood risk: a multi-level analysis. In A., Bronstert, A., Thieken, T., Petrow, & J. A., López-Tarazón (Ed.), The Effects of Global Change on Floods, Fluvial Geomorphology and Related Hazards in Mountainous Rivers (pp. 37-39). Postdam, Germany: Universität Potsdam.

    http://hdl.handle.net/2268/206585

Oral presentations or conference poster

As a first author

18. Bruwier, M., Mustafa, A., Archambeau, P., Erpicum, S., Pirotton, M., Teller, J., & Dewals, B. (2016). Contribution of future urbanisation expansion to flood risk changes. Paper presented at EGU General Assembly 2016, Vienna, Austria.

http://hdl.handle.net/2268/194614

19. Bruwier, M., Archambeau, P., Erpicum, S., Pirotton, M., & Dewals, B. (2017). Shallow water model with anisotropic porosity for flood modelling on Cartesian grids. Paper presented at 4th International Symposium of Shallow Flows, Eindhoven, Netherlands.

    http://hdl.handle.net/2268/207585

20. Bruwier, M., Mustafa, A., Aliaga, D., Archambeau, P., Erpicum, S., Nishida, G., Zhang, X., Pirotton, M., Teller, J., & Dewals, B. (2017). Systematic flood modelling to support flood-proof urban design. Poster session presented at European Geosciences Union 2017, Vienne, Autriche.

    http://hdl.handle.net/2268/207584

As a co-author

21. Arrault, A., Finaud-Guyot, P., Archambeau, P., Bruwier, M., Erpicum, S., Pirotton, M., & Dewals, B. (2016, October 25). A benchmark for urban flood modelling. Poster session presented at Belgian Hydraulic Days.

    http://hdl.handle.net/2268/203122

22. Dewals, B., Bruwier, M., El Saeid Mustafa, A. M., Archambeau, P., Erpicum, S., Teller, J., & Pirotton, M. (2017). Modèles de porosité pour les inondations urbaines [in French]. Presented at the Saint-Venant hydraulic laboratory, Chatou, France.

    http://hdl.handle.net/2268/213191

Reports

23. Bruwier, M., Archambeau, P., Erpicum, S., Pirotton, M., & Dewals, B. (2014). Potential damping of extreme floods in the river Meuse (Phase I): 1st progress report. University of Liege.

    http://hdl.handle.net/2268/174652

24. Bruwier, M., Archambeau, P., Erpicum, S., Pirotton, M., & Dewals, B. (2015). Potential damping of extreme floods in the river Meuse (Phase I): Final report. University of Liege.

    http://hdl.handle.net/2268/181462

25. Dewals, B., Bruwier, M., El Saeid Mustafa, A. M., Peltier, Y., Saadi, I., Archambeau, P., Erpicum, S., Orban, P., Cools, M., Dassargues, A., Pirotton, M., & Teller, J. (2014). Landuse change and future flood risk: the influence of micro-scale spatial patterns (FloodLand) - 1st progress report. Liege, Belgium: University of Liege (ULg).

    http://hdl.handle.net/2268/173317

26. Dewals, B., Bruwier, M., El Saeid Mustafa, A. M., Peltier, Y., Saadi, I., Archambeau, P., Erpicum, S., Orban, P., Cools, M., Dassargues, A., Pirotton, M., & Teller, J. (2014). Landuse change and future flood risk: the influence of micro-scale spatial patterns (FloodLand) - 2nd progress report. Liege, Belgium: University of Liege (ULg).

http://hdl.handle.net/2268/173316

27. Dewals, B., Bruwier, M., El Saeid Mustafa, A. M., Peltier, Y., Saadi, I., Archambeau, P., Erpicum, S., Orban, P., Cools, M., Dassargues, A., Pirotton, M., & Teller, J. (2015). Landuse change and future flood risk: the influence of micro-scale spatial patterns (FloodLand) - 3rd progress report. Liege, Belgium: University of Liege (ULg).

http://hdl.handle.net/2268/213276

28. Dewals, B., Bruwier, M., El Saeid Mustafa, A. M., Peltier, Y., Saadi, I., Archambeau, P., Erpicum, S., Orban, P., Cools, M., Dassargues, A., Pirotton, M., & Teller, J. (2016). Landuse change and future flood risk: the influence of micro-scale spatial patterns (FloodLand) - 4th progress report. Liege, Belgium: University of Liege (ULg).

http://hdl.handle.net/2268/213277

29. Dewals, B., Bruwier, M., El Saeid Mustafa, A. M., Peltier, Y., Saadi, I., Archambeau, P., Erpicum, S., Orban, P., Cools, M., Dassargues, A., Pirotton, M., & Teller, J. (2017). Landuse change and future flood risk: the influence of micro-scale spatial patterns (FloodLand) - 5th progress report. Liege, Belgium: University of Liege (ULg).

http://hdl.handle.net/2268/213278

30. De Cuyper, A., Bruwier, M., Archambeau, P., Erpicum, S., Pirotton, M., & Dewals, B. (2014). Towards enhanced estimates of future water demand in the Meuse basin: literature review. Liege, Belgium: University of Liege (ULg).

http://hdl.handle.net/2268/172973

ABSTRACT

Worldwide, flood risk is expected to increase over the 21st century due to the combined effect of climate and land use changes. However, while the impact of climate change on future flood risk was extensively studied, the effects of urbanization remain unclear. The goal of this PhD thesis is to contribute to a better understanding of the influence of future urban development on changes in inundation flows as well as on the related damage.

First, an original porosity-based model was developed, which enables efficient computation of urban flooding. It uses anisotropic porosity parameters to reproduce the influence of subgrid-scale obstacles on the flow. An original merging technique was implemented to optimize the computational efficiency in the presence of low values of the storage porosity parameter. Compared to a standard inundation model, the developed model enables speedup factors of the order of 100, while keeping the error on the flow variables at a few percent.

Second, we systematically investigated how the layout of buildings located in floodplains influences the inundation characteristics for a long-duration flood scenario. The anisotropic porosity-based model was used to compute the flow variables for 2,000 alternative urban patterns. Correlations between the computed water depths and the urban characteristics reveal which features of the layout of buildings influences most the severity of urban flooding. In particular, the results suggest how the hydraulic effect of new urban development can be effectively mitigated by a suitable location of the buildings preserving a higher flow conveyance at the district-scale. This result provides guidance for more flood-proof urban developments.

Finally, we evaluated the evolution of future flood damage as a result of urbanization along all the main rivers in the Walloon region, Belgium. The study was conducted at the regional level using detailed hydraulic results (resolution of 2 to 5 m). Despite high uncertainties in the considered urbanization scenarios, involving both urban expansion and densification, robust conclusions could be drawn, such as the overwhelming influence of banning new developments in flood-prone areas compared to the other tested facets of urban planning policy.

RÉSUMÉ

A travers le monde, une augmentation des risques liés aux inondations est attendue au cours du XXI^{ème} siècle suite aux effets combinés du changement climatique et de l'urbanisation croissante. Alors que l'impact du changement climatique sur les inondations a été largement étudié, la quantification des effets de l'urbanisation reste aujourd'hui moins complète. L'objectif de cette thèse est de contribuer à une meilleure compréhension de l'influence du développement urbain sur l'intensité des inondations en zone urbaine ainsi que sur les dommages occasionnés.

Premièrement, un modèle hydraulique original utilisant le concept de porosité a été développé dans le but de calculer des inondations en milieu urbain de façon efficace. Ce modèle permet de reproduire l'influence d'obstacles sur l'écoulement à une échelle plus grossière via des paramètres de porosité anisotropes. Une technique originale (*merging technique*) a été ajoutée au modèle afin d'accroitre l'efficacité du calcul en présence de faibles valeurs de la porosité de stockage. Le modèle développé permet de réduire le temps de calcul par un facteur de l'ordre de 100, tout en limitant les erreurs à quelques pourcents.

Deuxièmement, l'influence de l'agencement de bâtiments dans des zones inondables sur les caractéristiques de l'inondation a été analysée de manière systématique pour un scénario de crue de longue durée. Le modèle à porosité a été utilisé pour simuler l'écoulement pour 2,000 configurations urbaines. Une analyse statistique des résultats a permis de mettre en évidence quelles caractéristiques des configurations urbaines influencent le plus l'inondation. En particulier, nous avons montré comment l'impact hydraulique de nouvelles constructions peut être efficacement compensé par un agencement adéquat des bâtiments qui maintienne une capacité d'écoulement suffisante à l'échelle du quartier. Ces résultats permettent de formuler des recommandations pour un développement urbain plus résilient par rapport aux inondations.

Enfin, l'augmentation des dommages causés par les inondations suite à l'urbanisation a été étudiée le long des principaux cours d'eau en Région wallonne (Belgique). Cette étude au niveau régional a été menée sur base de résultats de modélisation hydraulique à haute résolution (2 m à 5 m). Malgré des incertitudes significatives sur les scénarios d'urbanisation, tant d'expansion urbaine que de densification, des conclusions robustes ont pu être tirées, parmi lesquelles l'influence prépondérante de mesures d'interdiction de bâtir en zones inondables par rapport à d'autres facettes des politiques d'aménagement du territoire.

TABLE OF CONTENTS

INTRODUCTION

This section is partly based on the paper "*Development trajectory of an integrated framework for the mitigation of future flood risk: results from the FloodLand project*" by I. Saadi, **M. Bruwier**, A. Mustafa, Y. Peltier, P. Archambeau, S. Erpicum, P. Orban, A. Dassargues, B. Dewals, M. Pirotton, J. Teller, J. and M. Cools, published in 2016 in *Transportation Letters*. The main contributions of the PhD candidate to this paper relate to the hydraulic model used to simulate future floods and the flood impact model.

i. Context

Worldwide, floods are the most frequent natural disasters and cause over one third of overall economic losses due to natural hazards (Munich Re, 2010). UNISDR (2011) defines flood risk as a combination of flood hazard, exposure and vulnerability of elements-at-risk. Based on this concept of flood risk, flood control policies throughout Europe are currently shifting from a search for full protection against flooding towards *flood risk management*, as promoted by the Floods Directive (2007). This involves the selection of cost-effective combinations of measures, i.e. not only reduce the frequency and intensity of flooding, but also mitigate their consequences.

Flood losses are particularly severe in urban environments and urban flood risk will further increase over the 21st century, as urbanization reduces infiltration and amplifies exposure of population and properties to floods (Chen et al. 2015). Flood risk is a growing concern in urban areas not only due to river flooding; but also due to extreme rainfall events which become more frequent and more intense (Lehmann et al. 2015, Mallakpour and Villarini 2015). In response to increasing urban flood risk, radical changes will take place in urban water management and urban design. Concepts such as *sustainable urban drainage*, *water-sensitive urban design*, resilient cities and the *sponge city* model are rapidly developing (Gaines 2016, Liu 2016). They all aim at resilient approach for flood management. However, integrated assessment tools are needed to inform sustainable urban flood risk management, based on accurate risk modelling and scenario analysis (Wright 2014).

Specifically, reliable predictions of flood *hazard* are a prerequisite to support flood risk management policies. This includes the accurate estimation of inundation extents, water depths,

discharge partition and flow velocity in urbanized flood prone areas, since these parameters are critical inputs for flood impact modelling (Kreibich et al. 2014). Based on climate scenarios provided by IPCC, many studies were conducted to evaluate the hydrological impacts of climate change (Drogue et al. 2004, Kundzewicz et al. 2005, Vansteenkiste et al. 2013). In the northwest of Europe, floods frequency and intensity are expected to increase over the 21st century (Ward et al. 2011) and flood risk will rise accordingly.

However, within such distant time horizons, other drivers than just climate, such as economic development and land use, will also have a significant influence on the future flood-risk. Among these, land use change will play a significant part. Land use change influences flood risk through multiple pathways, including climate (e.g., modified evapotranspiration), run-off in the catchment (reduced infiltration), inundation flows (obstruction by buildings) and flood exposure (higher value of elements-at-risk in the floodplains).

Compared to the vast body of literature about the hydrological impacts of climate change, less research addressed the quantitative effects of land use change on future flood risk. Among the few existing studies, some suggest an overwhelming contribution of land use change to the future increase in flood risk (Poelmans et al. 2011, Elmer et al. 2012). Nonetheless, the impact of small-scale spatial urban patterns on inundation characteristics has not yet been studied sufficiently.

Thus far, no study combined future land use modelling with building-scale inundation modelling, exposure analysis, and damage assessment. This is addressed by the multidisciplinary project FloodLand, in the context of which the present PhD thesis has been prepared. This project bridges numerous fields, including urban planning, transport engineering, hydrology, groundwater, environmental engineering, and economics.

The overall goal of the FloodLand project is a better understanding of the interactions between land use change, particularly urbanization, and future flood risk. As sketched in the flowchart in Figure i-1, the research relies on a chain of modelling tools, including:

1. stochastic land use change modelling at the catchment level (meso-scale);
2. generation of synthetic urban patterns (i.e. building layouts) at the floodplain level (micro-scale), based on procedural modelling;
3. efficient inundation modelling (based on an advanced porosity-based hydraulic model),
4. transport (traffic) modelling for passengers and goods,
5. direct damage estimation,
6. direct damage modelling.

In terms of *new modelling tools*, item 3 is a key contribution of the present PhD thesis. Items 1 and 2 were not developed in the framework of this PhD thesis; but our analyses build upon the modelling outcomes of items 1 and 2. We also use item 5, whereas items 4 and 6 lie out of the scope of this PhD research, such as links ❹ and ❺ in Figure i-1.

In terms of *research questions* addressed, the scientific contributions of this PhD thesis are mainly twofold: (*i*) the analysis of the influence of micro-scale urban patterns on flooding in urbanized floodplains (link ❸ in Figure i-1) and (*ii*) the investigation of the influence of urbanization on future flood exposure, damage and risk (links ❶ and ❷ in Figure i-1). The former contribution was made possible by the development of an original hydraulic model, based on anisotropic porosity parameters, which has been coded in the modelling system Wolf. This modelling system is briefly introduced in the next section.

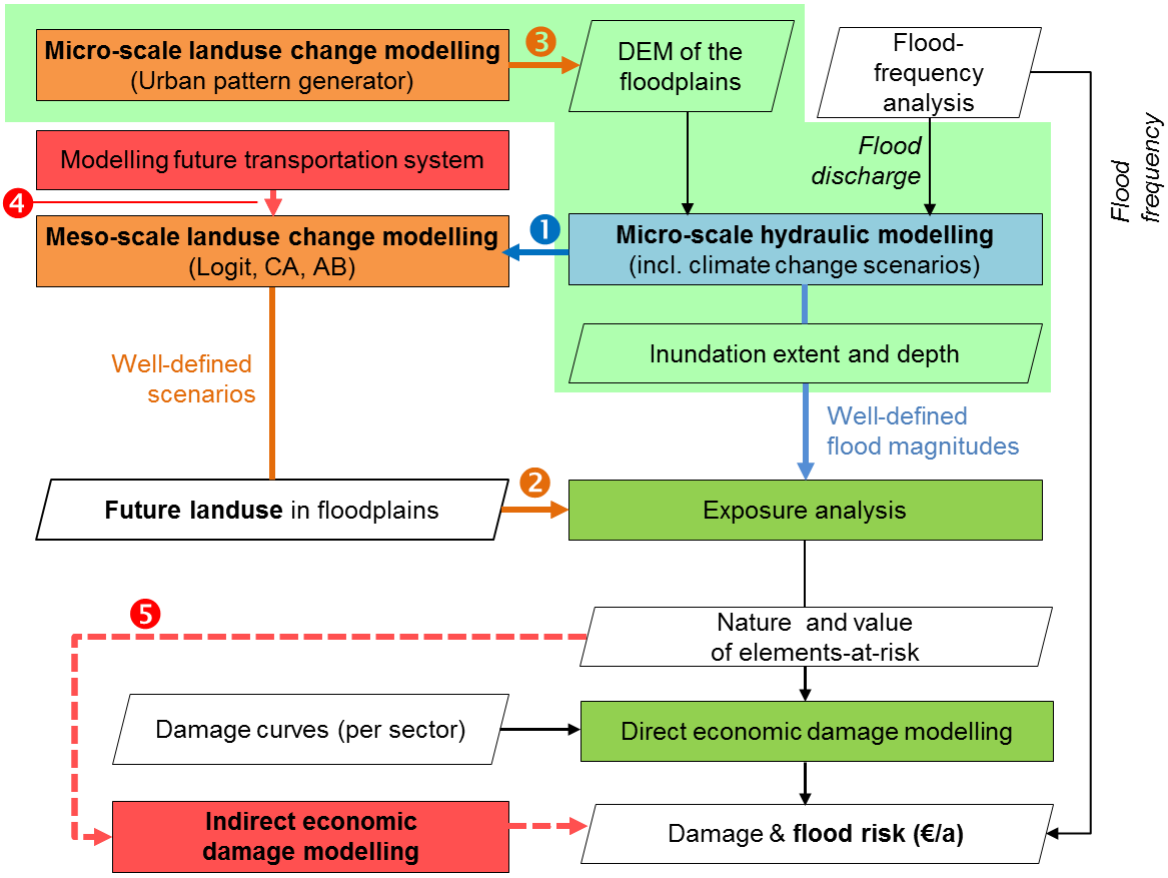

Figure i-1: Overall modelling framework set up within the FloodLand project.

ii. Wolf modelling system

The modelling system Wolf has been developed for about twenty years by the research group HECE of the University of Liege. It includes hydraulic models simulating a broad spectrum of flows of significance for environmental and civil engineering. The efficiency and reliability of these numerical models were verified for a wide range of theoretical, experimental and real-world applications (Rulot et al. 2012, Stilmant et al. 2013, 2015, Camnasio et al. 2014, Bruwier et al. 2015).

The original developments of this thesis are built on the model Wolf2D, which solves the two-dimensional shallow-water equations based on a shock-capturing finite volume scheme and a self-developed flux-vector splitting technique (Dewals et al. 2008, Erpicum et al. 2010a). Wolf2D provides detailed distributions of water depth and flow velocity, for steady and unsteady flows, on multiblock Cartesian grids.

The model Wolf2D handles datasets obtained from remote sensing, such as detailed digital surface models (DSM) resulting from the combination of laser altimetry (LIDAR) and, wherever available, sonar bathymetry. The typical grid spacing for real-world inundation modelling may be as low as 2 m, which is generally fine enough to represent the key features of complex flow patterns occurring at the scale of individual buildings and streets in urbanized floodplains (Ernst et al. 2010, Erpicum et al. 2010b). This model has been extensively applied since 2003 to prepare inundation maps throughout the Walloon region (Belgium) based on 2D hydraulic modelling of over 1,000 km of rivers, for which validation has been systematically conducted (Erpicum et al. 2010b).

iii. Scope and objectives of the thesis

In a *first contribution* of this thesis, we computed the characteristics of inundation flow for 2,000 alternative urban patterns, which were synthetized using procedural modelling. The results illuminate for the first time the quantitative **influence of micro-scale spatial patterns on inundation characteristics**.

While the detailed model Wolf2D is well-adapted for local analyses when the number of runs remains limited, the computational burden becomes too high when it comes to performing thousands of repeated runs, as required by the simulation of a large series of alternative urban patterns. Such a high number of runs is however needed to characterise in a stochastic approach

the influence of the micro-scale variability in buildings geometry and arrangement on inundation characteristics.

Various approaches have been followed to increase the performance of flood hydraulic models, such as reduced-complexity models (e.g., storage cells), simplified governing equations, parallelisation, including GPU coding (Brodtkorb et al. 2012) and grid coarsening (Dottori et al. 2013).

In this research, we opted for a grid coarsening approach in combination with a subgrid model preserving the detailed topographic information at a larger scale. This leads to highly efficient models which provide results with a suitable accuracy. Among other subgrid techniques, porosity-based hydraulic models capture the detailed building features at a coarse scale through porosity parameters representing the available storage within cells and the conveyance capacity along the edges (Sanders et al. 2008). Hence, in this PhD thesis, **we developed an original porosity-based hydraulic model** which was included in the modelling system Wolf. It handles anisotropic porosity properties on Cartesian grids as well as an original technique of cell merging to optimize the computational efficiency. This is a *second major contribution* of this PhD research.

In a *third contribution*, we evaluated the influence of land use change on future flood damage for main rivers in the Walloon region (Belgium). This regional analysis is based on future land use maps computed at the meso-scale for various time horizons up to the end of the 21st century. The underlying agent-based land use change model was developed and operated by the research group LEMA of the University of Liege, in the framework of the PhD thesis of Ahmed Mohamed El Saeid Mustafa. Using flood frequency analysis for a number of flood discharges and a flood damage model, we derived **the evolution of flood damage as a result of future urbanization in the floodplains**.

iv. Structure of the manuscript

This PhD thesis contains excerpts of several papers published in peer-reviewed journals, manuscripts either currently under review or to be submitted shortly, as well as communications at scientific conferences (Table iv-1). At the beginning of each chapter, we clearly state the corresponding sources.

The manuscript is divided into two parts: (*i*) the development and evaluation of the porosity-based hydraulic model, and (*ii*) the analysis of the impacts of urbanization on inundation flow as well as on flood damage.

The first part, related to the **advanced porosity-based hydraulic model**, includes four chapters:

- in **chapter 1**, the existing porosity-based hydraulic models are classified regarding their respective governing equations, underlying assumptions, range of validity and definition of the porosity parameters;
- motivated by the selection of a type of anisotropic porosity model based on the classification presented in chapter 1, we discuss in **chapter 2** the formulation of the different terms of the governing equations, considering the specificities of the numerical schemes used in the model Wolf2D;
- in **chapter 3**, we show theoretically that the incorporation of porosity parameters in the standard shallow-water equations influences the energy balance;
- the derivation and evaluation of the original anisotropic porosity model are presented in **chapter 4**, together with numerous test cases and examples of applications.

The second part of the PhD thesis relates to the **impact of urbanization on inundation flow as well as flood damage**. It includes:

- in **chapter 5**, the porosity-based hydraulic model is used along with an urban procedural model to investigate systematically the influence of several urban characteristics (street width, building coverage, distance between adjacent buildings, etc.) on inundation characteristics;
- the impact of urbanization on future flood damage is explored in **chapter 6** for several hundreds of kilometres of rivers throughout the Walloon region in Belgium.

At the end of the thesis, we draw general conclusions and present scientific perspectives of the present work.

		Thesis chapter	Source / reference
PART I: Advanced porosity-based hydraulic model	1	Classification of porosity concepts used for urban flood modelling	Partly based on a conference communication (Bruwier et al. 2014)
	2	Discretization of the pressure and bed slope terms	Partly based on a paper published in *Applied Mathematical Modelling* (Bruwier et al. 2016)
	3	Impact of conveyance porosity in terms of energy balance	Internal research report
	4	Anisotropic porosity model with merging on Cartesian grids	Based on: (*i*) a note accepted for publication in *Journal of Hydraulic Research* (Bruwier et al. 2017b), (*ii*) a manuscript currently under review for a peer-reviewed journal (Bruwier et al. 2017a), and (*iii*) excerpts of a paper published in *Natural Hazards and Earth System Sciences* (Arrault et al. 2016)
PART II: Impact of urbanization on flood risk	5	Influence of building layout on inundation flow in floodplains of lowland rivers	Based on a manuscript ready for submission to a peer-reviewed journal.
	6	Impact of urbanization on future flood damage in the Walloon region (Belgium)	Based on a manuscript under preparation for submission to a peer-reviewed journal

Table iv-1: Outline of the thesis and references on which the chapters are (partly) based.

PART I: POROSITY-BASED HYDRAULIC MODEL

1. Classification of porosity concepts used for urban flood modelling

This chapter is partly based on the conference communication "*Mathematical formulation of shallow water models with porosity for urban flood modelling*" published in the proceeding of the *11th International Conference on Hydroscience and Engineering*, Hamburg, 2014 (Bruwier et al. 2014).

ABSTRACT: Shallow-water models with porosity have been developed to increase computational efficiency while preserving some of the subgrid-scale information on the topography and obstacles in the floodplains. This subgrid topographic information is lumped into one or several porosity parameters. However, existing approaches for the derivation of porosity-based shallow-water equations differ in their mathematical formulations, in the underlying assumptions, in the applicability ranges of the models as well as in the definition of the porosities (grid-based vs. related to a representative elementary volume, isotropic vs. anisotropic, depth-dependent vs. -independent). In this chapter, we compare the different formulations and we highlight their respective strengths and limitations. This is based on quantitative analyses of not only idealized urban networks; but also of a real-world case study involving depth-dependent features. The analysis hints that grid-based, anisotropic and depth-dependent porosities should be preferred to reproduce optimally the detailed topographic data at a coarser scale.

1.1. Introduction

Due to climate change and other environmental changes such as growing urbanization, floods are expected to become more frequent and severe in the future. However, the magnitude of these changes remains highly uncertain. This calls for the analysis of a high number of scenarios and, therefore, many runs of the numerical models are necessary. Simultaneously, high-resolution topographic data have become widely available. Consequently, the present need is mainly for high performance computational models which take full benefit of the available detailed data.

Since detailed flood modelling in urban areas usually requires a fine discretization hardly compatible with computational efficiency, one option to improve this efficiency consists in using coarser grids while preserving some level of representation of obstacles (i.e. buildings, walls, …) within the cells by means of different subgrid modelling techniques.

One particularly crude approach relies simply on the standard shallow-water equations (SWE) with an additional flow resistance term to represent the overall influence of the obstacles. Despite its simplicity, a strong drawback of this approach is the poor use of the available topographic data (Yu and Lane 2006a, Dottori et al. 2013) and, hence, the sensitivity of the model to calibration (Yu and Lane 2006b).

Other subgrid parameterization methods enable the available topographic details to be preserved even on coarser grids thanks to the use of porosity parameters. These porosities represent the part of space not occupied by topographic obstacles, which are therefore free for water. For a given water level, the presence of these obstacles affects the volume of stored water and the exchange fluxes. Some authors use a single isotropic porosity parameter and therefore do not distinguish between storage and conveyance effects (Bates 2000, Defina 2000, Hervouet et al. 2000, Bates et al. 2003, Hervouet 2003, Guinot and Soares-Frazão 2006, Soares-Frazão et al. 2008, Velickovic et al. 2017), while others do distinguish these two effects by using anisotropic porosities (Lhomme 2006, Sanders et al. 2008, Chen et al. 2012a, 2012b, Guinot 2012, Schubert and Sanders 2012, Kim et al. 2014, 2015). Recently, Guinot et al. (2017) introduced the dual integral porosity model, in which the values of the variables at the cell edges are evaluated from the model solution by means of a closure equation. These porosity parameters are evaluated either at the scale of a Representative Elementary Volume (REV-scale porosity) (Hervouet et al. 2000, Hervouet 2003, Guinot and Soares-Frazão 2006, Lhomme 2006, Soares-Frazão et al. 2008, Guinot 2012, Velickovic et al. 2017) or at the grid scale (grid-scale porosity) (Bates 2000, Bates et al. 2003, Sanders et al. 2008, Chen et al. 2012a, 2012b, Schubert and Sanders 2012, Kim et al. 2014, 2015, Guinot et al. 2017). REV-scale porosity models are derived in the form of partial

differential equations, whereas grid-scale porosity models are formulated in discretized integral form (although a differential form can be derived to study the wave celerity, for instance). Since the scale of REVs is typically one order of magnitude larger than the typical grid scale, grid-scale porosity models enable resolving flow variability at a finer scale than REV-scale porosity models (Kim et al. 2015). In addition, Chen et al. (2012b) and Guinot (2012) account for separate flow paths within a cell thanks to, respectively, a multi-layered approach and a multiple porosity model. Some methods enable considering varying storage capacity in the cells and effective flow area across the cell edges as a function of the water level by means of relationships (e.g., look-up tables) linking directly the water level to these parameters, without referring explicitly to the concept of porosity (Yu and Lane 2006a, McMillan and Brasington 2007, Stelling 2012, Vojinovic et al. 2013, Volp et al. 2013), while others do refer explicitly to depth-dependent porosity parameters (Özgen et al. 2016b).

Each of the methods involving porosity parameters requires a specific mathematical reformulation of the SWE. Depending on the authors, the modified SWE are derived in various ways, involving specific assumptions and limitations. This chapter provides first a classification of the different porosity-based mathematical formulations used so far to simulate urban floods. Next, the main conceptual assumptions are discussed based on data from an idealized test case and from a real-world case study.

1.2. Formulations of the shallow-water equations with porosity

First, the key concepts and notations used in the porosity-based models are defined (section 1.2.1) and the integral formulation of the SWE with porosity is presented (section 1.2.2). Next, we discuss two classes of models, based respectively on the REV-scale (section 1.2.3) and on the grid-scale formulation of the equations (section 1.2.4).

1.2.1 Definitions of key concepts

To derive the SWE with porosity, the three-dimensional Reynolds-averaged Navier-Stokes equations are space-averaged over a Control Volume (CV). A CV can be defined around any point of the urban area, no matter whether that point corresponds to voids or to an obstacle. The considered CVs have vertical boundaries, except at the bottom and at the free surface (Figure 1-1). The total volume of the CV is noted V, while V_f is the part of V filled with water (Figure 1-1a). Similarly, the contour of V is noted ∂V, while ∂V_f is the part of ∂V through which water can be exchanged (Figure 1-1b). For a given level z, the total horizontal surface included

in the CV is noted Ω, while the part of Ω corresponding to water is Ω_f (Figure 1-1c). The contour of Ω is noted $\partial\Omega$, while $\partial\Omega_f$ is the part of $\partial\Omega$ through which fluid can be exchanged (Figure 1-1d).

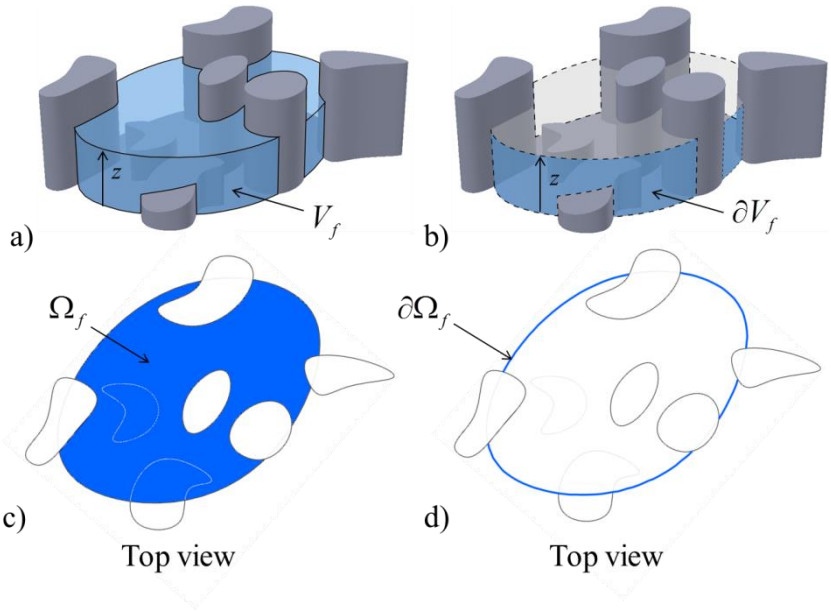

Figure 1-1 : Sketch of the CV and (a) the part V_f occupied by water, (b) the fluid-fluid exchange border ∂V_f, (c) a horizontal surface at a given level z within the CV and its part occupied by water Ω_f, as well as (d) the fluid-fluid exchange border $\partial\Omega_f$ of the horizontal surface.

For a given water level *z* in a CV, two types of porosities may be defined. The first one, called *storage porosity* (Φ), quantifies the actual volume available in the CV to store water despite the presence of obstacles such as buildings (i.e. the void fraction in the CV). In general terms, this porosity is expressed mathematically as: $\Phi(z) = V_f(z) / V(z)$. The second type of porosity, called *conveyance porosity* (Ψ), quantifies the blockage effect by obstacles on the surface area actually available to convey water through the contour of the CV. It may be expressed mathematically as: $\Psi(z) = \partial V_f(z) / \partial V(z)$. In the next sections, the porosity parameters Φ and Ψ are referred to as, respectively, *volumetric* storage porosity and *aerial* conveyance porosity.

In literature, the following alternative definitions of porosity parameters have been used extensively. At a given water level *z*, the *areal storage porosity* ϕ is the fraction of the horizontal surface within the CV which is free for water:

$$\phi(z) = \Omega_f(z) / \Omega(z) \qquad (1\text{-}1)$$

Similarly, the *linear conveyance porosity* ψ is the fraction of the length a border of Ω, which is free for water exchanges at a given water level *z*:

$$\psi(z) = \partial\Omega_f(z) / \partial\Omega(z) \qquad (1\text{-}2)$$

In most previous studies, the blockage rate by the considered obstacles is considered independent of the water level *z*. In such particular case, the following equalities hold between the different porosities defined above: $\Phi = \phi$ and $\Psi = \psi$. For this reason, many authors used only definitions (1-1) and (1-2), and referred neither to Φ nor to Ψ.

When the conveyance porosities are the same along *x* and *y* directions and are assumed equal to the storage porosity, all porosity effects are lumped into a single parameter which is called *isotropic* porosity. In others cases, the porosities are referred to as *anisotropic*.

The *Representative Elementary Volume* (REV) was originally defined as the smallest CV for which a property (such as porosity) becomes independent of the size of this CV. The concept of REV is used extensively in other fields of physics such as modelling of flow and transport processes in porous media (Bear 2013), rainfall-runoff modelling (Wood et al. 1988) or mechanics of heterogeneous, composite and granular material (Drugan and Willis 1996, Kanit et al. 2003, Wiacek et al. 2012).

The size of a REV depends on the expected accuracy in the estimation of the property and on the property itself. Typical sizes vary across several orders of magnitude. For instance, REV in a sand medium was estimated at about 10 mm^3 (Costanza-Robinson et al. 2011). For granular plant material, Wiacek et al. (2012) report REV sizes in-between five and twenty times the size of the largest particles, while REV sizes are evaluated in-between a thousand and ten thousand crystals in steel material (Bettaieb et al. 2012).

1.2.2 Integral formulation

The flow chart in Figure 1-2 provides an overview of the main approaches used in literature to derive SWE with porosity, as well as the different forms obtained. For each of them, Table 1-1 summarizes the main characteristics and limitations, as detailed hereafter. For each approach listed in Table 1-1, we report only the main references to this approach in Figure 1-2.

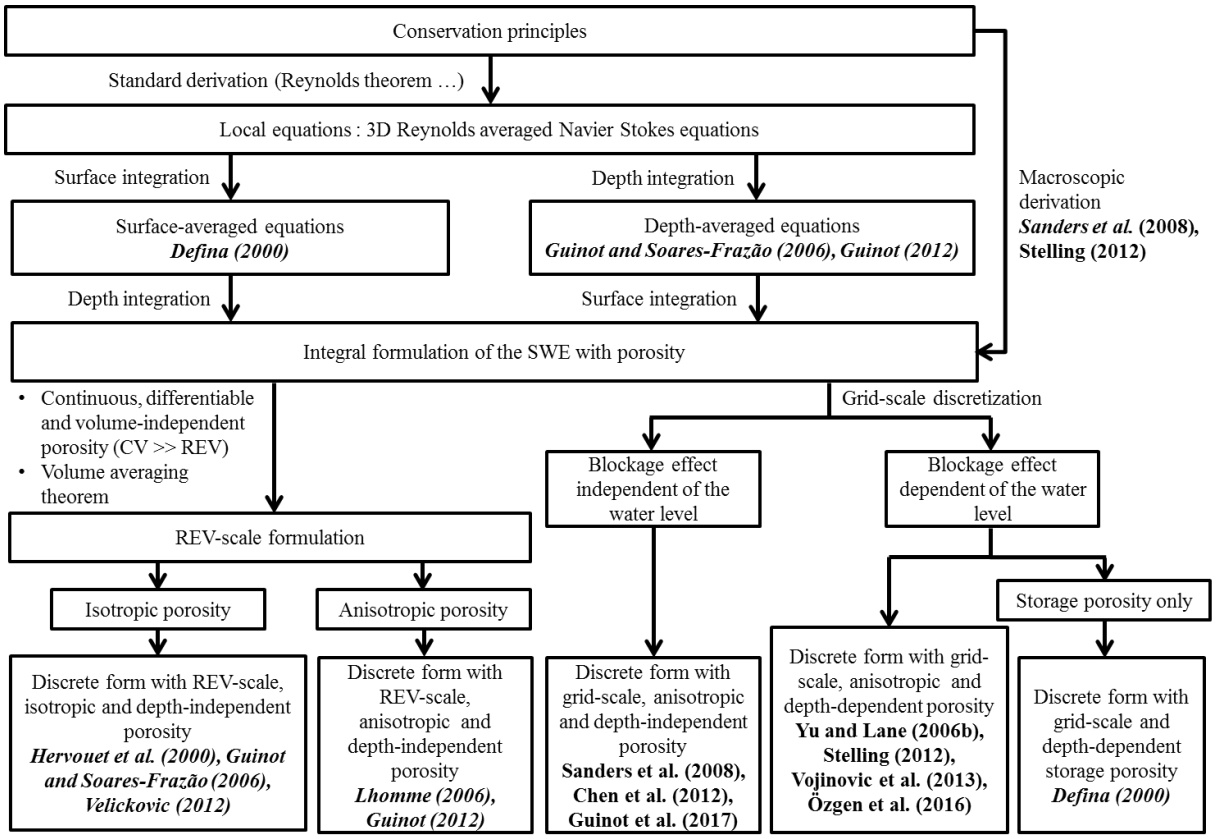

Figure 1-2 : Derivations and formulations of the porosity-based models. Only the former reference to each kind of approach listed in Table 1-1 are reported.

	Diffusive wave	Dynamic wave			
	Grid-based porosity parameters	REV-based porosity parameters		Grid-based porosity parameters	
	Non-isotropic	Isotropic	Non-isotropic	Isotropic	Non-isotropic
Depth-independent Porosity parameters	**Chen et al. (2012a)** & Chen et al. (2012b)	**Hervouet et al. (2000)** & Hervouet (2003) **Guinot and Soares-Frazão (2006)** & Soares-Frazão et al. (2008)	**Lhomme (2006)** **Velickovic et al. (2016)** **Guinot (2012)**		**Sanders et al. (2008)**, Schubert and Sanders (2012) & Kim et al. (2014, 2015) **Guinot et al. (2017)**
Depth-dependent Porosity parameters	**Yu and Lane (2006b)** & McMillan and Brasington (2007) **Vojinovic et al. (2013)**			**Defina (2000)**, Bates (2000) & Bates et al. (2003)	**Stelling (2012)** & Volp et al. (2013) **Özgen et al. (2016)**

Table 1-1: Summary of the porosity-based models, as well as the main characteristics and limitations.

To derive the SWE with porosity, the three-dimensional Reynolds-averaged Navier-Stokes equations, which express the conservation of mass and momentum, are integrated over a CV such as defined in section 1.2.1. Combined with the standard assumption of shallow flow (including hydrostatic pressure distribution), this leads to the integral formulation of the SWE with porosity.

In practical terms, the volume integration over the CV may involve a depth-averaging operation followed by a surface averaging over the horizontal projection of the CV, or vice-versa (Figure 1-2). Most authors used the former approach as they started from the standard SWE without porosity (Guinot and Soares-Frazão 2006, Guinot 2012); but Defina (2000) used a surface-average followed by a depth-average. While both approaches should result in identical volume-averaged equations, Defina (2000) only considered storage porosity in her formulation.

Instead of performing a mathematical integration of local equations over the CV, an alternate approach consists in applying directly the conservation principles to a CV involving obstacles and, hence in deriving macroscopically the integral formulation of the SWE with porosity. This approach was followed by Sanders et al. (2008) and Stelling (2012). Sanders et al. (2008) obtained the following expressions for the integral formulation of the SWE with porosity:

$$\frac{\partial}{\partial t}\int_{\Omega} ih d\Omega + \int_{\partial\Omega} ih\left[\mathbf{u}\cdot\mathbf{n}\right] d\partial\Omega = 0 \tag{1-3}$$

$$\begin{aligned} &\frac{\partial}{\partial t}\int_{\Omega} ih\mathbf{u} d\Omega + \int_{\partial\Omega} ih\left[\mathbf{u}\mathbf{u}\cdot\mathbf{n}\right] d\partial\Omega + \\ &\int_{\partial\Omega}\frac{1}{2} gih^2\mathbf{n} d\partial\Omega = \int_{\partial\Omega}\frac{1}{2} gih_{\eta_0}^2\mathbf{n} d\partial\Omega - \int_{\Omega} ic_D^f \boldsymbol{u} V d\Omega - S_{add} \end{aligned} \tag{1-4}$$

where i is a binary density function equal to 1 in void areas and to 0 otherwise, $\mathbf{u} = \left[u_x; u_y\right]$ the horizontal velocity, $\mathbf{n} = \left[n_x; n_y\right]$ the unit outward vector normal to $\partial\Omega$, g the gravity acceleration, h_{η_0} the water depth for a uniform free surface within the CV, c_D^f accounts for the bottom shear stress, $V = \sqrt{u_x^2 + u_y^2}$ and S_{add} is an additional loss term detailed hereafter.

The fluid pressures acting on the obstacles and on the bottom are lumped into a "quasi-conservative" divergence term (first term on the right hand side of Eq. (1-4)), consistently with the formulation introduced by Valiani and Begnudelli (2006). This divergence term is discussed in detail in section 2.3.

As reported in Table 1-2, the additional loss term may account for the drag force applied on buildings (Hervouet et al. 2000, Sanders et al. 2008, Guinot 2012, Özgen et al. 2016b). A generalized scalar drag formula is used to take into account energy losses near the obstacles:

$$S_{add} = \int_{\Omega} i c_D^b \boldsymbol{u} V d\Omega \text{ where } c_D^b = \frac{1}{2} c_D^0 a h \qquad (1\text{-}5)$$

where c_D^0 is a drag coefficient and *a* is an obstruction parameter defined as the average width of obstruction per unit of the CV area. The drag force term depends on the flow velocity magnitude and direction, as well as on the pattern of obstacles. Schubert and Sanders (2012) propose a simpler direction-independent formulation of the obstruction parameter based on the average width of obstructions at the cell edges. Guinot et al. (2017) proposed an anisotropic building drag term by extending the scalar drag coefficient c_D^b to a second order drag tensor.

For some authors, the additional loss term is simply a head loss term. Guinot and Soares-Frazão (2006), Lhomme (2006) and Soares-Frazão et al. (2008) use the additional head loss term to account for head losses due to crossroads, expansions and constrictions of the flow. While Lhomme (2006) use a second order tensor of head loss coefficients, Guinot and Soares-Frazão (2006) and Soares-Frazão et al. (2008) use a Borda-like formula which evaluates the head loss due to a sudden variation in the flow cross-sectional area through a so-called contraction coefficient. This formulation is based on two idealized arrangements of buildings (aligned vs. staggered) and on an initial estimation of the flow direction in the urban area. While the approach proved to be effective to reproduce flows in such idealized configurations, its applicability for real-world urban areas has not been proven yet.

Velickovic et al. (2016) consider the anisotropic nature of the drag loss term through a fourth order drag tensor of head losses. However, the authors acknowledge that future work is required to improve and generalize the methodology and to develop a general calibration procedure.

		No	Increased roughness coefficient	Additional loss term					
				Building drag term			Head loss term		
				General	2th order tensor	Simplified	Scalar	2th order tensor	4th order tensor
Depth-independent Porosity parameters	**Isotropic**			**Hervouet et al. (2000)** & Hervouet (2003)			**Guinot and Soares-Frazão (2006)** & Soares-Frazão et al. (2008)	**Lhomme (2006)**	**Velickovic et al. (2016)**
	Non-isotropic		**Chen et al. (2012a)** & Chen et al. (2012b)	**Sanders et al. (2008), Guinot (2012)**	**Guinot et al. (2017)**	**Schubert and Sanders (2012)** & Kim et al. (2014, 2015)			
Depth-dependent Porosity parameters	**Isotropic**	**Defina (2000)**, Bates (2000) & Bates et al. (2003)							
	Non-isotropic	**Stelling (2012)** & Volp et al. (2013), **Yu and Lane (2006b)** & McMillan and Brasington (2007)	**Vojinovic et al. (2013)**	**Özgen et al. (2016)**					

Table 1-2: Summary of the different formulation of the losses related to buildings.

1.2.3 REV-scale formulation

The integral formulation derived in section 1.2.2 gives an average description of the SWE at each point in space. Provided that the planar extent Ω of the CV is larger than the size of the REV related to the porosity parameter, the storage porosity becomes independent of Ω. Moreover, according to Sanders et al. (2008), the porosity becomes continuous, differentiable and isotropic if the size of the CVs for which porosities are computed is higher than the size of the REV. Therefore, the discontinuous binary density function *i* is replaced by a continuous, differentiable and isotropic function ϕ, representative of mathematical expectation values of the presence of void at the scale of the REV. The *REV-scale formulation* (called *differential formulation* by Sanders et al. (2008)) of the SWE with porosity is then derived from the application of the local volume averaging theorem (Whitaker 1967, Vafai and Tien 1981, Gray and Hassanizadeh 1989) to the integral formulation.

The REV-scale formulation of the SWE with porosity was introduced by Defina (2000) to handle partially wet and irregular topographies. His work was extended by Bates (2000) and Bates et al. (2003) to represent dynamic wetting and drying of cells in a finite volume scheme. The obtained equations involve a depth-dependent areal storage porosity. This is a unique feature of these

models since all subsequent contributions based on the REV-scale formulation of the equations assume that the porosity is depth-independent (Table 1-1).

Hervouet et al. (2000) proposed a REV-scale formulation of the SWE with depth-independent isotropic porosity for urban flood modelling. Guinot and Soares-Frazão (2006) derived mathematically an extended formulation, which was later applied by Soares-Frazão et al. (2008). Numerical discretizations of the SWE with isotropic porosity were proposed by Cea and Vázquez-Cendón (2010), Finaud-Guyot et al. (2010) and Mohamed (2014).

Compared to the standard SWE, the fluxes and source terms in the resulting equations were modified as follows (Guinot and Soares-Frazão 2006):

$$\frac{\partial}{\partial t}(\phi \mathbf{U}) + \frac{\partial}{\partial x}(\phi \mathbf{F}) + \frac{\partial}{\partial y}(\phi \mathbf{G}) = S\,, \tag{1-6}$$

with

$$\mathbf{U} = \begin{bmatrix} h \\ hu_x \\ hu_y \end{bmatrix},\ \mathbf{F} = \begin{bmatrix} hu_x \\ hu_x^2 + gh^2/2 \\ hu_x u_y \end{bmatrix},\ \mathbf{G} = \begin{bmatrix} hu_y \\ hu_x u_y \\ hu_y^2 + gh^2/2 \end{bmatrix},\ \mathbf{S} = \begin{bmatrix} 0 \\ S_{0,x} + S_{f,x} \\ S_{0,y} + S_{f,y} \end{bmatrix} \tag{1-7}$$

$$S_{0,x} = -\phi gh\frac{\partial z_b}{\partial x} + g\frac{h^2}{2}\frac{\partial \phi}{\partial x}\ ;\ S_{0,y} = -\phi gh\frac{\partial z_b}{\partial y} + g\frac{h^2}{2}\frac{\partial \phi}{\partial y} \tag{1-8}$$

$$\begin{aligned} S_{f,x} &= -\phi gh\left(u_x^2 + u_y^2\right)^{1/2} u_x\left(\frac{1}{K^2 h^{4/3}} + s_x\right); \\ S_{f,y} &= -\phi gh\left(u_x^2 + u_y^2\right)^{1/2} u_y\left(\frac{1}{K^2 h^{4/3}} + s_y\right) \end{aligned} \tag{1-9}$$

with h the water depth, ϕ the depth-independent isotropic porosity, u_x and u_y the x- and y-depth-averaged velocity components, $S_{0,x}$ and $S_{0,y}$ the topographic source terms in the x- and y- directions. $S_{f,x}$ and $S_{f,y}$ include the energy losses due to bottom and wall shear stress, as well as those due to variations of velocities in the x- and y- directions within the CV, z_b the mean bottom elevation, s_x and s_y the head loss coefficients accounting for the local variations of velocities in the x- and y- directions and K the Strickler coefficient. The additional term in $S_{0,x}$ and $S_{0,y}$ represents the pressure applied on the obstacles.

Lhomme (2006) extended Eq. (1-6) to anisotropic porosities. Besides the storage porosity ϕ, conveyance porosities ψ_x and ψ_y were introduced and assigned to the border fluxes **F** and **G**.

However, the anisotropic conveyance porosities were not properly defined by Lhomme (2006), who displayed the resulting equations but did not apply them for urban flood modelling.

Guinot (2012) described a multiple porosity model in which the domain is subdivided into five types of regions. They correspond, respectively, to obstacles without voids, regions with water at rest, regions of isotropic 2D flow, regions of anisotropic 1D flow and interconnections between the 1D anisotropic flow regions. These regions may exchange mass and momentum based on local differences in, respectively, water levels and energy heads. In each type of region, a specific formulation of the SWE is used for the computation of water depth and flow velocity. This multiple porosity model is reported to give more accurate results than a standard isotropic porosity model; but the a priori determination of the different flow regions is particularly complex for real-world urban areas.

Velickovic et al. (2016) proposed a new REV-scale formulation in which the anisotropy of the urban area is indirectly taken into account through a closure expression including drag and dispersion terms in the momentum equation. However, the authors acknowledge that these closure relations fail to reproduce real-world anisotropic flow and that calibration of the model remains an unsolved issue for general cases.

Based on simple considerations on idealized Cartesian and periodic urban networks, Guinot (2012) suggests that a REV would not exist for real-world urban areas. However, he argues that the error on the isotropic porosity evaluation is of the same order as other errors in the model, such as the estimation of the friction coefficient. According to him this enables the use of the REV-scale formulation to model urban floods with a reasonable accuracy.

1.2.4 Grid-scale formulation

The direct discretization of the integral formulation avoids questionable assumptions concerning the size of the REV because porosities are defined here directly at the grid scale as discrete cell-properties.

Sanders et al. (2008) discretized directly the integral formulation of the SWE based on a non-staggered grid and a Godunov-type finite volume method:

$$\left(\phi_j h_j \Omega_j\right)^{n+1} = \left(\phi_j h_j \Omega_j\right)^{n} - \Delta t \sum_k \left(\psi_k h_k \left[\mathbf{u}_k \cdot \mathbf{n}_k\right] \partial\Omega_k\right)^{n^*} \tag{1-10}$$

$$\begin{aligned} &\left(1 + \left(\Delta t \left(c_D^f + c_D^b\right) \frac{V_j}{h_j}\right)^{n^*}\right) \left(\phi_j h_j \Omega_j \mathbf{u}_j\right)^{n+1} \\ &= \left(\phi_j h_j \Omega_j \mathbf{u}_j\right)^{n} - \Delta t \sum_k \left(\psi_k \left(h_k \left[\mathbf{u}_k \mathbf{u}_k \cdot \mathbf{n}_k\right] + \frac{1}{2} g h_k^2 \mathbf{n}_k - \frac{1}{2} g h_{k,\eta_{0,j}}^2 \mathbf{n}_k\right) \partial\Omega_k\right)^{n^*} \end{aligned} \tag{1-11}$$

where n represent a time step and n^* is an intermediate time step in-between n and n+1.

The depth-independent porosities ϕ and ψ are defined at the grid scale as cell- and border-properties (Table 1-1), making them mesh-dependent. Moreover, since the conveyance porosities are computed at borders, a *conformal meshing* is required to capture correctly the conveyance impact of obstacles at borders (Sanders et al. 2008). This requirement of a conformal meshing is a limitation for the maximum size of the coarse meshes, particularly in heterogeneous urban areas. Sanders et al. (2008) and Kim et al. (2015) demonstrated that the grid-scale formulation gives more accurate results than the REV-scale formulation.

Yu and Lane (2006b) and McMillan and Brasington (2007) employed a depth-dependent parametrization of the volume of water stored within the cells and of the cross-sectional areas at their borders in the context of the 2D diffusive wave equations. A multi-layered model was developed by Chen et al. (2012b) to reflect separate flow paths within a single coarse cell using non-inertia SWE.

Among others, Cea et al. (2010) showed that fully dynamic two-dimensional models give generally better results than simplified descriptions such as diffusive wave-based description for urban flood modelling.

Stelling (2012), Volp et al. (2013) and Vojinovic et al. (2013) used finite volume approaches, based on staggered grids, for solving the integral formulation of the SWE with porosity (Table 1-1). The two main unknowns, i.e. the volume of stored water and the mean velocity, are

respectively assigned to cells and to borders. Lookup tables are used to relate the water level in each cell to, respectively, the available volume for water storage and the cross-sectional area for fluid exchange through the borders of the cells. This feature enables the model to account for the effect of obstacles on the available volume for water storage and on the fluxes even when these obstacles get submerged. Although these authors do not refer explicitly to porosities, the lookup tables act as depth-dependent anisotropic porosities and are therefore of particular relevance for the following of this chapter.

The depth-independent grid-scale formulation was extended to depth-dependent porosity by Özgen et al. (2016). However, the application of the depth-dependent formulation was restricted to rainfall-runoff in an idealized urban catchment.

Recently, Guinot et al. (2017) have improved the grid-scale formulation by distinguishing the fluid velocity at cell centres from those along the cell edges. They use a closure model to evaluate the latter from the value of the former. Additionally, they incorporate a transient momentum dissipation coefficient, which improves the reproduction of wave propagation speeds for highly transient positive waves; but it requires a case-by-case calibration. This model is not discussed here but in section 4.3.3.

1.3. Analysis of some major assumptions of the existing formulations

Most standard formulations of the SWE with porosity presented in Table 1-1 were derived considering *depth-independent* porosities. Moreover, all REV-scale formulations of the SWE with porosity were obtained under the following additional assumptions: *differentiability* of all variables (i.e. flow properties and porosities), as well as the *size of the CV being larger than the REV*. Finally, the absence of a proper definition of an anisotropic conveyance porosity in the REV-scale formulations leads to the use of an *isotropic* porosity by several authors. These major assumptions are analysed in this section based on an idealized urban network and on a real-world urban area.

1.3.1 Test cases: idealized urban network and real-world urban area

Guinot (2012) analysed the size of REVs for periodic Cartesian urban networks with depth-independent porosities. The extent of the urban network was assumed infinite in all directions. The widths of the streets W and of the obstacles W_b were considered as variable parameters to account for multiple configurations of the urban network (Figure 1-3). In each configuration and

for each location of the centre of CVs, the storage porosity may be evaluated for a square CV of edge size *e*.

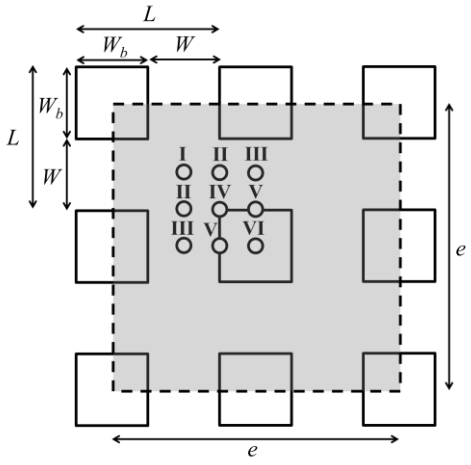

Figure 1-3 : Excerpt of the periodic Cartesian urban network defined by Guinot (2012).

Here, the analysis performed by Guinot (2012) is extended. Most importantly, we discriminate between storage porosity within the CVs and conveyance porosities at their four borders. We also analyse the sensitivity of the size of the REV with respect to the location of the point around which the considered CVs are centred. The nine points labelled I to VI in Figure 1-3 have been tested. Due to the symmetry of the results, some labels (II, III and V) refer to two different geometric locations, leading to identical results in terms of values of porosity.

To complement the analysis conducted by Guinot (2012), we consider here not only idealized urban networks; but also a real-world case study (centre of Liege, Belgium), involving depth-dependent porosities. The centre of the city of Liege is a densely urbanized area (Figure 1-4a). It is crossed by the river Meuse and its derivation channel. A detailed digital surface model (DSM) is available (Figure 1-5). It was obtained from airborne Lidar altimetry, and was processed and validated at a resolution of 5 m by 5 m. Four particular points (A, B, C and D in Figure 1-4a) were considered as centres of CVs for the analysis. To make the main text of this chapter easier to read, we report only the results for point D in the manuscript while results for other locations are displayed in Appendix A for the sake of completeness. Figure 1-5 represents the DSM around these points.

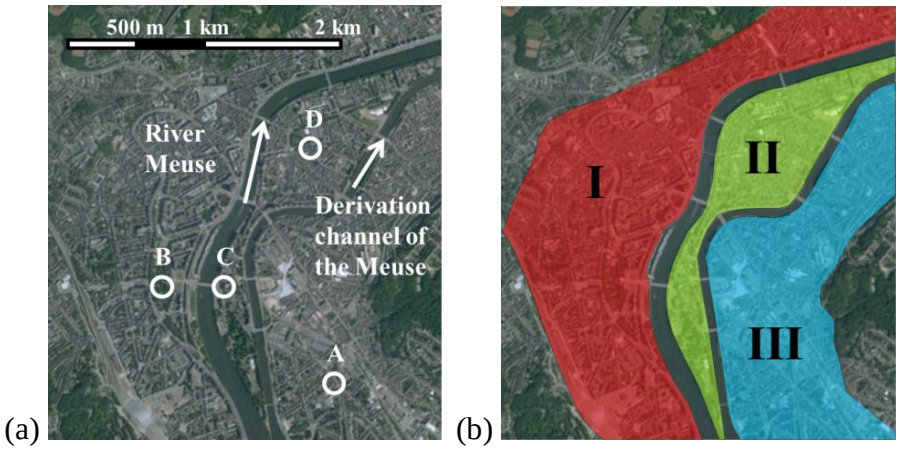

(a) (b)

Figure 1-4 : (a) Aerial picture of the city of Liege, Belgium, with the localization of the different locations (points A, B, C and D) around which square CV are determined. (b) Representation of the QHA.

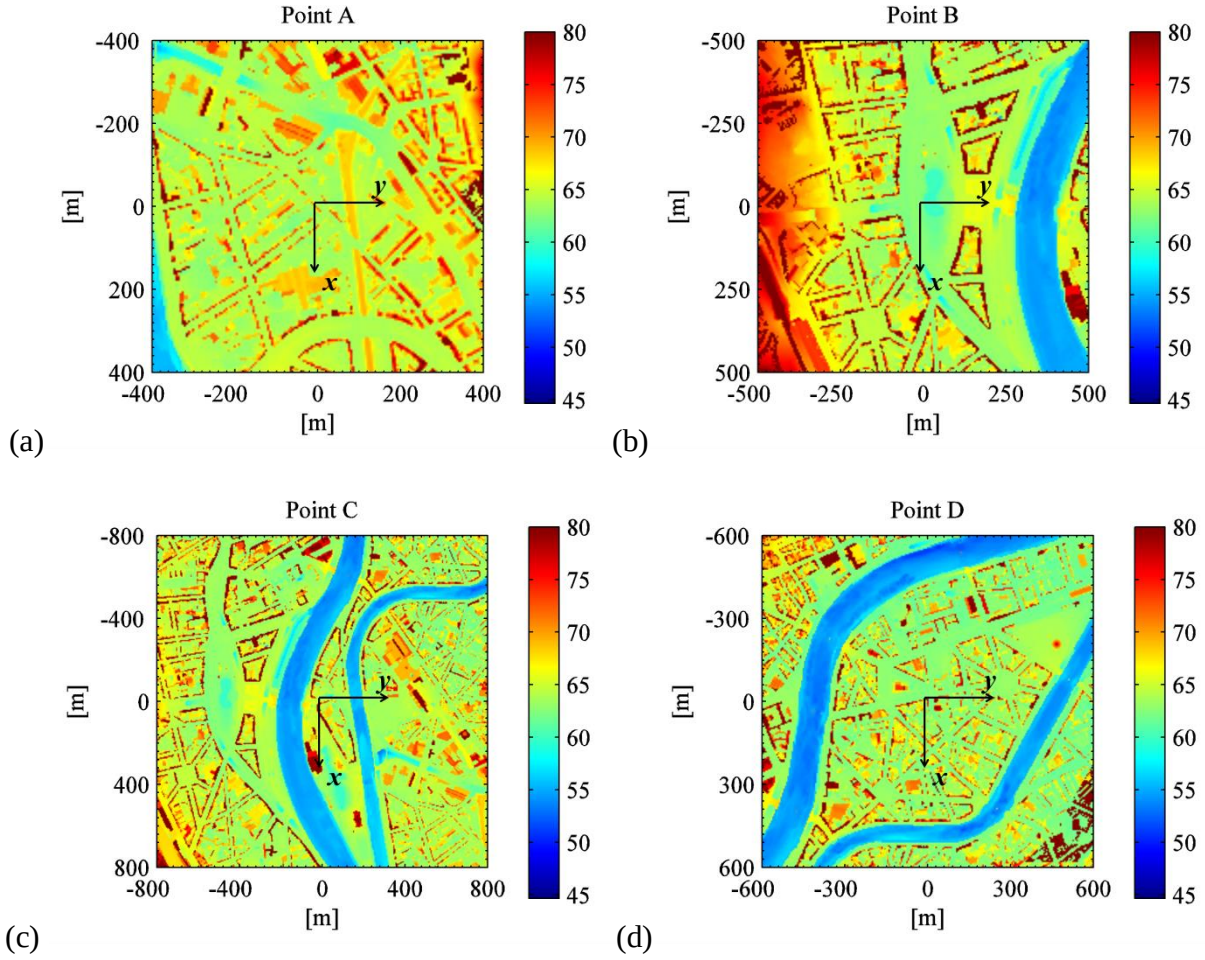

(a) (b) (c) (d)

Figure 1-5 : Digital surface models (DSM) around the four points considered in the city of Liege.

1.3.2 Representative elementary volume

Idealized urban network

Since the obstacles considered in the idealized urban network are prismatic along the vertical direction, the volumetric storage porosity Φ equals the areal storage porosity ϕ, which is here independent of z. Based on Eq. (1-1), the storage porosity has been computed as a function of the size of the CV and for different locations of the centre of the CV. The computed porosities for points I and VI are displayed in Figure 1-6 for four different configurations of the urban network (W/L = 0.1, 0.3, 0.5 and 0.7, with $L = W + W_b$). The results for points II to V are reported in Figure A-1. All results are presented using a normalized form of the size of the CV, corresponding to the side length e scaled by the size L.

As shown in Figure 1-6, the computed storage porosity tends towards an asymptotic value for large values of e/L (i.e. large CVs). This asymptotic porosity, noted ϕ_{as}, depends strongly on the parameter W/L which characterizes the urban network, while it obviously does not depend on the position of the point around which the CV is centred. In contrast, for relatively small CVs (i.e. low values of e/L), the porosity value depends also on the specific location of the centre of the CV.

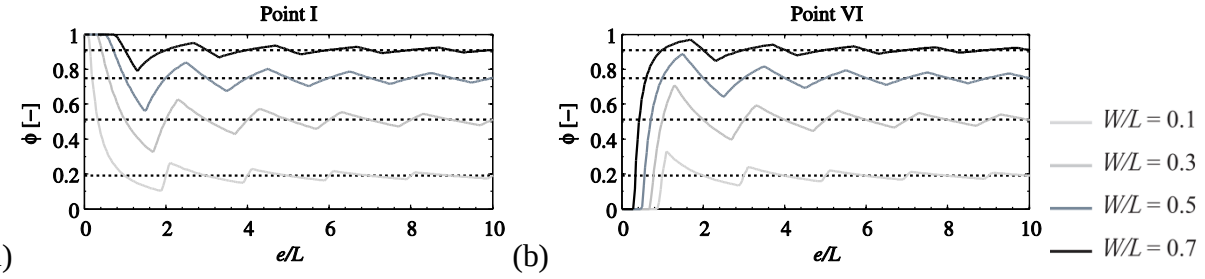

Figure 1-6: Evolution of the storage porosity ϕ for different sizes e/L of the CV and locations I and VI of the point around which the considered CV are located.

To estimate the REV size for porosity in the idealized urban network, the porosity values ϕ computed for gradually increasing sizes of the CV were compared to their corresponding asymptotic value ϕ_{as}. The REV is the smallest CV size above which the difference between ϕ and ϕ_{as} remains below a chosen threshold. We considered here a threshold of 5 %. Changing the value of this threshold between 1 % and 10 % was tested and it did not change the conclusions of the analysis.

Figure 1-7b and Table 1-3 show the non-dimensional size $(e/L)_{REV}$ of the REV as a function of, respectively, the configuration of the urban network (i.e. *W*/*L* was varied) and for different locations of the centre of the CV. Figure 1-7a displays the corresponding values of porosity.

Comparing Figure 1-7a and Figure 1-7b reveals that, although the different curves vary in shape, they all lead to larger REVs as the porosity decreases (i.e. for lower values of *W*/*L*). For the lowest values of *W/L*, the size of the REV is high because a small variation of the porosity induces an important relative variation due to the low porosity value. The size of the REV varies significantly depending on the location of the centre of the CV.

In this research, we focus on floods in urban areas, for which the actual values of *W/L* are relatively low. Therefore, the size of the REV is generally high. For example, with a spatial length *L* of 200 m, size *e* of the REV exceeds 1 km for *W/L* = 0.5 $\left(\phi_{REV} = 0.75\right)$ at points I and VI (Table 1-3).

Hence, this order of magnitude of $(e/L)_{REV}$ suggests that defining a REV in a realistic urban setting is hardly possible.

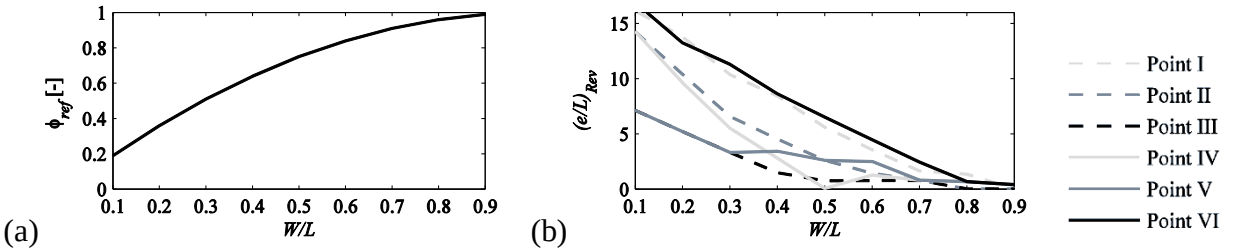

Figure 1-7 : (a) Reference storage porosity ϕ_{ref} and (b) size $(e/L)_{REV}$ of the porosity REV as a function of the urban network configuration (W/L) for different locations of the centre of the CV (points I to VI).

W/L	ϕ_{as}	$(e/L)_{REV}$					
		Point I	Point II	Point III	Point IV	Point V	Point VI
0.1	**0.19**	16.1	14.2	7.1	14.2	7.1	16.9
0.3	**0.51**	10.4	6.6	3.3	5.5	3.3	11.3
0.5	**0.75**	5.6	2.6	0.7	0.0	2.6	6.5
0.7	**0.91**	1.6	0.8	0.8	0.8	0.8	2.4

Table 1-3: Size of the porosity REV $(e/L)_{REV}$ and asymptotic storage porosity ϕ_{as} for different network configuration (W/L) and location of the point around which the CV is centred (points I to VI).

Real-world urban area

For the city of Liege, the porosity becomes depth-dependent and, hence, the areal storage porosity ϕ is not equal to the volumetric storage porosity Φ. To show the influence of the depth-dependency, the areal storage porosity ϕ was evaluated for different levels *z*, corresponding to typical water levels encountered during floods in Liege.

As shown in Figure 1-8 for point D, the storage porosities do not converge towards asymptotic values at large scale due to the non-homogeneity of real-world urban patterns even at large scales. Particularly strong variations of these porosities are encountered as a result of sharp topographic variations or specific features such as rivers, large parks, … To account for this macroscopic heterogeneity (Eaton 2006, Costanza-Robinson et al. 2011, Bear 2013), we introduce the concept of *Quasi-Homogeneous Area* (QHA), which is a suburban area homogeneous on macroscopic scale (Haque 2015). Inside these areas, the porosity variations are expected to converge to an asymptotic value for increasing sizes of CVs.

Three QHA were distinguished (Figure 1-4b). The first is the islet located between the river Meuse and its deviation channel (II). The two others (I and III) are limited by a waterway (Meuse or its derivation channel) on one side and by a sharp rise in the topography on the other side.

The behaviour of the curves in Figure 1-8 may be classified into two groups: those mainly representative of ground level variations (lower elevations) and those influenced by the presence of buildings (upper elevations).

The inhomogeneous patterns characterizing the urban networks do not guaranty a convergence of the porosity towards a single asymptotic value when the size of the CV increases. For point D (Figure 1-8a), the porosity values seem to stabilize at a depth-dependent level for CV sizes between 240 m and 720 m before varying again when leaving the QHA II.

In any case, a REV cannot be defined below practical CV sizes (10-100 m) and the determination of a single depth-independent storage porosity for each QHA seems here strongly arguable.

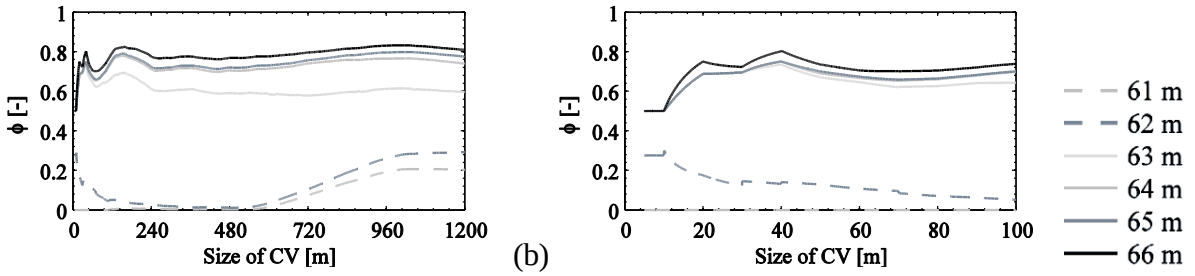

Figure 1-8: Evolution of the depth-dependent areal storage porosity ϕ as a function of the size of the CV at point D and for different levels.

1.3.3 Spatial variability of porosity

The analysis of the spatial variability of porosity of the idealized urban network is detailed in Appendix A.2.

For the city of Liege, the areal storage porosity ϕ was calculated for each grid cell along *x* and *y* directions using the available DSM with a grid size of 5 m. The considered CV sizes were varied between the size of the DSM grid (5 m) and 50 m. The spatial variations of the areal storage porosity near point D are shown in Figure 1-9. The areal storage porosity is depicted at a level *z* corresponding to a mean water depth of about 1 m, i.e. $z = 63$ m. Continuous lines show the porosities computed at each topographic cell (i.e. the CV was translated by steps of 5 m). The dashed line shows the porosity variations from one CV to the next one for a size of the CV equal to 50 m (i.e. the CV was translated by steps equal to its size).

When the size of the CV is the same as the resolution of the DSM grid (5 m), the areal storage porosity is binary: either the cell is free for water storage or it is not, and the porosity is highly discontinuous. When the size of the CV increases, the variations of porosity become more continuous. Nonetheless, for a size of the CV of 50 m, the variations of porosity between one CV and the next one (dashed line) remain abrupt and represent relatively poorly the actual variations

of porosity at a finer scale (black plain line). This is particularly true for the results obtained along the *y* axis.

Therefore, for practical grid scales, the spatial variability of porosity is high and is poorly reproduced when increasing the scale.

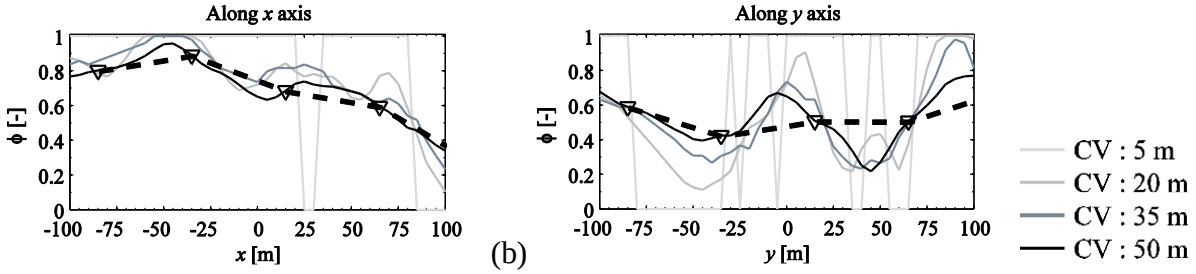

Figure 1-9: Spatial variation of the areal storage porosity ϕ at z = 63 m around point D.

1.3.4 Isotropic vs anisotropic porosities

For the city of Liege, the topographic data are available in raster form. Hence, evaluating the linear conveyance porosity ψ from Eq. (1-2) is not straightforward, particularly if the border of the CV is aligned with borders of the grid of the raster DSM. Therefore, we extended here definition (1-1) to assign a minimum "width" to the linear element for which the conveyance porosity ψ is computed. As a result, ψ was evaluated at a border of the CV as the void fraction of the rectangular area centred on the mid-point of the border, with the length equal to the border length and the width equal to DSM grid size (5 m).

In Figure 1-10a, the areal storage porosity ϕ of a CV is compared to the linear conveyance porosities ψ at the four borders of the CV. Here also, the conveyance porosities vary much more with the size of the CV than the storage porosity does. The computed conveyance porosities are totally different from one border to the other and their values do not match the storage porosity. This confirms the strongly anisotropic nature of conveyance porosities.

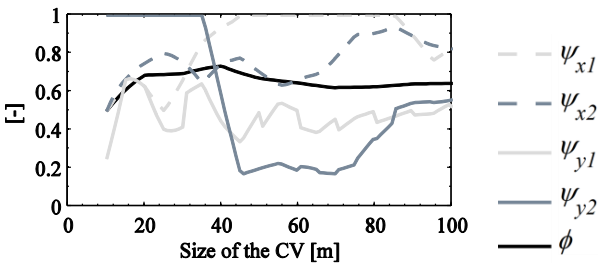

Figure 1-10: Evolution of areal storage ϕ and linear conveyance ψ porosities as a function of the size of the CV around point D at an altitude of 63 m.

The comparison between isotropic and anisotropic porosity, including mean conveyance porosities, is presented in Appendix A.3 for the idealized urban network.

1.4. Conclusion

This chapter reviews recent literature concerning urban flood modelling with the SWE involving porosity parameters. The derivations of the SWE with porosity are either related to a representative elementary volume (REV-scale) or to the grid-scale. The two approaches are critically analysed in terms of underlying assumptions and limitations.

To derive the REV-scale formulation of the SWE with porosity, the porosity parameters are usually assumed continuous, differentiable and isotropic. This implies the existence of a REV, which should in principle be smaller or of comparable size as the computational cell, and in any case smaller than the macroscopic length scale defining the extent of the urban area. Note that, in this chapter, we focused on porosity REVs, considering hence only geometric properties of the urban network, while other REVs can be found when flow dynamics are considered (such as friction REVs).

Based on quantitative analyses for idealized and real-world urban areas, it has been shown that none of these assumptions can be fulfilled for usual cell sizes as used in practice. This limitation does not arise in the case of models with porosities defined at the grid-scale, which seem more adequate for typical real-world urban flood modelling. However, the drawback of using anisotropic grid-scale porosity is the necessity of a conformal mesh, or a more advanced evaluation of the conveyance porosity at the cell borders, as discussed in Chapter 4 and particularly in section 4.3. In this research, we develop an **advanced anisotropic porosity model**, with **porosity parameters defined at the grid-scale**.

Finally, the use of depth-independent porosity does not allow for the consideration of the submersion of obstacles. In general, models would hence benefit from being built on depth-dependent porosities. Nonetheless, since we focus here on the impact of urbanization on flooding, the main obstacles of significance are buildings, so that we can reasonably consider that flood levels remain lower than building roofs and consequently we use **depth-independent porosity parameters**.

2. Formulation of the porosity-based shallow-water model

In section 1.4, we identified the anisotropic porosity model as the most suitable to this research. One example of such model is expressed by Eqs (1-10)-(1-11). Here, we discuss some specific aspects of the model formulation, as it has been used in this research.

In all existing porosity-based models, the storage and conveyance porosity parameters are included, respectively, in the local acceleration term and in the purely advective terms. In contrast, there is no general consensus concerning the formulation of the pressure and bed slope terms in the porosity-based SWE.

The wording *pressure term* refers here to the terms representing the resultant of the hydrostatic pressure along the edges of the computational cells, i.e. along both the fluid-fluid and fluid-solid interfaces. In section 2.1, we propose a formulation of the pressure term, which is physically-sound and also complies with the flux-vector splitting technique used in the model Wolf2D.

Some authors used the standard formulation of the *bed slope term* (SFB) (Hervouet et al. 2000, Erpicum et al. 2006, Guinot and Soares-Frazão 2006) while others used the divergence formulation (DFB) (Sanders et al. 2008, Özgen et al. 2016b, Guinot et al. 2017). In section 2.2, we highlight the benefits of using the DFB formulation rather than the SFB formulation in the porosity SWE for the specific case of a lake at rest over an irregular bed level and considering the porosity formulation of the pressure term introduced in section 2.1.

The use of the DFB formulation in Wolf2D requires additional developments to identify the optimal discretization of this term so that the well-balanced property of the system is preserved and that energy balance can be ensured as much as possible. This is detailed in section 2.3 for the SWE without porosity; and the resulting optimal discretization is transposed to the porosity-based SWE in the following of the manuscript. In section 2.3, the optimal discretization of the DFB term for the standard SWE is analysed theoretically (section 2.3.1) and numerically (section 2.3.3) based on two test cases:

- first, we consider a 1D steady flow in a smooth channel with an obstacle (section 2.3.3.1);
- second, based on energy conservation properties of Ritter solution for idealized dam break flow, we evaluate the proposed discretization of the DFB term for a 1D dam break flow in a channel with a bump (section 2.3.3.2).

Finally, we summarize in section 2.4 the porosity formulations of the pressure and bed slope terms resulting from developments in sections 2.1 and 2.3.

In this chapter, we consider a constant piecewise reconstruction of the variable from the cells to the edges. As highlighted in section 2.4, this enables a suitable formulation of the pressure and bed slope terms in the resulting porosity-based SWE.

2.1. Porosity formulation of the pressure term

In this section, we derive the discretised formulation of the pressure term in the anisotropic porosity model.

To do so, we consider a single computational cell *i* in a Cartesian grid. The cell size along the *x*- and *y*- directions is Δx and Δy, respectively, with $\Delta x = \Delta y$. We focus on the formulation of the pressure term along the *x* direction, while the result for the *y* direction can be derived based on a similar approach. The left and right edges of the cell are noted *L* and *R*. Only a fraction ψ of each edge length is free for water (void fraction, represented in blue in Figure 2-1a), while the remaining part is blocked by obstacles (shown in red in Figure 2-1a).

Conceptually, we split the cell in several strips, represented by different colour shadings in Figure 2-1b and corresponding respectively to:

- strips for which both the right and the left boundaries are fluid-fluid interfaces ( );
- strips for which both the boundary on either side is a fluid-fluid interface (or);
- strips for which both boundaries are blocked by obstacles ( ).

For each strip individually, the "conveyance porosities" corresponding to the fractions of the edges which constitute the boundaries of the strip, take a value of either 1 (fluid-fluid interface) or 0 (boundary blocked by an obstacle). These situations are handled in a standard SWE solver, such as Wolf2D, since it corresponds simply to boundaries which are either open for fluid exchange or on which a no-flow boundary condition would be prescribed. Therefore, it is possible to evaluate how the standard numerical scheme in Wolf2D would evaluate the pressure term for each strip individually. The rationale behind the derivation of the pressure term formulation in the porosity-based model is that this formulation should mimic the sum of the terms which would be evaluated by the existing numerical scheme in Wolf2D for all the strips.

The bulk pressure term along the *x*- direction is noted $\Delta F_{\mathrm{P},x}$. In the example sketched in Figure 2-1b, this term may be computed as follows:

$$\Delta F_{\mathrm{P},x} = \frac{1}{2} g \frac{\sum_{k=\mathrm{I}}^{\mathrm{VII}} \left(\left[h_k^2 \Delta y_k \right]_R - \left[h_k^2 \Delta y_k \right]_L \right)}{\Delta x}, \qquad (2\text{-}1)$$

which can be rewritten as:

$$\Delta F_{\mathrm{P},x} = \frac{1}{2} g \frac{\left[\sum_{k=\mathrm{I}}^{\mathrm{VII}} h_k^2 \Delta y_k\right]_R - \left[\sum_{k=\mathrm{I}}^{\mathrm{VII}} h_k^2 \Delta y_k\right]_L}{\Delta x}, \tag{2-2}$$

with notations $[\ ]_L$ and $[\ ]_R$ indicating a group of variables evaluated, respectively, at the left and right edges of the cell.

In configurations corresponding to the strips which have one or two boundaries blocked by obstacles, the numerical scheme available in Wolf2D uses the cell value h_i to approximate the value at the cell edge, leading therefore to different values of h at each side of the edge. Hence, Eq. (2-2) becomes:

$$\begin{aligned}
\Delta F_{\mathrm{P},x} &= \frac{1}{2} g \frac{\overbrace{\left(\Delta y_{II} + \Delta y_{III} + \Delta y_V + \Delta y_{VI}\right)}^{[\psi]_R \Delta y}\left[h^2\right]_R + \overbrace{\left(\Delta y_I + \Delta y_{IV} + \Delta y_{VII}\right)}^{[1-\psi]_R \Delta y} h_i^2}{\Delta x} \\
&- \frac{1}{2} g \frac{\overbrace{\left(\Delta y_{III} + \Delta y_{IV} + \Delta y_V\right)}^{[\psi]_L \Delta y}\left[h^2\right]_L + \overbrace{\left(\Delta y_I + \Delta y_{II} + \Delta y_{VI} + \Delta y_{VII}\right)}^{[1-\psi]_L \Delta y} h_i^2}{\Delta x} \\
&= \frac{1}{2} g \frac{\left[\psi h^2\right]_R - \left[\psi h^2\right]_L + \left(\left[\psi\right]_L - \left[\psi\right]_R\right) h_i^2}{\Delta x} \Delta y
\end{aligned} \tag{2-3}$$

In section 2.4, we use the result of Eq. (2-3) in combination with the discretized formulation of the bed slope term, as derived in section 2.3 hereafter, to come up with a final joined formulation of the pressure and bed slope terms, which is used all along the rest of the thesis.

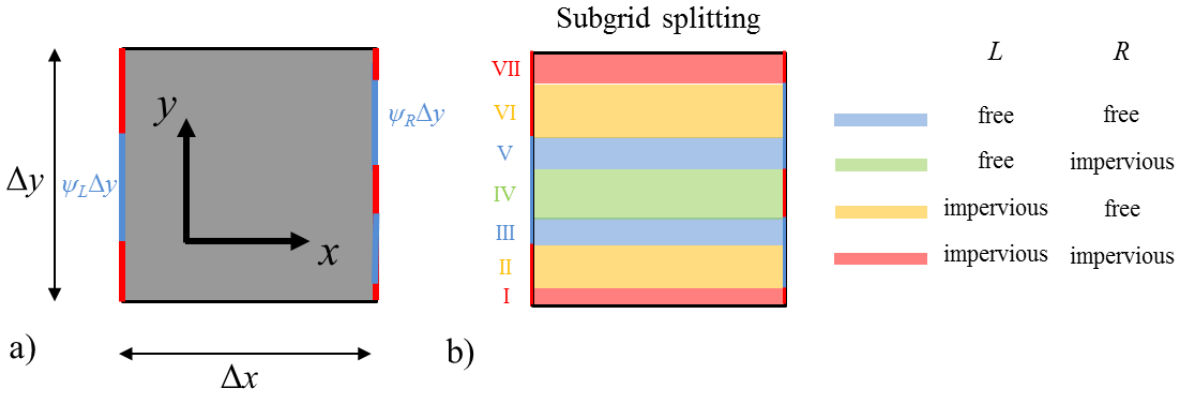

Figure 2-1 : (a) General representation of a computational cell whose the edges are partly free for water (blue for free length and red for obstacles) and (b) subgrid splitting of the cell along the x- direction.

We compared the discretization of the pressure term according to Eq. (2-3) to Eq. (2-4) used by Erpicum et al. (2006):

$$\Delta F_{\mathrm{P},x} = \frac{1}{2} g \frac{\left[h^2\right]_R - \left[h^2\right]_L}{\Delta x} \Delta y \qquad (2\text{-}4)$$

Numerical experiments have shown that the formulation used by Erpicum et al. (2006) is more sensitive to numerical instabilities than formulation (2-3) for cells with low porosity values. In the porosity shallow-water equations, the variation of the discharge in the momentum equation is inversely proportional to the storage porosity ($\partial(\phi q)/\partial t$). While the pressure term is not affected by the presence of obstacles in the formulation of Erpicum et al. (2006), its value changes due to the conveyance porosities in Eq. (2-3). Therefore, cells with low porosity values are more likely to be affected by discharge fluctuations in the formulation of Erpicum et al. (2006) than in Eq. (2-3) since the pressure term takes higher values in the former formula than in the latter one.

2.2. Standard vs. divergence formulations of the bed slope term

The SFB and DFB formulations are first briefly introduced in section 2.2.1 for the standard shallow-water equations (without porosity parameters). Then, the benefit of using the DFB formulation rather than the SFB formulation for porosity-based models is highlighted for the specific case of a lake at rest over an irregular bed level (sections 2.2.2 and 2.2.3).

2.2.1. Presentation of the SFB and DFB formulations

For a prismatic channel with a rectangular cross-section without lateral inflow nor outflow, the one dimensional (1D) SWE write:

$$\begin{cases} \dfrac{\partial h}{\partial t} + \dfrac{\partial q}{\partial x} = 0 \\ \dfrac{\partial q}{\partial t} + \dfrac{\partial}{\partial x}\left(\dfrac{q^2}{h} + g\dfrac{h^2}{2} \right) = S_i - S_f \end{cases} \tag{2-5}$$

with g the gravitational acceleration, h the water depth, q the specific discharge, t the time, x the spatial coordinate, S_i the bed slope source term and S_f the friction term.

In Eq. (2-5), the advective terms and the pressure gradient are written in divergence form, which is perfectly suitable for the application of a conservative numerical discretization, such as the finite volume method. In contrast, the bed slope source term S_i writes in a non-conservative form:

$$S_i = -gh\partial z_b / \partial x \tag{2-6}$$

with z_b the bottom elevation. Hereafter, this formulation is referred to as the standard formulation of the bed slope source term (SFB).

The divergence formulation of the bed slope term (DFB) consists in evaluating the bed slope term as the spatial variation of the pressure assuming a uniform water level η_0:

$$S_i = \frac{\partial}{\partial x}\left(\frac{1}{2} g h^2 \right)_{\eta_0} \tag{2-7}$$

where η is the free surface level. $(\ )_{\eta_0}$ means that the quantity in brackets is evaluated for a stationary water level $\eta = \eta_0$.

The equality between Eqs (2-6) and (2-7) is ensured as long as Eq. (2-7) is evaluated based on the assumption of a locally uniform free surface level η_0. This was shown by Valiani and Begnudelli (2006) as follows:

$$-gh\frac{\partial z_b}{\partial x} = -g\left(\eta\frac{\partial z_b}{\partial x} - z_b\frac{\partial z_b}{\partial x}\right) = g\frac{\partial}{\partial x}\left(\frac{z_b^2}{2} - \eta_0 z_b\right) = \frac{\partial}{\partial x}\left[\frac{1}{2}g\left(\eta_0 - z_b\right)^2\right] = \frac{\partial}{\partial x}\left(\frac{1}{2}gh^2\right)_{\eta_0} \quad . \text{(2-8)}$$

2.2.2. DFB formulation in the porosity-based model

We consider a lake at rest over an arbitrary bed level, a computational cell *i* and its left and right neighbours *L* and *R*.

The discretized formulation of the pressure term in the *x*-direction writes (section 2.1):

$$\Delta F_{\mathrm{P},x} = \frac{1}{2}g\frac{\left[\psi h^2\right]_R - \left[\psi h^2\right]_L + \left(\left[\psi\right]_L - \left[\psi\right]_R\right)h_i^2}{\Delta x}\Delta y \qquad \text{(2-9)}$$

Using the DFB term, it seems straightforward that the bed slope term should be discretized as follows:

$$S_{0,x}^{DFB} = \frac{1}{2}g\frac{\left[\psi h_{\eta_{0,i}}^2\right]_R - \left[\psi h_{\eta_{0,i}}^2\right]_L + \left(\left[\psi\right]_L - \left[\psi\right]_R\right)h_i^2}{\Delta x}\Delta y \qquad \text{(2-10)}$$

By comparing Eqs (2-9) and (2-10), it is obvious that the discretized pressure term and the discretized bed slope term are the same and will compensate exactly should the free surface level be horizontal.

2.2.3. SFB formulation in the porosity-based model

Using the SFB term, the discretization of the bed slope term writes:

$$S_{0,x}^{SFB} = -\phi g h_i\frac{\left[z_b\right]_R - \left[z_b\right]_L}{\Delta x}\Delta y \qquad \text{(2-11)}$$

For a horizontal free surface level, Eq. (2-11) rewrites:

$$S_{0,x}^{SFB} = \phi g h_i\frac{\left[h\right]_L - \left[h\right]_R}{\Delta x}\Delta y \qquad \text{(2-12)}$$

By contrast with the DFB formulation, it is not a direct result that Eqs (2-9) and (2-12) are the same. This should require a specific discretization of h_i. However, we failed to find a general expression of h_i guarantying the equality between Eqs (2-9) and (2-12).

2.3. Discretization of the differential form of the bed slope term

This section is based on the journal paper "*Discretization of the divergence formulation of the bed slope term in the shallow-water equations and consequences in terms of energy balance*" by **M. Bruwier**, P. Archambeau, S. Erpicum, M. Pirotton and B. Dewals, published in 2016 in *Applied Mathematical Modelling*.

Section 2.3.3.2 refers to Appendix C, which is based on the technical note "*Energy conservation properties of Ritter solution for idealized dam break flow*" by B. Dewals, **M. Bruwier**, S. Erpicum, M. Pirotton, and P. Archambeau, published in 2016 in *Journal of Hydraulic Research*. The PhD candidate was involved in all conceptual and mathematical derivations presented in the note.

ABSTRACT: In this research, the influence on energy balance of the discretization scheme of the divergence formulation of the bed slope term in the shallow-water equations is analysed theoretically (for a single topographic step) and based on two numerical tests. Different values of the main parameter controlling the discretization scheme of the divergence formulation are analysed to identify the formulation which minimizes the energy variation resulting from the discretization. For a wide range of ambient Froude numbers and relative step heights, the theoretical value of the control parameter minimizing the energy variation falls within a very narrow range, which can reasonably be approximated by a single "optimal" value. This is a result of high practical relevance for the design of accurate numerical schemes, as confirmed by the results of the numerical tests.

2.3.1. Introduction and background

The standard formulation of the bed slope source term (SFB) is introduced in Eq. (2-6) of section 2.2.1.

For general hyperbolic conservation laws with source terms, Bermúdez and Vázquez (1994) introduced the concept of upwind discretization of the source terms. The goal is to make the discretization of the source terms consistent with the discretization of the advective and pressure terms, so as to obtain a so-called well-balanced scheme. In the discretization of the SWE, this approach enables the preservation of an initial solution corresponding to quiescent water over an irregular bottom (Nujić 1995). The results obtained with well-balanced schemes were shown to be more accurate than those obtained with a simple pointwise evaluation (Garcia-Navarro and Vazquez-Cendon 2000, Delestre et al. 2012). This method has been extended for unstructured meshes (Bermúdez et al. 1998), quasi-steady problems (LeVeque 1998), flux-difference splitting schemes (Hubbard 1999, Vázquez-Cendón 1999, Garcia-Navarro and Vazquez-Cendon 2000) and flux-vector splitting schemes (Nujić 1995, Valiani et al. 2002, Liang and Marche 2009). A comparative analysis of different topography discretization techniques has been performed by Kesserwani (2013).

From the work of Zhou et al. (2001) on the surface gradient method, in which variables reconstruction is based on the free surface level instead of the water depth, Valiani and Begnudelli (2006a) introduced the divergence formulation of the bed slope term (DFB) of Eq. (2-7) in section 2.2.1.

This treatment of the bed slope term similarly to a flux term (instead of a source term) is particularly useful in domains with a highly discontinuous topography, such as in urban areas (Sanders et al. 2008, Schubert and Sanders 2012, Kim et al. 2014).

While Eq. (2-7) is close to a conservative formulation, the assumption of a locally uniform water level η_0 in each cell induces discontinuities between two adjacent cells if the water level η is actually inclined.

Whereas Eq. (2-7) has been derived independently from any numerical scheme and kind of discretization, the discretization of the DFB was shown very convenient when using a structured grid with quadrilateral cells (Valiani and Begnudelli 2006, 2008). Recently, Hou et al. (2013a, 2013b) extended the discretization of the DFB to unstructured grids.

The well-balanced discretization of the bed slope source term, as introduced by Nujic (1995) and others, enables water at rest to be properly reproduced; but still numerical errors occur in the energy balance. Indeed, although the mathematical expressions of momentum and energy conservation are equivalent for isothermal and incompressible flow, their discretized formulations do not lead to the same numerical results. The specific formulation used for the discretization of the bed slope term in the momentum equations has a substantial influence on the numerical errors induced in the energy balance. In the context of Godunov-type solvers, Murillo and García-Navarro (2013) introduced a specific formulation of the bed slope source term ensuring energy conservation by using a linear combination of the integral and differential formulations of this term. The parameter controlling the linear combination depends on the variations of the flow variables and on the flow regime. Under steady conditions, the resulting scheme verifies the energy conservation for continuous and frictionless flow conditions, and the momentum balance in case of hydraulic jumps. Murillo and García-Navarro (2014) generalized this method for flow in 1D non-prismatic channels of arbitrary cross-section. However, the approach developed by Murillo and Garcia Navarro (2013, 2014) is not straightforward to extend to the DFB, as the resulting expression for η_0 may lead to singularities, as shown in Appendix B.

So far, in all studies based on the DFB, at the knowledge of the authors, the uniform water level η_0 within a cell was evaluated as the average flow depth plus the average bed elevation of the cell (Valiani and Begnudelli 2006) or as the average of the free surface levels at the edges of this cell (Valiani and Begnudelli 2008, Hou et al. 2013b). In contrast, in the present research, we evaluate the uniform water level η_0 as a linear combination of the free surface levels at the edges of the cell, taking into account specific features of the flux-vector splitting technique considered here. Different values of the parameter involved in the linear combination are analysed and benefit is taken from this extra degree of freedom to identify the value of this parameter which leads to the minimum error in the energy balance. First, a theoretical analysis is performed for a 1D slopeless and frictionless channel with a topographic step (similarly to the work of Stelling and Duinmeijer 2003). Second, the sensitivity of the numerical results to the value of the control parameter is analysed for a 1D steady flow over a bump and for a 1D dam break flow in a channel with a bump, with and without friction. A remarkable agreement is obtained between the conclusions of the theoretical analysis and the results of the numerical test cases.

2.3.2. Optimal discretization of the DFB term without porosity: theoretical analysis

With the DFB, the momentum equation (2-5) for a 1D steady solution without friction writes:

$$\frac{\partial}{\partial x}\left(\frac{q^2}{h}\right)+\frac{g}{2}\frac{\partial h^2}{\partial x}=\frac{g}{2}\frac{\partial h_{\eta_0}^2}{\partial x} \tag{2-13}$$

and the conservation of mechanical energy gives:

$$\frac{1}{2}\frac{\partial}{\partial x}\left(\frac{q^2}{h^2}\right)+g\frac{\partial h}{\partial x}=-g\frac{\partial z_b}{\partial x}. \tag{2-14}$$

We propose here a simpler approach in which the constant free surface elevation $\eta_{0,i}$ within cell i is computed as a linear combination of the free surface levels η_i and η_{i+1} with a constant parameter α:

$$\eta_{0,i}=(1-\alpha)\eta_i+\alpha\eta_{i+1} \tag{2-15}$$

The influence of the discretization of the bed slope term on the energy conservation is analysed in the case of steady flow in a 1D slopeless and frictionless channel with a topographic step (Figure 2-2), as considered by Erpicum (2006). The water depths upstream and downstream of the bottom step are respectively called h_U and h_D. The topographic variation is referred to as Δz_b. On both sides of the topographic step, the specific discharge q is assumed constant and uniform.

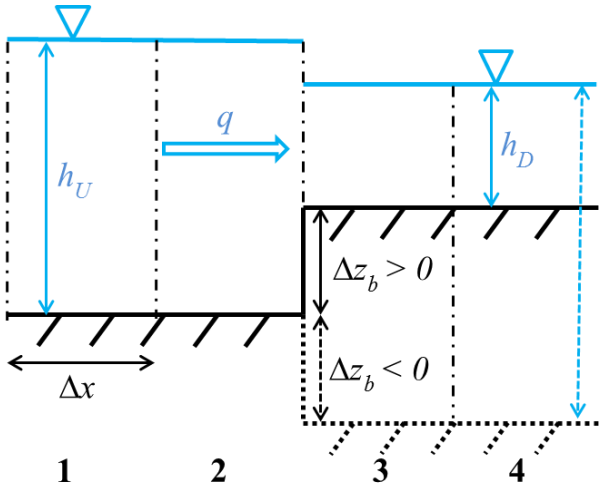

Figure 2-2 : 1D channel with a topographic step.

2.3.2.1. Methods

Reference solution

For a flow without energy dissipation (neither friction nor hydraulic jump), Eq. (2-14) of the conservation of the mechanical energy between the upstream side E_U and the downstream side E_D of the topographic step writes (Field et al. 1998, Castro-Orgaz et al. 2008):

$$E_U = \frac{q^2}{2gh_U^2} + h_U = \frac{q^2}{2gh_D^2} + h_D + \Delta z_b = E_D \tag{2-16}$$

Using the following non-dimensional parameters:

$$\mathrm{F_U^2} = \frac{q^2}{gh_U^3}\,, \quad \mathbf{h} = \frac{h_D}{h_U}\,, \quad \Delta\mathbf{z_b} = \frac{\Delta z_b}{h_U}, \quad \mathbf{F_D^2} = \frac{q^2}{gh_D^3} = \frac{\mathrm{F_U^2}}{\mathbf{h}^3} \tag{2-17}$$

Eq. (2-16) writes:

$$\mathbf{h}^3 - \mathbf{h}^2\left(\frac{\mathbf{F_U^2}}{2} + 1 - \Delta\mathbf{z_b}\right) + \frac{\mathbf{F_U^2}}{2} = 0 \tag{2-18}$$

This third order polynomial in $\mathbf{h}$ has two positive roots and one negative. Because Eq. (2-18) is valid for flows without hydraulic jump, only the root which preserves the same flow regime on either sides of the topographic step is considered here.

Discrete formulation of the DFB term

Consistently with the upwinding of the pressure terms towards downstream, the discretization of the DFB in cell i writes:

$$\begin{aligned}\frac{g}{2}\left[\frac{\partial h_{\eta_0}^2}{\partial x}\right]_{discr.,i} &= \frac{g}{2}\frac{\left[(1-\alpha)\eta_i + \alpha\eta_{i+1} - z_{b,i+1}\right]^2 - \left[(1-\alpha)\eta_i + \alpha\eta_{i+1} - z_{b,i}\right]^2}{\Delta x} \\ &= -g\frac{\left[2\left[(1-\alpha)h_i + \alpha h_{i+1}\right] + (1-2\alpha)\left(z_{b,i} - z_{b,i+1}\right)\right]}{2}\frac{z_{b,i+1} - z_{b,i}}{\Delta x}.\end{aligned} \tag{2-19}$$

This generalized discretization of the DFB contains two important particular cases.

Let us look at the following two particular cases, namely α = 0 and α = 1/2:

If α = 0, Eq. (2-19) becomes:

$$\frac{g}{2}\left[\frac{\partial h_{\eta_0}^2}{\partial x}\right]_{discr.,i} = -g\frac{2h_i + z_{b,i} - z_{b,i+1}}{2}\frac{z_{b,i+1} - z_{b,i}}{\Delta x}. \tag{2-20}$$

This particular discretization is referred hereafter as the standard discretization of the DFB, as used by Valiani and Begnudelli (2006a) and presented by these authors as very simple and requiring low computational effort. In contrast, if α = 1/2, Eq. (2-19) reduces to:

$$\frac{g}{2}\left[\frac{\partial h_{\eta_0}^2}{\partial x}\right]_{discr.,i} = -g\,\frac{h_i + h_{i+1}}{2}\,\frac{z_{b,i+1} - z_{b,i}}{\Delta x}. \tag{2-21}$$

This result is equivalent to the discretization of the SFB by Nujic (1995) and Erpicum et al. (2010a). This discretization is analogous to the ones used by Valiani and Begnudelli (2006b) and by Hou et al. (2013a). Hereafter, this discretization is referred to as the standard discretization of the SFB.

Application to a frictionless channel with a topographic step

Due to the non-conservative form of the bed slope source term, the equation of momentum conservation cannot be solved analytically in the presence of a topographic step. For the purpose of the present theoretical analysis, we focus here on the smallest possible numerical grid which enables a suitable resolution of the problem accounting properly for the typical boundary conditions. Hence, the domain is discretized with two cells on either sides of the topographic step, numbered from 1 (upstream) to 4 (downstream) (Figure 2-2).

Substituting Eq. (2-19) into the discretized formulation of Eq. (2-13) leads to:

$$\begin{aligned}&\frac{q^2}{\Delta x}\left(\frac{1}{h_i} - \frac{1}{h_{i-1}}\right) + \frac{g}{2}\,\frac{h_{i+1}^2 - h_i^2}{\Delta x} \\ &= -g\,\frac{2(1-\alpha)h_i + (1-2\alpha)z_{b,i} + 2\alpha h_{i+1} + (2\alpha-1)z_{b,i+1}}{2}\,\frac{z_{b,i+1} - z_{b,i}}{\Delta x}.\end{aligned} \tag{2-22}$$

Since the location where a boundary condition is prescribed on the water depth depends on the flow regime, Eq. (2-22) is solved differently depending on the flow regime.

In the case of a subcritical flow, the water depth h_D is prescribed as a boundary condition on the most downstream cell edge.

Applying Eq. (2-22) for the four cells described in Figure 2-2 leads to:

$$h_U = h_1 = h_2 = h_3 + \Delta z_b \tag{2-23}$$

$$q^2\left(\frac{1}{h_3} - \frac{1}{h_2}\right) + \frac{g}{2}\left(h_4^2 - h_3^2\right) = 0 \tag{2-24}$$

$$\frac{g}{2}h_4^2 = \frac{g}{2}h_D^2 + q^2\left(\frac{1}{h_D} - \frac{1}{h_3}\right). \tag{2-25}$$

Whatever the value of α, the free surface is found horizontal on either sides of the topographic step.

Grouping the results of Eqs (2-23), (2-24) and (2-25), the following relationship is obtained between h_U and h_D, independently of the value of α:

$$q^2\left(\frac{1}{h_D} - \frac{1}{h_U}\right) + \frac{g}{2}\left(h_D^2 - h_U^2\right) = -g\,\frac{2h_U - \Delta z_b}{2}\Delta z_b. \tag{2-26}$$

For a supercritical flow, the water depth h_U is set as boundary condition at the most upstream cell edge.

Applying Eq. (2-22) for the four cells described in Figure 2-2 leads to:

$$q^2\left(\frac{1}{h_1} - \frac{1}{h_U}\right) + \frac{g}{2}\left(h_2^2 - h_U^2\right) = 0 \tag{2-27}$$

$$q^2\left(\frac{1}{h_D} - \frac{1}{h_1}\right) = -g\left(h_D - \frac{1-2\alpha}{2}\Delta z_b\right)\Delta z_b \tag{2-28}$$

$$h_2 = h_3 = h_4 = h_D. \tag{2-29}$$

Grouping the results of Eqs (2-27), (2-28) and (2-29) leads to:

$$q^2\left(\frac{1}{h_D} - \frac{1}{h_U}\right) + \frac{g}{2}\left(h_D^2 - h_U^2\right) = -gh_D\Delta z_b + \frac{1-2\alpha}{2}g\Delta z_b^2. \tag{2-30}$$

The second term of the bed slope term of Eq. (2-30) vanishes in the standard discretization of the SFB (α = 1/2).

Non-dimensional forms

To enable systematic numerical evaluations of the energy variations obtained for different Froude numbers and different heights of the topographic step, Eqs (2-26) and (2-30) are rewritten using the non-dimensional parameters defined in Eq. (2-17):

$$\begin{aligned}
&\mathbf{h}^3 - \left(1 + 2\mathbf{F_U^2}\right)\mathbf{h} + \left(2 - \Delta\mathbf{z_b}\right)\Delta\mathbf{z_b}\mathbf{h} + 2\mathbf{F_U^2} = 0 \quad \mathbf{F_U} \le 1 \\
&\mathbf{h}^3 + 2\Delta\mathbf{z_b}\mathbf{h^2} - \left(1 + 2\mathbf{F_U^2}\right)\mathbf{h} - \left(1 - 2\alpha\right)\Delta\mathbf{z_b^2}\mathbf{h} + 2\mathbf{F_U^2} = 0 \quad \mathbf{F_U} \ge 1.
\end{aligned} \tag{2-31}$$

Energy variation

Similarly, the non-dimensional energy variation between upstream and downstream writes as:

$$\Delta\mathbf{E} = \frac{E_U - E_D}{E_U} = \frac{\mathbf{F_U^2} + 2 - \frac{1}{\mathbf{h^2}}\mathbf{F_U^2} - 2\mathbf{h} - 2\Delta\mathbf{z_b}}{\mathbf{F_U^2} + 2}. \tag{2-32}$$

For a given value of α and a given upstream Froude number $\mathbf{F_U}$, the energy variation resulting from the resolution of the discretized momentum equation may be quantified using the following indicators, namely the bias and the root-mean-square (RMS):

$$\text{bias}\left(\mathbf{F_U}, \alpha\right) = \left\langle \Delta\mathbf{E} \right\rangle. \tag{2-33}$$

$$\text{RMS}\left(\mathbf{F_U}, \alpha\right) = \sqrt{\left\langle \Delta\mathbf{E}^2 \right\rangle}. \tag{2-34}$$

Where the operator $\langle ... \rangle$ refers to an average over all non-dimensional step heights $\Delta\mathbf{z_b}$ between $\Delta\mathbf{z_b} = -1$ and $\Delta\mathbf{z_b} = 1$. The discretization step for $\Delta\mathbf{z_b}$ was selected small enough so that the values of bias and RMS are independent of this discretization.

The bias represents the arithmetic mean of the numerical energy variation among all the considered topographic steps. A positive value reflects dominant energy dissipation while a negative value represents dominant energy creation. The RMS represents the energy variation in absolute term for a given value of α and a given Froude number.

2.3.2.2. Results and discussion

Comparison between the exact solutions of the equation of conservation of mechanical energy and the solutions of the discrete equation of momentum conservation

The solutions of the non-dimensional Eq. (2-31) are shown in Figure 2-3 for the standard discretization of the SFB (α = 1/2 in dashed lines) and for the standard discretization of the DFB (α = 0 in dotted lines). The discrete solutions of the equation of momentum conservation are compared to the exact solution of the equation of energy conservation (plain lines). For negative (respectively positive) topographic steps, the zones representing subcritical or supercritical flows are, respectively, labelled zones 1 and 2 (respectively zones 4 and 3).

For negative topographic steps ($\Delta\mathbf{z_b} < 0$) in Figure 2-3a, the two curves in black represent the limits corresponding to an upstream Froude number tending towards unity, either from subcritical

(upper curve) or from supercritical (lower curve) flow regimes. These limits cannot be reached for positive topographic steps (Figure 2-3b) since critical flow corresponds to the minimum energy for a given discharge and, therefore, an approaching critical flow could not adapt to a positive topographic step.

For positive topographic steps ($\Delta \mathbf{z_b} > 0$) in Figure 2-3b, the limits for a downstream Froude tending towards unity from subcritical (lower curve) and supercritical (upper curve) flows are the curves in grey.

The discontinuous black line in Figure 2-3 represents the hypothetical limit of an infinite Froude number, in which case the water depth remains unaffected by the topographic step due to the high kinetic energy.

Figure 2-3 presents in dashed line the solutions of the discrete form of the momentum conservation equation with the standard discretization of the SFB (or the discretization of the DFB with the particular value of (α = 1/2). Although these results are similar to those of the analytical energy conservation, they are not exactly the same. The main differences appear for a positive topographic step in supercritical flow (e.g., $\mathbf{F_U} = 2$ in zone 3), for which two different flow conditions may be obtained for the same value of $\Delta \mathbf{z_b}$ and without change of the flow regime.

Figure 2-3 presents in dotted line the solution of the discrete form of the momentum conservation equation with the standard discretization of the DFB (α = 0). For subcritical flow, the solutions of the discrete momentum conservation equations with the standard discretization of the SFB and with the standard discretization of the DFB are identical, consistently with the independency of the corresponding part of Eq. (2-31) with respect to α. In contrast, for supercritical flows, the solutions are similar but not equal. The difference between the solution obtained with the energy conservation and the solution obtained with the momentum conservation with the standard discretization of the DFB tends to increase with the absolute value of the topographic step. While the momentum conservation with the standard discretization of the SFB only gives overestimations of the parameter $\mathbf{h}$ in supercritical flows, the momentum conservation with the standard discretization of the DFB overestimates or underestimates the values of $\mathbf{h}$ depending on the value of $\Delta \mathbf{z_b}$.

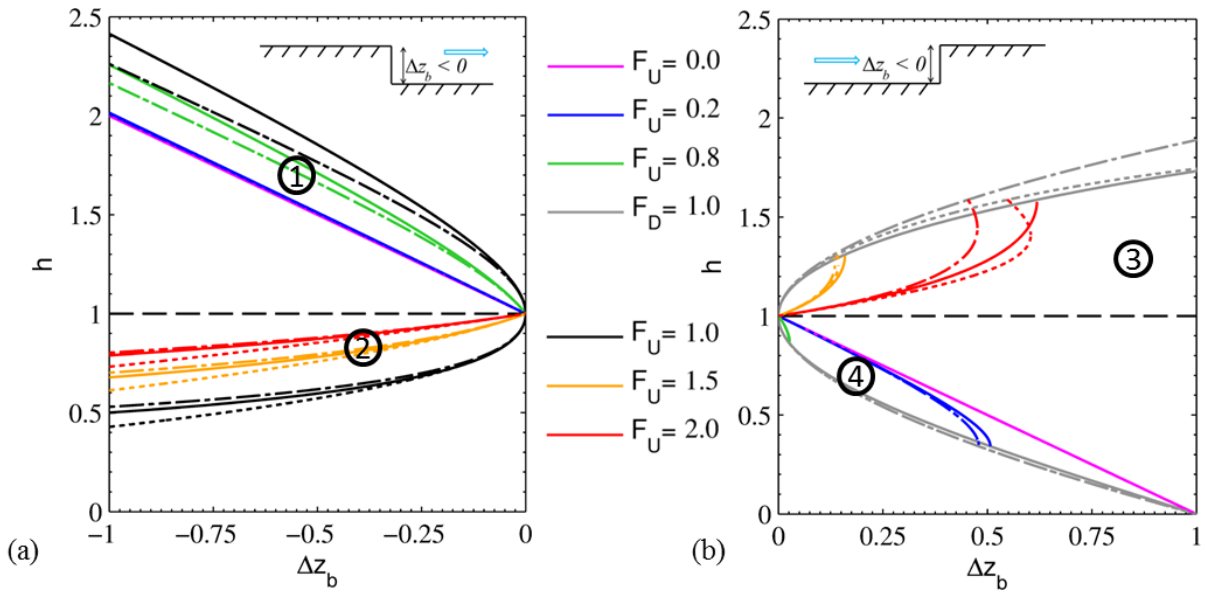

Figure 2-3 : Hydrodynamic characteristics ($\mathbf{h}, \Delta\mathbf{z_b}$) for a flow in a slopeless and frictionless 1D channel with a (a) negative or (b) positive topographic step – Comparison between the exact resolution of energy conservation (plain lines), the momentum conservation discretized with the standard discretization of the SFB (dashed lines) and the momentum conservation discretized with the standard discretization of the DFB (dotted lines). For negative (respectively positive) topographic steps, the zones representing subcritical or supercritical flows are respectively labelled zones 1 and 2 (respectively zones 4 and 3).

Energy variation of the discrete resolution of the momentum conservation equations

As shown in plain lines in Figure 2-4, only positive energy losses are observed with the standard discretization of the SFB, indicating that the discretization of the momentum conservation induces only numerical *dissipation* of energy. This dissipation tends to increase with the absolute height of the topographic. The range of variation of energy losses for subcritical and supercritical flows are represented in light grey with respectively circular markers and arrows at the tips. Moreover, for a given height of the topographic step, the dissipation is maximum for Froude numbers close to unity. For positive topographic steps (Figure 2-4a), the dissipation obtained in supercritical flow conditions generally exceeds the dissipation for subcritical flow.

The energy variation resulting from the discrete resolution of the momentum conservation equation with the standard discretization of the DFB is represented in dotted lines in Figure 2-4. Negative energy losses are obtained for supercritical flows with a negative topographic step (Figure 2-4a) and for some supercritical flows with a positive topographic step (Figure 2-4b). For negative topographic steps, the magnitude of the numerical energy variation increases when the

Froude number becomes closer to unity, while it is not necessary the case for positive topographic steps (e.g., $\mathbf{F_U} = 2.0$).

Energy variations for subcritical flows are identical for both formulations of the bed slope term. Concerning supercritical flows with the standard discretization of the DFB ($\alpha = 0$), numerical energy is created for negative topographic steps with absolute values greater than the dissipation of energy with the standard discretization of the SFB.

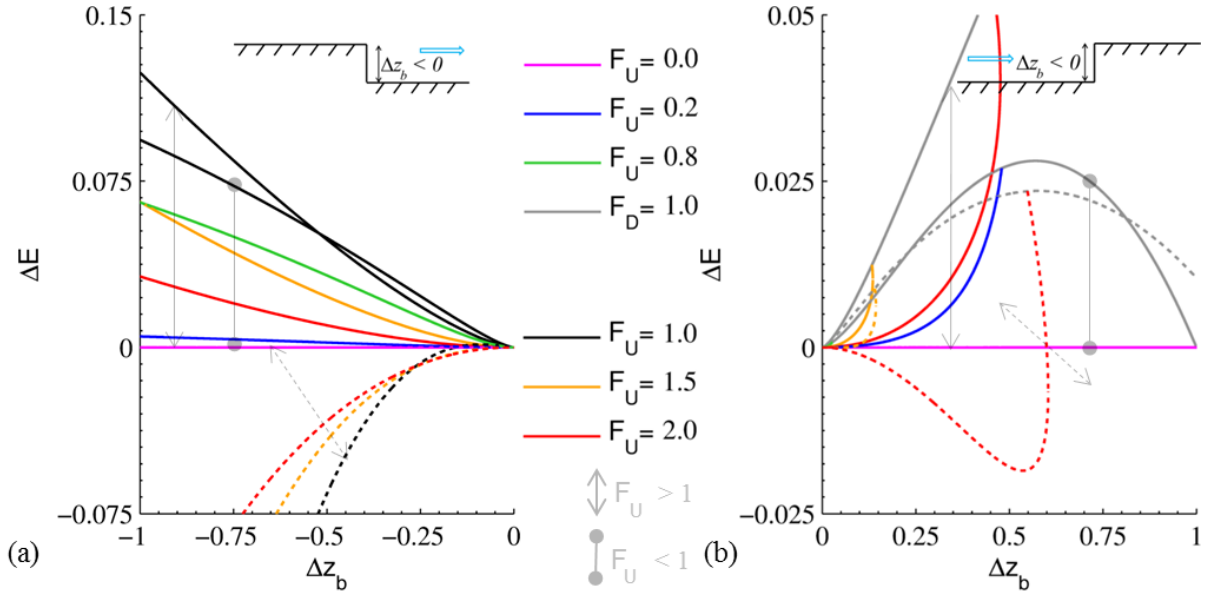

Figure 2-4 : Energy loss across a topographic step in a slopeless and frictionless 1D channel - Comparison between the momentum conservation with the standard discretization of the SFB (plain lines) and the momentum conservation with the standard discretization of the DFB ($\alpha = 0$) (dotted lines).

Optimal values of α to minimize the numerical energy variation

As shown in Figure 2-5a, for supercritical flows, the bias of energy is negative (i.e. dominating energy creation) for lowest values of α and positive (i.e. dominating energy dissipation) for highest ones. Whatever the value of α, the RMS tends towards zero for high upstream Froude numbers and is the highest for upstream Froude numbers close to one (Figure 2-5b).

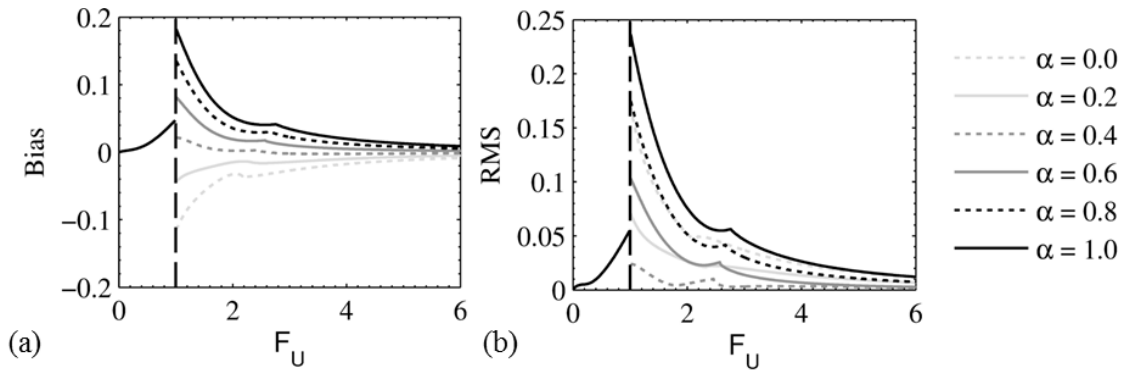

Figure 2-5 : Bias and RMS of the numerical variation of energy as a function of the upstream Froude number for different values of α in the discrete momentum conservation equation with the DFB.

Figure 2-6 shows the optimal values of α, i.e. those values which minimize the energy variation resulting from the numerical discretization. The values minimizing the bias are found slightly lower than those minimizing the RMS for upstream Froude numbers up to slightly more than 2. For higher upstream Froude numbers, the values of α minimizing the bias are very close to those which minimize the RMS. In any case, the variation of the optimal value of α with the upstream Froude number is found particularly low. In practice, this suggests the use of a single value of α (α = 0.4) whatever the upstream Froude number. This rule of thumb guarantees that the numerical energy variation remains always very close to its minimum. This optimal value of α is based on the minimization of the error on the energy whatever the remaining error should be a reduction or an augmentation of mechanical energy. When searching for a minimization of the numerical energy without any creation of energy, the optimal value of α is close to 0.5 which leads however to an increase of the RMS compared to a value of α = 0.4.

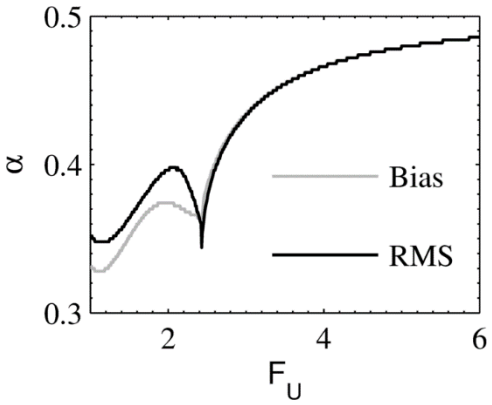

Figure 2-6 : Value of α minimizing the bias or the RMS of the numerical variation of energy for different upstream Froude numbers.

2.3.3. Optimal discretization of the DFB term without porosity: numerical analysis

The sensitivity of the numerical variation of mechanical energy to the discretization of the DFB is numerically analysed for a 1D steady flow over a slopeless and frictionless channel with a bump (Aureli et al. 2008) and for a 1D dam break flow over a channel with a bump, with and without friction. The first test case is a standard test case, often used to evaluate the accuracy of the treatment of the bed slope term by numerical models, as well as their efficiency to converge towards a steady solution (Valiani and Begnudelli 2006, Hou et al. 2013a, 2013b). The second test case is considered to assess the validity of our conclusions in cases with unsteadiness and friction.

Four discretizations of the DFB are tested: α = 0.0 which is equivalent to the standard discretization of the DFB, α = 0.4 hereabove presented as an optimal discretization, α = 0.5 referred to as the standard SFB discretization and α = 1.0.

2.3.3.1. 1D steady flow over a slopeless and frictionless channel

Methods

The bottom level is given by Eq. (2-35) $\left(-10m \le x \le 10m\right)$:

$$z(x) = \begin{cases} 0.8\left(1-\dfrac{x^2}{4}\right) & -2m \le x \le 2m \\ 0 & \text{elsewhere} \end{cases}. \qquad (2\text{-}35)$$

Two different sets of boundary conditions are analysed (Table 2-1). The first one leads to a subcritical flow while the second one corresponds to a supercritical flow. There is no hydraulic jump and, in the exact solution, the energy is therefore constant over the entire domain (assuming no friction within the fluid). For each test case, range of Froude number and energy value are given in Table 2-1.

Test ID	Upstream boundary condition	Downstream boundary condition	Analytical F range	Analytical energy
1	$q = 1m^2/s$	$h_D = 1.7m$	0.14 - 0.41	$E_{exact} = 1.718m$
2	$q = 1.5m^2/s; h_U = 0.25m$	Transmissive	2.31 - 3.83	$E_{exact} = 2.085m$

Table 2-1: Boundary conditions, analytical Froude range and analytical energy for a 1D steady flow over a bump.

The two tests are simulated with the hydraulic model Wolf2D, in which the DFB has been implemented. The model solves the fully dynamic shallow-water equations using a conservative finite volume scheme based on a flux-vector splitting technique (Dewals et al. 2008, Erpicum et al. 2010a). The computational domain is discretized with a 0.1 m grid spacing.

The mechanical energy at a border is evaluated by Eq. (2-36), consistently with the flux-vector splitting technique:

$$E_{i+1/2} = h_{i+1} + \frac{1}{2g}\frac{q_{x,i}^2}{h_{x,i}^2}. \qquad (2\text{-}36)$$

The differences between the analytical solution and the numerical ones are quantified with the L_1 error defined by Eq. (2-37):

$$L_1(y) = \frac{1}{N}\sum_{i=1}^{N}\left|\frac{y_{i,num} - y_{i,ref}}{y_{i,ref}}\right| \qquad (2\text{-}37)$$

where N is the number of computational cells, $y_{i,num}$ is a numerical solution and $y_{i,ref}$ is the analytical solution.

Results and discussion

The water depths are more sensitive to the discretization of the bed slope term for supercritical flows than for subcritical ones (Figure 2-7 and Table 2-2). For a supercritical flow, the order of magnitude of the differences between the water depths resulting from different discretizations of the bed slope term highlights the necessity of an accurate discretization of the bed slope term.

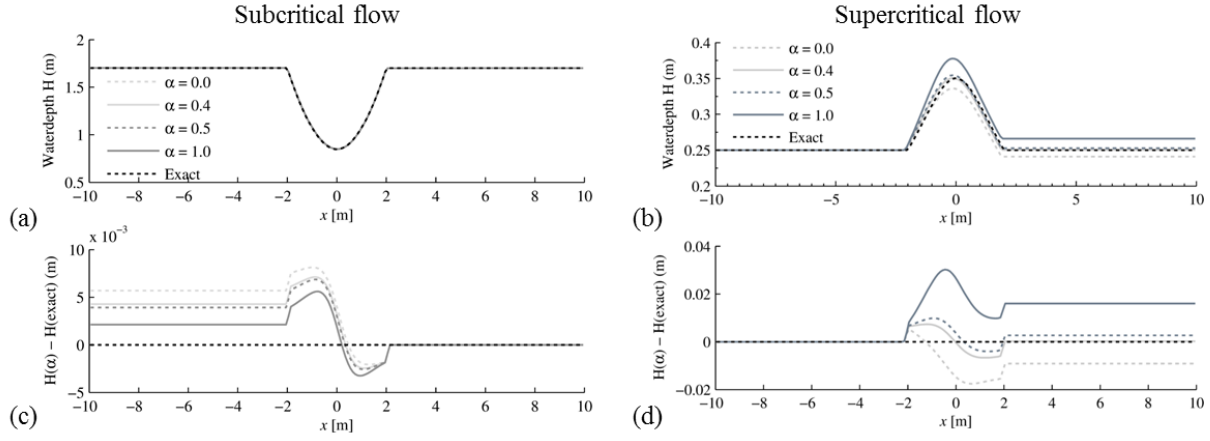

Figure 2-7 : Water depths (a, b) and energy variation (c, d) for a 1D steady flow over a bump and different values of α .

As shown in Figure 2-8, the numerical variations of energy are produced at the bump and propagate towards upstream for a subcritical flow (Figure 2-8a) and towards downstream for a supercritical flow (Figure 2-8b). In the first test, the errors on the energy increase when the value of α decreases, while, for the second test case, the errors increase when the value of α moves away from the value of α = 0.4. Concerning the second test case with a supercritical flow, dissipation of energy occurs for values of α equal to 0.5 and 1.0 while creation of energy occurs for α = 0.0, consistently with the results presented in Figure 2-5.

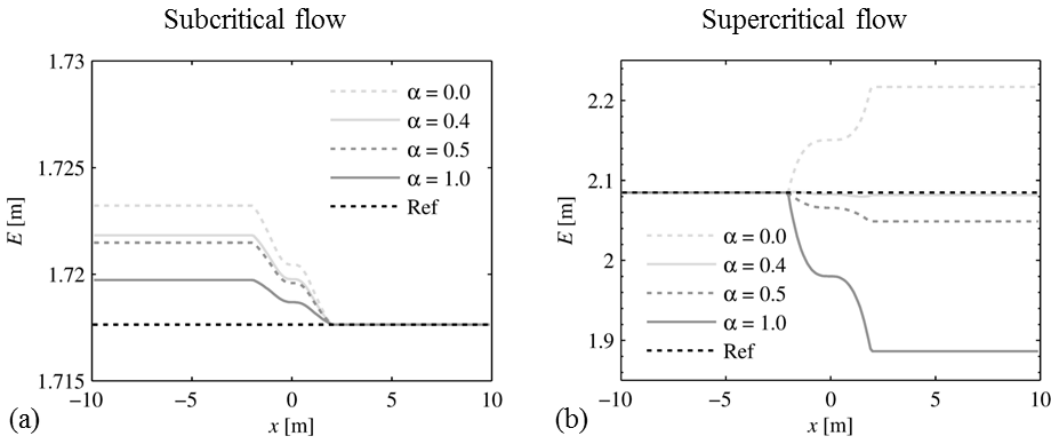

Figure 2-8 : Comparison of the mechanical energy between the analytical solution (black line) and the computed results for a 1D steady flow over a bump and different values of α *.*

As shown in Table 2-2, the error on energy may change by two orders of magnitude depending on the discretization of the DFB for supercritical flows while they show a lower sensitivity to the value of α for subcritical flows. Moreover, the order of magnitude of the lowest energy error for the second test is the same as the one obtained for the first test case, whatever the value of α. These results are consistent with the selection of an optimal value of α = 0.4 for the discretization of the DFB, as concluded from the theoretical analysis in section 2.3.1.

Test ID	α	$L_1(h)$	$L_1(E)$
1	0.0	3.2 x10^{-3}	2.8 x10^{-3}
	0.4	2.5 x10^{-3}	2.1 x10^{-3}
	0.5	2.4 x10^{-3}	1.9 x10^{-3}
	1.0	1.5 x10^{-3}	1.1 x10^{-3}
2	0.0	5.9 x10^{-3}	66.3 x10^{-3}
	0.4	1.2 x10^{-3}	1.6 x10^{-3}
	0.5	2.2 x10^{-3}	18.3 x10^{-3}
	1.0	10.1 x10^{-3}	100.7 x10^{-3}

Table 2-2: Errors on the water depths, unit discharges and mechanical energy for four discretizations of the DFB.

2.3.3.2. 1D dam break flow over a channel with a bump

Methods

This test case is based on an experimental setup (Alcrudo 1999) realized at the Laboratory of Hydraulic Research of Chatelet (Belgium). It consists in a dam break flow over a rectangular channel with a bump (Figure 2-9). Both the upstream (A) and downstream (B) ends are impervious plates. The channel is 38 m long (L_R) and a 15.5 m long and 0.75 m deep (h_0) water volume is initially retained at the upstream end by a sluice gate. The top of a symmetrical 6 m long and 0.4 m high bump is located 13 m downstream of the gate. The simulations were performed for (*i*) a frictionless channel and (*ii*) a channel with a uniform Manning coefficient n = 0.0125 s/m$^{1/3}$.

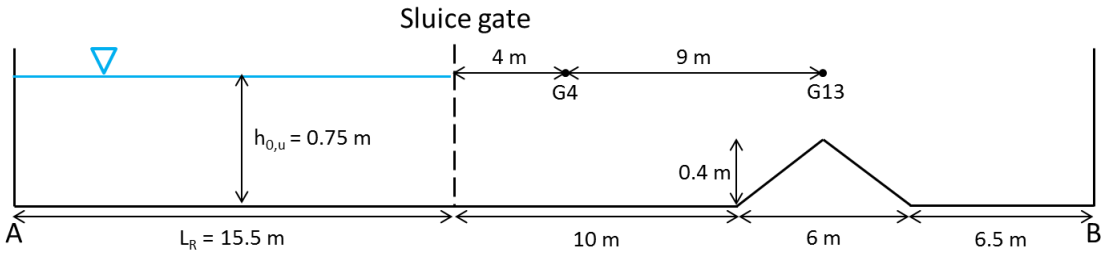

Figure 2-9 : Schematization of the test case of a 1D dam break flow over a channel with a bump.

Since the flow is unsteady, the inertia effects must be taken into account to assess the energy conservation in the computed results. To do this, we consider hereafter the sum of (*i*) the specific energy integrated over the whole flow area and (*ii*) the corresponding inertia term.

The specific energy E_s at any position (*x*,*z*) of the flow is the sum of the potential energy *z*, the pressure energy *h* and the kinetic energy $u^2/2g$ at that point. Since we consider hydrostatic pressure and uniform velocity, the specific energy is constant over the depth and equal to the energy head *E*:

$$E_s(x,z,t) = E(x,t) = h(x,t) + \frac{u(x,t)^2}{2g}. \tag{2-38}$$

The unsteady Bernouilli equation between two points x_i and x_j writes:

$$E(x_i,t) = E(x_j,t) + \int_{x_i}^{x_j} \frac{1}{g}\frac{\partial u}{\partial t}\,dx \tag{2-39}$$

where the second term of the right hand side represents the inertia contribution (E_I).

At a time *t*, the total mechanical energy Σ is defined as the sum of the integration over the whole flow area of the specific energy E_s and of the inertia contribution E_I :

$$\Sigma(t) = \int_A^B \left[h(x,t)\left(h(x,t) + \frac{u(x,t)^2}{2g} \right) + h(x,t)\int_A^x \frac{1}{g}\frac{\partial u(x',t)}{\partial t}\,dx' \right] dx. \tag{2-40}$$

For an unsteady inviscid flow over a frictionless channel, Σ is constant over time and remains equal to its initial value $L_R h_0^2$ (= 8.7187 m^3) provided that the flow does not reach the boundaries of the domain. This is detailed in Appendix C, which presents also an alternate derivation and more details on energy conservations properties of Ritter solution for idealized dam break flow.

Results and discussion

For gauges G4 and G13 (Figure 2-9), the time evolutions of the water depth are represented in Figure 2-10 for different values of α and for a channel with or without friction. At both gauges, the maximum water depth of the dam break wave depends significantly on the value of α, particularly at G4 with a frictionless channel where the maximum water depth reached by the wave for α = 0.0 is 8 cm above the value obtained for α = 0.5. The highest differences between the water depths obtained with a value of α = 0.4 and with the other values of α are of the order of 10^{-1} m at G4 and of 10^{-2} m at G13. Time logs are also observed between the time evolutions of computed water depths from different values of α, particularly at gauge G4. This suggests that the discretization of the bed slope term may have a significant impact on the results of a simulation of a dam break flow, both in terms of computed water depths and propagation times.

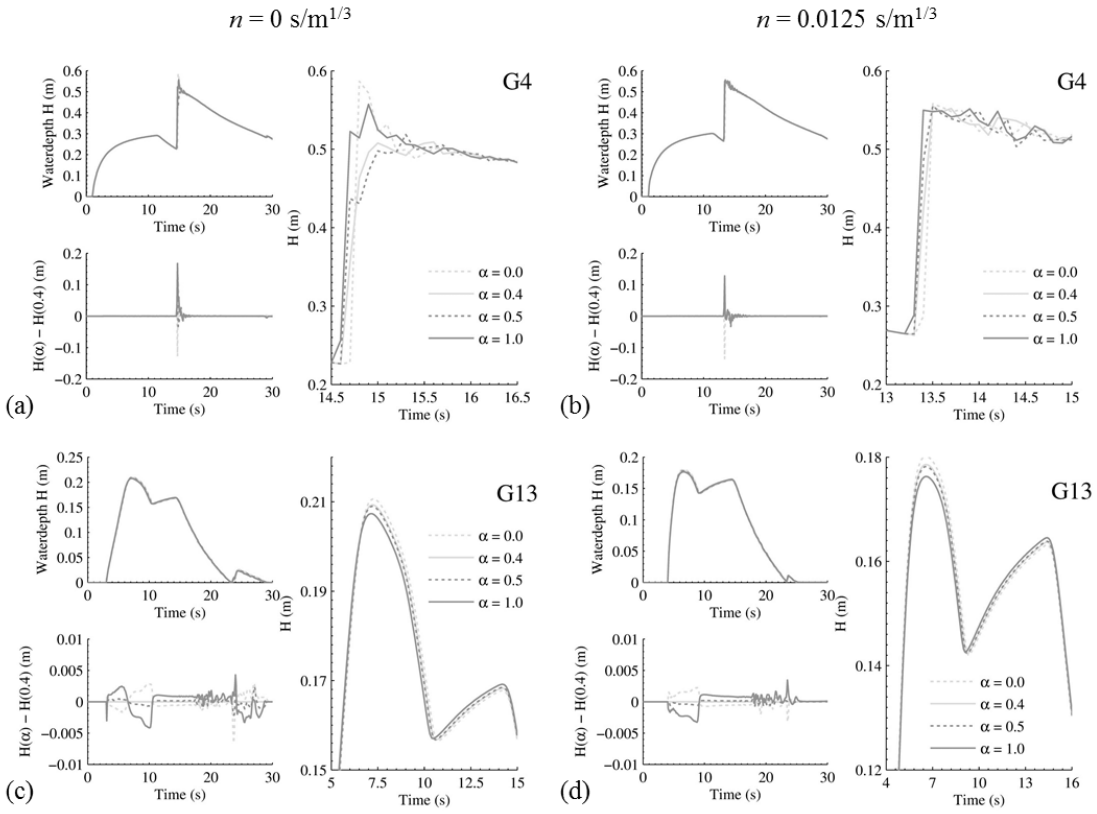

Figure 2-10 : Time evolution of the water depth at gauges G4 (a, b) and G20 (c, d) for different discretizations of the bed slope term and for a channel with (b, d) or without (a, c) friction.

In Figure 2-11, the time evolutions of $\sum$ for different values of α are compared to those obtained for the reference value α = 0.4, for a channel with (b) or without (a) friction. The time period represented in Figure 2-11 is such that the boundaries of the domain are not reached. The deviations of $\sum$ as a function of α remain relatively small compared to the initial value of

$\sum = L_R h_0^2$ (with a maximum relative difference of the order of 0.1%); but they increase very fast with time. The results are consistent with those obtained from the theoretical analysis and from the 1D steady flow with the bump (Figure 2-8b); i.e. an increase (resp. decrease) of the numerical variation of energy when the value of α is reduced (resp. increased) for a supercritical flow. The results obtained for a channel with friction are similar to the case of the frictionless channel, with mainly a time shift due to a reduction of the front velocity in the presence of friction.

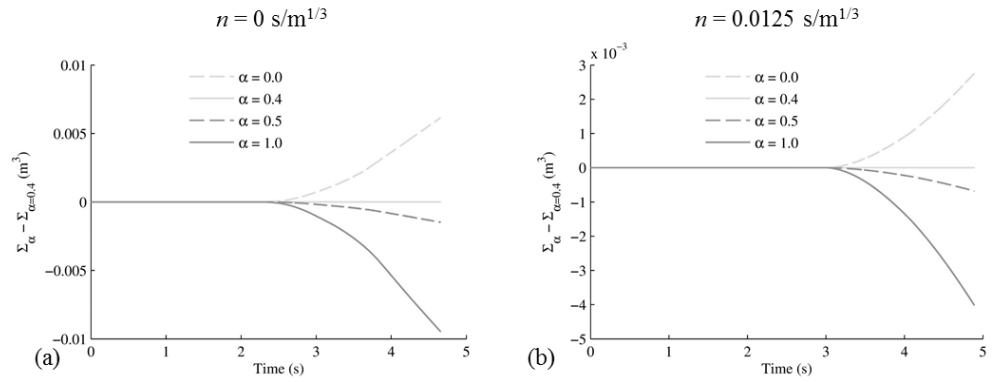

Figure 2-11 : Comparison of the time evolution of the total energy Σ for α = 0.4 to other discretizations of the bed slope term for a channel with (a) or without (b) friction.

2.3.4. Conclusion

Solving the discrete equation of momentum conservation induces numerical variations of energy, even in the case of a flow in a frictionless channel without physical energy dissipation.

In this section, we compare the resolution of the discrete equation of momentum conservation for two formulations of the bed slope term. The standard formulation of the bed slope term (SFB) involves the product of the water depth by the spatial derivative of the topographic level. The divergence formulation of the bed slope term (DFB) consists in evaluating the bed slope term as the spatial variation of the pressure assuming a constant free surface elevation.

A major difference in the results obtained with the two formulations of the bed slope term is that the discretization of the SFB induces only positive energy losses (i.e. dissipation of energy) while positive and negative energy losses are obtained with the discretization of the DFB.

An optimal discretization of the DFB, i.e. a scheme minimizing the numerical variation of energy, is proposed based on the theoretical analysis of the numerical variation of energy for a 1D continuous, slopeless and frictionless flow with a topographic step. Finally, two numerical test cases show results in good agreement with the findings of the theoretical analysis and highlight the practical relevance to minimize the energy variation due to the discretization of the bed slope term.

2.4. Final porosity formulation of the pressure and bed slope terms

Combining Eqs (2-3) and (2-10), the discretized formulations of the pressure and bed slope terms of the anisotropic porosity shallow-water equations for a computational cell *i* and its left (*L*) and right (*R*) edges are the following:

$$\begin{aligned}\Delta F_{\mathrm{P},x} - S_{0,x}^{DFB} &= \frac{1}{2} g \frac{\left[\psi h^2\right]_R - \left[\psi h^2\right]_L + \cancel{\left(\left[\psi\right]_L - \left[\psi\right]_R\right) h_i^2}}{\Delta x} \Delta y \\ &\quad - \frac{1}{2} g \frac{\left[\psi h_{\eta_{0,i}}^2\right]_R - \left[\psi h_{\eta_{0,i}}^2\right]_L + \cancel{\left(\left[\psi\right]_L - \left[\psi\right]_R\right) h_i^2}}{\Delta x} \Delta y \\ &= \frac{1}{2} g \frac{\left[\psi \left(h^2 - h_{\eta_{0,i}}^2\right)\right]_R - \left[\psi \left(h^2 - h_{\eta_{0,i}}^2\right)\right]_L}{\Delta x} \Delta y\end{aligned} \tag{2-41}$$

which is equivalent to the grid-scale formulation of Sanders et al. (2008).

The constant free surface elevation $\eta_{0,i}$ is computed as a linear combination of the free surface levels η_L and η_R with a constant parameter α close to 0.5, minimizing the numerical variation of energy. In the absence of porosity parameter, the classical numerical scheme of the Wolf2D solver is recovered from Eq. (2-41).

3. Impact of conveyance porosity in terms of energy balance

3.1. Introduction

In this chapter, we analyse the impact in terms of energy balance of the presence of a conveyance porosity multiplying the flux terms in the anisotropic porosity shallow-water equations. For the sake of simplicity, we consider a 1D steady and subcritical flow over a frictionless bed level.

In the absence of drag forces, the grid-scale formulation of the governing equations (1-10) and (1-11) writes:

$$\left[\psi uh\right]_R - \left[\psi uh\right]_L = 0 \tag{3-1}$$

$$\left[\psi u^2 h\right]_R - \left[\psi u^2 h\right]_L + \frac{1}{2} g \left(\left[\psi \left(h^2 - h_{\eta_{0,i}}^2 \right) \right]_R - \left[\psi \left(h^2 - h_{\eta_{0,i}}^2 \right) \right]_L \right) = 0 \tag{3-2}$$

where indices *L* and *R* referring to the left and right edges of the considered cell *i*, and $\eta_{0,i}$ the stationary free surface level, evaluated as a linear combination of the free surface levels η_L and η_R:

$$\eta_{0,i} = (1-\alpha)\eta_L + \alpha\eta_R \tag{3-3}$$

In this section, we use a value of α = 0.5 to recover the classical numerical scheme of Wolf2D in the absence of porosity (as detailed in section 2.3.1).

For a slopeless channel, Eq. (3-2) rewrites:

$$\left[\psi u^2 h\right]_R - \left[\psi u^2 h\right]_L + \frac{1}{2} g \left(\left[\psi h^2\right]_R - \left[\psi h^2\right]_L \right) = \frac{1}{2} g \left(\left[\psi\right]_R - \left[\psi\right]_L \right) \left(\frac{\left[h\right]_L + \left[h\right]_R}{2} \right)^2 \tag{3-4}$$

Let us assume a flow from left (upstream) to right (downstream) and consider the flux-vector splitting technique used in Wolf2D (Dewals et al. 2008, Erpicum et al. 2010a), which implies an upwinding towards upstream of the advective fluxes and an upwinding towards downstream of the pressure gradients. Equations of mass and momentum conservation write:

$$\left[\psi\right]_R \left(uh\right)_i - \left[\psi\right]_L \left(uh\right)_{i-1} = 0 \tag{3-5}$$

$$\begin{aligned}&[\psi]_R\left(u^2h\right)_i-[\psi]_L\left(u^2h\right)_{i-1}+\frac{1}{2}g\left([\psi]_R\left(h^2\right)_{i+1}-[\psi]_L\left(h^2\right)_i\right)\\&=\frac{1}{2}g\left([\psi]_R-[\psi]_L\right)\left(\frac{(h)_i+(h)_{i+1}}{2}\right)^2\end{aligned} \tag{3-6}$$

3.2. Theoretical analysis

3.2.1. Presentation of the numerical domains

Let us solve equations (3-5) and (3-6) for the smallest possible computational domains which enable a suitable resolution of the problem, accounting properly for the typical boundary conditions and for the presence of (1) a contraction zone, (2) an expansion zone or (3) a contraction-expansion zone. For the first two configurations, the domain considered here involves four cells (Figure 3-1a and Figure 3-1b), numbered from $i = 1$ (upstream) to $i = 4$ (downstream), while five cells are studied for the contraction-expansion zone (Figure 3-1c). The conveyance porosities are the following

$$\begin{aligned}&\text{Conf. 1:}\quad\begin{cases}\psi_{1/2}=\psi_{3/2}=1\\0<\psi_{5/2}=\psi_{7/2}=\psi_{9/2}=\psi\le1\end{cases}\\&\text{Conf. 2:}\quad\begin{cases}\psi_{7/2}=\psi_{9/2}=1\\0<\psi_{1/2}=\psi_{3/2}=\psi_{5/2}=\psi\le1\end{cases}\\&\text{Conf. 3:}\quad\begin{cases}\psi_{1/2}=\psi_{3/2}=\psi_{9/2}=\psi_{11/2}=1\\0<\psi_{5/2}=\psi_{7/2}=\psi\le1\end{cases}\end{aligned} \tag{3-7}$$

where the edge k between cells i and i+1 is numbered $k = i + 1/2$.

In Appendix D.1, we also detail a theoretical analysis similar to the domain with a contraction-expansion zone, but for a domain with four cells and a local obstruction over a single edge. The conclusions are very similar to those presented hereafter.

According to the theory of characteristics, the following boundary conditions are applied for a subcritical flow across the upstream and downstream boundaries of the domain:

- at the upstream boundary, the value $[hu]_{up}$ of the unit discharge is prescribed;
- at the downstream boundary, the value $[h]_{down}$ of the water depth is prescribed.

At the upstream boundary, the value of the water depth is taken equal to the corresponding value at the centre of cell 1.

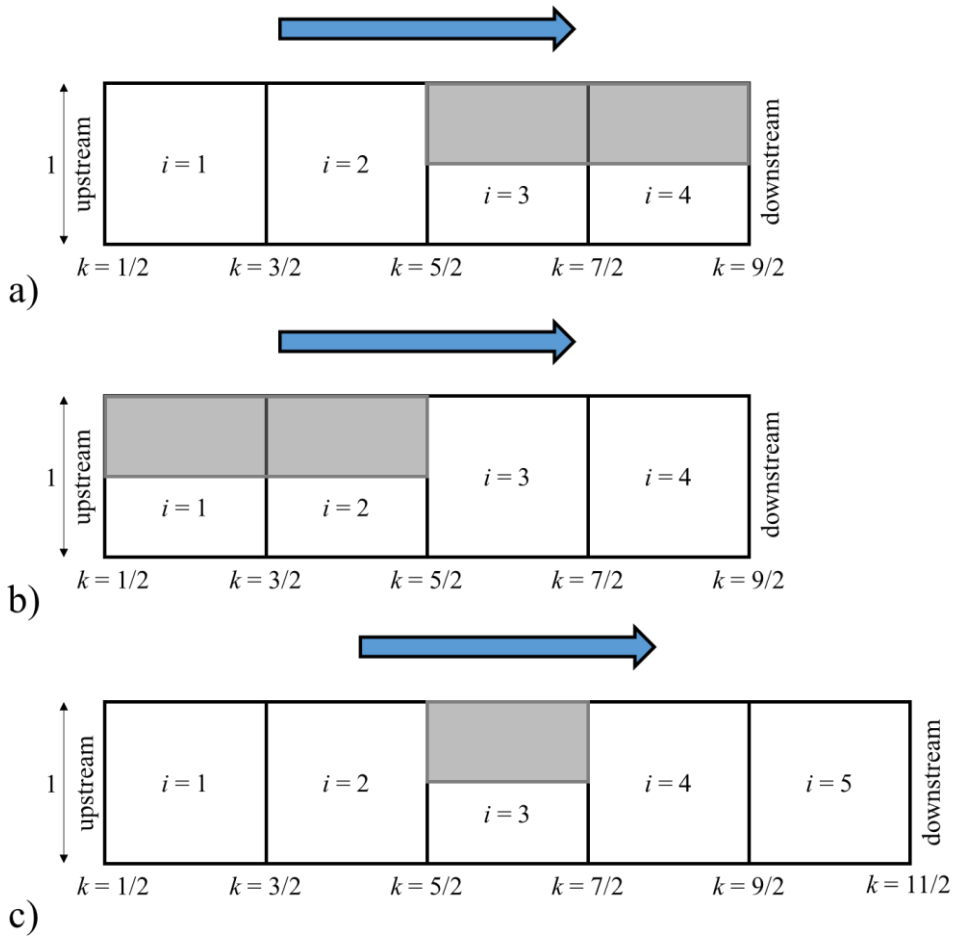

Figure 3-1 : Numerical domains with (a) four cells and a contraction or (b) an expansion zone and with (c) five cells and a contraction-expansion zone.

3.2.2. Derivation of the equations

Applying the equations of mass and momentum conservation for the cells of the numerical domains in a subcritical flow and considering the non-dimensional variables of Eq. (3-8), we derive the non-dimensional formulations of Table 3-1. Details on the derivation of the equations are available in Appendix D.2.

$$h_i^* = \frac{h_i}{h_1} \quad \text{and} \quad \mathrm{Fr}_{up}^2 = \frac{[hu]_{up}^2}{g h_1^3}, \tag{3-8}$$

For a given value of Fr_{up}, the equations of Table 3-1 constitute a system of four non-linear algebraic equations, which can be solved for the four (five) unknowns h_3^*, h_4^*, (h_5^*) and h_{down}^*. The equations can be solved sequentially.

Cell	Contraction zone	Expansion zone	Contraction-expansion zone
1	$h_1^* = h_2^* = 1$	$h_1^* = h_2^* = 1$	$h_1^* = h_2^* = 1$
2	$h_3^{*2}\frac{1+3\psi}{4} + h_3^*\frac{1-\psi}{2} + \frac{2\mathrm{Fr}_{\mathrm{up}}^2}{\psi}(1-\psi) - \frac{\psi+3}{4} = 0$	$h_1^* = h_3^* = 1$	$h_3^{*2}\frac{1+3\psi}{4} + h_3^*\frac{1-\psi}{2} + \frac{2\mathrm{Fr}_{\mathrm{up}}^2}{\psi}(1-\psi) - \frac{\psi+3}{4} = 0$
3	$h_4^{*2} = h_3^{*2} + \frac{2\mathrm{Fr}_{\mathrm{up}}^2}{\psi^2}\left(1-h_3^{*-1}\right)$	$h_4^{*2}\frac{3+\psi}{4} + h_4^*\frac{\psi-1}{2} - \frac{1+3\psi}{4} + 2\psi(\psi-1)\mathrm{Fr}_{\mathrm{up}}^2 = 0$	$h_4^{*2} = h_3^{*2} + \frac{2\mathrm{Fr}_{up}^2}{\psi^2}\left(1-h_3^{*-1}\right)$
4	$h_{down}^{2*} = h_4^{2*} - \frac{2\mathrm{Fr}_{\mathrm{up}}^2}{\psi^2}\left(\frac{1}{h_4^*} - \frac{1}{h_3^*}\right)$	$h_{down}^{2*} = h_4^{2*} - 2\psi^2\mathrm{Fr}_{\mathrm{up}}^2\left(\frac{1}{h_4^*} - 1\right)$	$h_5^{*2}\frac{1+3\psi}{4} + h_5^*h_4^*\frac{\psi-1}{2} - h_4^{*2}\frac{1+3\psi}{4} + \frac{2\mathrm{Fr}_{\mathrm{up}}^2}{\psi}\left(\psi h_4^{*-1} - h_3^{*-1}\right) = 0$
5	/	/	$h_{down}^{2*} = h_5^{2*} - 2\mathrm{Fr}_{\mathrm{up}}^2\left(\frac{1}{h_5^*} - \frac{1}{h_4^*}\right)$

Table 3-1: Non-dimensional formulations of the equations of mass and momentum conservations for the different numerical domains of Figure 3-1.

3.2.3. Results and discussion

The equations of Table 3-1were computed for upstream Froude numbers $\mathrm{Fr}_{\mathrm{up}}$ in the range 0.1 to 0.8, and for conveyance porosities ψ varying between 0.1 and 1.0. We stick to solutions in which the flow remains subcritical over the five cells. Flows leading to cells with Fr > 1 are not considered here because in such a case the computed variations in energy may not be attributed only to numerical artefacts related to the variation of the porosity; but they may also result from changes in the flow regime.

Consistently with the flux-vector splitting technique of Wolf2D, we evaluate the specific energy e_k at a cell edge by:

$$e_k = h_{k+1/2} + \frac{u_{k-1/2}^2}{2g} \tag{3-9}$$

The specific energy variation $\varepsilon_{e,k}$ is defined at an edge by comparing the energy at this edge to the energy at the upstream end (k = 1/2):

$$\varepsilon_{e,k} = \frac{e_{e,1/2} - e_{e,k}}{e_{e,1/2}} \tag{3-10}$$

The results are discussed hereafter for the numerical domain with a contraction zone (section 3.2.3.1), with an expansion (section 3.2.3.2) zone and with a contraction-expansion zone (section 3.2.3.3).

3.2.3.1. Contraction zone

In Figure 3-2, the contraction of the cross-section at the edge $k = 5/2$ leads to a decrease in the computed water depths in the downstream cells. At the downstream end, the water depths are systematically lower than at the upstream end. This difference increases for lower values of the conveyance porosity and upstream Froude numbers close to unity.

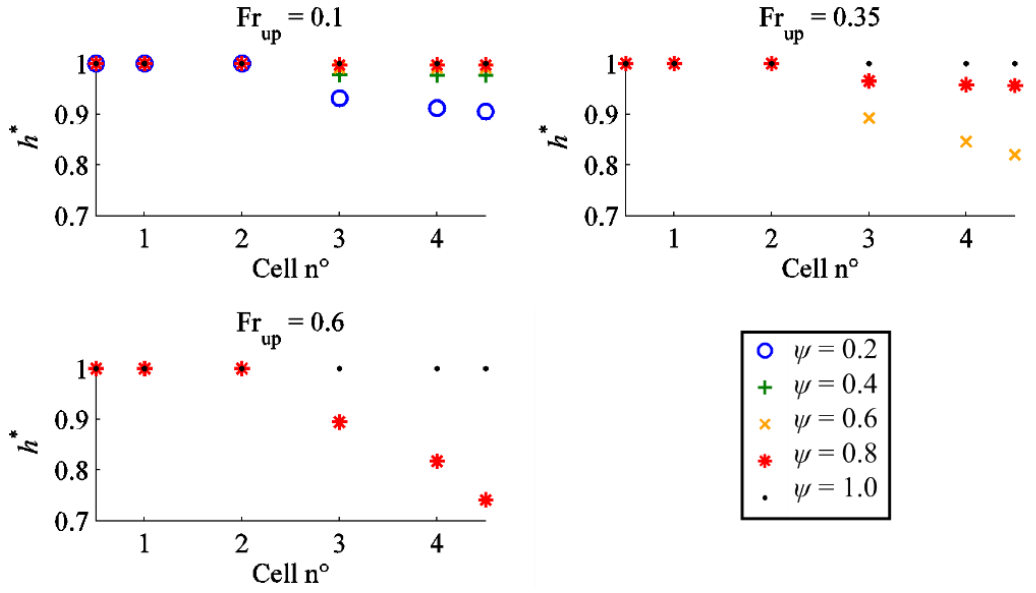

Figure 3-2 : Contraction zone - Water depth profiles for different upstream Froude numbers Fr_{up} *and conveyance porosities* ψ *.*

Figure 3-3 shows the specific energy variation per unit mass for different upstream Froude numbers and conveyance porosity values. The overall variation of specific energy between the upstream and downstream ends is higher for low values of the conveyance porosity and values of the upstream Froude number close to unity. For the lowest value of the upstream Froude numbers ($Fr_{up} = 0.1$), a numerical "creation" of specific energy occurs from the upstream end to the downstream end. On contrary, a loss of specific energy appears for the highest value of Fr_{up} ($Fr_{up} = 0.6$).

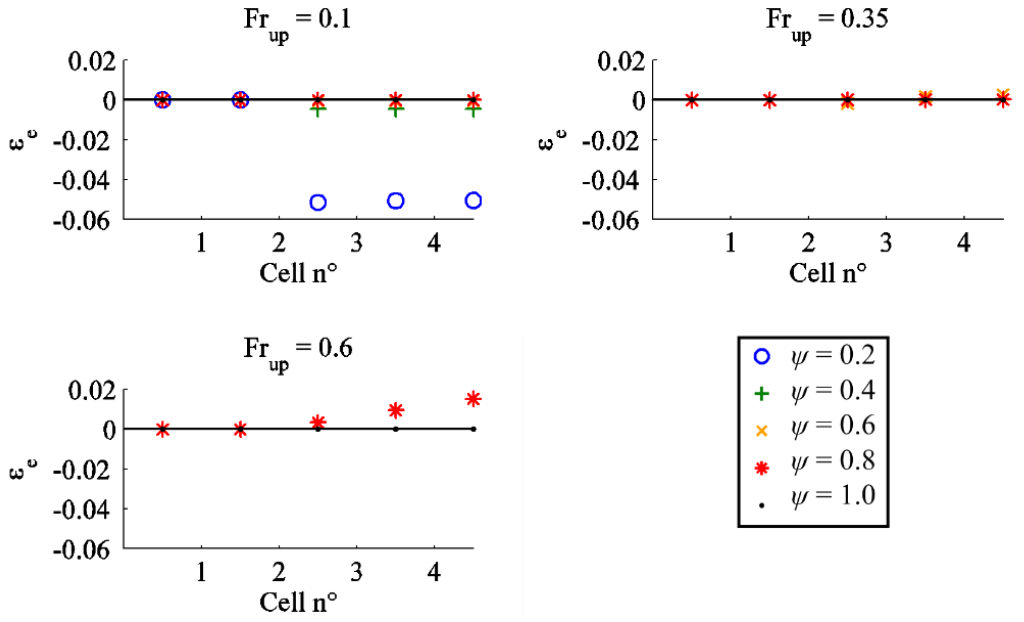

Figure 3-3 : Contraction zone - Loss of specific energy for different upstream Froude numbers and conveyance porosities.

The overall specific energy variation is shown for all values of conveyance porosity for different values of the upstream Froude number in Figure 3-4. For the highest values of the upstream Froude number (Fr_{up} = 0.35, 0.6 and 0.8), only a dissipation of energy occurs, which increases as the value of the conveyance porosity ψ becomes lower. For the lowest values of Fr_{up}, both a creation and a dissipation of energy are computed, depending on the value of the conveyance porosity. The specific energy variation globally increases as the value of the conveyance porosity decreases with some local drops. The reason for those should be investigated further.

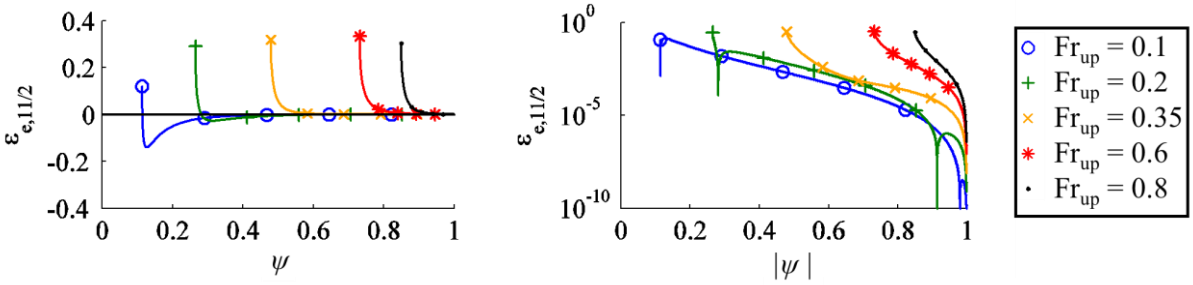

Figure 3-4 : Contraction zone - Overall variation of specific energy for different upstream Froude numbers as a function of the conveyance porosity.

3.2.3.2. Expansion zone

The expansion of the cross-section (increase in the value of the conveyance porosity) leads to an increase in the water depths in the expansion zone (Figure 3-5). This increase is maximum for high values of the upstream Froude number. Contrarily to the contraction zone (Figure 3-2), the change in water depth does not necessarily increase as the value of the conveyance porosity becomes lower.

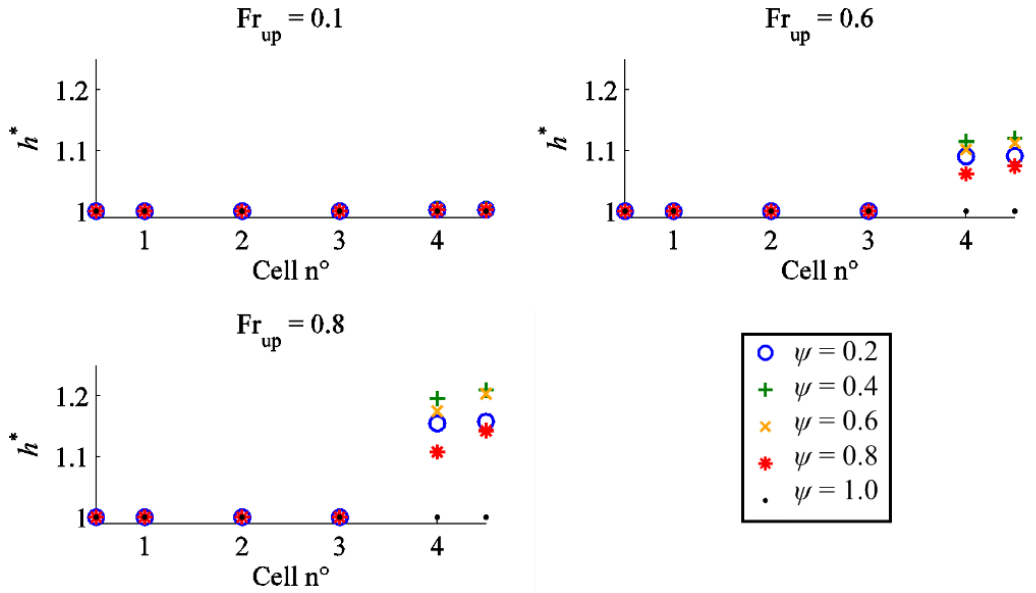

Figure 3-5 : Expansion zone - Water depth profiles for different upstream Froude numbers Fr_{up} and conveyance porosities ψ .

From upstream to downstream, a loss of specific energy is observed for all upstream Froude numbers and values of the conveyance porosity (Figure 3-6). As for the contraction zone, the change in specific energy is the highest for upstream Froude numbers close to unity and low values of the conveyance porosity.

As shown in Figure 3-7, the loss of specific energy may be computed for all values of the conveyance porosity since the value of the Froude number decreases after the expansion zone. The overall loss of specific energy increases gradually with decreasing values of the conveyance porosity ψ and with increasing values of the upstream Froude numbers.

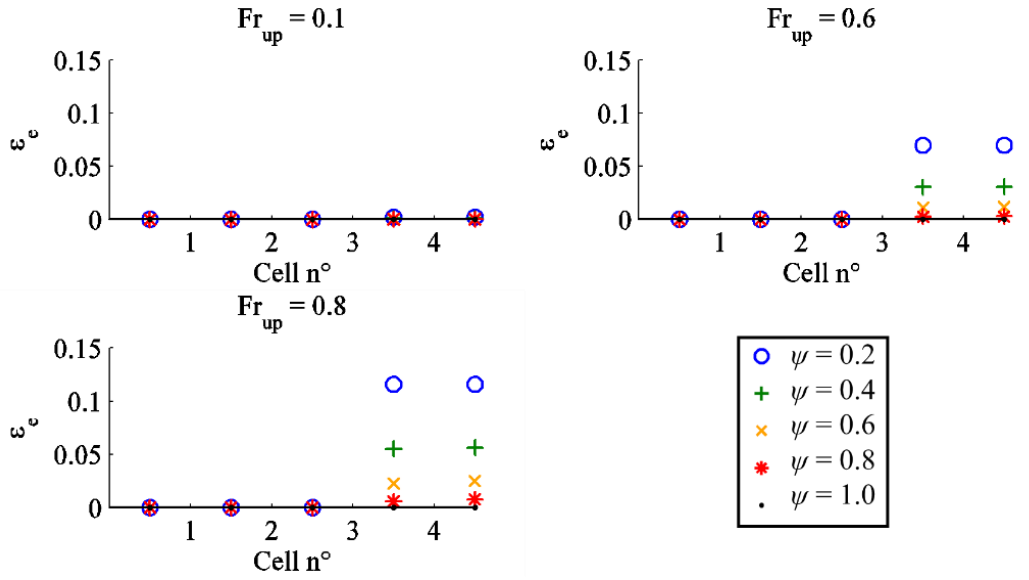

Figure 3-6 : Expansion zone - Loss of specific energy for different upstream Froude numbers and conveyance porosities.

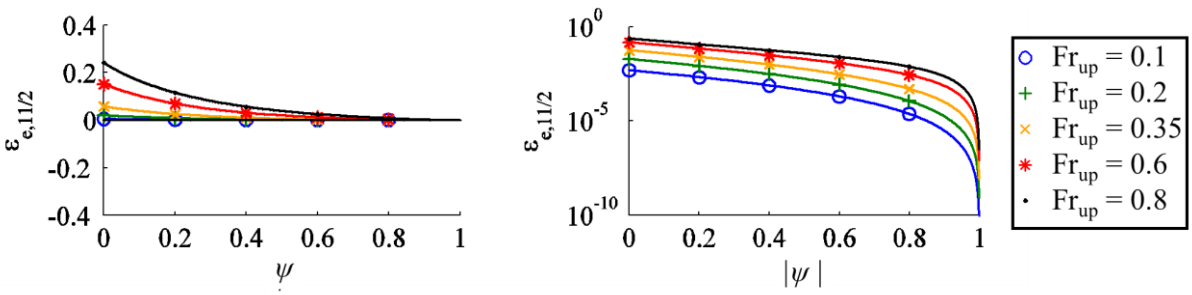

Figure 3-7 : Expansion zone - Overall variation of specific energy for different upstream Froude numbers as a function of the conveyance porosity.

3.2.3.3. Contraction-expansion zone

In Figure 3-8, the conveyance porosity at the edges $k = 5/2$ and $k = 7/2$ leads to decreases in the computed water depths in the cells located immediately downstream compared to the upstream level, consistent with the results obtained with the contraction zone (section 3.2.3.1). This drop in water depth is stronger for the cell downstream of the expansion (cell $i = 4$) compared to the cell downstream of the contraction (cell $i = 3$). After the expansion zone (cell $i = 5$ and edge $k = 11/2$), the water depths rise up to a value slightly lower than the upstream water depth, as observed for the expansion zone in section 3.2.3.2. The water depth variations within the domain are maximum for low values of the conveyance porosity and upstream Froude numbers close to unity.

Since the water depth at the downstream end ($k = 11/2$) is lower than at the upstream end ($k = 1/2$), an energy variation occurs. Since we do not consider any source term in the governing

equations (frictionless and slopeless channel without any drag force), the energy variations arise exclusively from the numerical discretization in the presence of varying values of the conveyance porosity.

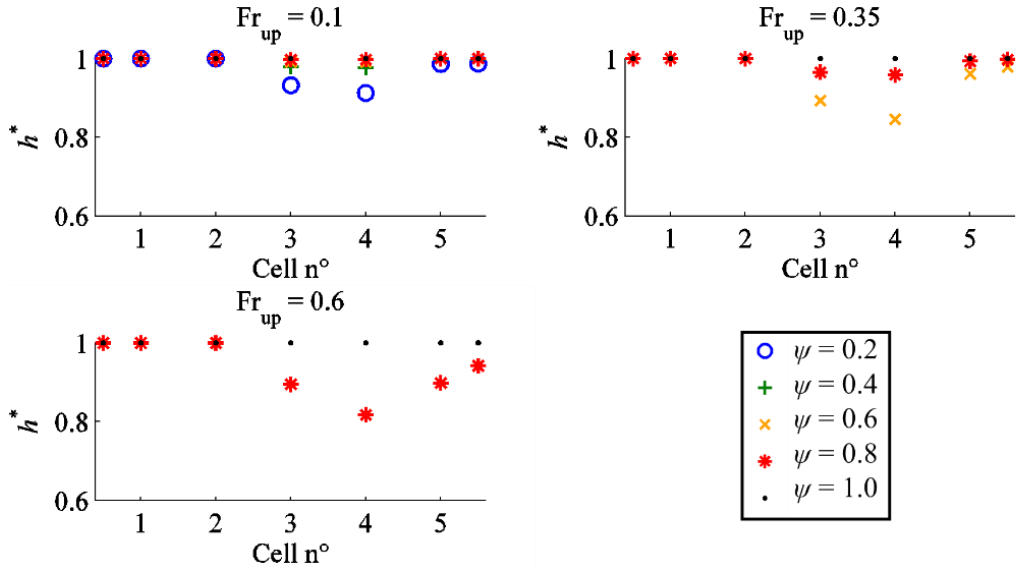

Figure 3-8 : Contraction-expansion zone - Water depth profiles for different upstream Froude numbers Fr_{up} and conveyance porosities ψ .

In Figure 3-9, the variations in conveyance porosity induce an overall dissipation of specific energy from upstream to downstream. For conveyance porosity values strongly different from unity (and relatively low upstream Froude numbers), the evolution of the specific energy is non-monotonous, while a gradual loss of specific energy appears when ψ remains at a value closer to unity. These results are consistent with those derived in sections 3.2.3.1 and 3.2.3.2 for the contraction and expansion zones:

- for Fr_{up} = 0.1: a "creation" of specific energy downstream of a contraction;
- for Fr_{up} = 0.6: a loss of specific energy downstream of a contraction;
- an overall loss of specific energy downstream of an expansion.

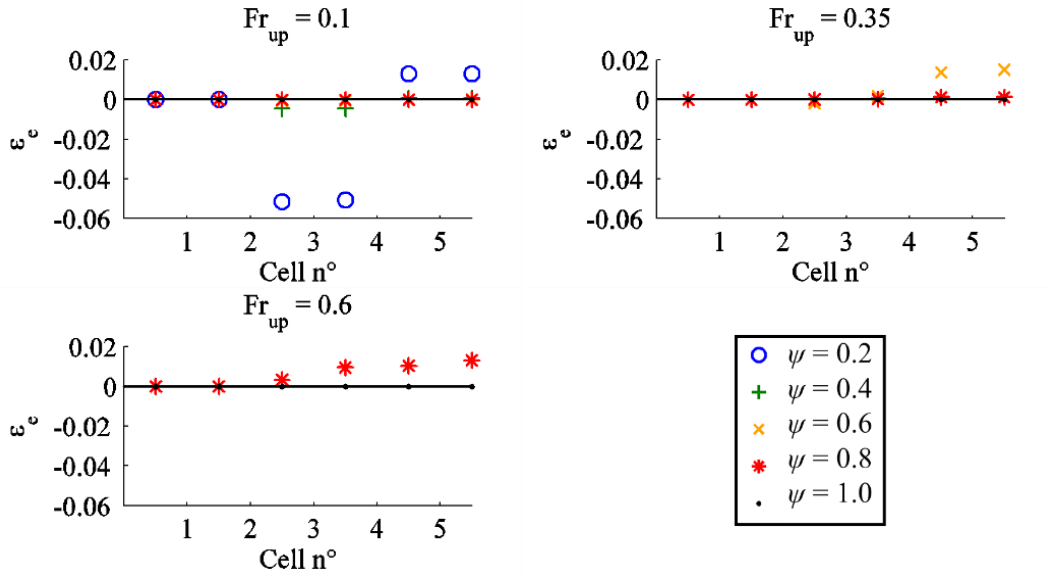

Figure 3-9 : Contraction-expansion zone - Loss of specific energy for different upstream Froude numbers and conveyance porosities.

Figure 3-10 shows the maximum Froude number over the five cells for different upstream Froude numbers as a function of the conveyance porosity. The maximum Froude number increases as the conveyance porosity decreases for the same upstream flow conditions. This increase is related to the reduction of water depths due to the conveyance porosity.

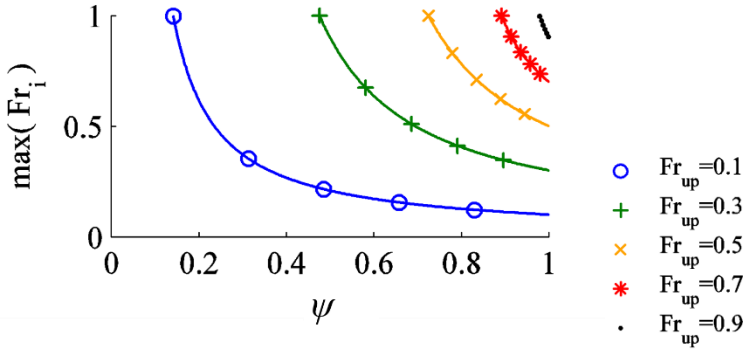

Figure 3-10 : Maximum Froude number over the five cells for different upstream Froude numbers as a function of the conveyance porosity.

For all upstream Froude numbers, the overall loss of specific energy $\varepsilon_{e,11/2}$ generally increases with a reduction of the conveyance porosity (Figure 3-11). While the numerical variation of specific energy remains low for most values of the conveyance porosity, significant values can arise consequently to the contraction zone (Figure 3-4).

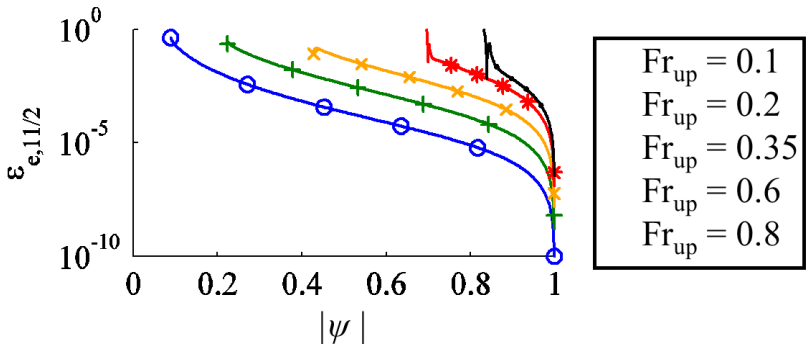

Figure 3-11 : Contraction-expansion zone - Overall variation of specific energy for different upstream Froude numbers as a function of the conveyance porosity.

3.3. Conclusion and perspective

Based on very simple theoretical test cases for sub-critical flow regimes, we show that the presence of a carrying conveyance porosity in the flux terms of the discretized porosity shallow-water equations leads to variation of the overall specific energy. While this purely numerical variation of specific energy remains low for a wide range of flow configurations, significant values can arise for specific combinations of upstream flow regime and conveyance porosities leading to Froude numbers close to unity in the obstruction zones. The variation of specific energy generally grows with a reduction of the conveyance porosity or with an increase in the value of the Froude number. After a contraction zone, either a “creation” or a loss of specific energy can arise depending on the value of the upstream Froude number. In contrast, only a loss of energy occurs downstream of an expansion zone. The results show that substantial variations in specific energy in a contraction-expansion zone can arise consequently to the reduction of the value of the conveyance porosity, while the expansion (rise in the value of the conveyance porosity) has a more limited impact.

Here, we used here the optimal discretization of the divergence formulation of the bed slope term (DFB) minimizing the energy variation related to the bed slope (section 2.3). The determination of the optimal discretization of the DFB leading to the minimum energy variation due to the conveyance porosity should be carried out and compared to the one obtained in section 2.3. Moreover, the specific energy variations computed in this chapter should be compared to those resulting from the bed slope. The analysis should also be extended to supercritical flow conditions.

4. Anisotropic porosity model with merging on Cartesian grids

In this section, we introduce the porosity-based model developed during this PhD thesis in section 4.1. The governing equations and the numerical discretization are presented in sections 4.2 and 4.3. The specific benefit of each contribution is highlighted through four tailored test cases in section 4.4. In section 4.5, we show the improvements in the reproduction of flow variables obtained with the porosity-based model for an experimental model of inundation flow in an urban district. The ability of the model to reproduce flow variables is shown in section 4.6 for an experimental set-up of a three-branch crossroad with obstacles located at different positions. Conclusions related to the development and validation of the porosity-based model are given in section 4.7.

Sections 4.1 to 4.4, as well as 4.7, of this chapter are based on the journal paper "*Shallow-water models with anisotropic porosity and merging for flood modelling on Cartesian grids*" by **M. Bruwier**, P. Archambeau, S. Erpicum, M. Pirotton and B. Dewals, accepted for publication in Journal of Hydrology.

ABSTRACT: Shallow-water models with porosity are used to compute floods at a relatively coarse resolution while accounting indirectly for detailed topographic data through porosity parameters. In many practical applications, these models enable a significant reduction of the computational time while maintaining an acceptable level of accuracy. In this paper, we improve the use of porosity models on Cartesian grids by three original contributions. First, a merging technique is used to handle cells with low porosity values which tend otherwise to seriously hamper computational efficiency. Next, we show that the optimal method for the determination of the porosity parameters depends on the modelling scale, i.e. the grid resolution compared to the characteristic size of obstacles and flow ways. Finally, we investigate the potential benefit of using a different porosity parameter in each term of the shallow-water equations. Five test cases, two of them being original, are used to validate the model and assess each contribution. In particular, we obtained speedup values between 10 and 100 while the errors on water depths remain around few percent.

4.1. Introduction

Shallow-water models are recognized as state-of-the-art for conducting inundation modelling for large scale real-world applications (El Kadi Abderrezzak et al. 2009, Costabile and Macchione 2015). The flow characteristics computed by such models are strongly affected by the quality of topographic data and by the relative size of the numerical model resolution compared to the typical size of obstacles and flow ways in the floodplains (Dottori et al. 2013). Today, topographic data have become widely available at a scale as fine as a few metres. While such high-resolution topographic data enable in principle the computation of surface flow variables with a high accuracy, solving the shallow-water equations at the metre-scale may become hardly tractable due to the computational burden.

In the following, we distinguish between three different modelling scales, as sketched in Figure 4-1 in the case of a Cartesian grid:

- *micro-scale*, i.e. all obstacles are resolved explicitly and with a fairly good accuracy (e.g., with about ten cells over the typical width of flow paths);
- *meso-scale*, i.e. the obstacles are explicitly represented by "holes" in the computational domain (as described by Schubert and Sanders, 2012); but they are poorly resolved (e.g., with just a couple of cells over the typical width of flow paths);
- *macro-scale*, i.e. the obstacles have a typical size comparable or smaller than the mesh size (e.g., the flow paths are generally smaller than the size of one computational cell).

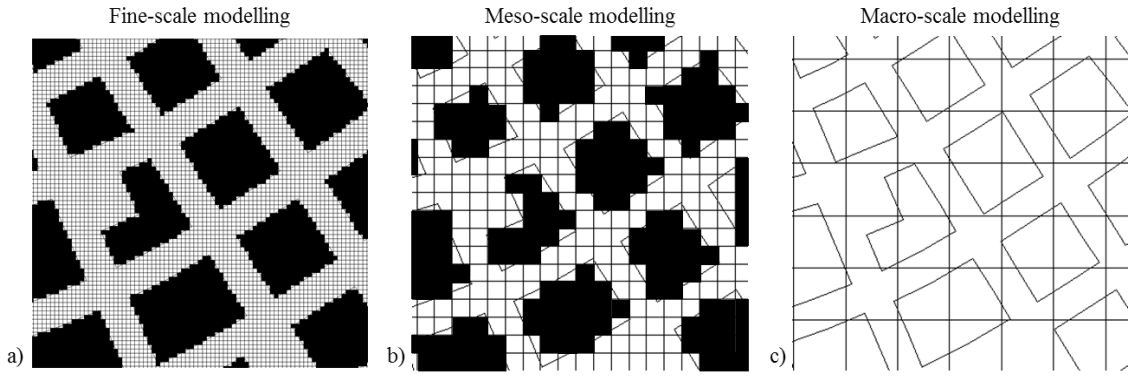

Figure 4-1 : Definition of (a) fine-scale, (b) meso-scale and (c) macro-scale modelling and representation of the obstacles explicitly represented by holes in the computational domain (dark cells).

Depending on the study objectives, meso-scale and/or macro-scale modelling may prove useful for inundation modelling over particularly large areas, or when a high number of model runs is necessary (scenario analysis, stochastic modelling …). In such cases, *subgrid models* may be

used to enhance the results accuracy. Subgrid models enable grid coarsening, while preserving to some extent the detailed topographic information.

Porosity models are one kind of subgrid models, in which fine-scale topographic information is reproduced at a coarser scale through porosity parameters. The role of these porosity parameters is to mimic at the coarse scale the influence of the unresolved subgrid obstacle features on the different terms of the shallow-water equations.

Some authors use the same porosity to reproduce the effect of obstacles on the conserved variables and on the flux terms of the shallow-water equations (Guinot and Soares-Frazão 2006). Such *isotropic porosity models* are based on a single porosity parameter ϕ_{REV} at the scale of a *Representative Elementary Volume* (REV), as detailed by Sanders et al. (2008). However, the scale required to obtain a REV is generally much greater than the cell size (Guinot 2012) which makes the determination of the isotropic porosity challenging.

Sanders et al. (2008) developed an *anisotropic integral porosity model* (IP) in which two types of porosity parameters are distinguished: a storage porosity ϕ (cell property) reflects the cell storage capacity and a conveyance porosity ψ (edge property) reflects the effect of obstacles on the flux terms. The storage porosity is evaluated as the geometrical void fraction within a cell. The conveyance porosity is computed as the void fraction along an edge, leading to conveyance porosities very sensitive to the mesh design. For this reason, Sanders et al. (2008) recommend the use of a *gap-conforming mesh* in which the mesh intersects optimally the obstacles to capture the conveyance effects of these obstacles. Since the porosity parameters are explicitly mesh-dependent, the governing equations are written directly in a discretized form. Recently, Guinot et al. (2017) proposed a *dual integral porosity model* (DIP), which outperforms the anisotropic integral porosity model. It distinguishes cell-based and edge-based flow variables, and it involves a transient momentum dissipation model.

The use of Cartesian grids is of practical relevance (Kim et al. 2014) as it makes the computational mesh consistent with commonly available gridded data, as obtained from most remote sensing techniques. Moreover, explicit numerical schemes computed on Cartesian grids are well adapted for parallelization techniques like GPUs (Brodtkorb et al. 2012). In this thesis, similarly to the integral porosity models, we start directly from the discretized form of the equations and we make three new contributions to improve the application of the porosity models on Cartesian grids.

For stability reasons, the computational time may dramatically increase in the presence of cells with a very low storage porosity. As a first contribution, this chapter introduces a *merging technique* to address this issue.

Up to now, anisotropic porosity models were preferably used with unstructured meshes as they require a gap-conforming mesh for the determination of the conveyance porosity (Kim et al. 2014). As a second contribution, we compare the standard method determining the conveyance porosity directly along edges of the computational cells (footprint method) to an original approach taking into account the presence of obstacles in a region defined around the edge. We show that the performance of the two methods are influenced by the relative sizes of the computational cells compared to the obstacles (meso- vs. macro-scale modelling).

In general terms, porosity parameters should be different in each term of the governing equations to reproduce optimally the effects of obstacles at a coarse scale. As a third contribution, the potential benefit of distinguishing the porosity parameters in the various terms of the governing equations is explored here for an idealized urban network.

The governing equations of the models with anisotropic porosity are introduced in sections 4.2.1 (integral form) and 4.2.2 (discrete form). The numerical resolution of the governing equations is presented in section 4.3. The new contributions are evaluated based on test cases in section 4.4.

4.2. Governing equations

4.2.1. Integral form

The integral form of the porous two-dimensional shallow-water equations writes for a control volume as (Sanders et al. 2008, Guinot et al. 2017):

$$\frac{\partial}{\partial t}\int_{\Omega} i\,\mathbf{U}\,d\Omega + \int_{\partial\Omega} i\,\mathbf{M}\,\mathbf{F}\cdot\mathbf{n}\,d\partial\Omega = \int_{\Omega} i\,\mathbf{S}\,d\Omega \qquad (4\text{-}1)$$

with Ω the total horizontal surface of the control volume, $\partial\Omega$ the boundary of the control volume, t the time, $\mathbf{n}=\left[n_x, n_y\right]^T$ the x- and y-normal unit vector components and i the binary phase function equal to 0 where obstacles stand and to 1 in the voids.

The conserved vector variable **U**, the momentum dissipation term **M**, the fluxes **F** and the source term **S** are:

$$\mathbf{U}=\begin{bmatrix} h \\ uh \\ vh \end{bmatrix}, \qquad \mathbf{M}=\begin{bmatrix} 1 & 0 & 0 \\ 0 & 1-\mu_{xx} & -\mu_{xy} \\ 0 & -\mu_{yx} & 1-\mu_{yy} \end{bmatrix},$$

$$\mathbf{F}=\begin{bmatrix} uh & vh \\ u^2h+\frac{1}{2}g\left(h^2-h_{\eta_{0,x}}^2\right) & uvh \\ uvh & v^2h+\frac{1}{2}g\left(h^2-h_{\eta_{0,y}}^2\right) \end{bmatrix}, \qquad \mathbf{S}=-\begin{bmatrix} 0 \\ \left(c_D^f+c_{D,xx}^b+c_{D,xy}^b\right)uV \\ \left(c_D^f+c_{D,yy}^b+c_{D,yx}^b\right)vV \end{bmatrix}, \tag{4-2}$$

with h the water depth, u and v the x- and y-velocity components, $V=\sqrt{u^2+v^2}$, g the gravitational acceleration, μ_{xx}, μ_{xy}, μ_{yx} and μ_{yy} the components of the transient momentum dissipation tensor, c_D^f the roughness coefficient, $c_{D,xx}^f$, $c_{D,xy}^f$, $c_{D,yx}^f$ and $c_{D,yy}^f$ the components of the drag tensor accounting for the resistance of obstacles to the flow. The term $gh_{\eta_0}^2/2$ corresponds to the divergence formulation of the bed slope term with h_{η_0} representing a water depth evaluated for a piecewise stationary water level $\eta=\eta_0$, as detailed in section 2.3 (Valiani and Begnudelli 2006).

The transient momentum dissipation tensor was introduced by Guinot et al. (2017). This additional term improves the reproduction of the propagation speed of a positive wave, at the expense of an additional parameter to be calibrated. Here, we mostly focus on steady and quasi-steady flow configurations, so that this tensor does not need to be considered $(\mu_{xx}=\mu_{xy}=\mu_{yx}=\mu_{yy}=0)$; except in our fifth test case focusing on wave propagation (section 4.4.5).

The drag tensor formulation introduced in Eq. (4-2) reflects the anisotropic nature of the drag force. However, in the following, we opt for a simplified scalar formulation (i.e. assuming $c_{D,xy}^b=c_{D,yx}^b=0$ and $c_{D,xx}^b=c_{D,yy}^b$), as originally used by Sanders et al. (2008):

$$c_{D,xx}^b=c_{D,yy}^b=\frac{c_D^0 ah}{2}, \tag{4-3}$$

where c_D^0 is a dimensionless drag coefficient, while a is the width of obstructions in the direction normal to the flow, per unit of planform area. This scalar drag formulation is a substantial

limitation of the present study, as further discussed in section 4.4.2.4. Recently, a more advanced head loss model was proposed by Velickovic et al. (2017). The model was tested for networks of perpendicular streets constituted by arrays of 5 × 5 aligned buildings. Based on a generalized tensor formulation and a so-called amplification factor, it accounts explicitly for the non-alignment of the main streets to the main flow direction and for the deviation of the bulk velocity to the direction of the streets. Nonetheless, further work is required to adapt the methodology and the calibration strategy to more general configurations.

4.2.2. Discrete form

Over a computational cell *j*, the average water depth $\langle h \rangle_j$ and unit discharges $\langle uh \rangle_j$ and $\langle vh \rangle_j$ are defined as:

$$\langle h \rangle_j = \frac{\int_{\Omega_j} ih \, d\Omega}{\int_{\Omega_j} i \, d\Omega}; \langle uh \rangle_j = \frac{\int_{\Omega_j} iuh \, d\Omega}{\int_{\Omega_j} i \, d\Omega}; \langle vh \rangle_j = \frac{\int_{\Omega_j} ivh \, d\Omega}{\int_{\Omega_j} i \, d\Omega} \tag{4-4}$$

Based on Eq.(4-4), other average variables can be deduced:

$$\langle u \rangle_j = \frac{\langle uh \rangle_j}{\langle h \rangle_j}; \langle v \rangle_j = \frac{\langle vh \rangle_j}{\langle h \rangle_j}; \langle V \rangle_j = \sqrt{\langle u \rangle_j^2 + \langle v \rangle_j^2} \tag{4-5}$$

Porosity parameters of the cell are defined as:

$$\phi_j = \frac{1}{\Omega_j} \int_{\Omega_j} i \, d\Omega; \phi_{s_x,j} = \frac{\int_{\Omega_j} iuV \, d\Omega}{\langle uV \rangle_j \Omega_j}; \phi_{s_y,j} = \frac{\int_{\Omega_j} ivV \, d\Omega}{\langle vV \rangle_j \Omega_j} \tag{4-6}$$

We introduce different edge porosity parameters for each type of flux term: ψ_c, ψ_{m,A_1}, ψ_{m,A_2} and ψ_{mP} respectively for the continuity flux term, the two advective terms and the pressure term. For a cell edge *k*, of length $\partial\Omega_k$, the edge porosity parameters are defined as:

$$\psi_{c,k} = \frac{\int_{\partial\Omega_k} iuh \, d\partial\Omega}{[uh]_k}; \psi_{mA_1,k} = \frac{\int_{\partial\Omega_k} iu^2 h \, d\partial\Omega}{[u^2 h]_k}; \psi_{mA_2,k} = \frac{\int_{\partial\Omega_k} iuvh \, d\partial\Omega}{[uvh]_k}; \psi_{mP,k} = \frac{\int_{\partial\Omega_k} h^2 \, d\partial\Omega}{[h^2]_k}, \tag{4-7}$$

where notation $[\ ]_k$ denotes the flow variables at the edges, as estimated by a piecewise constant reconstruction of the average values $\langle\ \rangle_j$ at the cells. The porosity parameters for the *y*- direction are defined similarly as for the *x*- direction.

Unlike standard definitions of the porosity, the parameters defined in Eq. (4-7) lump geometric effects, flow-related effects (similar to those reflected by Boussinesq coefficients in the usual shallow-water equations) and effects of the flow field reconstruction. Parameters $\phi_{s_x,j}$ and $\phi_{s_y,j}$, as defined in Eq. (4-6), also combine geometric and flow-related effects. Therefore, in the following, the quantities $\psi_{c,k}$, $\psi_{mA_1,k}$, $\psi_{mA_2,k}$, $\psi_{mP,k}$, $\phi_{s_x,j}$ and $\phi_{s_y,j}$ are all referred to as "porosity parameters" (instead of just "porosities").

Substituting definitions (4-4), (4-6) and (4-7) in Eq. (4-1) and considering the roughness and drag coefficients as uniform over each cell, the discrete formulation of the shallow-water model with anisotropic porosity parameters writes as:

$$\frac{\partial \langle \mathbf{U} \rangle_j}{\partial t} + \frac{1}{\Omega_j} \sum_{k=1}^{K} [\mathbf{F}]_k \, \partial\Omega_k = \langle \mathbf{S} \rangle_j \tag{4-8}$$

where the discrete average variable $\langle \mathbf{U} \rangle$, average fluxes $[\mathbf{F}]$ and average source term $\langle \mathbf{S} \rangle$ are given by:

$$\langle \mathbf{U} \rangle = \phi \begin{bmatrix} \langle h \rangle \\ \langle uh \rangle \\ \langle vh \rangle \end{bmatrix},$$

$$[\mathbf{F}] = \begin{bmatrix} \psi_{c,x}[uh] & \psi_{c,y}[vh] \\ \psi_{mA_1,x}\left[u^2 h\right] + \psi_{mP,x} \frac{g}{2}\left([h]^2 - h_{\eta_0,x}^2\right) & \psi_{mA_2,y}[uvh] \\ \psi_{mA_2,x}[uvh] & \psi_{mA_1,y}\left[v^2 h\right] + \psi_{mP,y} \frac{g}{2}\left([h]^2 - h_{\eta_0,y}^2\right) \end{bmatrix}, \tag{4-9}$$

$$\langle \mathbf{S} \rangle = -\begin{bmatrix} 0 \\ \phi_{s_x}\left(c_D^f + c_{D,x}^b\right)\langle uV \rangle \\ \phi_{s_y}\left(c_D^f + c_{D,y}^b\right)\langle vV \rangle \end{bmatrix}$$

Appendix E details the eigenvalue analysis of the system of governing equations for a one-directional flow over a horizontal and frictionless bottom. It shows that hyperbolicity of the system is ensured when $\psi_{mA_1} \geq \psi_c$.

In practice, the determination of each independent porosity parameter is challenging and may require an a priori knowledge of the flow field. For this reason, unless otherwise stated, the cell porosity ϕ_s is replaced in the following by the storage porosity ϕ while the edge porosity parameters ψ_c, ψ_{m,A_1}, ψ_{m,A_2} and ψ_{mP} are merged into a single conveyance porosity ψ. Under

this assumption, Eqs (4-8) and (4-9) become identical to those derived by Sanders et al. (2008). Only in section 4.4.4, the potential improvement brought by discriminating the different edge porosity parameters is analysed for an idealized urban network. It is also discussed in section 4.4.5.

For the determination of the drag term, we use in the following the simplified formulation introduced by Schubert and Sanders (2012) to approximate parameter *a* independently from the flow direction:

$$a = \frac{1}{K\Omega}\sum_{k=1}^{K}(1-\psi_k)\,\partial\Omega_k\,, \tag{4-10}$$

where *K* is the number of edges.

4.3. Numerical model

4.3.1. Spatial discretization

The governing equations are solved with the hydraulic model Wolf2D using a first-order conservative finite volume scheme based on a flux-vector splitting technique applied on a Cartesian grid (Erpicum et al. 2010a). The piecewise stationary free surface elevations $\eta_{0,x}$ and $\eta_{0,y}$ used in the divergence formulation of the bed slope term are evaluated as a linear combination of the free surface levels at the edges of the computational cell. The weighting factors in the linear combination are chosen to minimize the error in the energy balance, as detailed by Bruwier et al. (2016).

4.3.2. Time discretization

The time integration is performed using an explicit Runge-Kutta method. The stability of the scheme is ensured by a Courant-Friedrichs-Lewy criterion, modified by Sanders et al. (2008) to consider the porosity parameters. The criterion writes:

$$\Delta t \le CFL \min_j\left(\frac{\phi_j\,\Omega_j}{\max_K(\psi_k\partial\Omega_k)}\frac{1}{c_j}\right), \tag{4-11}$$

where Δt is the time step, $c_j = \sqrt{gh_j} + V_j$ the wave celerity of cell *j*, *CFL* the Courant number depending on the Runge-Kutta method.

4.3.3. Models summary

Depending on the method used for the determination of the porosity parameters, different porosity-based models can be derived from the governing equations (4-8) and (4-9), as detailed in Table 4-1.

If all porosity parameters are set to unity, the classical shallow-water model (CS) is retrieved.

If the storage and edge porosity parameters are set to the same value ϕ_{REV}, the isotropic porosity model (PS-I) is obtained.

If different values are used for the storage and edge porosity parameters, the model becomes anisotropic (PS-A). Different PS-A models can be derived depending on how the edge porosity parameters are evaluated:

- The standard approach in literature is based on a direct determination of a single conveyance porosity as the linear void fraction along each computational edge, which make it highly mesh-dependent. Here, this approach is referred to as model PS-A-1.
- While the gap-conforming property required for PS-A-1 models can be ensured using an unstructured mesh (Sanders et al. 2008), this is hardly feasible based on a Cartesian grid, as used here. Indeed, the determination of the conveyance porosities directly along the edges can fail to detect the presence of nearby obstacles, as highlighted by Chen et al. (2012) and Özgen et al. (2016). For this reason, we compare the PS-A-1 model to an original method, which consists in relating the conveyance porosity of an edge to the minimum fraction of free length parallel to this edge over half a computational cell on either sides of the edge (Figure 4-2). We call this model PS-A-2. Although this model remains mesh-dependent to some extent, the porosity parameters are less sensitive to the mesh design than those of the PS-A-1 model.

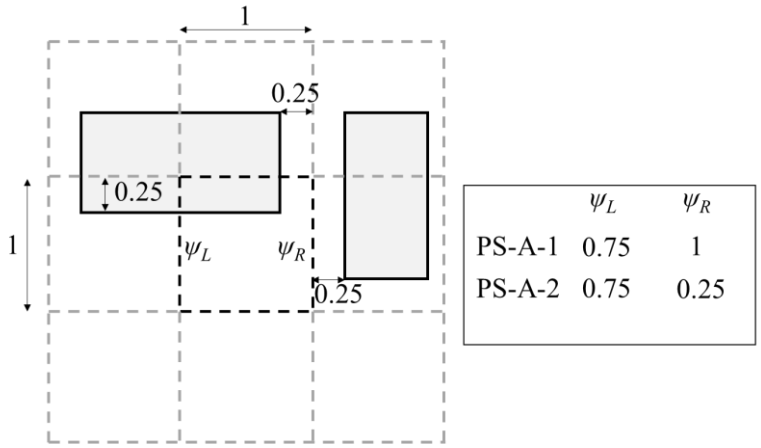

	ψ_L	ψ_R
PS-A-1	0.75	1
PS-A-2	0.75	0.25

Figure 4-2 : Example of determination of conveyance porosities with the PS-A-1 and PS-A-2 models.

In the case of meso-scale modelling (Figure 4-1b), the mesh is close to be gap-conforming and the PS-A-1 model is therefore expected to perform well (Arrault et al. 2016). In contrast, in the case of macro-scale modelling (Figure 4-1c), the obstacles are generally reproduced on the coarse grid only through the porosity parameters since they are not resolved explicitly. The mesh is mainly non gap-conforming and the PS-A-2 model is expected to improve the determination of conveyance porosity parameters.

Finally, two models distinguish different edge porosity parameters ψ_c, ψ_{m,A_1}, ψ_{m,A_2} and ψ_{mP}:

- In the recent dual integral porosity model (DIP) of Guinot et al. (2017), the edge porosity parameters are obtained from a closure model based on mass conservation considerations and on the assumption that obstacles have a significant influence on flow velocity but a negligible one on the free surface elevation. The resulting edge porosity parameters are combinations of the storage and conveyance porosities, ϕ and ψ, as detailed in Table 4-1. In the following, this model is referred to as model PS-A-1-D.
- In one of the test cases (idealized urban network), we also introduce a model (PS-A-D model) in which the edge porosity parameters are estimated from an a priori estimation of the main flow characteristics, as detailed in section 4.4.4.

Acronym	Guinot et al. (2017)	Storage porosity	Edge porosity parameters	Evaluation of the edge porosity parameters
CS		1	1	/
PS-I	Single porosity model (SP)	ϕ_{REV}	ϕ_{REV}	/
PS-A-1	Integral porosity model (IP)	ϕ	ψ	Geometrically along the edge (footprint method)
PS-A-2				Minimum free length parallel to the edge over half a cell on either sides of the edge
PS-A-1-D	Dual integral porosity model (DIP)		$\psi_c = \phi$, $\psi_{m,A_1} = \frac{\phi^2}{\psi} = \psi_{m,A_2}$, $\psi_{mP} = \psi$	Closure relation involving ϕ and ψ determined by the footprint method
PS-A-D			ψ_c, ψ_{m,A_1}, ψ_{m,A_2}, ψ_{mP}	Based on an a priori estimation of the flow features

Table 4-1: Summary of the porosity-based models, as well as the main characteristics and limitations.

4.3.4. Merging technique

From the stability criterion given by Eq. (4-11), the time step is expected to decrease dramatically in the presence of very low values of the storage porosity. A crude approach to circumvent this problem consists in removing from the computational domain the cells having a storage porosity lower than a threshold $\phi_{\min}$. A more elaborate technique consists in *merging* such cells with neighbouring cells, following a similar approach as developed by Causon et al. (2000) for cutcells. This technique was adapted here. It follows a four-step procedure, as sketched in Figure 4-3:

1) Identify all computational cells with a storage porosity lower than a threshold $\phi_{\min}$ (cell C in Figure 4-3).

2) The low porosity cell is merged with the neighbouring cell sharing the border with the highest conveyance porosity (cell B). If several of these borders have the same conveyance porosity parameters, the merging is performed with the neighbouring cell having the lowest storage porosity. If several of these neighbouring cells have the same storage porosity, the merging is split evenly between all of them.
3) The merging of the cells consists in increasing the storage porosity of the neighbouring cell by the storage porosity of the low porosity cell. If the merging involves multiple neighbouring cells, the storage porosity of the low porosity cell is shared equally between the neighbouring cells.
4) The topology of the edges is also updated by the cell merging. In Figure 4-3, the right edge of cell D (DC) is connected to cell B while the left edge of cell B (AB) becomes connected to cells A and D (edge AB + DC). The bottom edge of cell B is set impervious.

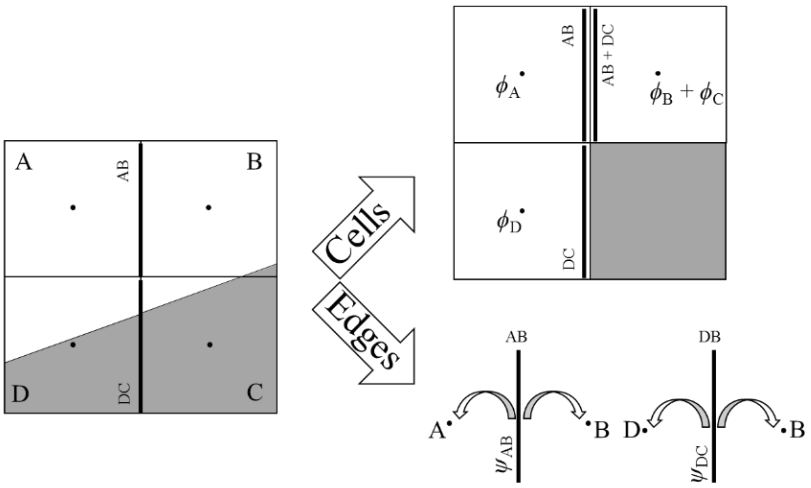

Figure 4-3 : Representation of an application of the merging technique on cell C.

4.4. Test cases

Five test cases are presented in this section, two of them being original. As detailed in Table 4-2, each of the first four test cases enables assessing one specific contribution of the manuscript, while in the fifth test, the ability of the porosity model to reproduce wave propagation is evaluated.

Based on a simple configuration involving a straight channel of varying orientation, the first original test case demonstrates the gain in efficiency and accuracy obtained thanks to the merging technique (section 4.4.1). This technique is then used in all subsequent test cases.

The second and third test cases (sections 4.4.2 and 4.4.3) aim at comparing different methods for the determination of the conveyance porosity parameters at meso- and macro- scale. In section

4.4.2, steady flows are computed in three synthetic but quasi-realistic urban networks. The PS-A-1 model is used for two urban networks discretized at the meso-scale. The PS-A-1 and PS-A-2 models are compared for the third urban network which lies at the transition between the meso-scale and the macro-scale. In section 4.4.3, the two models PS-A-1 and PS-A-2A are compared for the computation of a dam-break flow over an isotropic array of buildings discretized at the macro-scale.

Based on an idealized urban network, the fourth test case (section 4.4.4) shows the potential benefit of distinguishing the porosity parameters involved in each term of the governing equations (PS-A-D model). This test case also compares the PS-A-D model to the DIP model of Guinot et al. (2017).

In a fifth test case, the PS-A-D model is used with the transient momentum dissipation model introduced by Guinot et al. (2017) to reproduce a dam-break flow (positive and negative wave) over an idealized urban area.

Objective	Test case 1	Test case 2	Test case 3	Test case 4	Test case 5
Assess the merging technique	■	□	□	□	□
Compare different evaluations of the conveyance porosity for *meso-scale* modelling		■			
Compare different evaluations of the conveyance porosity for *macro-scale* modelling			■	■	
Explore the use of distinct porosity parameters in the various fluxes				■	□
Assess model performance in reproducing positive and negative wave propagation					■

Table 4-2: Overview of the five test cases and their specific objectives. Symbol ■ indicates that the corresponding model feature is tested systematically in the test case, while symbol □ refers to model features which are used in the test case but the test case is not specifically dedicated to their assessment.

In all test cases, the *average error L* is used as a metrics to quantify the difference between the results computed with the porosity models (w_1) and a set of N reference values (w_2):

$$L = \frac{1}{N}\sum_{i=1}^{N}\left|w_2 - w_1\right| \tag{4-12}$$

In line with Kim et al. (2015), we distinguish here five types of errors:

- the *structural model error* L_1 reflects the differences between micro-scale results and measurements;
- the *scale error* L_2 results from the averaging of the micro-scale results to the coarse scale (called hereafter "CS-P predictions");
- combining errors L_1 and L_2, the *pore-scale error* L_{1+2} represents the differences between the CS-P predictions and measurements.
- the *coarse model error* L_3 corresponds to the difference between the results of a coarse scale model and the CS-P predictions. If the coarse scale model is a porosity model, error L_3 is called *porosity model error*;
- finally, the *total error* L_0 is obtained by comparing directly the (coarse) model results to the measurements.

Note that errors L_1, L_2 and L_{1+2} are independent of the considered porosity model.

4.4.1. Rectangular channel with varying orientation

4.4.1.1. Description of the test case

We first consider the simple configuration of a normal flow in a prismatic channel for a discharge Q. The channel is characterized by a constant rectangular cross-section of width W, a bed slope i, a length L and a Manning roughness coefficient n. The values of these parameters are taken as representative of one reach of a realistic large river (Table 4-3).

Parameter	Symbol	Value
Length	L	15 km
Width	W	120 m
Longitudinal slope	i	0.2%
Manning roughness coefficient	n	0.025 $sm^{-1/3}$
Discharge	Q	2,000 m^3/s
Theoretical normal water depth	h_u	2.517 m
Mesh size	dx	30 m

Table 4-3: Parameters of the rectangular channel.

Using a shallow-water model on a Cartesian grid and prescribing the normal water depth h_u as a downstream boundary condition, the computed water depths remain equal to h_u all along the channel if the channel is oriented along the Cartesian grid (Figure 4-4a). In contrast, if the channel is not aligned with the grid (Figure 4-4b), the computed water depths are higher than the theoretical normal water depth and the flow variables fluctuate spatially due to abrupt changes of cross-section resulting from the banks discretization. At some distance from the downstream end of the channel, the computed water depths along the centreline fluctuate around a mean value $\hat{h}_u$ (Figure 4-5), which we consider here as a "numerical" normal water depth.

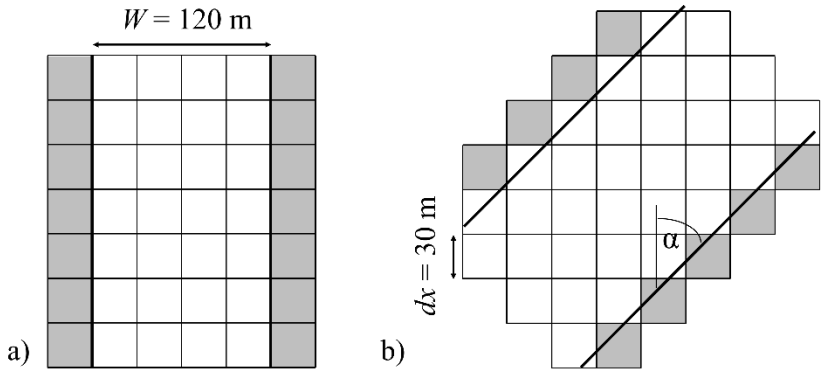

Figure 4-4 : (a) Channel aligned with the grid (α = 0°) and (b) channel of a different orientation than the grid, leading to artificial changes of cross-section in the numerical discretization.

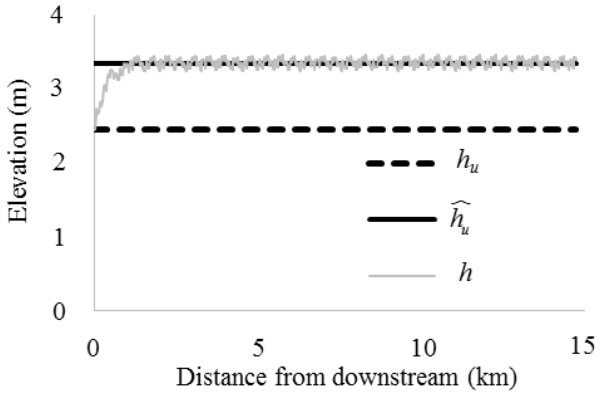

Figure 4-5 : Spatial variation of the water depth h along the centreline of the channel, theoretical normal water depth h_u and numerical normal water depth $\hat{h}_u$ (angle α = 15°).

In the following, we compare the numerical normal water depth value $\hat{h}_u$ and the theoretical one h_u using the ratio $\hat{h}_u/h_u$.

4.4.1.2. Classical shallow-water model vs. porosity-based model

Simulations were performed for an orientation of the channel varying between α = 0° and α = 45°, with a step of 1°. Using the CS model, the numerical normal water depth $\hat{h}_u$ steadily increases when α is varied between 0° and 20° (Figure 4-6). The numerical values of the normal water depth overestimate the theoretical one by almost 40% for angles α in-between 20° and 35°. This overestimation is gradually reduced as α increases from 35° up to 45°.

The results of CS model are compared to those obtained with the PS-A-1 model. For all orientation angles α, the PS-A-1 model leads to numerical normal water depths $\hat{h}_u$ much closer to the theoretical ones. In addition, the remaining overestimation of the normal water depth decreases significantly when the threshold porosity $\phi_{\min}$ is reduced. This demonstrates the ability of the PS-A-1 model to compensate almost completely for the staircase effect resulting from the discretisation of the oblique boundaries of the channel on a Cartesian grid.

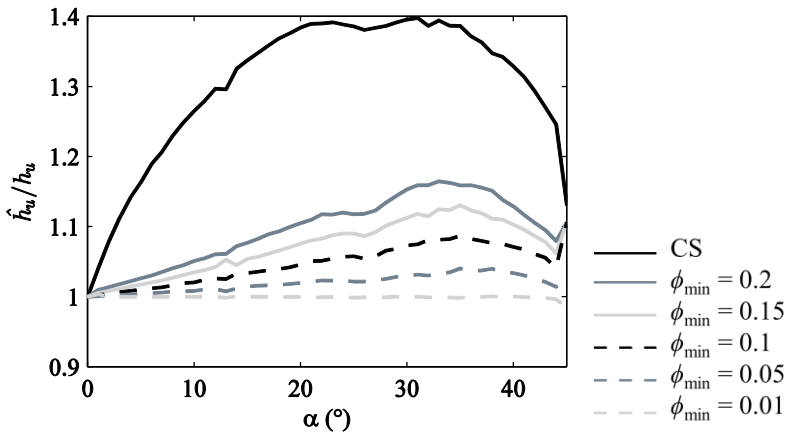

Figure 4-6 : Numerical normal water depth $\hat{h}_u$ compared to the theoretical one as a function of the orientation angle α, using the CS model and the PS-A-1 model for different threshold porosities ϕ_{min} (dx = 30 m).

4.4.1.3. Porosity model with merging

When the merging technique is used, the computed normal water depths $\hat{h}_u$ become much closer to the theoretical value h_u, even for relatively high values of $\phi_{\min}$ (Figure 4-7 and Figure 4-8a). For instance, for a $\phi_{\min}$ value of 0.2, the overestimation of h_u is reduced from ~16% (no merging) to ~1% (with merging). For low values of $\phi_{\min}$, the numerical normal water depth is even underestimated with the PS-A-1 model with merging, but this underestimation remains lower than 5%.

For a given threshold porosity, the computational time (CT) with merging is slightly higher than without (Figure 4-8b). However, since the merging technique enables the use of much higher values of $\phi_{\min}$ to reach a given accuracy, the benefit of this technique in terms of computation time is great.

For instance, to limit the numerical error on h_u at 5%, a threshold porosity of $\phi_{\min} = 0.05$ is required without merging ($\max_{\alpha} |\hat{h}_u/h_u - 1| \approx 4\%$) while a value of $\phi_{\min} = 0.75$ may be used in combination with the merging technique ($\max_{\alpha} |\hat{h}_u/h_u - 1| \approx 3\%$) (Figure 4-8a). For these values, the PS-A-1 model without merging is 14.5 times computationally more expensive than the CS model, whereas the PS-A-1 model with merging is only 1.9 times more expensive.

Using a micro-scale CS model with cell sizes of 5 m, the maximum relative error $\max_{\alpha} |\hat{h}_u/h_u - 1|$ is around 11%. Since the computation cost scales theoretically with Δx^3, the computation time for the CS model with a cell size of 5 m is about 6^3 times higher than with the CS model with a cell size of 30 m, which is around two orders of magnitude slower than the PS-A-1 model with merging for a similar accuracy.

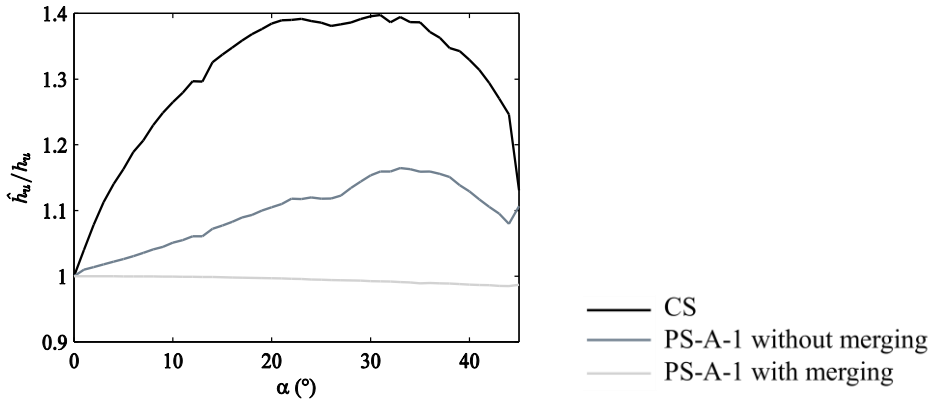

Figure 4-7 : Numerical normal water depth $\hat{h}_u$ compared to the theoretical one as a function of the orientation angle α, using the CS model and PS-A-1 models without and with merging for $\phi min = 0.2$ (dx = 30 m).

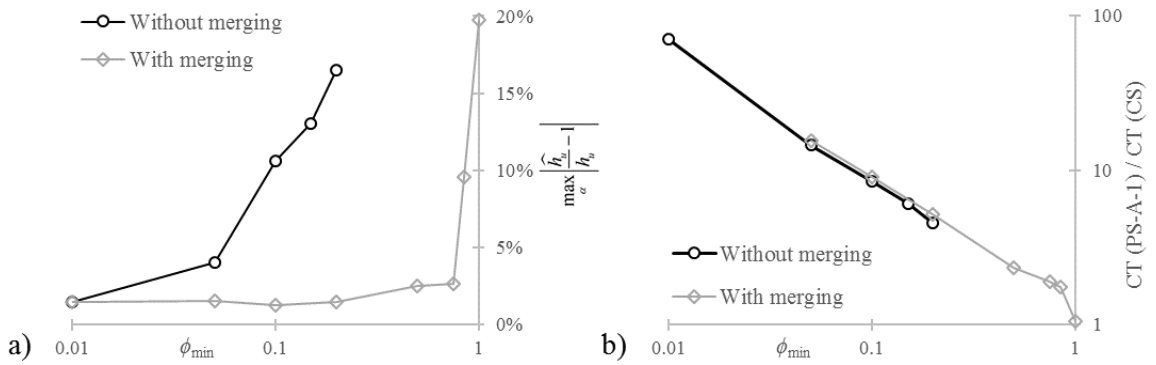

Figure 4-8 : (a) Maximum relative error between the numerical normal water depth $\hat{h}_u$ and the theoretical one h_u over all the orientation angles α for the PS-A-1 model without and with merging; (b) Ratio between the computational time (CT) of the PS-A-1 model without and with merging and the CT of the CS model as a function of the threshold porosity ϕ_{min} (dx = 30 m).

4.4.2. Synthetic urban networks

This original test case is based on three synthetic urban configurations (Figure 4-9) characterized by strongly contrasting geometric parameters (i.e. different streets widths and curvatures, buildings areas, building coverage ratios …).

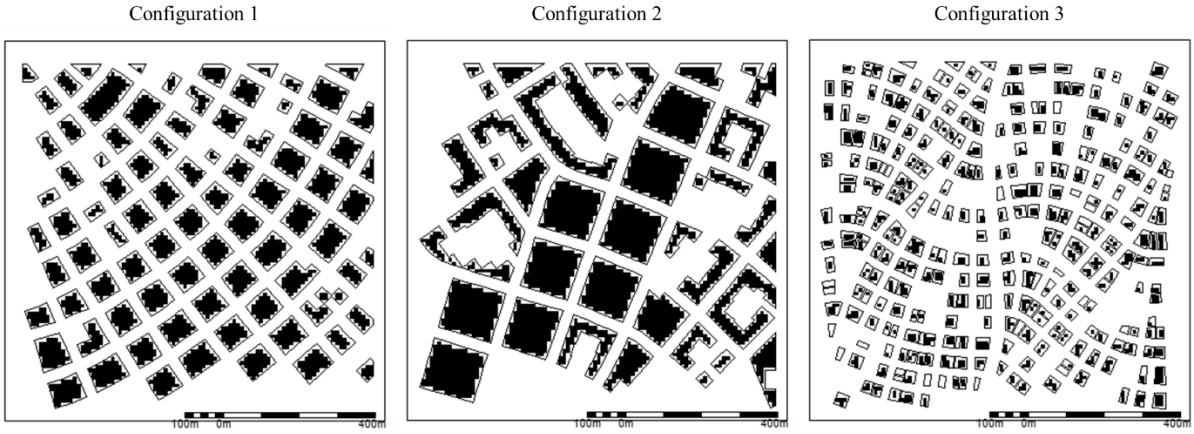

Figure 4-9 : Definition of the three synthetic urban configurations (contour lines) and explicit representation of the buildings on a Cartesian grid of 10 m (black areas).

4.4.2.1. Description of the test cases

The considered urban networks extend over a domain of 1 x 1 km^2 with flat bottom and a uniform Manning roughness coefficient of n = 0.04 $sm^{-1/3}$.

A total inflow discharge of 200 m^3/s is prescribed uniformly along the left and bottom sides of the domain (upstream boundary). The following weir formula is used as downstream boundary condition along the right and top sides of the urban area:

$$q = 0.5\sqrt{2g\left(h-0.3\right)^3} \qquad (4\text{-}13)$$

The average areas of the buildings of configurations 1, 2 and 3 are respectively 3,861 m^2, 8,423 m^2 and 744 m^2.

4.4.2.2. Numerical models

Different computations have been performed for the three configurations:

- Reference values for the hydraulic variables were generated at a micro-scale of 1 m with the CS model (CS-1m.). The computed water depths and unit discharges are displayed in Figure F-1 of the Appendix F.
- Configurations 1 and 2 were computed at a coarse scale of 10 m. At this scale, the cell area remains more than one order of magnitude smaller than the average area of the buildings (Figure 4-9a,b), corresponding thus to meso-scale modelling. Computations were performed with the CS (CS-10m) and PS-A-1 models with merging ($\phi_{\min} = 0.5$) considering different values for the drag coefficient c_D^0.
- Configuration 3 was simulated at the coarse scale of 10 m with the porosity models with merging ($\phi_{\min} = 0.1$). The threshold $\phi_{\min}$ was taken at a lower value than for configurations 1 and 2 to reproduce more accurately the narrow streets between buildings. While some obstacles are physically represented in the computational domain (meso-scale), 10.6% of obstacles are only reproduced through the porosity parameters (macro-scale). The ability of PS-A-1 and PS-A-2 models to reproduce the reference results at the coarse scale is analysed and compared without drag term and with an optimal drag coefficient of $c_D^0 = 2$.

The water depths computed with the different numerical models are compared along the upstream boundary, while the distribution of the unit discharges is compared along the downstream boundary.

4.4.2.3. Results

Using the CS model at the coarse scale (CS-10m) for configurations 1 and 2, the water depth profiles along the upstream border are overestimated (Figure 4-10) and the coarse model errors on water depths $L_{3,h}$ are around 5% of the mean water depths (Figure 4-11). The PS-A-1 model without drag term underestimates the water depths; but the corresponding $L_{3,h}$ values decrease to around 2%. A very satisfactory reproduction of the water depth profiles is obtained with the drag term, for which the coarse model errors are reduced to about 0.5%.

The normal unit discharge profiles along the downstream borders are visually close to each other (Figure F-2). Differences mainly occur at the extremities of the profiles where the flow does not cross the urban area. The coarse model errors on discharges $L_{3,q}$ are reduced by using the PS-A-1 models instead of the CS-10m model but are not significantly influenced by the drag term.

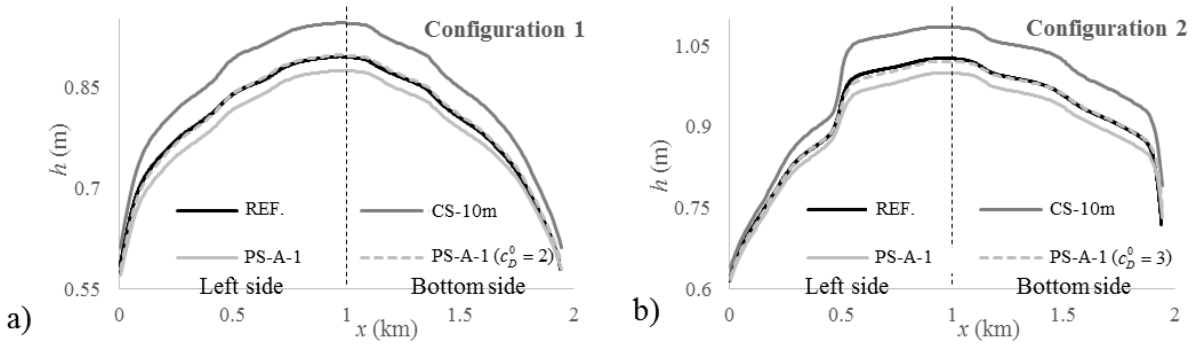

Figure 4-10 : Computed water depths along the inflow boundaries, i.e. along the left and bottom sides of the urban area in configurations 1 (a) and 2 (b).

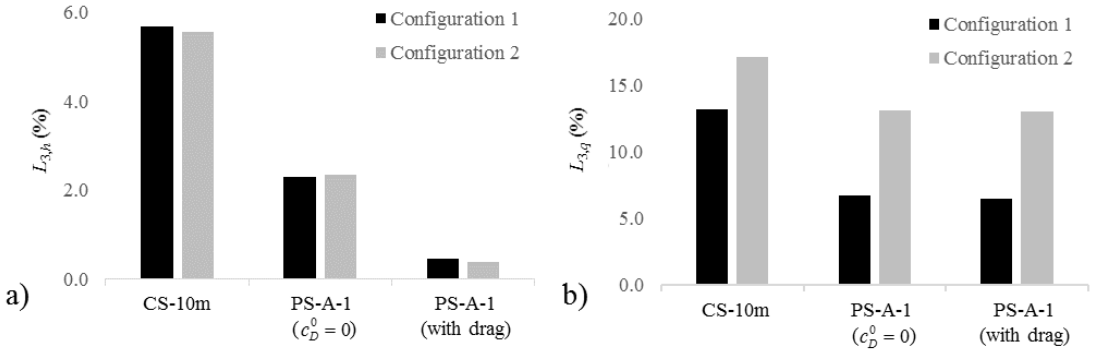

Figure 4-11 : Coarse model errors L_3 on the water depth (a) and unit discharge profiles (b) for configurations 1 and 2.

In configuration 3, the water depths along the upstream boundary are underestimated with the PS-A-1 model and slightly overestimated with the PS-A-2 model when no drag term is considered (Figure 4-12). The results in Figure 4-13 show that, without any calibration ($c_D^0 = 0$), the PS-A-2 model ($L_{3,h} \approx 1\%$) performs significantly better than the PS-A-1 model ($L_{3,h} \approx 4\%$), for a configuration at the transition between meso- and macro- scale modelling. The PS-A-1 model with a drag term gives a value of the porosity model error on the water depth $L_{3,h}$ (0.5%) similar to the best values obtained for configurations 1 and 2. The normal unit discharges remain weakly affected by the method used for the determination of the conveyance porosities and by the drag term (Figure 4-13b and Figure F-3).

Overall, the three meso-scale configurations considered here reveal that evaluating the conveyance porosity directly along the edges by the standard footprint method (i.e. model PS-A-

1) leads to accurate results. Using the PS-A-1 model at a coarse scale of 10 m lead here to a reduction of the computational time by about two orders of magnitude compared to a simulation at a micro-scale of 1 m while preserving accuracies on the upstream water depths around 0.5% of the mean value.

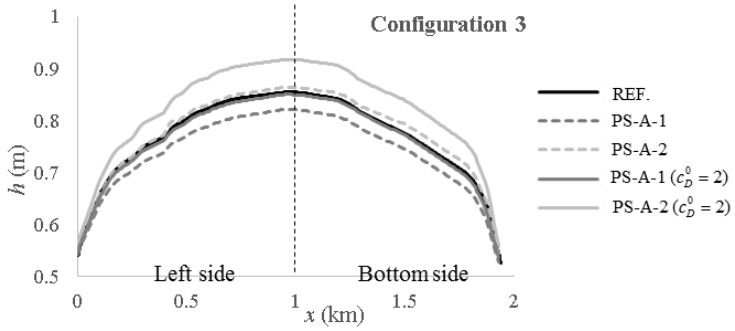

Figure 4-12 : Computed water depths along the inflow boundaries, i.e. along the left and bottom sides of the urban area in configurations 3.

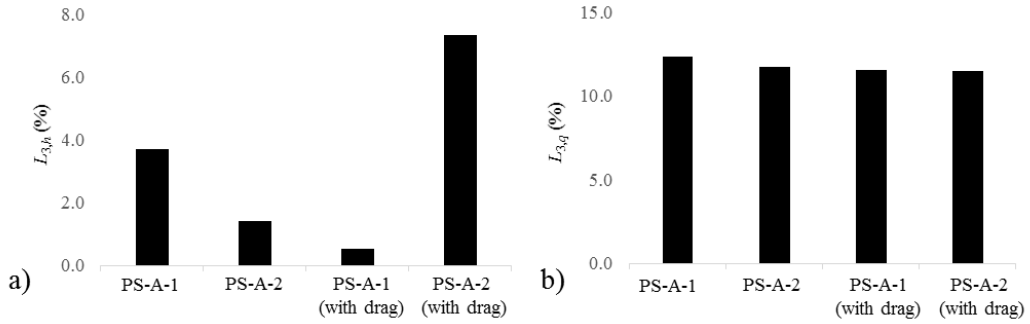

Figure 4-13 : Porosity model errors L_3 on the water depth (a) and unit discharge profiles (b) for configuration 3 with a grid size of 10 m.

4.4.2.4. Limitation of the scalar formulation of the drag term

Additional computations were performed for Configuration 1 (Figure 4-9) with two different sets of flow boundary conditions (Table 4-4). The results presented in section 4.4.2.3 were obtained by considering inflow boundary conditions along the left and bottom sides of the urban area, and downstream boundary conditions along the right and top sides. Here, the computations were repeated by setting the inflow and outflow boundary conditions along two opposite sides of the domain (i.e. left and right, or bottom and top sides), while the two remaining sides were considered as impervious.

The profiles of computed water depths along the upstream sides of the urban area are displayed in Figure 4-14, which is similar to Figure 4-10. Compared to the results of a standard shallow-

water model (CS-10m model), the water depths computed with the anisotropic porosity model (PS-A-1 model) are closer to the reference (CS-P predictions). For both the left-to-right and the bottom-to-top flow configurations, the coarse model errors on water depths $L_{3,h}$ range between 2% and 5% of the mean water depth when the drag coefficient is varied between $c_D^0 = 0.0$ and $c_D^0 = 2.0$. This is substantially lower than when no porosity model is used (10% with the CS-10m model).

The optimal values of the drag coefficient for the left-to-right and bottom-to-top flow configurations is the same ($c_D^0 = 0.5$). This is in agreement with the overall orientation of the network of streets almost along the diagonals of the computational domain, which makes the two flow configurations approximately equivalent. In contrast, we find that the optimal drag coefficient differs between the initial set of flow boundary conditions (section 4.4.2.3) and the two flow configurations considered here (left-to-right and bottom-to-top). In the former case, the optimal value of c_D^0 was equal to 2.0, whereas here the coarse model error on water depths is minimal when c_D^0 is reduced to 0.5. This result confirms a fundamental limitation of the scalar formulation of the drag term, which fails to capture the dependence of drag effects on the orientation of the main flow direction compared to the network of street. The loss in accuracy resulting from this limitation remains nonetheless lower than the enhancement in accuracy brought by the use of a porosity model instead of a standard shallow-water model (CS-10m). Although only tested so far for idealized periodic urban networks, the more advanced tensor formulation introduced by Velickovic et al. (2017) paves the way for the development of generalized drag models as needed for simulating complex urban flooding in realistic street networks.

Flow boundary conditions	According to section 4.2.1	Left-to-right	Bottom-to-top
Left side	Inflow boundary	Inflow boundary	Impervious
Right side	Outflow boundary	Outflow boundary	Impervious
Bottom side	Inflow boundary	Impervious	Inflow boundary
Up side	Outflow boundary	Impervious	Outflow boundary
Optimal drag coefficient	$c_D^0 = 2.0$	$c_D^0 = 0.5$	$c_D^0 = 0.5$

Table 4-4: Considered flow boundary conditions and corresponding optimal values of the drag coefficient.

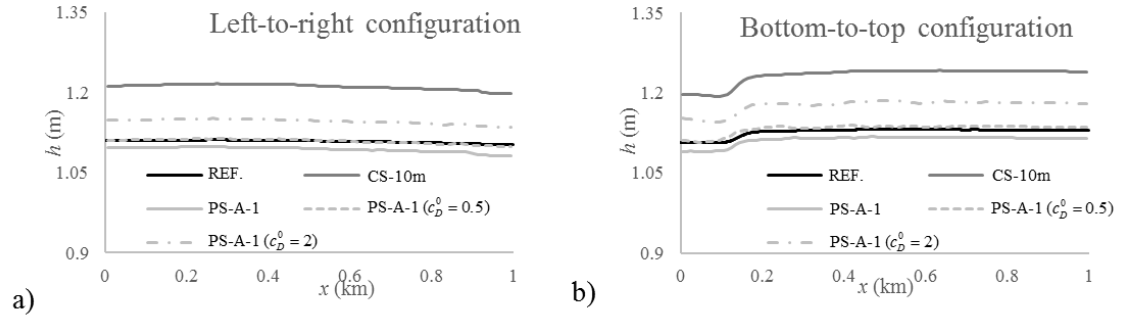

Figure 4-14 : Water depths along the upstream boundaries in the "left-to-right" (a) and "bottom-to-top" (b) flow configurations.

4.4.3. Dam-break flow over an anisotropic array of buildings

4.4.3.1. Test case description

We consider a dam-break flow over an urban area consisting of 18 identical buildings of 20×20 cm^2, as shown in Figure 4-15 and described by Yoon (2007). The urban network is anisotropic as the street widths are different in both directions. Experimental measurements of the time evolution of water depths are available at 17 locations within and nearby the urban area. The initial water depth in the reservoir is 0.3 m. Transmissive boundary conditions are prescribed along the open sides of the floodplain. Consistently with Kim et al. (2015), we use the friction formula of Haaland (1983) with a Nikuradse sand-grain roughness height of $k_s = 3 \times 10^{-4}$ m.

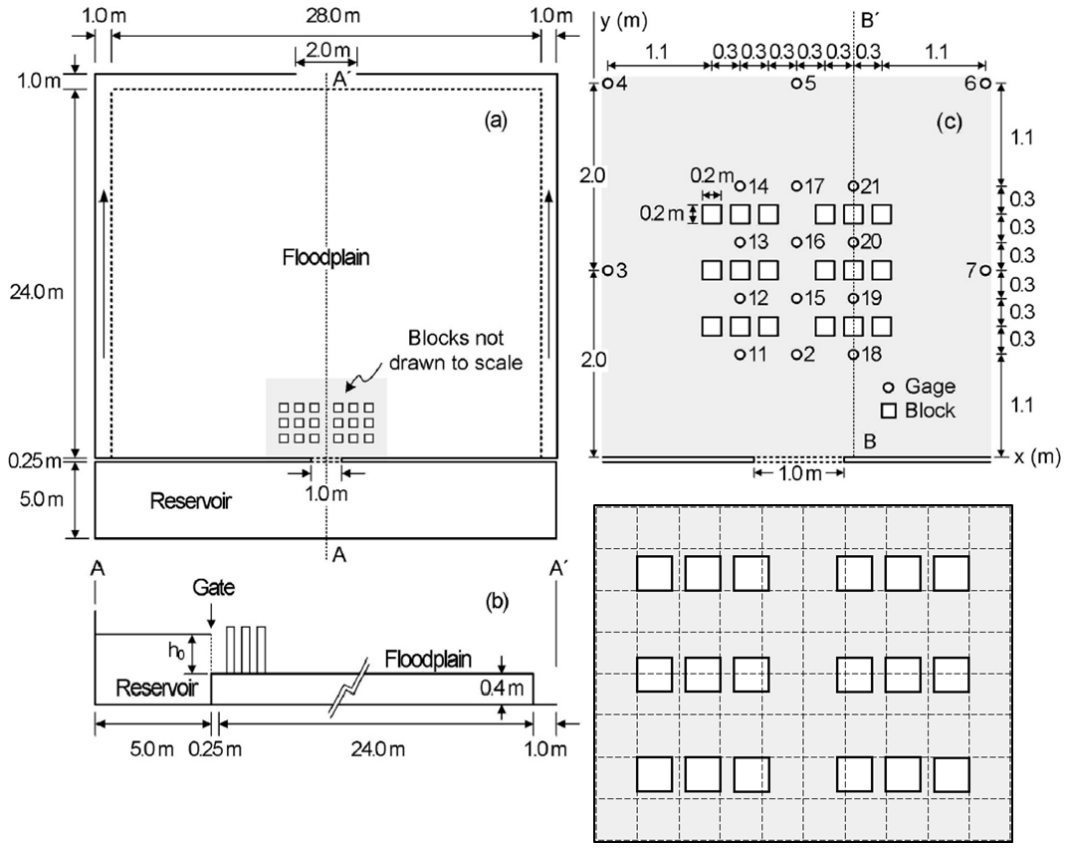

Figure 4-15 : Experimental set-up of Yoon (2007), as described by Kim et al. (2015), and discretization on a Cartesian grid at a resolution of 0.25 m.

4.4.3.2. Pore-scale error

Reference results were generated by using the CS model with a fine resolution of 0.05 m. In this mesh, all computational cells are either filled by obstacles or entirely free for water. The micro-scale results of the CS model were then aggregated at the coarse scale of 0.25 m by averaging the flow variables of the cells not occupied by obstacles (CS-P predictions).

Comparing the CS-P predictions of water depths to the measurements, the pore-scale error L_{1+2} (averaged over all time steps and all stations) is around 0.68 cm, which represents 16% of the average measured water depths over the first 300 sec.

4.4.3.3. Tested porosity models

Kim et al. (2015) applied an unstructured porosity model to reproduce the experimental results with a gap-conforming mesh and cell sizes ranging between 0.25 m and 0.33 m. Here, we apply porosity models on a Cartesian grid with a resolution of 0.25 m.

Since the cell size is larger than the building size, the discretisation corresponds to macro-scale modelling. We compare the results obtained with the PS-A-1 and PS-A-2 models. Because the

optimal drag coefficient c_D^0 is known to depend on the model used (Kim et al. 2015, Özgen et al. 2016b), four values of c_D^0 (1, 2, 3 and 4) were tested in combination with each model.

Since the positive wave crosses the two blocks of buildings in a few seconds, which is negligible compared to the total transient phase of 600 seconds, the transient momentum dissipation model is not useful in this *quasi-steady* test case.

4.4.3.4. Influence of porosity model and drag coefficient

As shown in Table 4-5, the PS-A-2 model, which captures the presence of nearby obstacles, gives in all cases more accurate results than the PS-A-1 model, in which the conveyance porosity is evaluated locally at the edges. This difference prevails both for the total error L_0 and for the porosity model error L_3, evaluated either for water depth or for flow velocity.

The drag coefficient minimizing the porosity model errors L_3 corresponds to $c_D^0 = 3$ when considering the water depths and $c_D^0 = 2$ for the fluid velocities; but both values perform actually very similarly. Based on an unstructured mesh, Kim et al. (2015) reported an optimal value of $c_D^0 = 1$ for both hydraulic variables, which suggests some dependence of the optimal drag coefficient on the porosity model used.

The minimum value for porosity model errors on water depths with the Cartesian grid ($L_{3,h}$ = 0.32 cm) is twice lower than the pore-scale error.

	PS-A-1				PS-A-2			
	$c_D^0 = 1$	$c_D^0 = 2$	$c_D^0 = 3$	$c_D^0 = 4$	$c_D^0 = 1$	$c_D^0 = 2$	$c_D^0 = 3$	$c_D^0 = 4$
$L_{0,h}$	1.58 (36%)	1.44 (33%)	1.04 (24%)	0.87 (20%)	1.07 (24%)	0.92 (21%)	0.85 (19%)	0.81 (18%)
$L_{3,h}$	1.13 (28%)	0.97 (24%)	**0.51 (13%)**	0.60 (15%)	0.53 (13%)	0.36 (9%)	**0.32 (8%)**	0.33 (8%)
$L_{3,V}$	18.6 (28%)	22.3 (34%)	**16.6 (25%)**	21.6 (33%)	15.0 (23%)	**14.0 (21%)**	15.3 (23%)	16.9 (26%)

Table 4-5: Total errors L_0 and porosity model errors L_3 for water depths (cm) and velocity magnitudes (cm/s). The relative values in brackets are determined by comparing the absolute values to the average of the reference flow variables over the firsts 300 sec.

4.4.3.5. Time series

Figure 4-16 compares the time evolution of water depths predicted by the PS-A2 model ($c_D^0 = 3$) to the reference computation (CS-P) and to the observations at different gage stations. The results show that the differences between the observations and the CS-P predictions are distinctively higher than those between the PS-A-2 model and the CS-P values. Additionally, the PS-A-2 model captures satisfactorily the peak values and the time evolution of the water depths at most stations. As shown in Figure F-4, the CS-P predictions for velocity magnitudes are fairly well reproduced by the PS-A-2 model for most stations except along the centreline, were high velocities occur. This was also noticed by Kim et al. (2015).

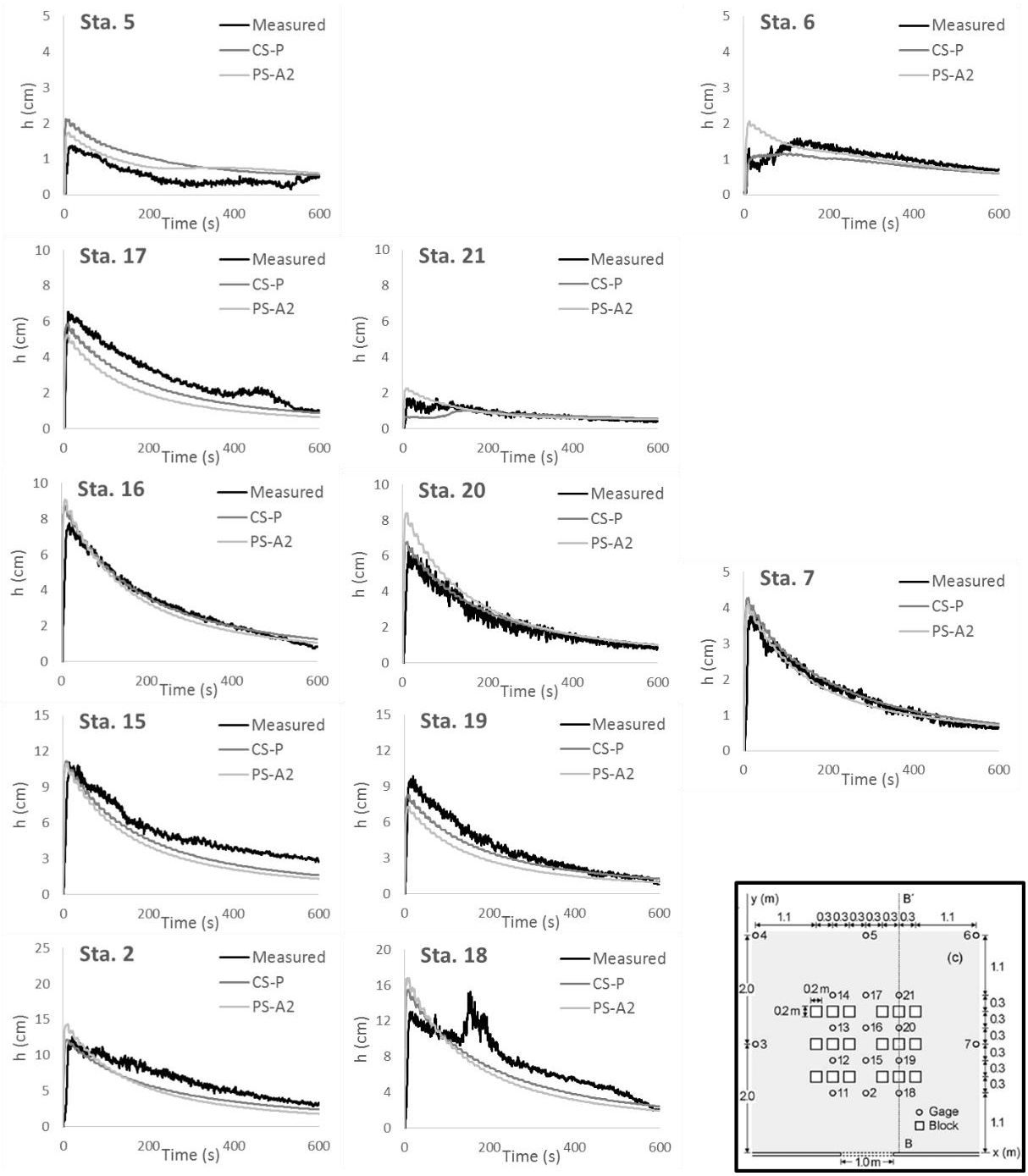

Figure 4-16 : Comparison of water depth measurements, CS-P predictions and computations with the PS-A-2 model using the optimal value of $c_D^0 = 3$ *for water depths.*

4.4.4. Idealized urban network

The potential benefit of discriminating the porosity parameters between the different terms of the governing equations (PS-A-D model in Table 4-1) is discussed here for an idealized urban network made of single-size aligned buildings. Key flow features can be estimated a priori because of the simple geometry of the urban network. Therefore, the values of the porosity

parameters may be set to reproduce the expected impact of obstacles on each term. The results computed with the PS-A-D model are also compared to those of the PS-I, PS-A-1 and PS-A-1-D models.

4.4.4.1. Description of the test case

The considered domain is divided into four parts (Part I to Part IV from upstream to downstream in Figure 4-17), all with a frictionless bottom. Parts I to III are flat while a slope of 10% is introduced in Part IV to prescribe a transmissive boundary condition at the downstream end. Part II is made of a symmetric and isotropic urban network in which the building grid is aligned with the main flow direction. The average storage porosity in part II is equal to 0.75. A uniform unit discharge of 10 m^2/s is prescribed at the upstream end over the entire width.

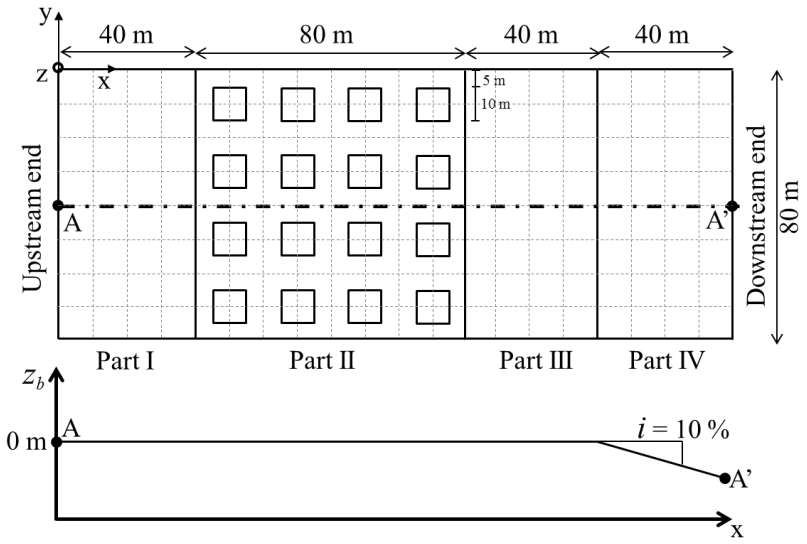

Figure 4-17 : Idealized urban network: simulation domain and discretization at the coarse scale.

4.4.4.2. A priori estimation of porosity parameters for the PS-A-D model

We first estimate the porosity parameters to be used in the governing equations of the PS-A-D model so that this model mimics the micro-scale model. Based on a simplified, yet realistic, description of the flow field (Figure 4-18), we assume *(i)* a uniform value h_e of water depth in the urban network; *(ii)* no transverse velocity and a uniform streamwise velocity u_e in the streets aligned with the x-axis; *(iii)* negligible velocities in the wake of buildings.

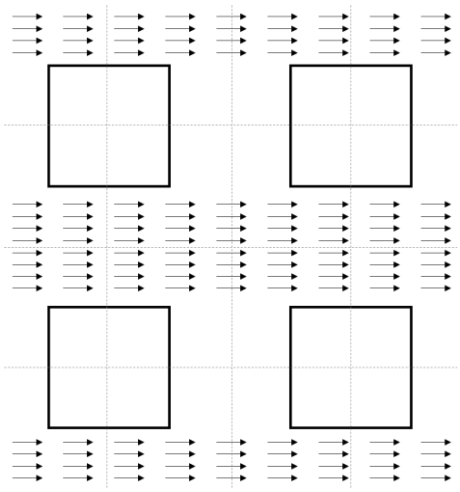

Figure 4-18 : A priori estimation of flow field in the urban area (part II).

Consequently, the macro scale water depths $\langle h \rangle$ and velocities $\langle u \rangle$ and $\langle v \rangle$ within a coarse cell of the urban area are estimated by:

$$\begin{cases} \langle h \rangle = h_e \\ \langle u \rangle = \dfrac{1/2\Delta x \Delta y}{3/4\Delta x \Delta y} u_e = \dfrac{2}{3} u_e \\ \langle v \rangle = 0 \end{cases}, \tag{4-14}$$

with Δx and Δy the lengths of the cell edges.

Based on this a priori estimation of the flow field and considering that the streamwise velocity component occurs over one-half of the length of the edges normal to the streamwise direction, the fluxes at these edges may be estimated by:

$$[\mathbf{F}]\partial\Omega = \begin{bmatrix} h_e u_e & 0 \\ \left(h_e u_e^2 + 0\right) & 0 \\ 0 & 0 \end{bmatrix} \frac{\Delta x}{2} \tag{4-15}$$

Using Eq. (4-14) to express the a priori estimation of the flow variables h_e and u_e as a function of the coarse scale variables leads to:

$$[\mathbf{F}]\partial\Omega = \begin{bmatrix} \dfrac{3}{2}\langle h \rangle \langle u \rangle & 0 \\ \dfrac{9}{4}\langle h \rangle \langle u \rangle^2 & 0 \\ 0 & 0 \end{bmatrix} \frac{\Delta x}{2} \tag{4-16}$$

Assuming a constant reconstruction of the flow variables from the cells to the edges and comparing Eq. (4-16) to Eq. (4-9), this leads to the following estimation of the porosity parameters: $\psi_c = 3/4$ and $\psi_{m,A_1} = 9/8$. These values are consistent with the condition $\psi_{mA_1} \geq \psi_c$ ensuring the hyperbolicity of the system of equations. The edge porosity parameter ψ_{m,A_1} used for the computation of the advective term is higher than 1. This results from the macro scale value $\langle u \rangle^2$ being lower than half of u_e^2: $\langle u \rangle^2 = 4/9 u_e^2$.

Since the pressure fluxes vanish in the case of a horizontal free surface, the corresponding edge porosity $\psi_{m,P}$ remains undetermined. In contrast, at the transitions between the urban (Part II) and non-urban areas (Parts I and III), the pressure term becomes significant since the free surface profile is not close to horizontal. Therefore, we have analysed the sensitivity of the results to the value of $\psi_{m,P}$ by testing $\psi_{m,P} = 0.5$ and $\psi_{m,P} = 1.0$ (PS-A-D0.5 and PS-A-D1.0 models, respectively).

Note that, at the edges partly occupied by an obstacle, the porosity parameters are identical in the PS-A-D0.5 and PS-A-1-D models ($\phi = 3/4$ and $\psi = 1/2$). In contrast, along the edges free of obstacles, the value of ϕ remains the same ($\phi = 3/4$) but the values of ψ are different: $\psi = 1/2$ in the PS-A-D0.5 model and $\psi = 1$ in the PS-A-1-D model.

4.4.4.3. Results and discussion

Here, micro-scale modelling refers to a cell size of 1 m and the coarse scale models are based on a cell size of 10 m. We consider as a reference the results computed with the CS model at the micro-scale (CS-1m), averaged over the coarse cells of 10 m (CS-P predictions). Hence, these reference data incorporate the scale error. Hydraulic variables computed with the different models are compared along the longitudinal profile A-A' (Figure 4-17). As shown in Figure 4-19, the results reveal the following.

- In the urban area (Part II), the free surface levels and velocities computed with the micro-scale CS-1m model do not evolve significantly. The unit discharge in this part (~22 m^2/s) is slightly higher than twice the uniform discharge prescribed at the upstream end (10 m^2/s). This tends to confirm that the flow is concentrated along the longitudinal streets free of obstacles, as assumed in the a priori estimation of the flow field.
- The scale error between the CS-1m model and CS-P values are generally limited for the water depths; but they are significant for the dynamic variables. At the downstream end, differences between CS-1m and CS-P are related to the cross-waves expanding from

downstream of the building area. The scale errors between CS-1m and CS-P are generally lower than the porosity model errors for water depths while they are higher for velocities and unit discharges. This shows a strong dependence of the scale error on the considered flow variable.

- The PS-I, PS-A-1 and PS-A-1-D models underestimate the water depths and overestimate the velocities in the urban area when no drag term is used. Using the PS-A-1 model, an optimal value of the drag coefficient regarding the reproduction of the free surface level at the upstream end was found equal to $c_D^0 = 1.75$. In the urban area (Part II), the PS-A-1 model with an optimal drag coefficient overestimates the water depths. PS-I, and PS-A-D models (same results for PS-A-D1.0 and PS-A-D0.5 models) enable a good reproduction of unit discharges in the urban area while the PS-A-1 and PS-A-1-D models same results for $c_D^0 = 0$ and $c_D^0 = 1.75$) induce oscillations. These oscillations result from the changes in the value of the porosity parameters from one edge to the following one. The PS-A-D0.5 model reproduces all flow variables with a good accuracy.

These results show that discriminating the porosity parameters between the various terms of the governing equations based on considerations of the flow dynamic can improve the reproduction of the effects of the obstacles on these terms. However, such a discrimination is feasible in practice only for simple urban networks for which general characteristics of the flow pattern can be estimated a priori. It remains hardly transferable to more complex urban geometries due to the lack of an ad hoc methodology.

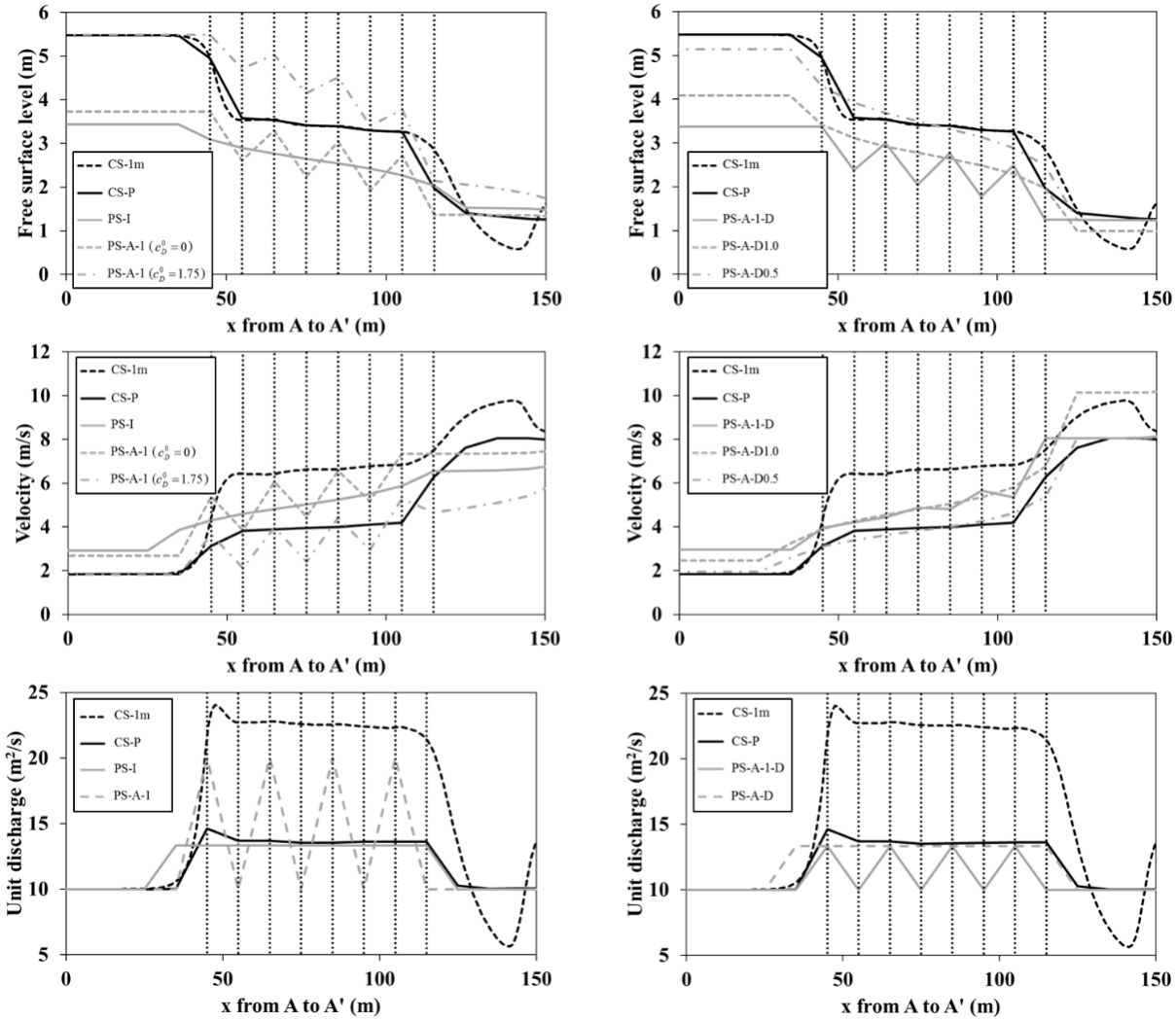

Figure 4-19 : Free surface levels, velocity magnitudes and unit discharges along A-A' for the different models. Vertical dotted lines represent the location of the buildings.

4.4.5. Wave propagation

We consider a dam-break flow over a horizontal and frictionless bottom with a large number of obstacles as represented in Figure 4-20. This test case is similar to those introduced by Guinot (2012) and used by Özgen et al. (2016) and Guinot et al. (2017). The initial water depth is 10 m for negative abscissa and 1 m for positive ones.

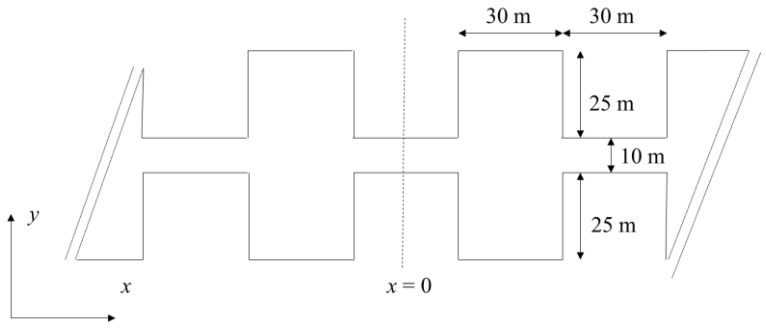

Figure 4-20 : Channel geometry for the test case assessing wave propagation.

Computations were performed with a fine resolution CS model (1 m) and with the porosity models PS-A-D1.0 ($\psi_{mP} = 1.0$) and PS-A-D1/6 ($\psi_{mP} = 1/6$, consistently with the geometry of the contraction) using a cell size of 60 m. The transient momentum dissipation coefficient μ was calibrated to reproduce optimally the propagation speed of the front of the positive wave. Using a similar a priori estimation of the flow field as for the test case of section 4.4.4, the porosity parameters are $\phi = 7/12$, $\psi_c = 7/12$ and $\psi_{mA} = 49/24$. These values turn out to be identical to those derived with the dual integral porosity model (Guinot et al., 2017) if the cell edges are located at the contractions ($\phi_\Omega = 7/12$ and $\phi_\Gamma = 1/6$, leading to $\phi = 7/12$, $\psi_c = \phi = 7/12$, and $\psi_{mA} = \phi_\Gamma \beta^2 = \phi_\Omega^2 / \phi_\Gamma = 49/24$). This is a remarkable result, since the two estimations of the porosity parameters stem from two independent lines of reasoning.

The computed water depths profiles are shown in Figure 4-21 at the time t = 200 s. As reported by Guinot et al. (2017), the transient momentum dissipation model enables a considerable improvement in the reproduction of the speed of positive waves. Like in section 4.4.4, PS-A-D model provides more accurate results if the edge porosity ψ_{mP} is representative of the smallest free length (PS-A-D1/6 model). This supports the closure model introduced by Guinot et al. (2017). Surprisingly, the value of the optimal transient momentum dissipation coefficient (μ = 0.60) is quite different from the one (μ = 0.41) obtained by Guinot et al. (2017), showing the high sensitivity of this coefficient to the geometry which is here slightly different from the geometry used by Guinot et al. (2017).

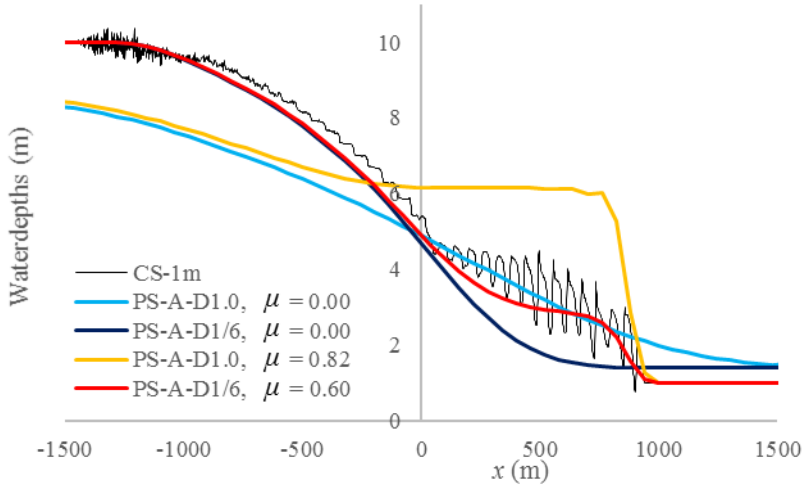

Figure 4-21 : Comparison of the water depth profiles between the refined CS models and the PS-A-D models at t = 200 s.

4.5. Application 1: Inundation flow in a typical urban district

This section includes excerpts of the journal paper "*Hydrodynamics of long-duration urban floods: Experiments and numerical modelling*" by A. Arrault, P. Finaud-Guyot, P. Archambeau, **M. Bruwier**, S. Erpicum, M. Pirotton and B. Dewals, published in 2016 in *Natural Hazards and Earth System Sciences*. The PhD candidate was in charge of section 5.3: *Porosity-based approach* of the paper.

ABSTRACT: In this study, we present an experimental model of inundation flow in a typical European urban district and we compare the experimental observations with predictions by a 2D shallow-water numerical model. The experimental setup is 5 m × 5 m and involves seven streets along each direction, leading to 49 intersections. The numerical model reproduces satisfactorily most of the observed flow features. The main limitation of the numerical model results from the Cartesian grid used, which can be overcome by using a porosity-based formulation of the shallow-water equations.

4.5.1. Methods

4.5.1.1. Experiments

The experiments considered here were conducted by Araud (2012) at the laboratory ICube in Strasbourg (France). Compared to previous studies, the experimental setup representing an urban district achieves a relatively high degree of realism by involving streets of various widths and intersections of different types (both normal branches and branches of different inclinations). The study focused on *long-duration* and *extreme* events, i.e. a steady state was considered and the flow through the underground networks was assumed negligible and was not reproduced in the model. Only an overview of the experimental setup and procedure is given here, while all details were described by Araud (2012).

4.5.1.2. Laboratory setup

The experimental setup represents an idealized urban district. It extends over 5 m by 5 m, has a horizontal bottom and contains 64 impervious blocks in Plexiglass (Figure 4-22). These blocks define a total of 14 streets. Seven of them (noted 1 to 7) are aligned along the east-west direction, while seven other streets (noted A to G) follow the north-south direction. All streets have a width of 5 cm, except streets 4, C and F which are 12.5 cm wide. The coordinates of the geometry of the model are provided in Araud (2012). They correspond to the "as-built" coordinates of the obstacles.

The street inlets are located along the north and west faces of the model, while the outlets are on the south and east faces. Fourteen pumps were used to control individually the inflow discharge into each street. The discharge was distributed between the streets of each face proportionally to their widths. The model was fed with water, assuming no sediment transport and no debris in the flow. The outlets enable free flow conditions thanks to chutes.

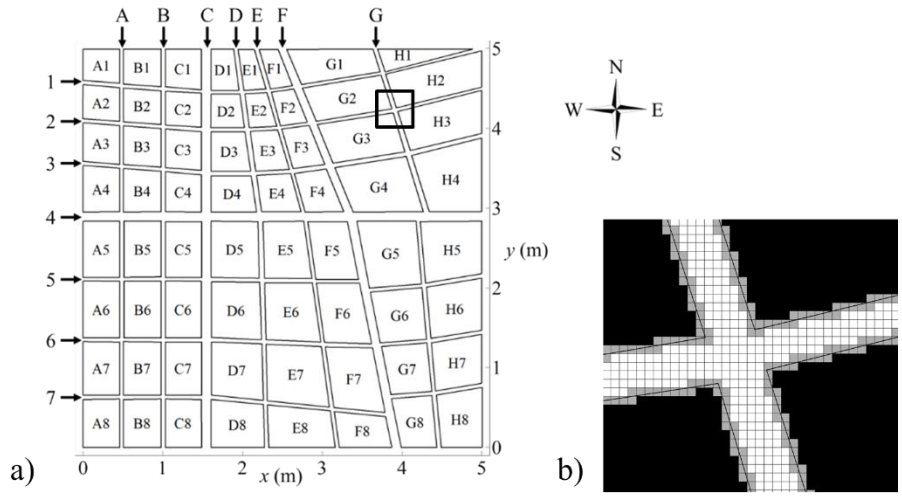

Figure 4-22 : (a) Plane view of the idealized urban district considered in the experiments, adapted from Araud (2012)*, and (b) discretization on a Cartesian grid at a resolution of 1 cm. Grey colour corresponds to computational cells with a storage porosity lower than unity.*

4.5.1.3. Instrumentation

The outflow discharge in each street was determined from the rating curve of calibrated weirs located downstream of the street outlets. An ultrasound sensor was used for measuring the water level upstream of each weir. With a measurement window of minimum 40 s, the uncertainty on the outflow discharge was shown to remain below 3.5 % (Araud 2012). Given the calibration procedure of the regulation system of the pumps, the uncertainty on the inflow discharge is the same as for the outflow discharge (3.5 %).

4.5.1.4. Test program

The total inflow discharge was varied from 10 m^3/h up to 100 m^3/h, with three intermediate values of discharge (20, 60 and 80 m^3/h). The partition of inflow discharge was kept equal between the west and the north faces.

The outflow discharge was measured downstream of each street for all the tests.

4.5.2. Numerical model

The ability of a standard shallow-water model to predict the observed discharge partitions and water depths was tested using the numerical model Wolf2D. In the applications considered here, the bottom shear stress was estimated using Darcy-Weisbach formulation and the friction coefficient was evaluated by Colebrook formula as a function of a roughness height *k* defined by

the modeller. Unless otherwise stated, all simulations were performed with a roughness height of zero, consistently with the smooth walls and bottom of the experimental model.

The geometry of the scale model was implemented in the numerical model by using the building hole method (Schubert and Sanders 2012). The cell size is uniform and was taken equal to 1×1 cm². This choice was made to obtain a realistic number of cells over the width of each streets (about 7 to 12) compared to the relative grid resolution used in practice for inundation modelling.

The inflow discharge was prescribed as a boundary condition upstream of each street, while a free flow was considered at the downstream boundaries. The boundary conditions for the turbulence model were set according to Camnasio et al. (2014) and Choi and Garcia (2002).

The time step used in the computations is optimized based on the Courant-Friedrichs-Lewy (CFL) stability condition (e.g., Bates et al., 2010). It takes values of the order of 10^{-3} s for simulations of the laboratory model.

4.5.3. Results and discussion

4.5.3.1. Standard shallow-water model

Figure 4-23 details the partition street by street of the outflow discharge for five different inflow discharges. The highest outflow discharges correspond to the widest streets, particularly those which are straight and start more upstream in the model i.e. closer to the north-west corner (streets C and 4).

At the outlet of street C, which is 2.5 times wider than streets A and B, the observed outflow discharge is about 2.3 to 2.5 times higher than the corresponding discharges in streets A and B. This leads to similar unit discharges in the different streets and may results from the similar configurations of streets A, B and C in terms of shape (all three are straight) and encountered types of intersections. In contrast, street 4 collects in-between 2.0 and 3.0 times more discharge than streets 1, 2 and 3, while the ratio of the street widths is also 2.5. These larger deviations may result from the different configurations of streets 1, 2 and 3 compared to street 4, since the latter is straight while the former are curved, leading to different types of intersections.

Another example of influence of the shape of the streets and intersections may be noticed by comparing streets 1 and A. Their inflow discharges are the same; but street A has an observed outflow discharge in-between 60 % and 70 % higher than the observed outflow in street 1. The number of intersections is the same for both streets. However, street A has mostly right-angle intersections while all intersections in street 1 have different angles, which seems to promote

more flow to be diverted towards the lateral streets. The difference in the outflow discharges results most likely from this difference in the shapes of the streets. Similarly, street F, which is as wide as street C, discharges at the outflow only about 55-58 % of the discharge from street C, as street F is curved and located further from the "upstream" corner (north-west).

Similarly as for the discharge partition between the faces, the observed portion of outflow discharge in each street remains essentially independent of the total inflow (Figure 4-23). For a total inflow varying by one order of magnitude (from 10 m³/h to 100 m³/h), the scaled sensitivity of the outflow discharges in the different streets is in average 4% and it does not exceed 12%, except in street G where it reaches 19 %.

In the computed results, the outflow from the streets with the highest discharges (4 and C) are overestimated by 10-30 % compared to the experimental results. The opposite is observed for some of the streets with the lowest discharges (1-3, D-F), while the outflows from streets 5-7 and G are fairly well represented by the numerical model. The outflow discharges from the streets with intermediate discharges (A, B and F) are also generally well predicted by the model.

As the obtained discrepancies are maximum in curved streets (1, 2 and 3), it is likely that they partly result from the Cartesian grid used, which relies on a "staircase" approximation of the obstacles not aligned with the grid. A Cartesian grid remains however of high relevance in practice (Kim et al. 2014), as it makes it generally straightforward to handle contemporary gridded data obtained from remote sensing technologies (e.g., Light Detection And Ranging, LIDAR).

Another possible explanation for the discrepancies stems from the complexity of the actual flow fields at the intersections, involving different flow regimes, hydraulic jumps and waves as described in the literature cited in the Introduction section. Here, it is however difficult to identify which intersection is responsible for the main discrepancies as they all interact with each other and the experimental flow partition between the streets is only available at the downstream end of each street and not in-between all the intersections.

A closer look at the computed results reveals that the higher the total discharge, the higher the outflow from the widest straight streets 4 and C (+ 0.6 % and + 1.75 % respectively for a total inflow varying from 10 m³/h to 100 m³/h). In the streets with the lowest outflow discharges (1-3, 5-7, D, E and G), the computed variation is opposite: minus 0.4 % in average. In contrast, the variations observed experimentally are not monotonous as the numerical results are (e.g., in streets 1, 3, 4 and C).

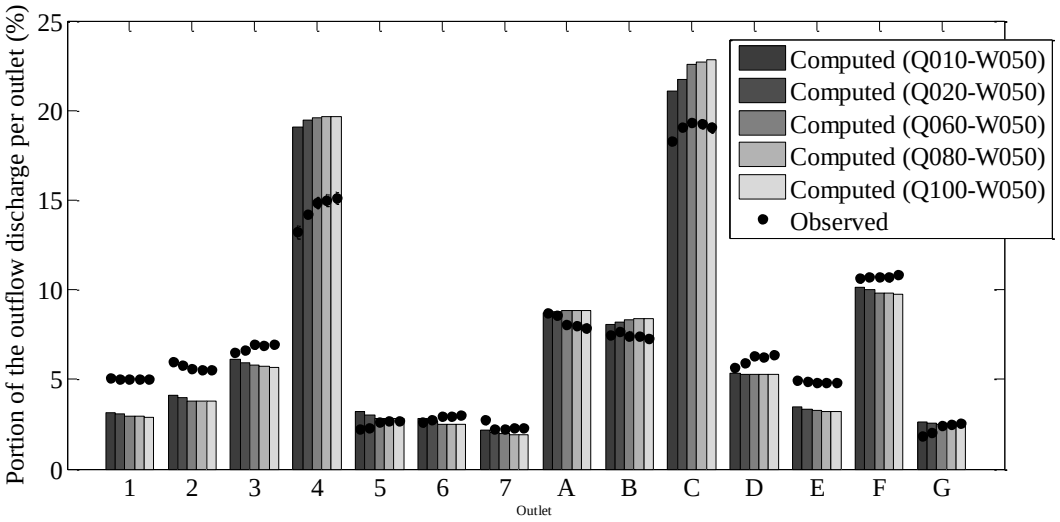

Figure 4-23 : Observed and computed contributions of each street to the total outflow discharge for five different inflow discharges.

4.5.3.2. Porosity-based model

In section 4.5.3.1 above, the discrepancies between computed and observed results were to a large extent attributed to the intrinsic limitations of Cartesian grids to reproduce oblique boundaries. To investigate this effect further, we tested an extended shallow-water model involving anisotropic porosity parameters to improve the representation of complex boundaries in a Cartesian grid framework. This approach is similar to the *cut-cell* technique (Causon et al. 2000, Kim and Cho 2011, An et al. 2015).

The partition of outflow discharges at the street level has been computed using the model with porosity. The results are displayed in Figure 4-24, which should be compared to Figure 4-23. While the outflow from streets 4 and C are overestimated by 10-30 % when the standard shallow-water model is used, this discrepancy is reduced here to around 10 %. Similarly, the outflow discharges through the narrower streets 1-3 and D-F were significantly underestimated by the standard model, whereas these outflows are now predicted with an error not exceeding 8 %. This leads to a root mean square error on the outflow discharge which is reduced from 19 % down to 6.6 % as a result of using the shallow-water equations with porosity.

The model based on anisotropic porosity parameters described here is certainly a viable approach for practical applications as it leads to substantially better predictions of the outflow discharges at the street level. For the considered experiments, all porosity parameters were *deduced* directly from geometric data and there was no calibration of these porosity parameters: ϕ is simply the void fraction in the cell, while ψ is given by the fraction of each cell interface which is not blocked by obstacles. The same approach may apply for real-world cases, for which a digital terrain model

(DTM) is used to describe the topography and vector data are available to locate the position of the buildings. Among others, Schubert and Sanders (2012) applied such a technique ("building porosity" approach) to simulate the Baldwin Hills urban dam break scenario. Sanders et al. (2008) applied a similar model to the Toce Valley flash flood, using a so-called "gap-conforming" mesh.

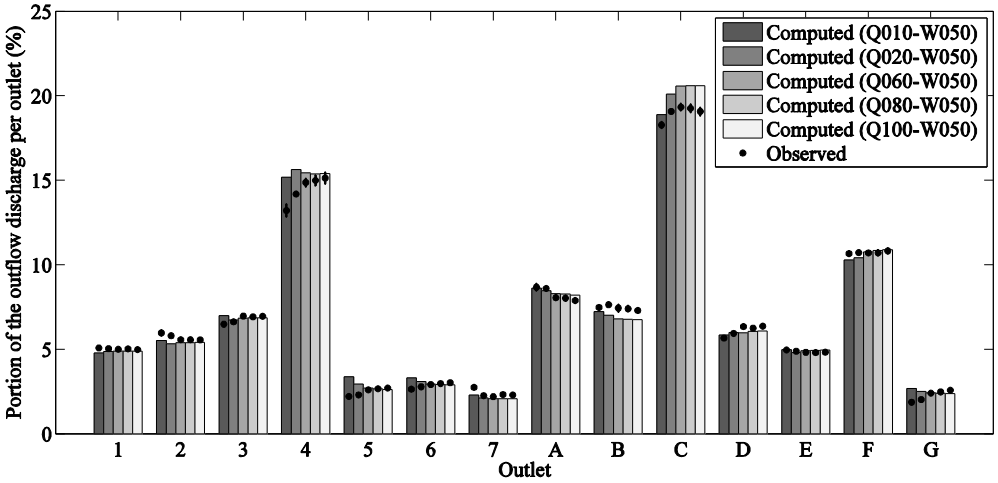

Figure 4-24 : Contributions of each street to the total outflow discharge for five different inflow discharges: observations vs. results computed with the shallow-water equations with porosity.

4.6. Application 2: Flooding of crossroads with obstacles

This section is based on a Discussion paper by **M. Bruwier**, S. Erpicum, P. Archambeau, M. Pirotton and B. Dewals of the journal paper "*Computing flooding of crossroads with obstacles using a 2D numerical model*" by P.H. Bazin, E. Mignot and A. Paquier, accepted for publication in *Journal of Hydraulic Research*.

ABSTRACT: Based on an operational 2D shallow-water model, Bazin et al. (2016) computed subcritical dividing flow at a three-branch crossroad, considering obstacles located at different positions. The numerical predictions were compared to observations from Mignot et al. (2013). Two issues are addressed here, related respectively to the efficiency and relevance of the turbulence model, and to the representation of the obstacles in operational flood models.

4.6.1. Brief presentation of the experimental data

This test case involves a three-branch dividing flow observed experimentally by Bazin (2013) and Mignot et al. (2013). Considering a single inlet, the two outlets are respectively aligned with the inlet and forming a 90° angle (Figure 4-25). A set of 14 subcritical flow configurations were tested. For each configuration, the discharge distribution between the two downstream branches were measured without obstacle and with a single obstacle, located at one of the seven different possible positions as depicted in Figure 4-25.

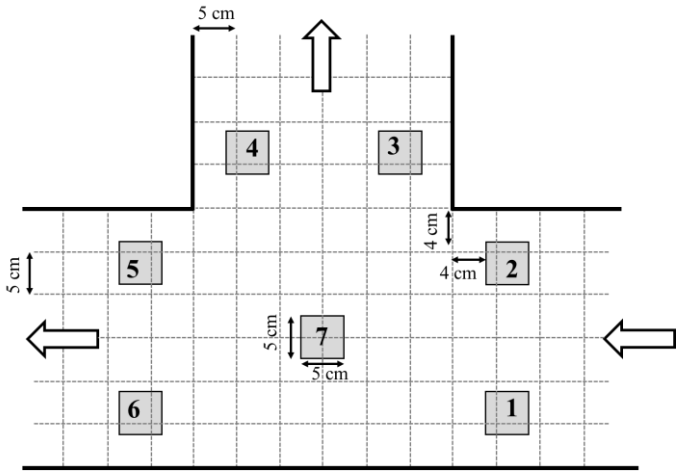

Figure 4-25 : Possible locations of the obstacle in the crossroad and representation of the Cartesian grid of 5 cm × 5 cm.

4.6.2. Turbulence model

Bazin et al. (2016) tested a single turbulence model, which is based on a constant eddy viscosity and leads to "acceptable results" after calibration. They argue that a more elaborate turbulence model is "not affordable for large-scale flood studies" due to an additional computational effort. Here, we show that a k-ε turbulence model competes with a simple turbulence model in terms of overall computational efficiency as the former requires no calibration.

For the case without obstacle, we simulated the 14 flow configurations considered by Bazin et al. (2016) (Table 1 in their paper) without turbulence model and with a k-ε turbulence model. The academic code Wolf2D was used with a coarse Cartesian grid of 5 cm × 5 cm (e.g., Arrault et al., 2016), leading to a similar accuracy on the discharge partition as in Bazin et al. (2016). Running the code with the k-ε turbulence model was about 1.6 times more demanding in terms of computational cost than one simulation without turbulence model. However, since the simple turbulence model used by Bazin et al. (2016) requires at least two runs for calibrating the constant

eddy viscosity coefficient *K* and/or for assessing the sensitivity of the results to the value of *K*, the overall computational burden of the *k-ε* turbulence remains lower than the use of the simple turbulence model.

As shown in Figure 4-26 and in Figure G-1 (Appendix G), the values of the eddy viscosity computed by the *k-ε* turbulence model agree in average with the values tested by Bazin et al. (2016) (between 0 and 10^{-3} m^2/s); but they vary substantially in space and from one flow configuration to the other. This challenges the operational validity of a constant eddy viscosity model since flood models are generally calibrated based on observed flood data, while they are subsequently used for more extreme flood scenarios.

Although the turbulence model does not alter significantly the computed discharge partitions, it provides more realistic velocity fields. This of practical importance in flood risk management, for instance for assessing hydraulic loads on obstacles and their stability. This finding, also reported by Bazin et al. (2016), is consistent with another recent flood study in a more complex urban setting involving a total of 49 crossroads (Arrault et al. 2016). Indeed, based on the *k-ε* turbulence model and a Cartesian grid, Arrault et al. (2016) showed that activating the turbulence model does not alter the discharge distribution in-between the 14 different streets of their setup, by more than 2 % compared to a computation without turbulence model. Slightly higher variations were found at some crossroads within the urban district, as a result of changes in flow structures such as control sections (e.g., Figure 11 in Arrault et al. 2016). In contrast, as highlighted by Bazin et al. (2016) (Figure 3 in their paper), the computed recirculation lengths were affected considerably by the turbulence model (Figure 10 in Arrault et al., 2016).

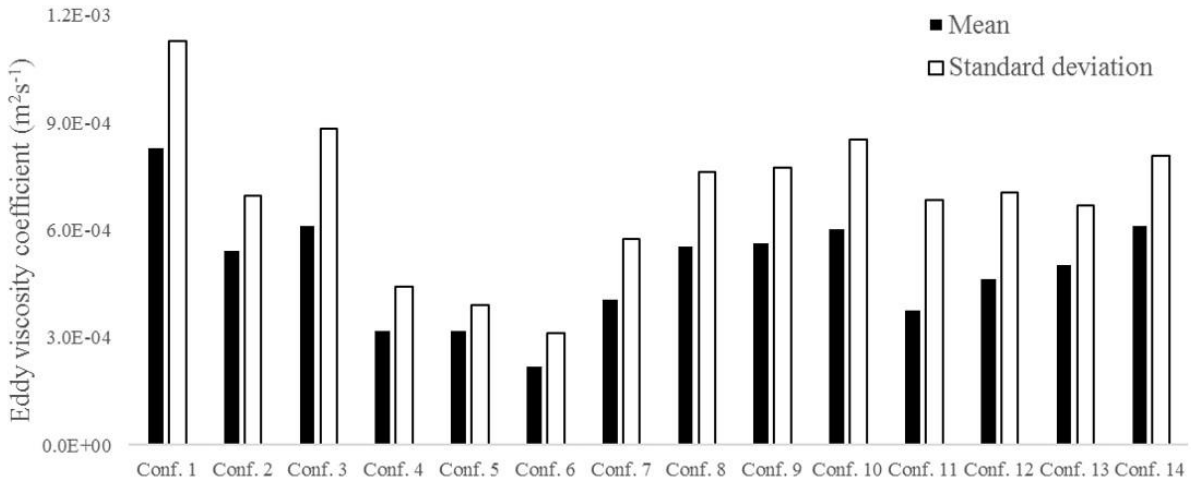

Figure 4-26 : Mean value and standard deviation of the eddy viscosity computed with the k-ε turbulence model over the entire domain in the 14 flow configurations.

4.6.3. Porosity-based model with a Cartesian grid

As stated in their Introduction, Bazin et al. (2016) aim "to identify which meshing strategy (method for including obstacles …) is required" to estimate the large-scale effects of obstacles on the flow. Three approaches can be considered to account for obstacles at a large scale (Schubert and Sanders 2012, Dottori et al. 2013): (*i*) increasing the roughness parameter, (*ii*) representing the obstacles as holes in the mesh or (*iii*) using a porosity-based model. Bazin et al. (2016) analysed only the second one. The first one is indeed particularly crude; but Schubert and Sanders (2012) showed that the porosity-based model leads to the best balance between accuracy and run-time efficiency. Therefore, this third option must also be considered to come up with a more general conclusion. Here, we compare the results obtained by Bazin et al. (2016) based on a standard shallow-water model and a non-uniform mesh (Run A of Bazin et al., 2016) with the predictions of a porosity-based shallow-water model applied on a relatively coarse Cartesian grid of 5 cm × 5 cm (Figure 4-25).

4.6.3.1. Numerical model

The shallow-water model with anisotropic porosity used here is the same as described in section 5.2 of Arrault et al. (2016). It involves two types of porosity parameters: a *storage* porosity, defined at the centre of each cell, represents the void fraction in the cell; while a *conveyance* porosity, defined at the edges of the computational cells, reproduces the blockage effect due to obstacles (Sanders et al. 2008, Chen et al. 2012a, Özgen et al. 2016b). To capture the presence of obstacles nearby the edges, the value of the conveyance porosity is set to the minimum fraction of free length parallel to the edge over half a cell on either sides of the edge (PS-A-2 model), in agreement with the findings of section 4.4.3 for macro-scale modelling. The momentum equations involve the same drag loss term as in the formulation of Schubert and Sanders (2012). The drag coefficient c_D^0 is set to its standard value for 2D flow and square shape obstructions: $c_D^0 = 2$ (Munson et al. 2006).

4.6.3.2. Results

Tests without obstacles

To ensure that the models of Bazin et al. (2016) and Arrault et al. (2016) behave similarly when no porosity parameters are considered in the latter, we first compare their respective results for a configuration without obstacle (see section 2.3 in the original paper). To evaluate the computed discharge partitions against the experimental observations, we use the same metrics as in the

original paper: the relative bias $\delta\left(Q_{b0}^{*}\right)$[1] and the relative root mean square error $\sigma\left(Q_{b0}^{*}\right)$, both averaged over the 14 hydraulic conditions considered by Bazin et al. (2016).

As shown in Table 4-6, both models lead to virtually the same relative bias $\delta\left(Q_{b0}^{*}\right)$, while the value of $\sigma\left(Q_{b0}^{*}\right)$ is higher for the model used in Arrault et al. (2016), which was applied here with an overall grid spacing slightly coarser (5 cm) than the non-uniform grid (3 - 5 cm) of Bazin et al. (2016). Moreover, as shown in Figure G-2 (Appendix G), the difference in the value of $\sigma\left(Q_{b0}^{*}\right)$ is mostly related to the results of test series S2, while both models perform very similarly for test series S1 and S3. Finally, this difference in the models performance is deemed limited compared to the probable values of experimental uncertainties, which are not reported in Table 1 of the original paper.

Numerical model	Computational mesh	Cell size	$\delta\left(Q_{b0}^{*}\right)$	$\sigma\left(Q_{b0}^{*}\right)$
Run A in Bazin et al. (2016)	Non-uniform	3.5-5 cm	-1.88%	2.50%
Porosity model used by Arrault et al. (2016)	Coarse Cartesian grid	5 cm	-1.89%	3.56%

Table 4-6: Main characteristics and performance of the models used by Bazin et al. (2016) and Arrault et al. (2016) for configurations without obstacles.

Tests with obstacles

Next, we use the porosity-based shallow-water to simulate, on a coarse Cartesian grid, configurations with obstacles which cannot be properly represented by a direct discretization on the Cartesian grid. A total of 98 simulations have been conducted, corresponding to the 14 different hydraulic conditions and the 7 distinct locations of the obstacle presented by Bazin et

$$Q_{b0}^{*}=\frac{Q_{b0,SIM}-Q_{b0,MES}}{Q_{b0,MES}}$$

[1] $\delta\left(Q_{b0}^{*}\right)=\frac{1}{14}\sum_{l=1}^{14}Q_{b0}^{*}$ with $Q_{b0,SIM}$ and $Q_{b0,MES}$ the simulated and measured flow channel

$$\sigma\left(Q_{b0}^{*}\right)=\sqrt{\frac{\sum_{l=1}^{14}Q_{b0}^{*\,2}}{14}}$$

al. (2016). Here also, the performance of the model is assessed based on the same metrics as introduced in Eqs (9) to (13) of the original paper.

The errors $\delta\left(\Delta R_{q1-7}\right)$ and $\sigma\left(\Delta R_{q1-7}\right)$ on the discharge partition modification ΔR_{q1-7} [2] obtained with the porosity-based model are relatively close to the values of Bazin et al. (2016), even if the relative bias $\delta\left(\Delta R_{q1-7}\right)$ has an opposite sign (Table 4-7). The absolute value of $\delta\left(Q^*_{b1-7}\right)$ is significantly lower with the model of Arrault et al. (2016), while the error $\sigma\left(Q^*_{b1-7}\right)$ is smaller for the model of Bazin et al. (2016). For most simulations, Bazin et al. (2016) and the porosity-based model used by Arrault et al. (2016) obtain very similar discharge partitions (Figure 4-27). As highlighted by Bazin et al. (2016), discrepancies mainly occur for high upstream Froude numbers and for obstacles located upstream of the crossroad.

Extra-simulations have been conducted with the porosity model to evaluate the sensitivity of the results to the value of the drag coefficient (Table 4-7). Two extreme values reported in literature (Kim et al. 2015) have been tested: $c_D^0 = 1$ and $c_D^0 = 3$. The errors $\sigma\left(\Delta R_{q1-7}\right)$ and $\sigma\left(Q^*_{b1-7}\right)$ are found minimum for the standard value of $c_D^0 = 2$, while the values of $\delta\left(\Delta R_{q1-7}\right)$ and $\delta\left(Q^*_{b1-7}\right)$ are hardly affected (Table 4-7). This reflects a good predictive capacity of the porosity-based model since it performs best based on standard value of the drag coefficient, without the need for a case-by-case calibration.

$\Delta R_{qi,SIM} = R_{q0,SIM} - R_{q0,SIM}$

[2] $\Delta R_{qi,MES} = R_{qi,MES} - R_{q0,MES}$

$\Delta R_{qi} = \Delta R_{qi,SIM} - \Delta R_{qi,MES}$

where 0 indicates a simulation without obstacle while *i* = 1-7 refers to a simulation with an obstacle.

Numerical model	$\delta\left(\Delta R_{q1-7}\right)$	$\sigma\left(\Delta R_{q1-7}\right)$	$\delta\left(Q^*_{b1-7}\right)$	$\sigma\left(Q^*_{b1-7}\right)$
Run A in Bazin et al. (2016)	-0.37%	1.13%	-2.80%	3.79%
Arrault et al. (2016) - $c_D^0 = 2$	0.35%	1.25%	-0.65%	5.43%
Arrault et al. (2016) - $c_D^0 = 1$	0.32%	1.41%	-0.70%	5.94%
Arrault et al. (2016) - $c_D^0 = 3$	0.37%	1.4%	-0.61%	5.73%

Table 4-7: Quality indicators obtained with the models used by Bazin et al. (2016) and Arrault et al. (2016) for simulations with obstacles.

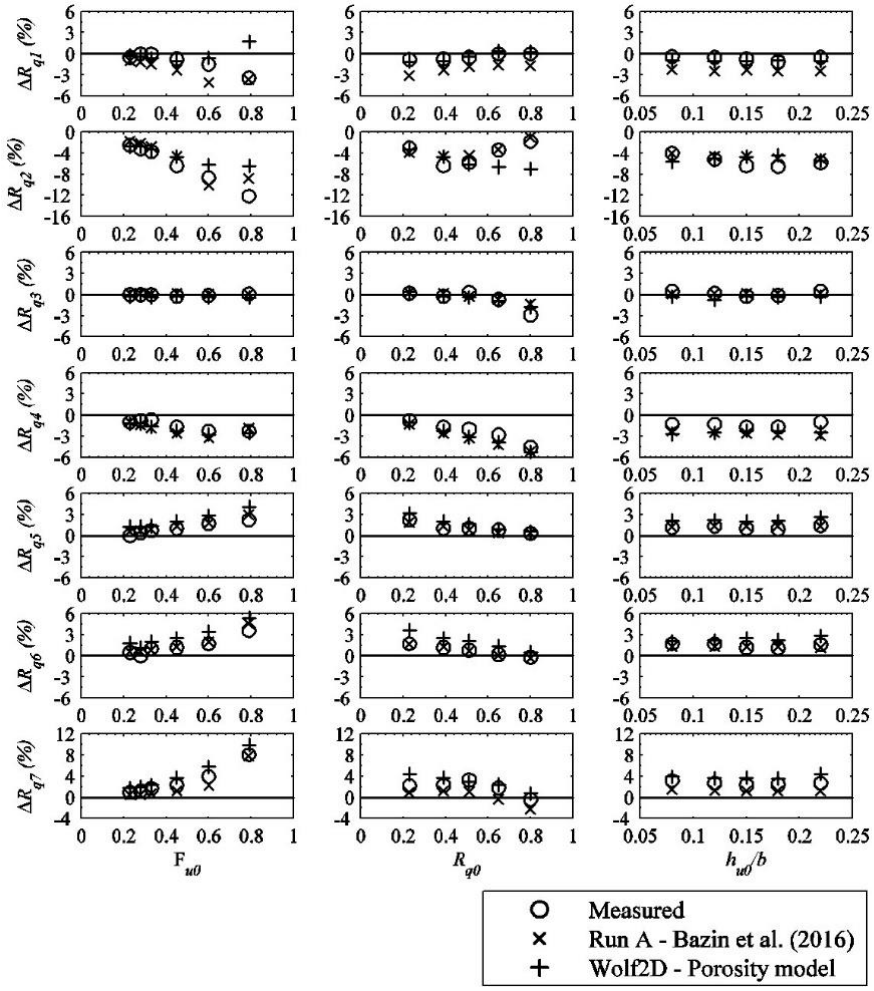

Figure 4-27 : Change in the discharge partition due to the presence of the obstacle, as obtained from the experimental observations as well as from the numerical models of Bazin et al. (2016) and Arrault et al. (2016).

4.6.4. Interpretation

In terms of overall computational efficiency, we show that a k-ε turbulence model outperforms a constant eddy viscosity model, which requires calibration and/or sensitivity analysis for operational flood modelling. Moreover, the values of the eddy viscosity are found highly dependent on the flow configuration. The added value of a turbulence model stems from the improved prediction of the velocity field, which is of practical importance for assessing issues such as the stability of obstacles, the impact of floating debris or scour effects.

We compared the numerical results obtained by Bazin et al. (2016) using a standard shallow-water model with a non-uniform mesh, to computations performed on a coarse Cartesian grid with a shallow-water model including anisotropic porosity parameters. We obtained a similar accuracy in the results with a slightly lower number of cells. In addition, the porosity-based approach is much more flexible to account for complex obstacle geometries. If the obstacles considered by Bazin et al. (2016) were not aligned with the channel walls, the meshing technique they used would fail and a more complex unstructured mesh would be needed. In contrast, our approach based on porosity parameters can accommodate any obstacle shape with a reduced number of cells. Although the time step is a function of the value of the storage porosity, techniques exist to overcome stringent time step limitations (e.g., the merging technique applied by Causon et al. 2000, 2001 in combination with a cut-cell approach). Finally, the use of Cartesian grids is particularly appealing since they enable a straightforward overlay of the computational mesh with widely available gridded data, such as digital elevation models obtained from remote sensing techniques (Kim et al. 2014). This hints that porosity-based shallow-water models combined with Cartesian grids may be of high relevance for inundation mapping in practice.

4.7. Conclusion

The main contributions of this chapter are three improvements of porosity-based models on Cartesian grids: (*i*) the use of a merging technique for cells with low storage porosity values, leading to a high increase in computational efficiency, (*ii*) the comparison of different methods for the determination of edge porosity parameters on Cartesian grids and (*iii*) a discussion of the potential benefit of distinguishing the values of flow-dependent porosity parameters to be used in the different terms of the governing equations.

- At the meso-scale, cells with low storage porosity values reduce significantly the computational efficiency due to the stability condition. We implemented a technique

which consists in merging cells having a storage porosity below a threshold to neighbouring cells. In the case of a rectangular channel discretised on a Cartesian grid, this technique enables both accurate and efficient computations.

- We defined two different modelling scales depending on the relative sizes of obstacles compared to the cell size. At the "meso-scale", the obstacles remain explicitly discretized on the grid, while at the "macro-scale", the presence of obstacles is reflected only through the porosity parameters. In the case of porosity models applied on Cartesian grids, we found that the optimal method for evaluating the conveyance porosity depends on the modelling scale. At the meso-scale, the obstacles intersect the computational edges and the conveyance porosity can therefore be evaluated directly along the edges. In contrast, at the macro-scale, the presence of obstacles not intersecting the cell edges must be considered when evaluating the conveyance porosities. Based on a dedicated test case involving synthetic urban networks, we found that taking the minimum fraction of free length parallel to the edge over half of a cell on either sides of the edge gives more accurate results than the determination of the conveyance porosity locally along the edges.
- In our derivation of the porosity model we introduced different porosity parameters in the different terms of the governing equations. Considering an idealized urban network for which key features of the flow field can be estimated a priori, we estimated physically relevant values for each porosity parameter, reflecting the specific effect of obstacles on each term of the governing equations at the coarse scale. While this approach proved promising, its generalization to more complex flows remains challenging.

The resulting anisotropic porosity model was validated against four tailored test cases and used in two applications involving urban flooding. Computations were performed for a large range of urban configurations at the meso- and macro- scales. The results show that a satisfactory level of accuracy is maintained at a coarse resolution with the porosity-based model used with an optimal calibration of the drag loss coefficient, enabling hence an improvement of the computation efficiency. The optimal value of the drag coefficient was found to remain in-between 1.75 and 3.0 for a wide range of urban layouts, flow configurations and relative sizes of the mesh resolution compared to the typical size of obstacles and flow ways in the floodplains

The above-mentioned porosity models consider that the obstacles are sufficiently high so that they cannot be overtopped by the flood. The porosity parameters are therefore independent of the flow depth. Özgen et al. (2016a) introduced recently a depth-dependent anisotropic porosity model to consider the possible submergence of low-level obstacles. This is certainly a path to follow for further generalizing the model presented here.

PART II: IMPACT OF URBANIZATION ON FLOODS

5. Influence of building layout on inundation flow in floodplains of lowland rivers

This chapter is based on a manuscript ready for submission to a peer-reviewed journal. It relates also to the conference communication "*Influence of urban patterns on floods*" presented at the *37th IAHR World Congress*, Kuala Lumpur, 2017 (Bruwier et al. 2017c). The PhD candidate was in charge of the porosity-based hydraulic computations, the statistical analysis, the sensitivity analysis and the development of the conceptual model. Procedural modelling was performed by Ahmed Mustafa of the research group LEMA.

ABSTRACT: The objective of this chapter is to investigate the respective influence of various urban pattern characteristics on inundation flow. A set of 2,000 synthetic urban patterns were generated using an urban procedural model providing locations and shapes of streets and buildings over a square domain of 1 x 1 km². Steady two-dimensional hydraulic computations were performed over the 2,000 urban patterns with identical hydraulic boundary conditions. To run such a large amount of simulations, the computational efficiency of the hydraulic model was improved by using an anisotropic porosity model. This model computes on relatively coarse computational cells, but preserves information from the detailed topographic data through porosity parameters. Relationships between urban characteristics and the computed inundation water depths have been based on multiple linear regressions. Finally, a simple mechanistic model based on two district-scale porosity parameters, combining several urban characteristics, is shown to capture satisfactorily the influence of urban characteristics on inundation water depths. The findings of this study give guidelines for more flood-proof urban planning.

5.1. Introduction

In literature, most existing studies analyse many aspects of the influence of urbanization on floods but generally disregard the impact of the urban pattern geometry on the severity of flooding. However, the urban characteristics (e.g. street width, orientation or curvature) may have a strong influence on inundation flow since they influence the discharge partition between the streets as well as the flow depths and velocities.

Vollmer et al. (2015) and Lin et al. (2016) investigated the interactions between urbanization and inundation flow for the rehabilitation of Ciliwung River in Jakarta, Indonesia. The inundation extent and water depths were compared between different rehabilitation scenarios to identify the most effective one to mitigate floods. Since these authors considered rehabilitation scenarios specific to their case study, their conclusions are difficult to generalize to other urban areas. Huang et al. (2014) studied the impact of building coverage on the increase of water depths for a rectangular flume with an array of aligned buildings obstructing the flow. They proposed a method to update the Manning roughness coefficient according to the blockage effect of buildings but consider only one urban characteristic (the building coverage) of an idealized urban network.

In this chapter, we present a more systematic analysis to determine the respective influence of various urban planning characteristics on inundation water depths. We followed a three-step procedure. First, we used an urban procedural model to generate 2,000 quasi-realistic building layouts by varying randomly the values of 10 urban model parameters: average street length, street orientation, street curvature, major and minor street widths, parks coverage, mean parcel area and three different building setback values.

Second, we computed the inundation flow field for each building layout by considering the same hydraulic boundary conditions. To make the hydraulic computation tractable for the 2,000 synthetic urban configurations, we used subgrid models which enable a reduction of the computational cost thanks to a coarsening of the computational grid while preserving the essence of the detailed topographic information. We opted for an anisotropic porosity model, in which fine scale topographic information are preserved at the coarse scale by means of porosity parameters involved in the governing equations (Sanders et al. 2008).

Finally, the influence of nine urban characteristics on the computed water depths were analysed based on multiple linear regressions (MLR) and on Pearson correlation coefficients. Additionally, a conceptual model was developed to investigate the relationships between the inundation water depths and district-scale storage and conveyance porosity parameters, evaluated as a combination of the urban characteristics. The results show a good predictive capacity of the model based on

just the two porosity parameters, with a prevailing influence of district-scale conveyance porosity. Hence, this model enables quantifying to which extent flood-related impacts of an increase in the building coverage (i.e. new developments) can effectively be mitigated by an appropriately chosen layout of the buildings.

In the present analysis, we decided to keep the terrain slope equal to zero and to consider just one steady flooding scenario so as to focus on the influence of the urban planning characteristics. Therefore, the conclusions do not apply for floodplains involving steep slopes; but are instead representative of floodplains of lowland rivers which are flooded gradually and with moderate flow velocity. The steady flow conditions considered here are a valid representation of long duration floods (e.g., in lowland rivers such as the Rhine or the Meuse); but neither for short duration floods in steep rivers nor for flash flood events.

In section 5.2, we introduce the procedural modelling used to generate the synthetic building layouts, and we briefly describe the hydraulic model used to compute the flow characteristics in the urban area. We also present the statistical approach followed to process the modelling results. The results are presented in section 5.3, in terms of generated building layouts, computed flow fields and influence of urban characteristics on the flood severity upstream of the urban area. Finally, we provide an in-depth discussion of the results (section 5.4), by testing their sensitivity with respect to the number and choice of input variables, the sample size and the model selection, as well as by developing a conceptual model (based on district-scale porosity parameters) which agrees remarkably well with the results of the detailed numerical simulations.

5.2. Method

As sketched in the flowchart of Figure 5-1, we set up a three-step methodology to analyse the influence of the building layout on inundation flow:

- first, procedural modelling was used to generate about 2,000 synthetic urban layouts considering ten input parameters, including typical street length, width and curvature, parcel size, setbacks … (section 5.2.1);
- second, by means of a porosity-based hydraulic model, the flow characteristics were computed for each urban layout, considering identical hydraulic boundary conditions (section 5.2.2);
- finally, based on Pearson correlation coefficients and on multiple linear regression, we highlight the sensitivity of inundation flow to the input parameters (section 5.2.3).

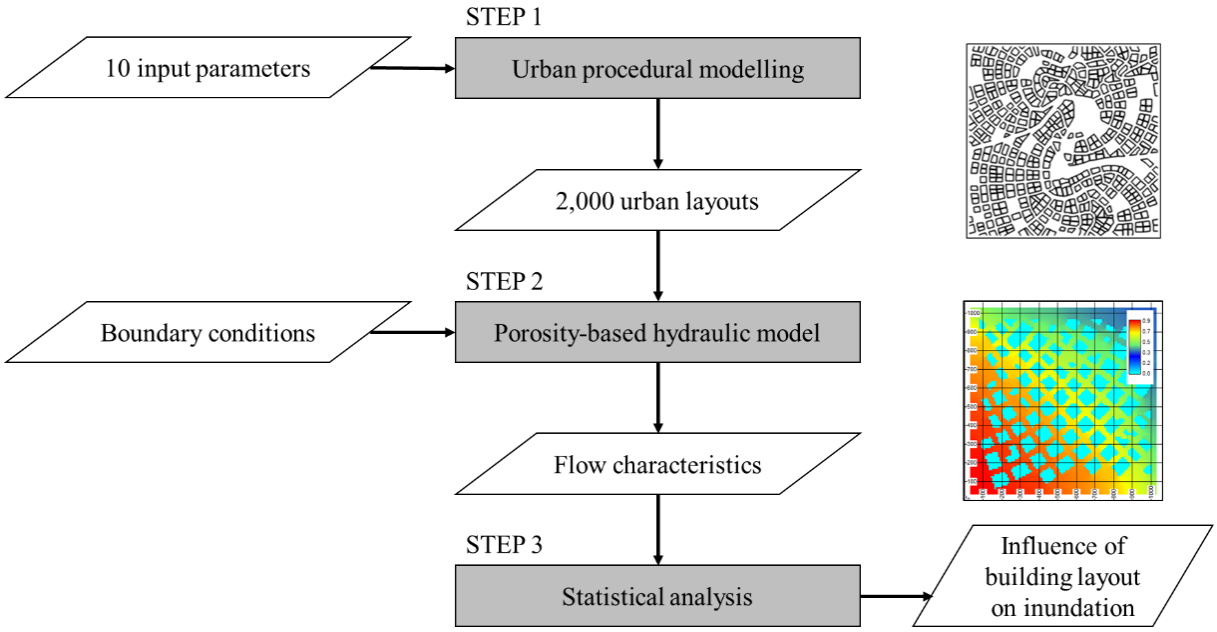

Figure 5-1 : Methodology for the determination of the influence of building layout on inundation characteristics.

5.2.1. Procedural modelling of urban layouts

Procedural modelling of urban layouts consists in automatically generating urban layouts based on a set of rules and parameter values (Prusinkiewicz and Lindenmayer 1990). The output of procedural modelling is a collection of locations and shapes of streets and buildings.

Here, we used an upgraded version of the method originally proposed by Parish and Müller (2001), as described in Vanegas et al. (2009) to support more variations in the street networks. The procedural modelling technique used is deterministic, in the sense that, for a given set of values of the input parameters, it generates a single urban layout.

We considered ten input parameters, which are all of practical relevance for urban planning. They include street characteristics (typical length, orientation, curvature and width), park coverage, parcel size and setbacks (Table 5-1).

As sketched in Figure 5-2, the procedural modelling involves mainly three steps:

- generation of a "skeleton" of the network of streets (i.e. the street centrelines), based on the typical street length L_s, orientation α and curvature χ (Figure 5-2a);
- calculation of parcels based on the widths W and w of major and minor streets, the park coverage P_c and the mean parcel area A_p (Figure 5-2b);
- creating of the building footprints based on the front, rear and side setbacks s_f, s_r and s_s (Figure 5-2c).

To ensure the representativity of real-world urban configurations, plausible ranges of variation of the input parameters were determined from cadastral data of urban areas in the Walloon region, Belgium (Table 5-1). By selecting randomly parameter values in their respective ranges of variation, we generated 2,000 urban layouts, covering each a square area of 1 km by 1 km. In Table 5-1, the minimum value of the side setback is 1 m. Therefore, configurations with a free space enclosed within a building (s_s = 0) are not considered. However, the findings the study can be extended to these specific urban patterns by increasing the building coverage to reproduce the lack of access of the flow to the enclosed free-spaces.

	Urban parameter	Minimum	Maximum
L_s	Average street length	40 m	400 m
α	Street orientation	0°	180°
χ	Street curvature	0 km^{-1}	10 km^{-1}.
W	Major street width	16 m	33 m
w	Minor street width	8 m	16 m
P_c	Park coverage	5%	40%
A_p	Mean parcel area	350 m^2	1,100 m^2
s_f	Building front setback	1 m	5 m
s_r	Building rear setback	1 m	5 m
s_s	Building side setback	1 m	5 m

Table 5-1: Input urban parameters for the urban procedural modelling.

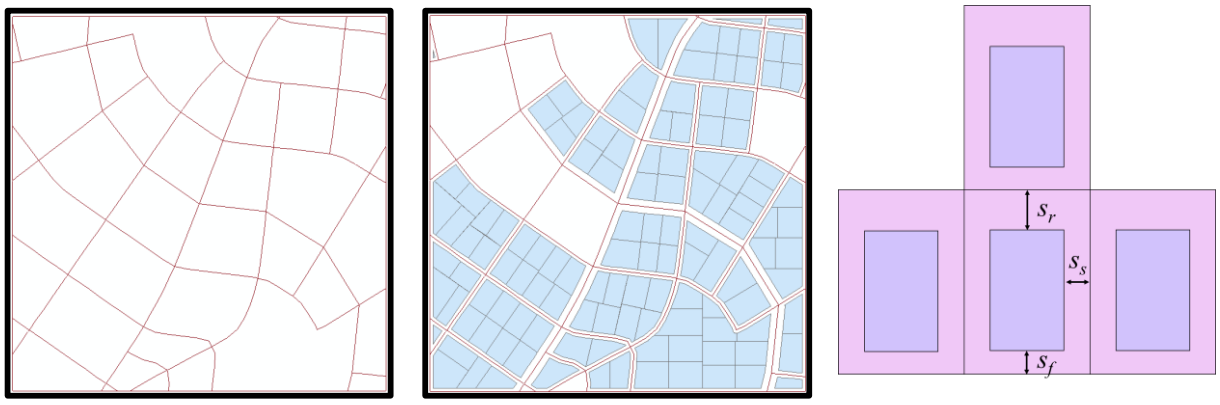

(a) Definition of the tensor field of the streets. *(b) Definition of the parcels and park areas.* *(c) Definition of building footprint in each parcel.*

Figure 5-2 : Main steps of procedural modelling of urban layouts.

Only the building footprints have an influence on the performed hydraulic computations. This enables merging some of the parameters listed in Table 5-1. For instance, parameters W (or w) and s_f should not be considered independently. Indeed, urban layouts characterized by distinct values of the street width W (or w) and front setback s_f, but with the same value of the sum $W + 2\ s_f$ (or $w + 2\ s_f$) would lead to the same distance between the buildings located on either sides of a street. This distance should be retained as the parameter which actually controls the flow conveyance through this street, instead of W (or w) and s_f independently. Therefore, although the parameters listed in Table 5-1 are the real inputs of the procedural modelling, we performed the statistical analysis of the results by considering a slightly modified set of variables (Table 5-2):

- Parameters W, w and s_f were replaced by just two variables: $x_4 = W + 2\ s_f$ and $x_5 = w + 2\ s_f$.
- To account for the periodicity in the street orientation resulting from the symmetry of the domain and boundary conditions, the orientation parameter α was replaced by variable $x_2 = \left|\sin\left(2\left(\alpha - 45°\right)\right)\right|$ (Figure 5-3).
- The park coverage P_c was not kept alone; but lumped into an overall *building coverage* ratio x_9, evaluated as the ratio between the total area of building footprints and the area of the whole district (1 km^2). Variable x_9 is a function of all input parameters.
- All other variables were each kept equal to one of the remaining input parameters listed in Table 5-1.

Variable definition	Minimum	Maximum
$x_1 = L_s$	40 m	400 m
$x_2 = \left\|\sin\left(2\left(\alpha - 45°\right)\right)\right\|$	0	1
$x_3 = \chi$	0 km^{-1}	10 km^{-1}
$x_4 = W + 2\ s_f$	18 m	38 m
$x_5 = w + 2\ s_f$	10 m	21 m
$x_6 = A_p$	350 m^2	1,100 m^2
$x_7 = s_r$	1 m	5 m
$x_8 = s_s$	1 m	5 m
$x_9 = f(L_s, \alpha, \chi, W, w, P_c, A_p, s_r, s_f, s_s)$	0%	43%

Table 5-2: Variables used for the statistical analysis of the modelling results.

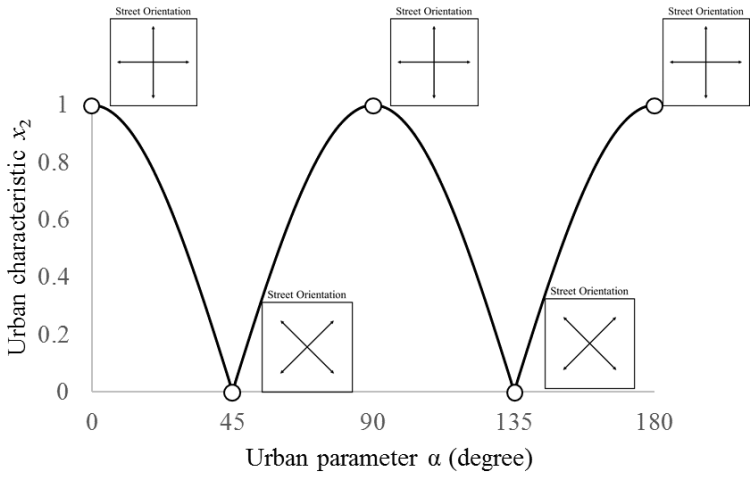

Figure 5-3 : Relation between variable x_2 and street orientation parameter α.

5.2.2. Porosity-based hydraulic modelling

In a second step, we applied an efficient hydraulic model to compute the flow characteristics for each of the 2,000 building layouts, under the same hydraulic boundary conditions. The terrain was assumed horizontal and infiltration in the soil was neglected because it has a limited influence on river flooding in urbanized floodplains.

Model description

Two-dimensional shallow-water hydraulic models are considered state-of-the-art for the simulation of inundation flow in urban areas (El Kadi Abderrezzak et al. 2009, Ghostine et al. 2015). In such model, the buildings were idealized as impervious obstacles sufficiently high for not being overtopped by the flood. In general, three approaches can be considered to account for obstacles in inundation modelling (Schubert and Sanders 2012, Dottori et al. 2013): (*i*) increasing the roughness parameter, (*ii*) representing the obstacles as holes in the mesh or (*iii*) using a porosity-based model. The first one is particularly crude and requires calibration on a case-by-case basis. In the second one, each building needs to be explicitly resolved in the computational mesh, which makes this approach not suitable to investigate efficiently the 2,000 building layouts. In contrast, Schubert and Sanders (2012) showed that porosity-based models lead to the best balance between accuracy and run-time efficiency. They enable a coarsening of the mesh size by roughly one order of magnitude while preserving a good level of accuracy (Schubert and Sanders 2012, Kim et al. 2014, 2015, Özgen et al. 2016b, Bruwier et al. 2017a). Therefore, we opted here for this third option.

The shallow-water model with porosity used here was described in Sect. 5.2 of Arrault et al. (2016) as well as in Bruwier et al. (2017b), and a comprehensive validation is presented in Bruwier et al. (2017a). It involves two types of porosity parameters: a storage porosity, defined at the centre of each cell, represents the void fraction in the cell while anisotropic conveyance porosities, defined at the edges of the computational cells, reproduce the blockage effect due to obstacles (Sanders et al. 2008, Chen et al. 2012a, Özgen et al. 2016a). The values of these porosity parameters were determined geometrically from the building footprints.

The momentum equations involve the same drag loss term as in the formulation of Schubert and Sanders (2012). The drag coefficient c_D was set to the standard value $c_D = 3.0$. Bottom friction is modelled by Manning formula with a uniform roughness coefficient $n = 0.04$ sm$^{-1/3}$. This value of the roughness coefficient is comparable to the values suggested by Bazin (2013) and Mignot et al. (2006) to account for the various sources of flow resistances in urban areas such as bottom friction and small scale obstacles (debris, cars, urban furniture, etc.).

The numerical discretization is based on a conservative finite volume scheme and a self-developed flux-vector splitting (Erpicum et al. 2010a). We used a Cartesian grid with a grid spacing of 10 m, which is comparable to the typical size of the buildings (> 15 m) but the porosity parameters enable the fine-scale geometric features to be accounted for.

To enhance computational efficiency in the presence of low values of the storage porosity ϕ, we used a merging technique which consists in merging each cell having a low value of storage porosity ($\phi < \phi_{min} = 10\%$) with a neighbouring cell (Bruwier et al. 2017a).

As detailed in Arrault et al. (2016) and Bruwier et al. (2017a, b), the model was successfully validated against fine scale computations and against experimental data for flow conditions similar to those prevailing here. The model is part of the academic code Wolf2D which was used in multiple flood risk studies (Ernst et al. 2010, Beckers et al. 2013, Bruwier et al. 2015).

Boundary conditions

The west and south sides of the computational domain are the upstream boundaries, while the east and north sides are the downstream ones. Along the upstream sides of the computational domain, a 30-m wide strip was kept free of buildings.

A steady inflow discharge of 200 m^3/s, uniformly distributed, was prescribed as boundary condition along the upstream sides. Along the downstream sides, the outflow discharge q_j in each cell j was prescribed as a function of the computed water depth h_j in the cell by using a rating curve:

$$q_j = C_1 \Delta x \sqrt{2g\left(h_j - C_2\right)^3} \qquad (5\text{-}1)$$

with Δx the grid spacing, g the gravity acceleration and constants C_1 and C_2 respectively equal to 0.5 and 0.3. These boundary conditions are somehow arbitrary; but they lead to flow conditions in the network of streets which are representative of typical flooding in floodplains of lowland rivers.

5.2.3. Statistical analysis

The outcome of steps 1 and 2 of the methodology (Figure 5-1) consists in a set of 2,000 gridded flow characteristics data, representing the water depth and the two components of horizontal flow velocity in the 10,000 cells of the computational mesh. To make the subsequent analyses tractable, we synthetized the dataset by means of a single indicator y of flood severity for each of the 2,000 building layouts. We focused on the increase of the 90th percentile of the computed water depths along the upstream boundary of the domain (noted Δh_{90}) compared to a configuration without any buildings (h_{90} = 61 cm). This quantity is representative of the overall flow resistance (or loss of flow conveyance) induced by the layout of buildings and, hence, of the increase in flood levels that the presence of the buildings causes upstream of the considered area. If the buildings result from new development, indicator $y = \Delta h_{90}$ reflects the impact of this development on flood danger upstream.

We performed the statistical analysis of the results by considering standardized variables, noted $\bar{x}_i$ (i = 1 to 9) and $\bar{y}$, defined as:

$$\bar{x}_i = \frac{x_i - x_{i,\text{mean}}}{x_{i,\text{std}}} \quad \text{and} \quad \bar{y} = \frac{y - y_{\text{mean}}}{y_{\text{std}}} \qquad (5\text{-}2)$$

with $x_{i,\text{mean}}$ and $x_{i,\text{std}}$ (resp. y_{mean} and y_{std}) the mean and standard deviation of the variable x_i (resp. y) over all the building layouts.

We introduce the matrix notations $\mathbf{X}$ and $\mathbf{Y}$ with $\bar{x}_i^N$ and $\bar{y}^n$ the values of $\bar{x}_i$ and $\bar{y}$ corresponding to the n^{th} building layout:

$$\mathbf{X} = \begin{bmatrix} \bar{x}_1^1 & \bar{x}_2^1 & \dots & \bar{x}_9^1 \\ \bar{x}_1^2 & \bar{x}_2^2 & \dots & \bar{x}_9^2 \\ \vdots & \vdots & \ddots & \vdots \\ \bar{x}_1^N & \bar{x}_2^N & \dots & \bar{x}_9^N \end{bmatrix} \quad \text{and} \quad \mathbf{Y} = \begin{bmatrix} \bar{y}^1 \\ \bar{y}^2 \\ \vdots \\ \bar{y}^N \end{bmatrix} \qquad (5\text{-}3)$$

with N being the number of building layouts.

The influence of each of the nine variables x_i on the inundation indicator y was determined using a multiple linear regression (MLR). The outputs of the regression are the least square linear coefficients $\mathbf{A} = [a_1, a_2, ..., a_9]^T$, computed from Eq. (5-4) and representing the sensitivity of y with respect to each variable x_i:

$$\mathbf{A} = \left(\mathbf{X}^{\mathrm{T}}\mathbf{X}\right)^{-1}\mathbf{X}^{\mathrm{T}}\mathbf{Y}\,. \tag{5-4}$$

We also used Pearson correlation coefficients ρ_i (section 5.4.1.4), defined as:

$$\rho_i = \frac{\mathrm{cov}(x_i, y)}{x_{i,\mathrm{std}}\ y_{\mathrm{std}}} = \frac{1}{N-1}\sum_{k=1}^{N}\left(\frac{x_i^k - x_{i,\mathrm{mean}}}{x_{i,\mathrm{std}}}\right)\left(\frac{y^k - y_{\mathrm{mean}}}{y_{\mathrm{std}}}\right) = \frac{1}{N-1}\sum_{k=1}^{N}\bar{x}_i^k\,\bar{y}^k\ . \tag{5-5}$$

5.3. Results

In this section, we first describe examples of synthetic building layouts obtained by procedural modelling (subsection 5.3.1). Next, we discuss the results of the hydraulic simulations (subsection 5.3.2) and, finally, we detail the outcomes of the statistical analysis of the simulation results (subsection 5.3.3).

5.3.1. Urban layouts

Figure 5-4 displays six of the 2,000 generated building layouts to enable the reader to appreciate the influence of the main input parameters (Table 5-1 and Table 5-2). The variables x_1 to x_9 corresponding to the six building layouts of Figure 5-4 are given in Table 5-3.

Layout (a) and (b) in Figure 5-4 correspond to the same input parameters, except for the average street length x_1 and street curvature x_3. In layout (a), the average street length is about 3.4 times higher than in layout (b). This results in a more "fragmented" urban pattern in layout (b) compared to layout (a). Indeed, apart from the change in street curvature, layout (a) shows substantially larger building blocks than in layout (b). This observation also applies when layouts (c) and (d) are compared, as the average street length x_1 in layout (c) is almost three times higher than in layout (d). Layout (d) exemplifies an urban pattern characterized by a high value of the street curvature x_3. Comparing the building layouts (c) and (d) also reveals that the mean parcel area x_6 has a significant influence on the size of the building footprints, as x_6 takes a value roughly three times larger in the case of layout (c) than for layout (d).

The street orientation (x_2) has a strong influence on the connectivity between the different faces. For instance, in layout (a) ($x_2 = 0$) the building alignment tends to guide the flow entering through

the west (resp. south) upstream face towards the north (resp. east) downstream face. In contrast, layout (f) ($x_2 \approx 1$) seems to promote flow connection from the west (resp. south) upstream face towards the east (resp. north) downstream face.

The building rear setback x_7 is of little significance in our analysis as it mainly controls the distance between the back of the buildings and the limit of the corresponding plot of land. This distance has no direct influence on the flow computation. In contrast, the side setback x_8 plays a major part since it controls the distance in-between adjacent buildings and hence the possibility for water to penetrate inside a block of buildings. This is exemplified by building layouts (e) and (f). The side setback x_8 in the former layout is twice smaller than in the latter.

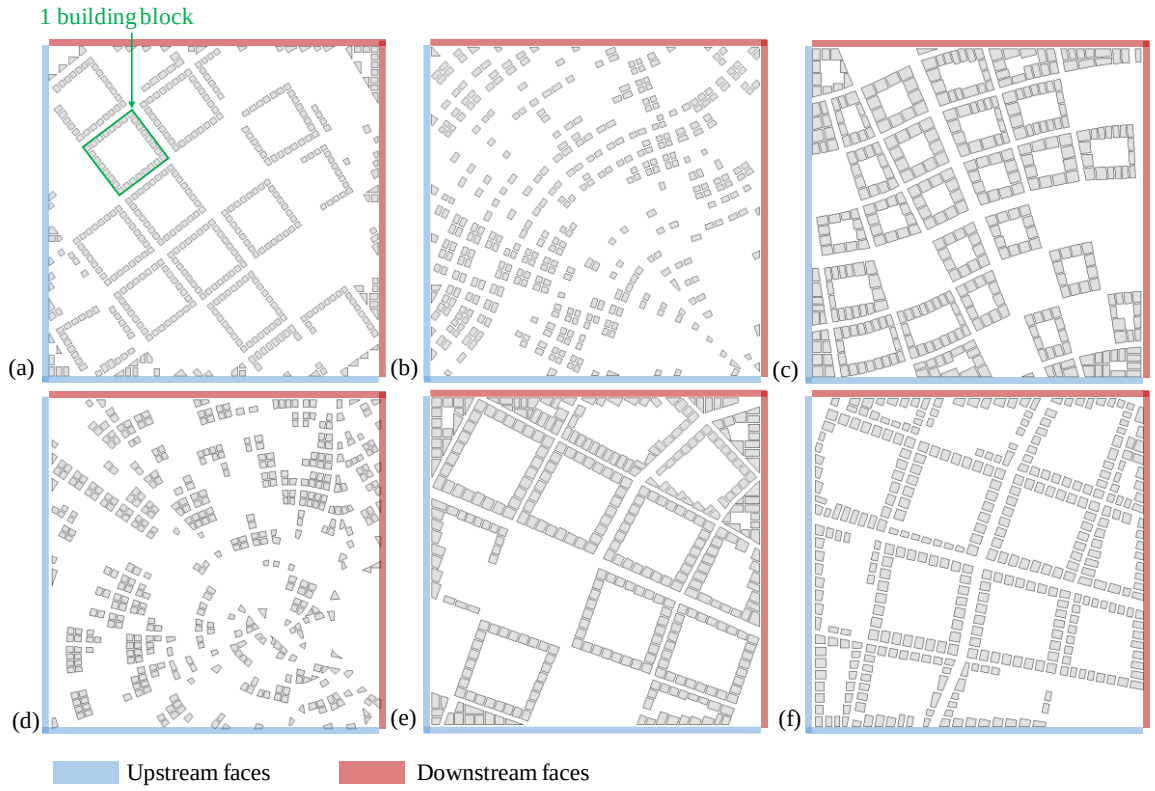

Figure 5-4 : Building footprints for six out of the 2,000 layouts generated by procedural modelling.

Conf.	x_1	x_2	x_3	x_4	x_5	x_6	x_7	x_8	x_9	h_{90}
a)	199 m	0	0.5 km^{-1}	28 m	18 m	500 m^2	3.0 m	3.0 m	13%	0.79 m
b)	59 m	0	1.7 km^{-1}	28 m	18 m	500 m^2	3.0 m	3.0 m	13%	0.74 m
c)	165 m	0.58	0.7 km^{-1}	35 m	15 m	1066 m^2	2.2 m	2.1 m	33%	1.02m
d)	57 m	0.15	3.9 km^{-1}	29 m	12 m	370 m^2	1.4 m	2.0 m	15%	0.75 m
e)	274 m	0.97	1.4 km^{-1}	28 m	11 m	880 m^2	2.5 m	2.3 m	26%	1.00 m
f)	293 m	0.97	0.5 km^{-1}	28 m	11 m	872 m^2	2.3 m	4.6 m	22%	0.86 m

Table 5-3: Variables x_1 to x_9 characterizing the six building layouts displayed in Figure 5-4.

5.3.2. Hydraulic simulations

5.3.2.1. Calibration / validation of the porosity-based model

As shown in section 4.4.2, the coarse model errors on the water depths are expected to be lower than 5% without any drag loss term while a reduction up to only 0.5% error can be obtained with an optimal calibration of the drag coefficient. Based on very different building layouts, it was shown that the range of variation of the optimal drag coefficient falls between 2.0 and 3.0 for the urban configurations considered in this study. Therefore, using a constant drag coefficient $c_{D,0}^{b} = 3.0$ for all computations, the coarse model error on the water depths should not exceed a few percent.

5.3.2.2. Computed water depths and velocity fields

The results of the hydraulic simulations are 2D maps of computed water depths and velocity fields. Figure 5-5 shows examples of hydraulic modelling results for the building layouts (c), (d) and (f) defined in Figure 5-4. The white areas in the maps of Figure 5-5 correspond to holes in the computational domain, i.e. cells which are inactive because they are mostly included within a building and therefore excluded from the computation. For layouts (c) and (f), virtually all buildings are reproduced explicitly by holes in the computational domain and the porosity parameters enable improving the geometric description of inclined boundaries. In contrast, much of the urban pattern of layout (d) is reflected only through the porosity parameters because in this case the buildings have a typical size comparable to the grid spacing. This results from the relatively low value of the mean parcel area x_6 in layout (d) (Table 5-3).

The computed water depths are minimum close to the downstream faces (north and east) and maximum along the upstream faces (west and south), due to the overall flow resistance induced by the buildings. The selected flood level indicator h_{90} along the upstream faces varies between 0.61 m and 1.14 m. Hence, for the tested configurations, varying the building layout may change the upstream flood level by a factor of almost two.

Overall the flow remains relatively slow within the urban area, with a Froude number $F = ||\boldsymbol{v}|| / (g\, h)^{0.5}$ of the order of 0.1 ($||\boldsymbol{v}||$ represents the velocity magnitude). The maximum value of F does not exceed about 0.4. The velocity increases at local contractions. This is particularly visible in layout (f), which is characterized by a side setback x_8 more than twice larger than for layouts (c) and (d), enabling hence more intense flow exchanges between the streets and the void areas inside building blocks ("courtyards"). This is also remarkably shown by the higher flow velocity computed inside the building block in layout (f) (velocity magnitude ~ 0.20 m/s)

compared to layout (c) (velocity magnitude ~ 0.1 m/s). This results also from the higher side setback value (x_8) in the former layout compared to the latter (Figure 5-4), making the void area whitin the building blocks more accessible to the flow in layout (f). The absolute velocities are high around the top-left and bottom-right corners where the flow avoids passing through the building area.

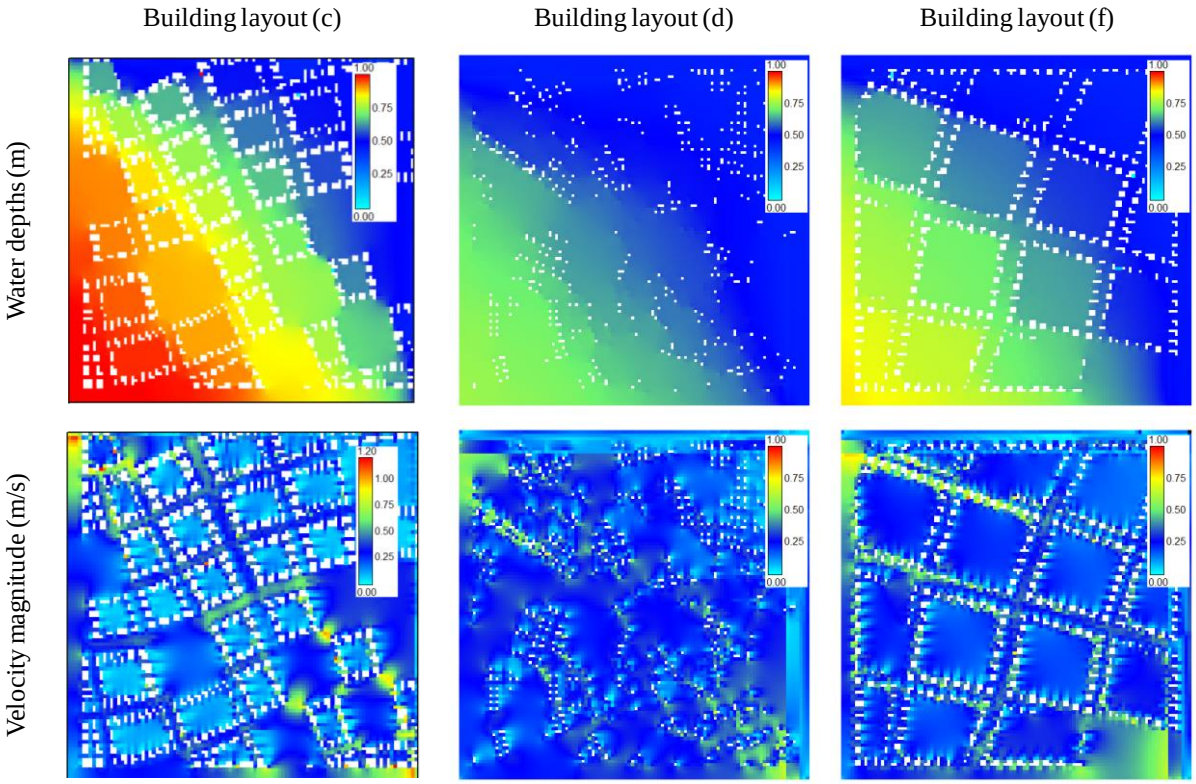

Figure 5-5 : Representation of water depths and flow fields for some urban patterns.

5.3.3. Influence of urban characteristics on inundation water depths

Figure 5-6 shows the regression coefficients a_i computed with Eq. (5-4) for an inundation indicator $y = \Delta h_{90}$ computed based on the 90th percentile of the computed water depths along the upstream boundaries of the domain (section 5.2.3). A positive value for a regression coefficient a_i indicates that an increase in the corresponding variable x_i leads to an increase in the water depths, and conversely for a negative value of the regression coefficient. Using the regression coefficients of Figure 5-6, the Δh_{90} values can be predicted with a mean absolute error and a root mean square error of, respectively, 2.3 cm and 2.9 cm. This represents less than 15% of the mean value of Δh_{90} (21.3 cm).

The results of the multiple linear regression (MLR) show that the building coverage (x_9) is by far the most influential urban characteristics. Besides the building coverage, the average street length

(x_1) has also a substantial influence on the water depths, because it controls the size of the building blocks. As shown in section 5.3.1, the lower the value of the average street length is, the more "fragmented" the urban patterns are. This contributes to avoid the creation of void areas surrounded by buildings, which are therefore not easily accessible to the flow. In a more fragmented urban pattern, a larger portion of void area contributes to the flow conveyance. Similarly, reducing of the building side setback (x_8) leads to higher water depths (section 5.3.2), due to the reduction of the conveyance capacity between adjacent buildings. This is consistent with the negative value obtained for coefficient a_8.

The increase in building size resulting from an increase in the mean parcel area (x_6) leads to higher water depths, as reflected by the positive value of a_6. The street orientation (x_2) and curvature (x_3) seem to have no significant influence on the water depths. This is certainly a result of the relatively low values of flow velocity in the considered urban area ($F \sim 0.1$), which are typical of lowland rivers. This finding is expect not to apply in the case of floodplains characterized by steeper topographic gradients, where the flow velocity would be higher and more dynamic effects would prevail.

The insignificant influence of the rear setback (x_7) can be explained by the weak influence of this variable on the flow conveyance since it mainly describes the void area within building blocks, which contribute anyway only very little to the overall flow conveyance through the urban area.

While the results of the MLR show no influence of the major street width (x_4) on the inundation water depths, a slight influence is shown for the minor street width (x_5). This should be explained by the high number of minor streets in the urban domain compared to only two major streets.

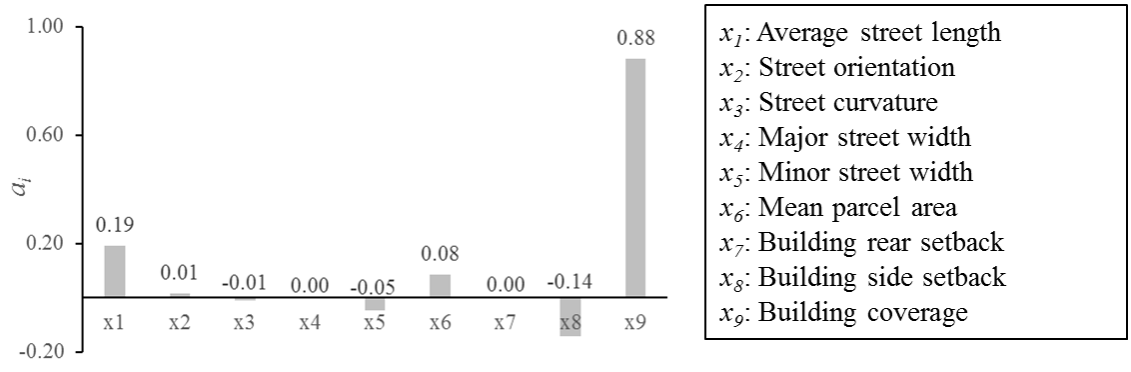

Figure 5-6 : Regression coefficients a_i of the urban characteristics for Δh_{90}.

5.4. Discussion

The results are discussed here, based on a comprehensive sensitivity analysis (subsection 5.4.1) and by comparing them with those of a simple conceptual approach (subsection 5.4.2).

5.4.1. Sensitivity analysis

5.4.1.1. Indicator of inundation water depths

The performed analysis is based on the increase of the 90th percentile of the water depths computed along the upstream boundaries of the urban area: Δh_{90}. Here, we test to which extent the conclusions of the analysis remain valid when another indicator of flood severity is chosen instead of Δh_{90}. To do so, we repeated the analysis by considering percentiles from 50th to 90th with a constant step of 5th and these percentiles were evaluated either along the upstream boundaries of the domain, or throughout the whole domain.

In Figure 5-7a, the sensitivity of the results of the MLR to the selection of the indicator of flood severity is shown through boxplots representing the variation of each coefficient a_i when all options described in 5.3.3 are tested. This sensitivity remains low for all coefficients a_i. Coefficients a_1 and a_6 corresponding to the influence of the average street length (x_1) and the mean parcel area (x_6) show the highest sensitivity with values ranging respectively from 1.3×10^{-1} to 2.1×10^{-1} and from 1.0×10^{-2} to 8.3×10^{-2}. Nonetheless, the findings described in section 5.3.3 remain generally valid whatever the choice of the indicator of flood severity. Comparing Figure 5-7b and Figure 5-7c, the sensitivity of the results to the percentiles is higher when they are evaluated throughout the whole domain than along the upstream boundary.

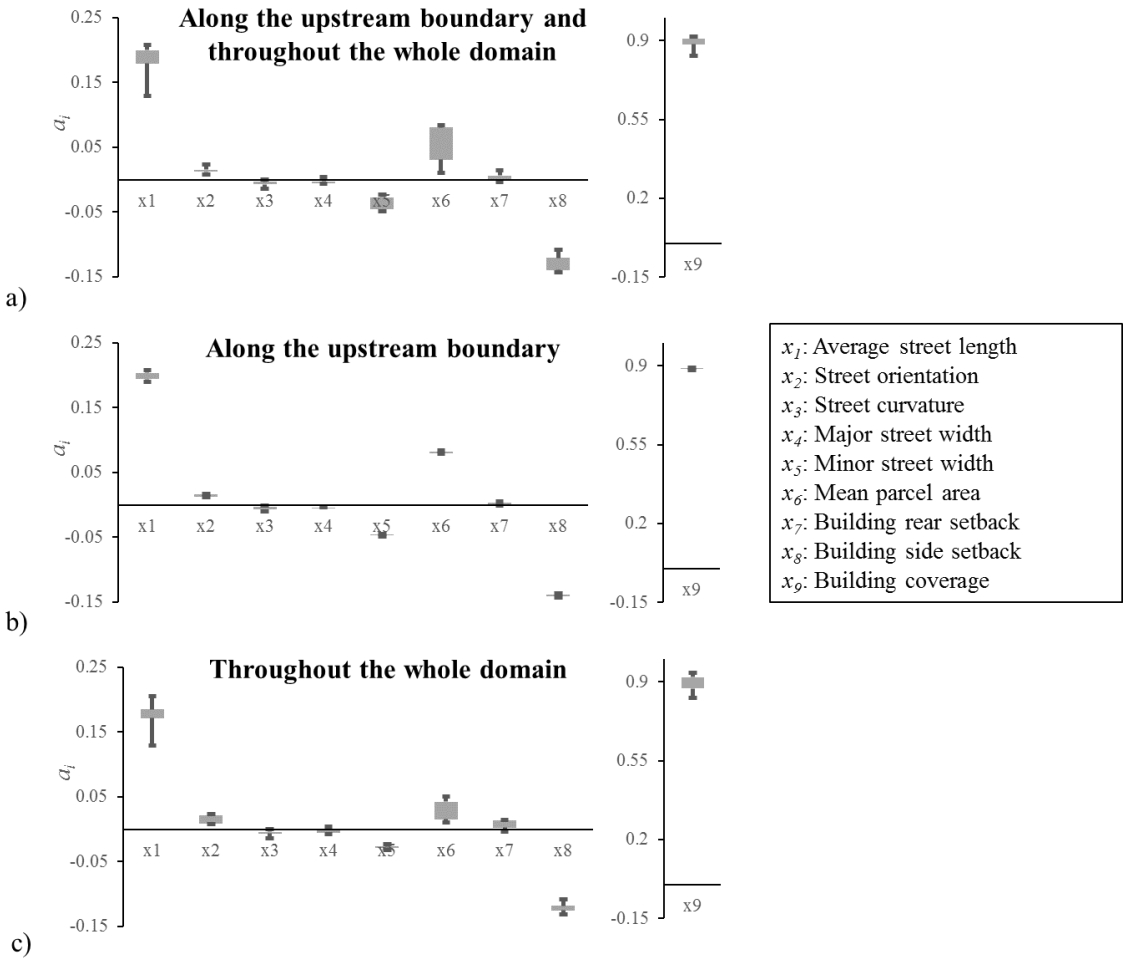

Figure 5-7 : Sensitivity of the regression coefficients to choice of the indicator of flood severity by considering percentiles from 50th to 90th computed (a) either along the upstream boundaries of the domain, or throughout the whole domain and (b) along the upstream boundaries of the domain and (c) throughout the whole domain.

5.4.1.2. Sample size

We investigated whether the sample size (2,000 building layouts) is large enough to produce robust and reliable results. For this purpose, we selected randomly 1,500, 1,000, 500 and 250 configurations out of the initial sample. For each sub-sample, the random selection was performed 10,000 times to assess the sensitivity of the results to the selected configurations.

Like in Figure 5-7, we display the results in the form of boxplots obtained from the sets of regression coefficients corresponding to the 10,000 different sub-samplings (Figure 5-8). Again, the findings of section 5.3.3 are hardly affected by a reduction of the sample size, at least when the subsample size remains above 1,000 (Figure 5-8). In all cases, the most influencing urban characteristic remains the building coverage (x_9) and only variables x_1, x_5, x_6, x_8 and x_9 show a significant influence on the computed water depths. Even for a sample size lower than 1,000,

most of the results remain consistent with the findings of section 5.3.3, and only some coefficients show substantial variations. Hence, the sample size of 2,000 different building layouts is deemed sufficient.

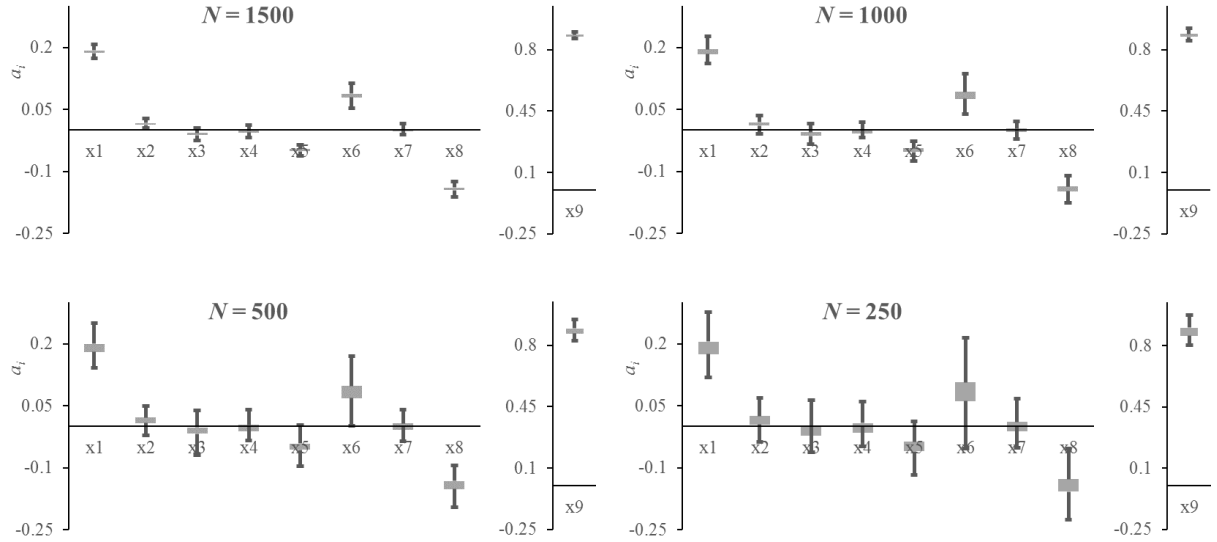

Figure 5-8 : Sensitivity of the absolute values of the regression coefficients of the urban characteristics for Δh_{90} to the sample size (N).

5.4.1.3. Number of urban characteristics used in the regression analysis

The respective influence of each of the nine selected urban characteristics on the computed water depths was shown to be very different, suggesting that some of the urban characteristics could be neglected in the regression analysis. Here, we compare the predictive capacity of regressions based either on all urban characteristics (variables x_1 to x_9) or just on the most influential ones. The predictive capacity of each regression is assessed through the resulting root mean square error.

Using only the building coverage (x_9) for the linear regression leads to a root mean square error roughly 37% higher than with the MLR based on all variables (Table 5-4). The prediction of Δh_{90} based on the five most influential variables (x_1, x_5, x_6, x_8 and x_9) gives an accuracy similar to the one obtained with all nine variables.

Considered variables	x_9	x_1, x_5, x_6, x_8 and x_9	x_1 to x_9
Root mean square error (cm)	4.01	2.93	2.93

Table 5-4: Root mean square errors on the estimation of Δh_{90} for sets of urban characteristics used in the MLR.

5.4.1.4. Model choice

In all analyses above, a linear relationship was assumed between the rise in water depth $y = \Delta h_{90}$ and variables x_1 to x_9:

$$\overline{y} = a_0 + \sum_{i=1}^{9} a_i \overline{x}_i \tag{5-6}$$

Here, we check whether our findings are affected by the choice of another model. For this purpose, we tested two approaches:

- First, we used an alternate model, assuming that Δh_{90} can be predicted by means of a power law involving all parameters x_1 to x_9:

$$\frac{y}{y_{\text{mean}}} = b_0 \prod_{i=1}^{9} \left(\frac{x_i}{x_{i,\text{mean}}} \right)^{b_i}, \tag{5-7}$$

  in which b_0 to b_9 are coefficients to be calibrated. Coefficients b_i certainly do not take the same values as parameters a_i; but still their relative values provide an indication on which of the variables x_i have more influence on the determination of Δh_{90}.
- Second, we computed *Pearson correlation coefficients* ρ_i, which also reflect the link between variables, but it does so independently of the choice of a particular model.

In practice, the estimation of coefficients b_i in Eq. (5-7) is performed by means of a MLR, after applying a logarithmic transformation to variables x_i and y:

$$\ln\left(\frac{y}{y_{\text{mean}}} \right) = \ln b_0 + \sum_{i=1}^{9} b_i \ln\left(\frac{x_i}{x_{i,\text{mean}}} \right). \tag{5-8}$$

The configurations involving a street orientation (x_2) equal to zero were disregarded; but they represent only 2.5 % of all building layouts in the sample.

Coefficients a_i, b_i and ρ_i are compared in Figure 5-9. Each set of coefficients has been scaled so that the sum of the nine absolute values is one. The following observations can be made.

- In all three approaches, variables x_9 is shown to have a substantial influence on, or be strongly correlated with, the flood severity indicator Δh_{90}. The prevailing influence of the building coverage is therefore a robust outcome of the analysis.
- A difference between the different approaches is found for the mean parcel area (x_6). The Pearson correlation coefficients suggest that the importance of x_6 is similar to that of the building coverage (x_9), while has some influence in the standard MLR and multiple linear regression with logarithmic transform, but of a lower magnitude than that of x_9. This

difference may result from the existing positive correlation between x_6 and x_9, as revealed in Figure 5-10. Given this correlation, the lower weight given to x_9 by the Pearson correlation compared to the standard MLR is simply compensated by a higher weight given to x_6.

- In all approaches, the coefficients assigned to the minor street width (x_5) and the building side setback (x_8) are consistently negative and of substantial magnitude. This confirms that considering variables x_5 and x_8 as strongly controlling the flow through the urban area is a robust outcome of the analysis.
- Similarly, the coefficients associated to the major street width (x_4) and the building rear setback (x_7) take consistently negative values of small magnitude, while those related to x_2 (street orientation) are also consistently small but positive. Therefore, these variables may safely be disregarded, as shown also in Table 5-4.
- The regression coefficients related to the average street length (x_1) and the street curvature (x_3) (a_1, a_3 and b_1, b_3) have an opposite sign compared to the corresponding Pearson correlation coefficients (ρ_1 and ρ_3). This is a result of the significant negative correlation between x_1 and x_3, as revealed in Figure 5-10. Although this correlation makes sense from an urban planning point of view, as a stronger street curvature implies more short streets in the inner area of the curved streets, it somehow hampers drawing truly robust conclusions on the relation between the street length and the upstream flood severity.
- Another interesting finding obtained from the Pearson regression coefficients is that several variables have a similar importance to x_9, while according to the standard MLR and the MLR with logarithmic transform, only x_9 seemed to be of prevailing influence. This result is consistent with those presented in the next section, which indicate that the building coverage is of lower importance than another composite indicator of flow *conveyance* at the scale of the urban area (district-scale), while x_9 is *stricto sensu* a proxy for the *storage* capacity (and not the conveyance capacity) in the urban area.

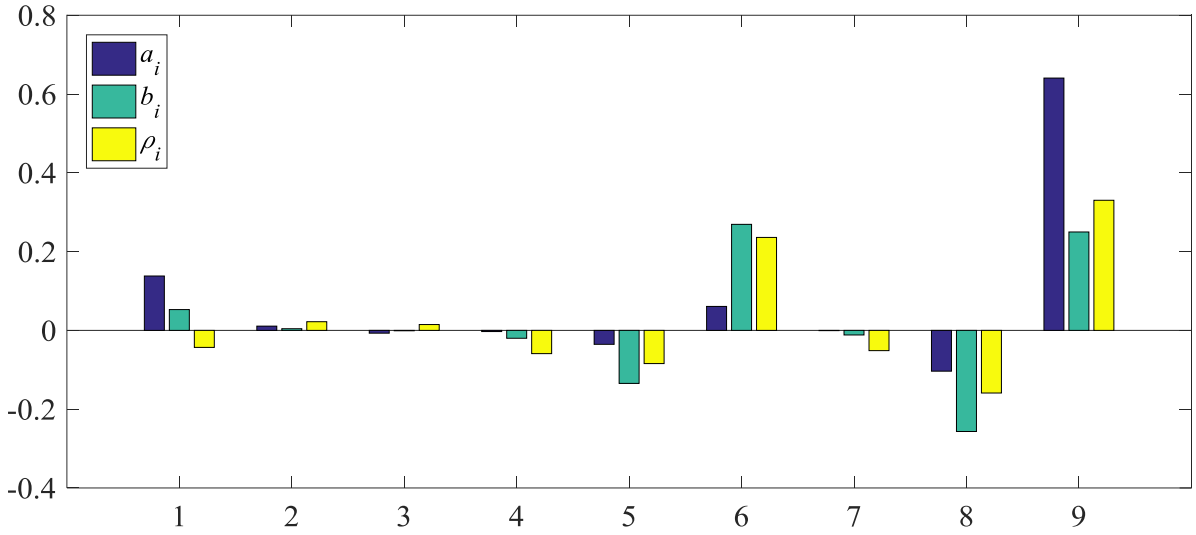

Figure 5-9 : Comparison of regression coefficients a_i and b_i obtained from multiple linear regression, without and with logarithmic transform, and with Pearson correlation coefficients ρ_i. Each set of coefficients has been scaled so that the sum of the nine absolute values is one.

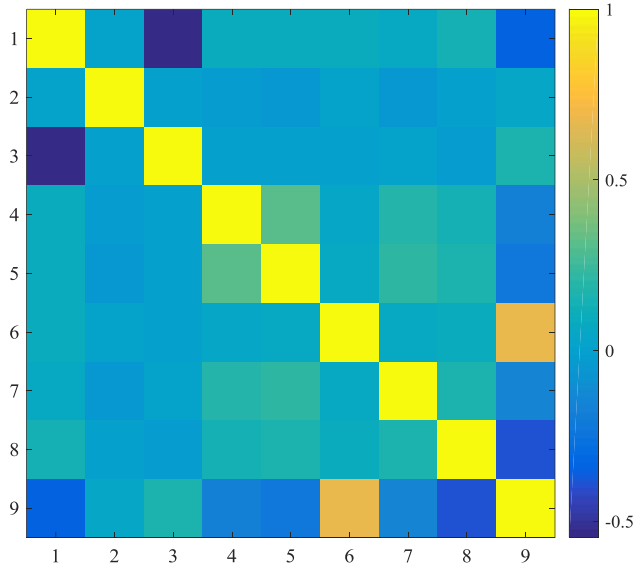

Figure 5-10 : Pearson correlation coefficients between all variables x_1 to x_9.

5.4.2. Conceptual approach

The set of input variables $x_1 \ldots x_9$ were selected for their significance in terms of urban planning. However, as such, they are neither optimal for statistical analysis (Figure 5-9) nor of direct relevance for hydraulic analysis. Therefore, we present here a simple conceptual model, which relates these urban planning parameters to just two parameters of direct relevance for hydraulic analysis: a district-scale storage porosity Φ_D, and a district-scale conveyance porosity Ψ_D.

The district-scale storage porosity is straightforward to evaluate from the building coverage ($\Phi_D = 1 - x_9$), while the district-scale conveyance porosity was estimated based on an idealization of the geometry of the considered urban layouts. Despite a number of simplifying assumptions, we show that these two district-scale porosity parameters explain amazingly well the results obtained in section 5.3 for the whole set of 2,000 quasi-realistic urban configurations.

5.4.2.1. Conceptualization

First, we aim to derive an expression relating the district-scale conveyance porosity Ψ_D to the input parameters of relevance for urban planning, as listed in Table 5-1. To do so, we introduce the following simplifying assumptions, which enable obtaining analytical expression for Ψ_D (Figure 5-11):

- the street orientation and curvature are neglected ($\alpha = \chi = 0$), so that all streets are straight and aligned either along the west-east direction or the north-south direction;
- these streets are separated by building-blocks of identical size;
- the size of a building-block is given by the average street length L_s;
- all minor (resp. major) streets have the same width equal to w (resp. W);
- each building-block is split into several identical square parcels of length equal to the square root of the mean parcel area A_p;
- the size of a building is determined from the parcel area and the three setbacks s_f, s_r and s_s;
- we estimate the conveyance porosity as the minimum void fraction in a section normal to the west-east direction (as if the flow as aligned with this direction).

Consistently with the procedural modelling presented in section 5.2.1, the idealized building layouts considered here also comply with the following rules:

- one single major street is introduced in each direction;
- only the external parcels of the building-blocks are urbanized while the others remain undeveloped.

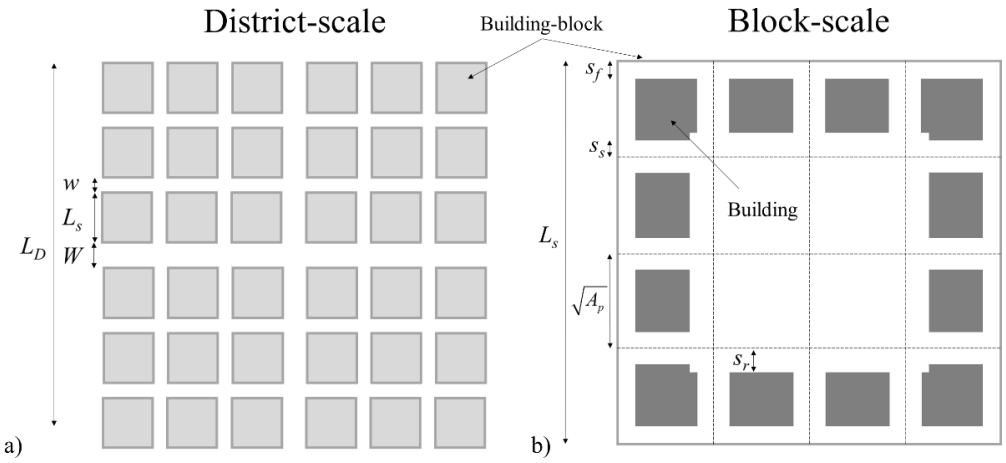

Figure 5-11 : Idealized urban pattern at the district-scale (a) and block-scale (b).

Under these simplifying assumptions, the number n of building-blocks over the length L_D of the urban area can be derived from the urban parameters by:

$$L_D = (n-2)(L_s + w) + 2\left(L_s + \frac{w+W}{2}\right) \quad \Rightarrow \quad n = \frac{L_D - (W-w)}{L_s + w} \quad . \tag{5-9}$$

The number n_b of buildings (or parcels) over the length L_s of a building-block is simply equal to: $L_s / \sqrt{A_p}$.

The block-scale conveyance porosity Ψ_B is estimated as the ratio between the minimum free length along the north-south or east-west direction and the total length of the building-block L_s:

$$\Psi_B = \left(\frac{L_s}{\sqrt{A_p}} - 2\right)\frac{2s_s}{L_s} + 2\frac{s_s + s_f}{L_s} \Rightarrow \Psi_B = 2\left(\frac{s_s}{\sqrt{A_p}} + \frac{s_f - s_s}{L_s}\right). \tag{5-10}$$

Similarly, the district-scale conveyance porosity Ψ_D is computed as:

$$\begin{aligned} \Psi_D &= (n-2)\frac{\Psi_b L_s + w}{L_D} + 2\frac{\Psi_b L_s + \frac{W+w}{2}}{L_D} \\ \Rightarrow \Psi_D &= \frac{\Psi_b L_s + w}{L_s + w} + \frac{w}{L_D}\left(\frac{W}{w} - 1\right)\left(1 - \frac{\Psi_b L_s + w}{L_s + w}\right) \end{aligned} \tag{5-11}$$

5.4.2.2. Results

Based on the district-scale storage and conveyance porosities, Φ_D and Ψ_D, a regression analysis was performed using Eq. (5-12):

$$\Delta h_{90} = a\,(1-\Phi_D)^b\,(1-\Psi_D)^c \qquad (5\text{-}12)$$

Since $\Delta h_{90} = 0$ for $\Phi_D = \Psi_D = 1$, Δh_{90} in Eq. (5-12) is logically expressed as a function of 1 - Φ_D and 1 - Ψ_D. The values of parameters *a*, *b* and *c* were determined by minimizing the root mean square error between Δh_{90} derived from Eq. (5-12) and the corresponding values extracted from the hydraulic simulations of the 2,000 building layouts (section 5.3.2.2).

Figure 5-12 shows the remarkable correlation obtained between Eq.(5-12), with calibrated coefficients *a* = 1.63, *b* = 0.75 and *c*= 2.24, and the reference values. The mean absolute and root mean square errors on the prediction of Δh_{90} from Eq. (5-12) over the 2,000 computed urban patterns are respectively equal to 2.0 cm and 2.6 cm.

Considering only the district-scale storage porosity in the regression analysis (*c* = 0) gives optimal coefficient *a* = 1.00 and exponent *b* = 0.91. The mean absolute and root mean square errors increase by respectively 47% and 57% when neglecting the district-scale conveyance porosity in the regression analysis. Neglecting the district-scale storage porosity (*b* = 0), the errors increase dramatically by more than a factor 3.

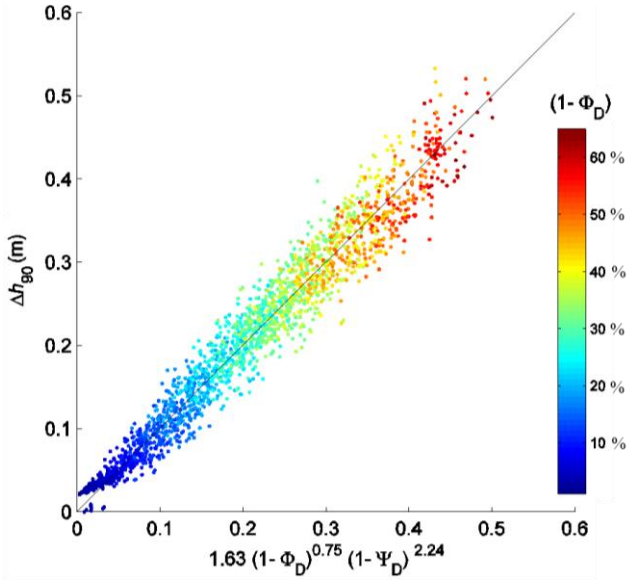

Figure 5-12 : Relationships between the optimal regression analysis of the district-scale porosities Φ_D and Ψ_D and the inundation indicator Δh_{90} for the 2,000 computed urban patterns.

5.4.2.3. Interpretation

Although the conceptual model is based on an idealization of the building layouts and on relatively crude assumptions, the results obtained with this simple model are very promising. While the minimum value of the root mean square error computed with a regression analysis based on the nine urban characteristics is 2.9 cm (section 5.3.3), this error is found here to drop to 2.6 cm when only the two district-scale porosity parameters are used.

The standard MLR analysis indicates that the storage porosity (i.e. the building coverage) is by far the urban characteristic influencing most the water depths (section 5.3.3); but this is somehow misleading since we find here, based on parameters of direct hydraulically significance, that the conveyance porosity has actually an even stronger influence (exponent $c = 2.24 \sim 3 \times$ exponent b). This aspect was already suggested in section 5.4.1.4, which highlighted that other parameters than the building coverage (x_9) seem to have a similar importance when a logarithmic transformation was applied to all variables, as well as based on Pearson regression coefficients.

However, the storage porosity is a key parameter to capture the influence of urban patterns on inundation water depths. While the accuracy of the conceptual model decreases by around 50% when neglecting the conveyance porosity, it drops by a factor 3 when the storage porosity is not considered.

5.4.2.4. Implication for urban planning

Figure 5-13 provides two examples of pairs of building layouts leading to similar water depths upstream, although they are characterized by significantly different building coverage ratios, i.e. different values of the district-scale storage porosity ($\Phi_D \sim 0.6$ vs. $\Phi_D \sim 0.8$). In both cases, the higher value of the building coverage is compensated by a higher value of the district-scale conveyance porosity.

These results are fully consistent with Eq. (5-12), which highlights that potential detrimental effect of reduction of the storage porosity (i.e. new developments increasing the building coverage) can be effectively mitigated by means of a suitable layout of the buildings which increases the conveyance porosity. This finding is of high relevance to guide more flood-proof urban developments.

Eqs (5-10) and (5-11) reveal that the district-scale conveyance porosity can be increased mainly in two ways:

- at the district-scale, increasing the fragmentation of the urban pattern (i.e. increasing the value of n) by reducing the average street length L_s or by favouring a high number of narrow streets to a low number of large ones;
- at the building-block-scale, increasing the building side setback s_s or reducing the building size (i.e. reducing the mean parcel area $\sqrt{A_p}$).

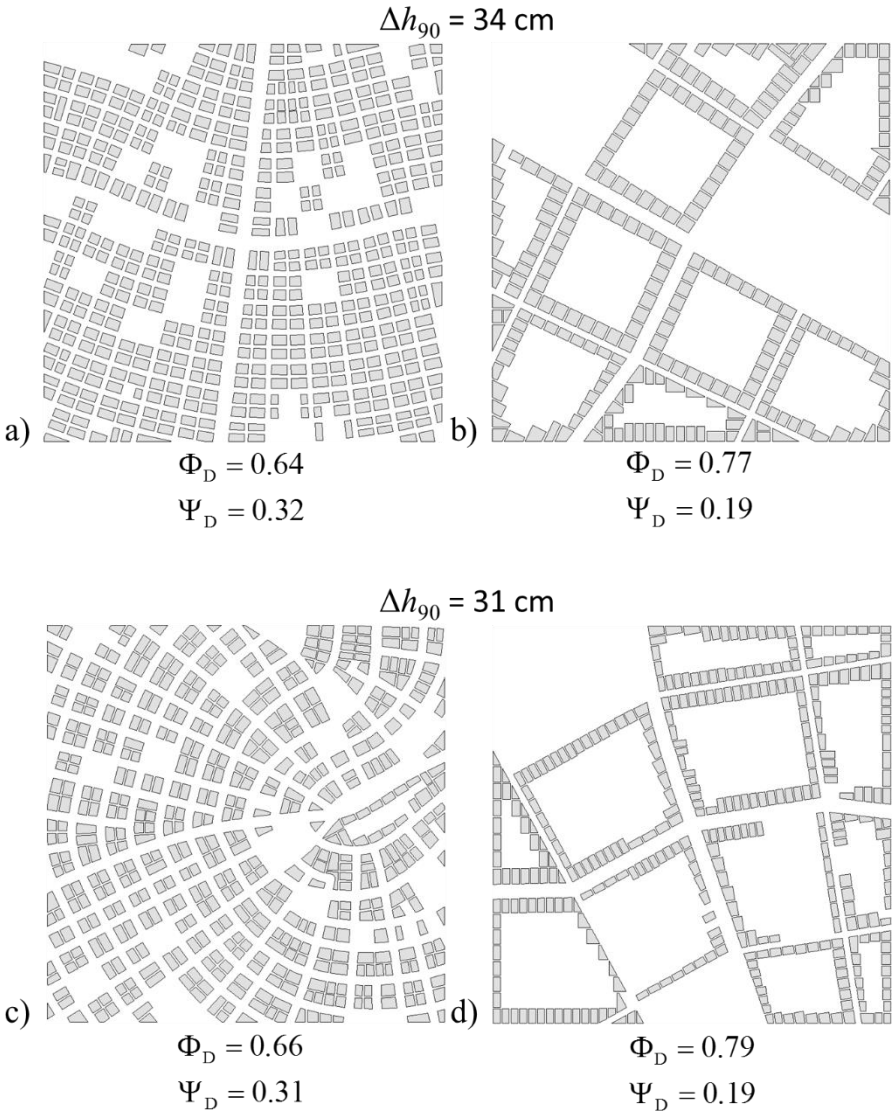

Figure 5-13 : Urban patterns with different district-scale porosity values leading to similar upstream water depths.

5.5. Conclusion

This chapter presents a unique systematic study of inundation flow in quasi-realistic urbanized areas, which links hydraulic modelling results to parameters of direct significance for urban planning. Based on porosity-based hydraulic computations of inundation flow for a set of 2,000 different building layouts, the relative influence of nine urban characteristics (average street length, street orientation and curvature, major and minor street widths, mean parcel area, rear and side building setbacks and building coverage) on inundation water depths were assessed. We focused on the water depth upstream of the considered urban area, as it reflects the impact of the developed area on the severity of flooding upstream. The terrain slope was neglected, so that the analysis results apply mostly to floodplains of typical lowland rivers.

The most influential parameters were found to be the building coverage, the mean parcel area (controlling directly the building size), the building side-setbacks, and to a lesser extent, the length and width of the streets. For the tested configurations, the more fragmented the urban pattern is (relatively small parcel sizes and street length), the lower the upstream water depths. This aspect is related to urban design at the district and building-block scales. Additionally, increasing the voids in-between the buildings (i.e. larger side setbacks) was shown to also contribute to a decrease in the upstream waterdepth. This aspect relates to urban planning at the local level of a single parcel.

We also built a simple conceptual model based on storage and conveyance porosity parameters determined at the district-scale. Although particularly simple, the model was shown to provide surprisingly accurate predictions of the influence of the building layout on upstream water depths. The model parameters reveal that an increase in building coverage in an urban area (i.e. new developments, leading to a decrease in the district-scale storage porosity) can be effectively compensated by a suitable location of the buildings so that the district-scale conveyance capacity increases.

This study paves the way for more quantitative approaches in water-sensitive urban design, based on process-oriented modelling of the interactions between complex urban systems and flooding mechanisms, enabling more flood-proof urban developments.

Further research is needed to reach a deeper understanding of the influence of environmental parameters, such as the terrain slope and imperviousness, man-made structures (sewage system, underground structures …) and obstacles (cars, trees …) as well as varying hydraulic conditions (unsteady flood waves, pluvial flooding …).

6. Impacts of urbanization on future flood damage in Wallonia, Belgium

This chapter is based on a manuscript under preparation for a peer reviewed journal. It relates also to the communication "*Impacts of urban expansion on future flood damage: a case study in the river Meuse basin, Belgium*" presented at the *4th IAHR Europe Congress*, Liège, 2016 (Mustafa et al. 2016), in which the PhD candidate was in charge of all hydraulic analyses and of damage modelling.

The personal contributions of the PhD candidate to this chapter include the determination of the inundation characteristics, the flood damage assessment, the sensitivity analysis and the whole discussion of the results. The land use evolution model was developed by A. Mustafa, who also generated the future land use maps.

ABSTRACT: Besides climate change, urban development is a key factor influencing future flood damage. This paper evaluates the impact of urbanization on future flood damage for rivers flowing throughout the Walloon Region, Belgium. An original agent-based model is used to generate future land use maps up to 2100. These maps give the spatial distribution of different building density classes for residential and industrial categories. The uncertainty related to future urban developments is considered by the definition of 18 urbanization scenarios. The results of the study show that future flood damages and their spatial distributions strongly vary depending on the urbanization scenario. Without any building regulation in flood-prone areas, the total flood damage increases in-between respectively 10-25%, 20-45%, 35-65% and 50-100% for the time horizons 2030, 2050, 2070 and 2100. The restriction of urbanization in flood-prone areas leads to a substantial mitigation of the rise in flood damage. Finally, the determination of the spatial distribution of the increase in flood damage due to land use changes enables the identification of the most sensitive locations to guide more flood-proof urban developments.

6.1. Introduction

It is widely accepted that the magnitude and frequency of inundations is currently increasing in Northwest Europe (Robson 2002, Hannaford and Marsh 2008, Moel and Aerts 2011). Besides climate change, increases in flood damage can mainly be attributed to urban development in flood-prone areas (Moel and Aerts 2011). Therefore, there is a high policy interest in clarifying the links between urban development and flood damage.

The estimation of the economic consequences of a flood event involves the determination of four main components (Messner et al. 2007) : (*i*) the intensity of inundation, generally represented by flood water depths, (*ii*) the type of elements at risk, generally given by land use maps, (*iii*) the values of the elements at risk and (*iv*) their susceptibility against inundation.

The urban development affects the flood damage in multiple ways: reduction of the infiltration of water into the soil, modification of the flow field or increase of the flood exposure. Many of existing studies analyse the influence of urbanization on hydrological processes. In section 5, the impact of urban patterns on inundation flow was investigated. Beckers et al. (2013) evaluated the contribution of urbanization to future flood damage along the river Meuse in the Walloon region for the time horizon 2100. They show that urbanization increases the flood damage by 1.01 to 1.4 for a 100-year flood. Additionally, they concluded that careful building regulations in flood-prone areas can effectively mitigate the impact of land use changes on flood damage.

In this study, an urbanization model is used to analyse the influence of urban development for the time horizons 2030, 2050, 2070 and 2100 along several hundreds of kilometres of rivers throughout Wallonia, Belgium. The urbanization model is an original agent-based model giving the future urban development of residential and industrial categories through the spatial distribution of building density classes with a mesh resolution of 100×100 m^2.

Strengths of this research consist in the determination of the spatial distribution of the impact of urbanization on future flood damage and in the consideration of the uncertainty in future urban developments through the use of different urbanization scenarios.

The material and methods are presented in section 6.2. The study area is described in section 6.2.1 and the original urbanization model is introduced in section 6.2.2. The hydrological characteristics of the floods are deduced from 2D hydraulic computations performed in the context of the generation of flood hazard maps for the Walloon Administration (section 6.2.3). The methodology used for the assessment of flood damage is discussed in section 6.2.4.. In section 6.3, we analyse the influence of some characteristics of land use information on the results

of the flood damage computation. Finally, the spatial distribution of changes in flood damage due to urban changes are presented and discussed in section 6.4, considering different urbanization scenarios.

6.2. Material and methods

6.2.1. Study area

The Walloon region covers an area of 16,844 km^2 in the south of Belgium. The hydrographic network is structured in four hydrographic districts (corresponding each to a portion of the Meuse, Rhine, Escaut or Seine basin), 15 hydrographic sub-basins (Figure 6-1) and 6,208 so-called PARIS sectors, which correspond each to a river stretch with relatively homogeneous characteristics in the main riverbed and in the floodplains. In this study, we only consider the two main districts (Meuse and Escaut) which cover respectively 73% and 22% of the Walloon region. The areas of most sub-basins in the Meuse district are larger than in the Escaut district, while the population density is generally lower in the former (Table 6-1). The "Meuse aval" (i.e. lower Meuse) sub-basin is the largest in Wallonia and the most densely inhabited in the Meuse district. Four sub-basins in the Meuse district have a population density lower than 100 inhabitant/km^2 while it remains higher than 175 inhabitant/km^2 for all the sub-basins in the Escaut district.

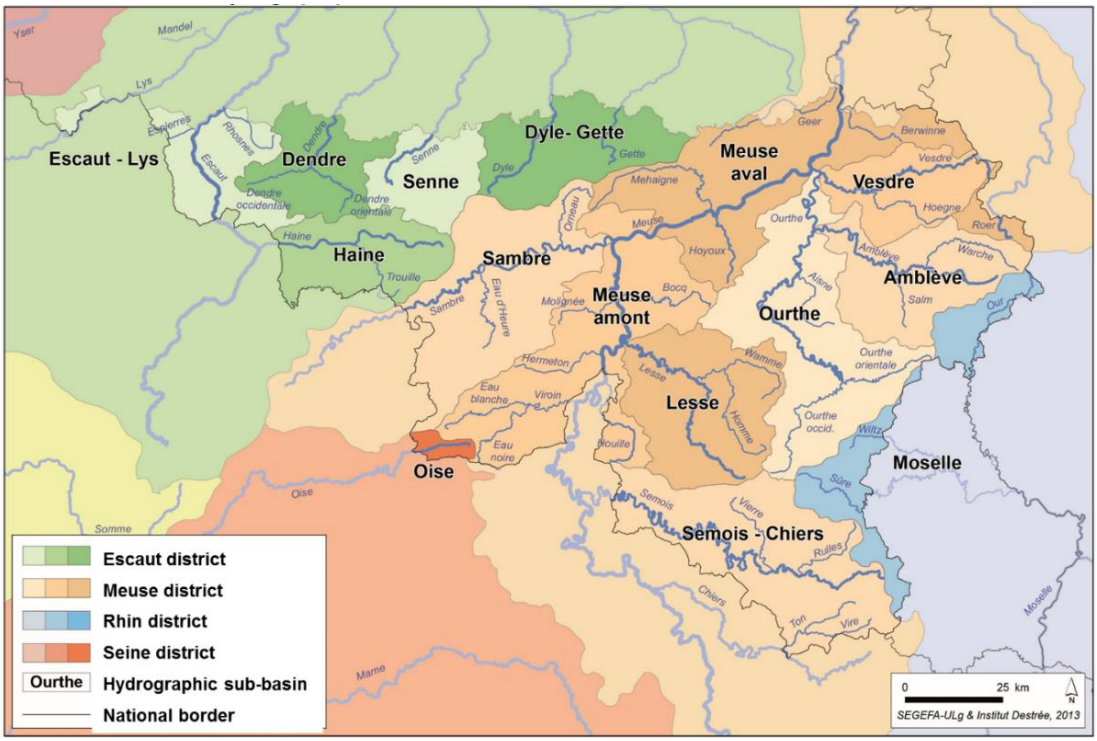

Figure 6-1 : Representation of the 4 hydrographic districts and 15 hydrographic sub-basins in the Walloon region (adapted from http://connaitrelawallonie.wallonie.be).

District	Sub-basin	Main river	Area	Population density (2009)
Meuse	Meuse aval	Meuse	1,924 km^2	373 inhabitant /km^2
	Meuse amont	Meuse	1,923 km^2	116 inhabitant /km^2
	Ourthe	Ourthe	1,843 km^2	83 inhabitant /km^2
	Semois-Chiers	Semois	1,759 km^2	74 inhabitant /km^2
	Sambre	Sambre	1,703 km^2	361 inhabitant /km^2
	Lesse	Lesse	1,343 km^2	52 inhabitant /km^2
	Amblève	Amblève	1,077 km^2	72 inhabitant /km^2
	Vesdre	Vesdre	703 km^2	305 inhabitant/km^2
Escaut	Dyle-Gette	Dyle and Gette	944 km^2	273 inhabitant/km^2
	Haine	Haine	802 km^2	512 inhabitant/km^2
	Escaut-Lys	Scheldt	766 km^2	287 inhabitant/km^2
	Dendre	Dender	673 km^2	175 inhabitant/km^2
	Senne	Senne	569 km^2	372 inhabitant/km^2

Table 6-1: Hydrographic sub-basins in Wallonia in the Meuse and Escaut districts and their respective main river, area and population density (DGO3 2015a, 2015b).

In the context of the determination of flood hazard maps for the Walloon Administration in 2003, maps of inundation extents and water depths were computed for several hundreds of kilometres of rivers throughout the Walloon region by the research group HECE of the University of Liege (Erpicum et al. 2010b). Figure 6-2 shows the hydrographic sectors for which results of these computations are available. In the Escaut district, only a limited portion of all the sectors was computed, except for the Escaut-Lys sub-basin where results are available all along the river Scheldt. No river was computed in the Haine sub-basin. In the Meuse district, computations were performed all along the rivers Amblève, Meuse, Ourthe, Sambre, Vesdre and Viroin. In the Lesse and Semois-Chiers sub-basins, results are only available for some reaches of the rivers Lesse and Semois.

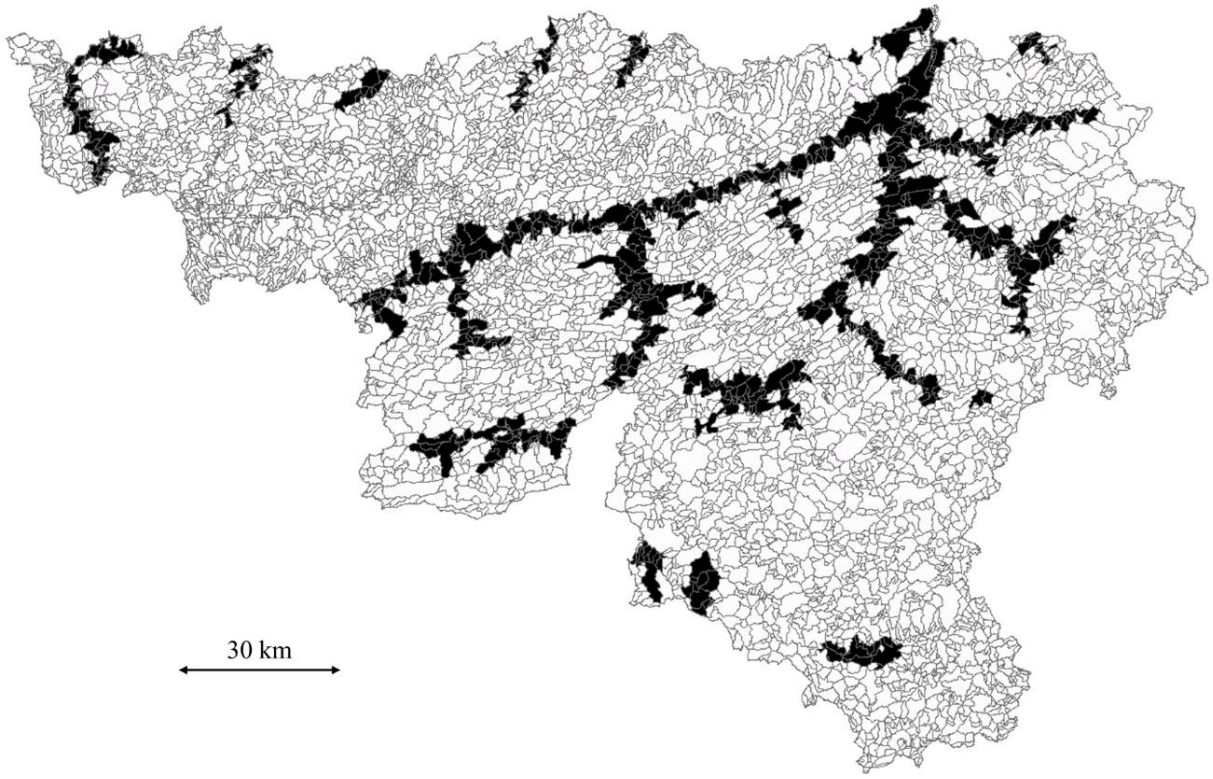

Figure 6-2 : Hydrographic sectors for which computations were performed by the HECE in the context of the preparation of flood hazard maps (Erpicum et al. 2010b).

6.2.2. Urbanization model

Datasets

Built-up maps for 1990, 2000 and 2010 were generated on a 100×100 m^2 raster-grid giving the spatial distribution of building density classes.

The Belgian Cadastral Database (CAD) contains the vector contour of buildings and their construction dates. The building contours were rasterized on a 100×100 m^2 raster-grid and a building density value was assigned to each cell based on the building footprint within it. Cells with building density values lower than 1/100 were considered as non-built cells (class 0), consistently with the average-sized of 100 m^2 for residential building in Belgium (Tannier and Thomas 2013). Finally, the building density values were classified in five building density classes (Table 6-2) using the natural-breaks technique (Jenks and Caspall 1971).

Building density class	Min. density	Max. density
0	0.00	0.01
1	0.01	0.06
2	0.06	0.14
3	0.14	0.26
4	0.26	0.49
5	0.49	1.00

Table 6-2: Building density classes for the 2010 CAD.

The built-up development driving factors were operationalized to be included in the model. Table 6-3 gives the selected factors for this study. The elevation data were obtained from the Belgian National Geographic Institute. The distance to the different road categories comes from a vector dataset made available by Navteq Company. The location of railway stations was provided by Walphot SA Company. This study considers distances to large cities (population above 90,000 inh.) and medium-sized Belgian cities (population between 20,000 and 90,000). The socio-economic data (employment rate and wealth index) come from the Belgian statistics, published by the Walloon Institute for Evaluation, Prospective and Statistics. Finally, zoning areas were obtained from the regional zoning plan, commonly named as PdS (Plan de Secteur) in Wallonia. Finally, a residential or industrial category was assigned to each cell based on the current zoning plan.

Factor	Name	Type	Unit
E	Elevation (DEM)	Continuous	Meter
S	Slope	Continuous	Percent rise
DR1	Dist. to Road1	Continuous	Meter
DR2	Dist. to Road2	Continuous	Meter
DR3	Dist. to Road3	Continuous	Meter
DR4	Dist. to Road4	Continuous	Meter
DRS	Dist. to railway stations	Continuous	Meter
DLC	Dist. to large-sized cities	Continuous	Meter
DMC	Dist. to medium-sized cities	Continuous	Meter
EMP	Employment rate	Continuous	Percent
RI	Wealth index	Continuous	Percent
NCL1	Number of class-1 cells in 3×3 neighbour		Number
NCL2	Number of class-2 cells in 3×3 neighbour	Continuous	Number
NCL3	Number of class-3 cells in 3×3 neighbour	Continuous	Number
NCL4	Number of class-4 cells in 3×3 neighbour	Continuous	Number
NCL5	Number of class-5 cells in 3×3 neighbour	Continuous	Number

Table 6-3: Selected built-up driving factors.

Agent-based model

In this study, an original agent-based model (AB model) was developed. The model considers two built-up processes: built-up expansion (transitions from non-built-up to built-up) and built-up densification (transitions from lower built-up densities to higher ones).

The AB model is a 100 × 100 m² grid-based model whereby transactions in built-up areas are simulated through land developers decisions (Figure 6-3). The agents are categorized into three agent groups with different characteristics and goals: developers, planning permission authority

and existing residents. For each time step of one year, developer agents select locations for urban development taking into account global and local considerations through specific weights assigned to each built-up driving factors of Table 6-3. Based on these specific weights, a utility function is used to determine the suitability of a location for a developer agent. Then, the planning permission authority permits, severely restricts or prohibits urbanization in the cells selected by the developer agents. Relationships between existing residents and developer agents are generally conflicting. On one hand, each developer agent tends to build within the existing built-up area (densification) or close to it to benefit from existing services. On the other hand, existing residents usually want to live in low density areas (Rand et al. 2005). In this study, a 3×3 neighbourhood window is used to consider local neighbouring interactions (Table 6-3).

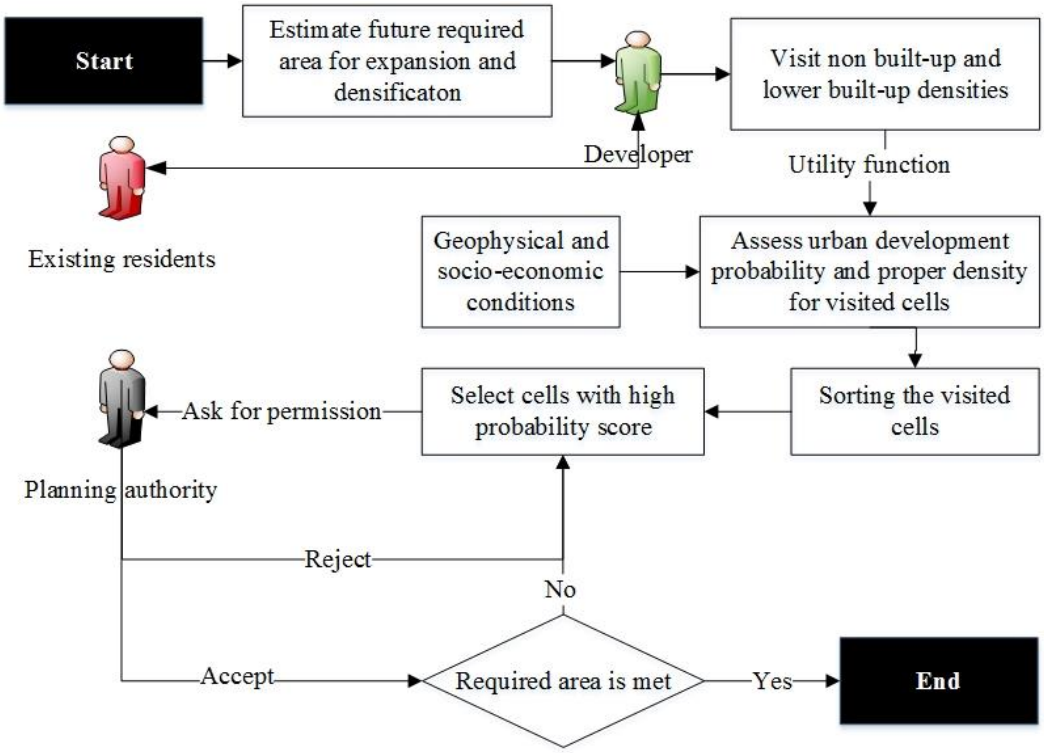

Figure 6-3 : Overall framework of the agent-based model.

Calibration/validation of the model

The weights parameters of the driving factors were calibrated with a genetic algorithm based on the urbanization changes between 1990 and 2000.

The validity of the model was assessed by comparing the simulated land use map in 2010 to the actual one. Performance indicators are comparable to those reported in literature (Long et al. 2013, Wang et al. 2013, Han and Jia 2017).

Uncertainty and future urbanization scenarios

Future urbanization is influenced by dynamics that occur at large spatial and temporal scales and involve complex macro-economic and demographic changes (Veldkamp and Lambin 2001). Commonly, the estimates of future urbanization rates are based on simulations of different scenarios based on extrapolation of the past trends, population expansion or socio-economic transitions (Poelmans et al. 2010, Cammerer et al. 2013). Based on linear extrapolations of the real expansion and densification between 1990, 2000 and 2010 in Wallonia, three urbanization rates are proposed for the future: low-, medium- and high-demand. These scenarios were derived by extrapolating respectively the trends between 2000 and 2010, 1990 and 2010, and 1990 and 2000.

As detailed in Table 6-4, a set of 18 different urbanization scenarios was generated by varying the urbanization rate, the urbanization policy (densification with/without expansion), and different levels of ban on new developments in flood-proof zones. In this respect, we consider three types zones represented in the official inundation maps (Erpicum et al. 2010b):

- zones of "low flood hazard", referred to hereafter as "zone 1";
- zones of "medium flood hazard", referred to hereafter as "zone 2";
- zones of "high flood hazard", referred to hereafter as "zone 3";

The business as usual scenario is in line with the recent built-up developments. In the densification scenarios, the required new areas for expansion are taken from the next density level. For instance, the expansion from class-0 to class-1 and class-2 is substituted by densifying the same area from class-1 to class-2. In cases where the available area of a specific class is not sufficient to be further densified, the model densifies the required expansion area of the next density class.

	Urbanization rate	High (1990-2000)	Medium (1990-2010)	Low (2000-2010)
	Ban on new developments in flood-prone areas			
Business as usual	None	BH	BM	BL
Expansion and densification	In zones 2 and 3	BHR-23	BMR-23	BLR-23
	In all zones	BHR-123	BMR-123	BLR-123
Densification only	None	DH	DM	DL
	In zones 2 and 3	DHR-23	DMR-23	DLR-23
	In all zones	DHR-123	DMR-123	DLR-123

Table 6-4: Urbanization scenarios.

6.2.3. Hydrological characteristics

The computation of inundation extents and water depths for the generation of the flood hazard maps in Wallonia was performed for steady flows corresponding to return periods of 25, 50 and 100 years, using the 2D hydraulic model Wolf2D with mesh sizes as fine as 2 to 5 m (Ernst et al. 2010, Erpicum et al. 2010a, Beckers et al. 2013, Bruwier et al. 2015, Detrembleur et al. 2015).

Although other flow variables like flood duration, flow velocity, … may influence flood damage, we only consider here the water depth to determine the flood damage. The water depth is indeed by far the most influential driving factor of flood damage (Wind et al. 1999, Merz et al. 2007), particularly for direct flood damage which are those evaluated in this study. For instance, flow velocity is likely play a part in different contexts, involving typically steep slopes more prone to flash flood events. Inundation water depths were not computed at the location of buildings since they are represented in the hydraulic model by holes impervious to the flow. Therefore, in this study, we interpolated the water depths within each building. Finally, floodplain maps were obtained by removing the riverbed from the inundation maps.

Also, similarly to the work of Beckers et al. (2013), the computed flow characteristics were not altered as a result of growing urbanization. We assume that the changes in flooding characteristics induced by urbanization have a lower effect on flood damage than the increase in exposure to flood. Moreover, we do not consider the impact of climate change on the occurrence of flood discharge. For the same study area, Beckers et al. (2013) showed that the contribution of land use changes on the increase in flood damage between 2009 and 2100 is larger than that of climate

change in a dry climate scenario. In contrast, the impact of climate change may become more influential for other scenarios.

6.2.4. Flood damage assessment

Figure 6-4 gives an overview of the methodology used for assessing flood damage. The result is a map giving the spatial distribution of direct and tangible flood damage at a mesh-resolution of 5 x 5 m^2, representative of the resolution of the hydraulic computation (section 6.2.3).

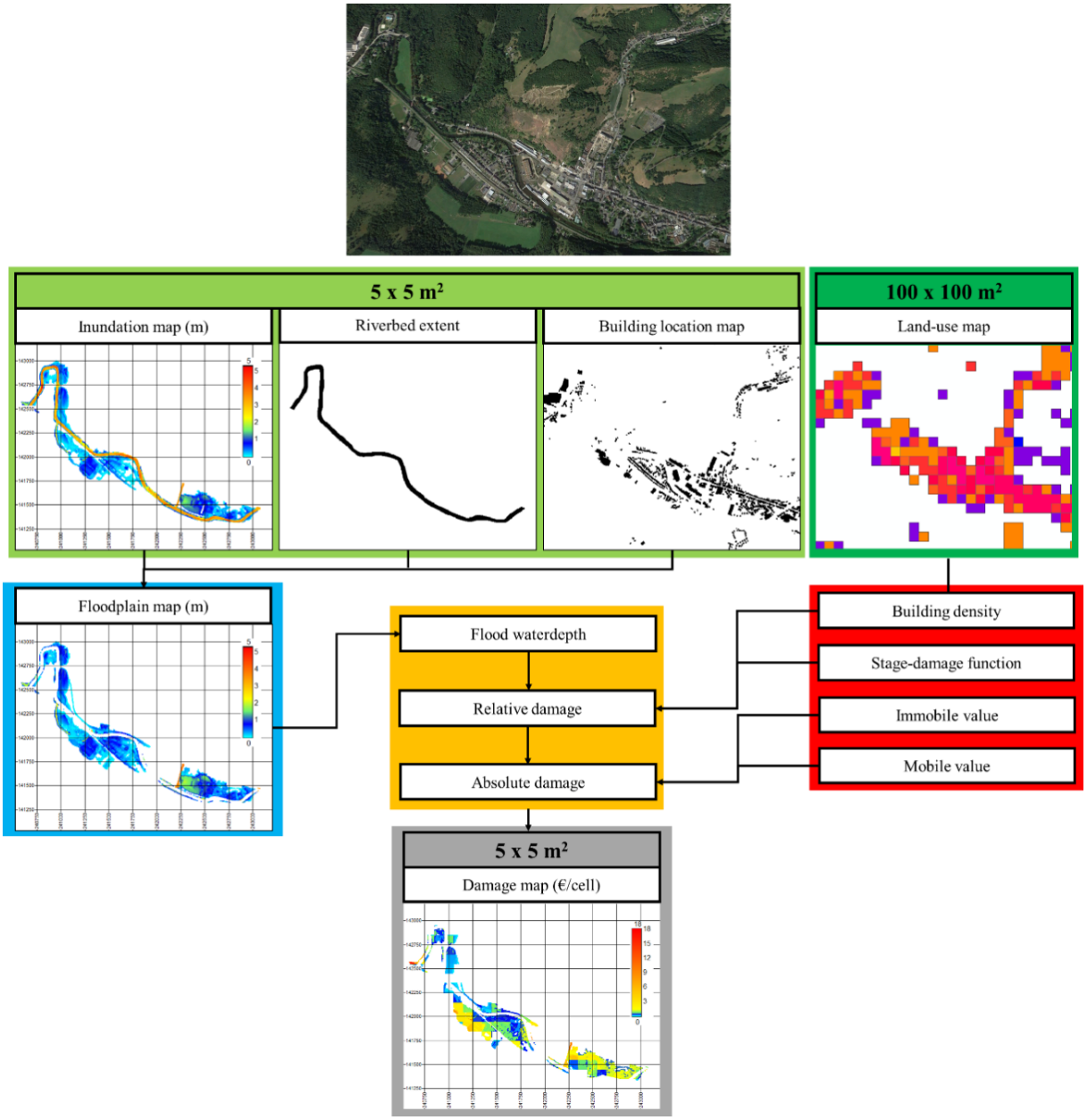

Figure 6-4 : Methodology for the estimation of flood damage.

The land use category of each floodplain cell (5 × 5 m²) was determined from the land use map at a resolution of 100 × 100 m². The urbanization model (section 6.2.2) considers two land use categories: residential and industrial. Therefore, only damages related to buildings are computed in this study and we do not consider damages related to other land use categories like infrastructure, agriculture and forest.

For each land use category, the urbanization model distinguishes different building density classes. For each cell, the building density is the portion of the cell which is actually built up. As detailed in section 6.2.2, the distinction of different building density classes enables the investigation of the impacts on flood damage of not only urban expansion (i.e. more urbanized cells) but also densification (i.e. augmentation of the building density of an already urbanized cell). To the best of the author's knowledge, this is an original feature of this study.

The susceptibility of a building to flooding was assessed by a stage-damage function giving the relative damage (i.e. the share of the total value of a building which is damaged by the flood) as a function of the water depth. In this study, we used the stage-damage functions for residential and industrial categories defined by the Flood Loss Estimation Model (FLEMO) (Kreibich et al. 2010). The damage assigned to residential and industrial buildings is split between mobile and immobile assets. Figure 6-5 shows the single FLEMO stage-damage function used for both assets for residential buildings and the two functions for industrial ones.

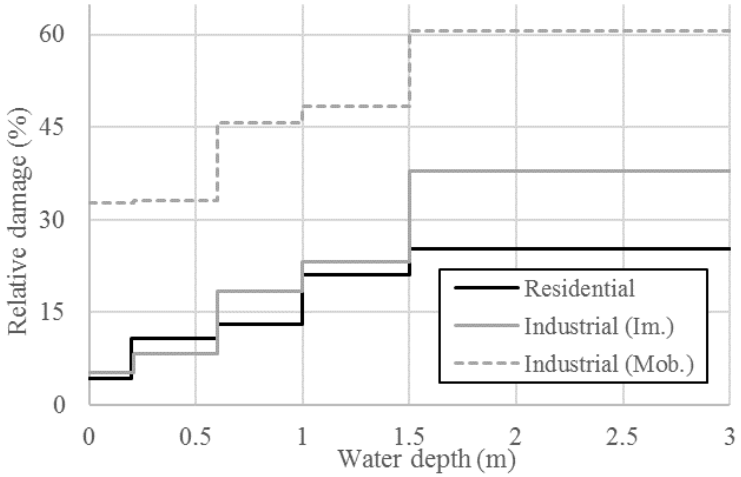

Figure 6-5 : FLEMO stage-damage functions for residential and industrial land use categories.

The determination of flood damage in monetary value requires the assignment of a specific value to the buildings. Beckers et al. (2013) used mobile and immobile values derived from ATKIS data (Muller 2000) and adapted from Germany to the Walloon region. In our study, the monetary values of residential and industrial buildings were chosen so that in the baseline scenario, the estimated flood damages are similar to those computed by Beckers et al. (2013) along the river

Meuse for a 100-year flood. We took identical monetary values for both residential and industrial categories and assume that immobile values are four times higher than mobile ones, which is close to the proportions in-between the values used by Beckers et al. (2013). In Table 6-5, the resulting immobile and mobile values are significantly higher than the values used by Beckers et al. (2013). This results from the type of elements for which the monetary values are assigned: parcels for Beckers et al. (2013) and buildings in this study.

	Beckers et al. (2013)		This study	
Element at risk	Parcel		Building	
	Immobile	Mobile	Immobile	Mobile
Residential	389 €/m^2	119 €/m^2	2000 €/m^2	500 €/m^2
Industry	343 €/m^2	90 €/m^2	2000 €/m^2	500 €/m^2

Table 6-5: Prices of the residential and industrial categories.

The United Nations define the risk as the combination of the probability of an event to occur and its negative consequences (UNISDR 2009). Considering N flood events with a return period T_i and causing a damage D_i, the risk R was evaluated by Ernst et al. (2010) as the expectation value of damage by the following expression:

$$R = \sum_{i=1}^{N} \left[\left(\frac{1}{T_{i-1}} - \frac{1}{T_i} \right) \frac{D_{i-1} + D_i}{2} \right] \quad (6\text{-}1)$$

In this study, Eq. (6-1) was computed based on the three return periods T_{25}, T_{50} and T_{100} without extrapolation neither to lower nor to higher return periods for which data are not available consistently for all the considered river reaches. It results that Eq. (6-1) gives an indicator of the flood risk and not the risk itself since the risk curve should be integrated over the entire range of flood probability. This indicator is however useful for the determination of the impact of urbanization on flood damage with a single scalar value representative of the damage occurring in-between the three return periods considered in this study.

6.3. Sensitivity analysis to the land use information

In this section, we investigate the sensitivity of the computed flood damage to (*i*) the number of building density classes, (*ii*) the rasterizing land use data and (*iii*) the source of the land use information. The analysis was performed along 14 reaches of the river Meuse (152 km in the Walloon region) for the baseline scenario.

6.3.1. Influence of the number of building density classes

As reported in section 6.2.2, the land use maps distinguish different classes of building density for the residential and industrial categories. Here, the sensitivity of the computed flood damage to the number of building density classes is assessed for flood discharges Q_{25} and Q_{100}. Using from 1 to 9 classes of building density for each land use category, the flood damage D_d computed with d classes of building density is compared to the results obtained with the highest number of classes of building density, using the following relative difference E_d:

$$E_d = \frac{D_d - D_9}{D_9} \qquad (6\text{-}2)$$

As shown in Figure 6-6, the computed flood damages are overestimated by 48% to 105% when a single class of building density is used. When the number of classes is increased, the value of the computed flood damage converges rapidly towards values close to D_9, and fluctuates slightly around this value. When 5 classes of building density are used, the relative error remains lower than 5% for the two flood discharges Q_{25} and Q_{100}. Beyond this number of classes, the relative difference E_d seems not to decrease significantly. For this reason, in the following of the study, we systematically use 5 classes of building density for each land use categories (residential and industrial).

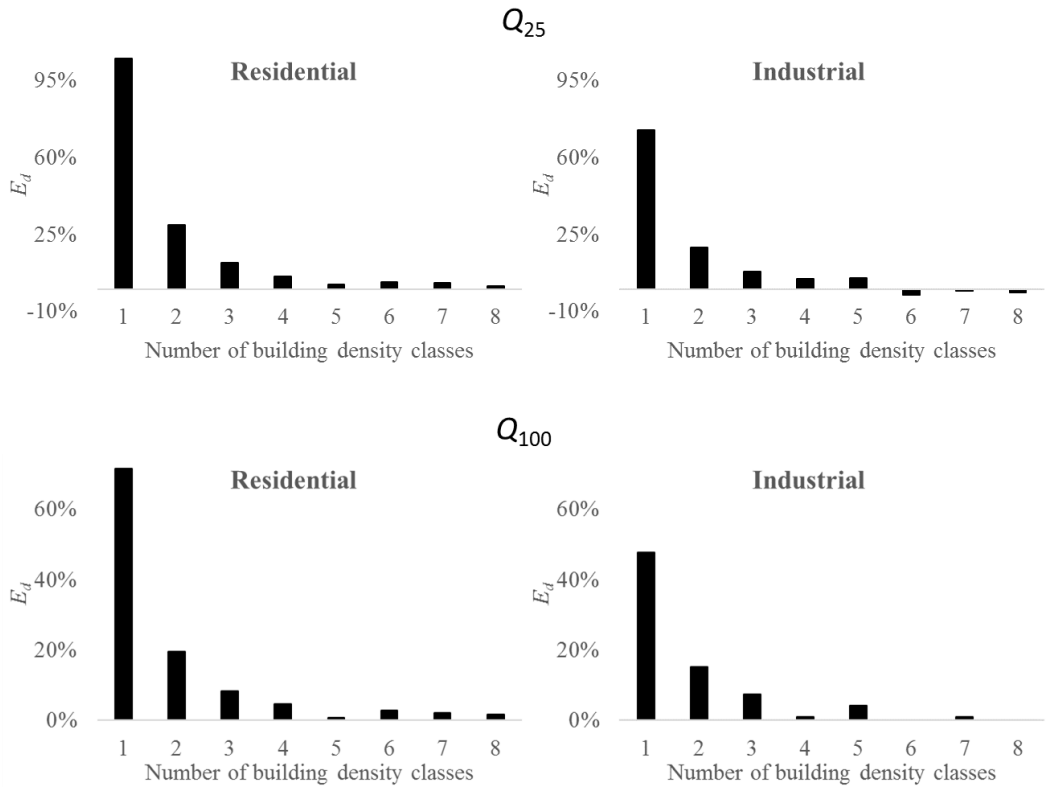

Figure 6-6 : Sensitivity of the total flood damage computed with different numbers of classes of building density, for flood discharges Q_{25} and Q_{100}.

6.3.2. Effect of rasterizing land use data

For the baseline scenario, micro-scale land use information is available through cadastral data (in vector form), giving the exact location of each building. This enables comparing flood damage estimates computed with the meso-scale land use maps used throughout this study to those obtained based on the original vector data. The meso-scale raster map (100×100 m^2) for the baseline scenario was built directly from these cadastral data, so that the comparison performed here focuses precisely on the effect of rasterizing land use data.

As shown in Table 6-6, the built-up inundated area is overestimated when it is evaluated based on the raster meso-scale data. The overestimation ranges in-between 6% and 26% depending on the flood scenario. The relative error on the built-up inundated area rises as the flood discharge decreases due to smaller built-up inundated area which are poorly captured when spread over relatively large raster cells. Similarly, the built-up inundated area for industrial buildings are not accurately captured at the meso-scale, whatever the considered flood scenario. This results from the particularly low share of industrial buildings in the floodplains (10 to 20% of the total built-up inundated area).

Flood discharge	Land use resolution	Residential	Industrial	Total
Q_{25}	Micro-scale	23 ha	2 ha	25 ha
	Meso-scale	28 ha	3 ha	31 ha
	Relative difference	**22%**	**79%**	**26%**
Q_{50}	Micro-scale	36 ha	4 ha	40 ha
	Meso-scale	39 ha	6 ha	45 ha
	Relative difference	**7%**	**62%**	**12%**
Q_{100}	Micro-scale	50 ha	6 ha	57 ha
	Meso-scale	53 ha	11 ha	64 ha
	Relative difference	**6%**	**68%**	**13%**
Q_{100}+30%	Micro-scale	373 ha	74 ha	447 ha
	Meso-scale	385 ha	91 ha	476 ha
	Relative difference	**3%**	**23%**	**6%**

Table 6-6: Built-up inundated area for different flood scenarios, computed based on micro- and meso- scale land use data (vector vs. raster).

At the meso-scale, the relative error E_i on the computed flood damage D_i in reach i is computed by:

$$E_i = \frac{D_{i,meso} - D_{i,micro}}{\sum_{k=1}^{14} D_{k,micro}} \qquad (6\text{-}3)$$

Consistently with the values in Table 6-6, Figure 6-7 shows that, for the flood scenarios corresponding to moderate events (Q_{25}), the computed flood damage is significantly affected by the type of land use data used, while this influence becomes very limited for the more severe flood scenario Q_{100} (relative errors of respectively 7% and 28% for the residential and industrial buildings). Over the different reaches of river Meuse, the results show strong variations in the relative error.

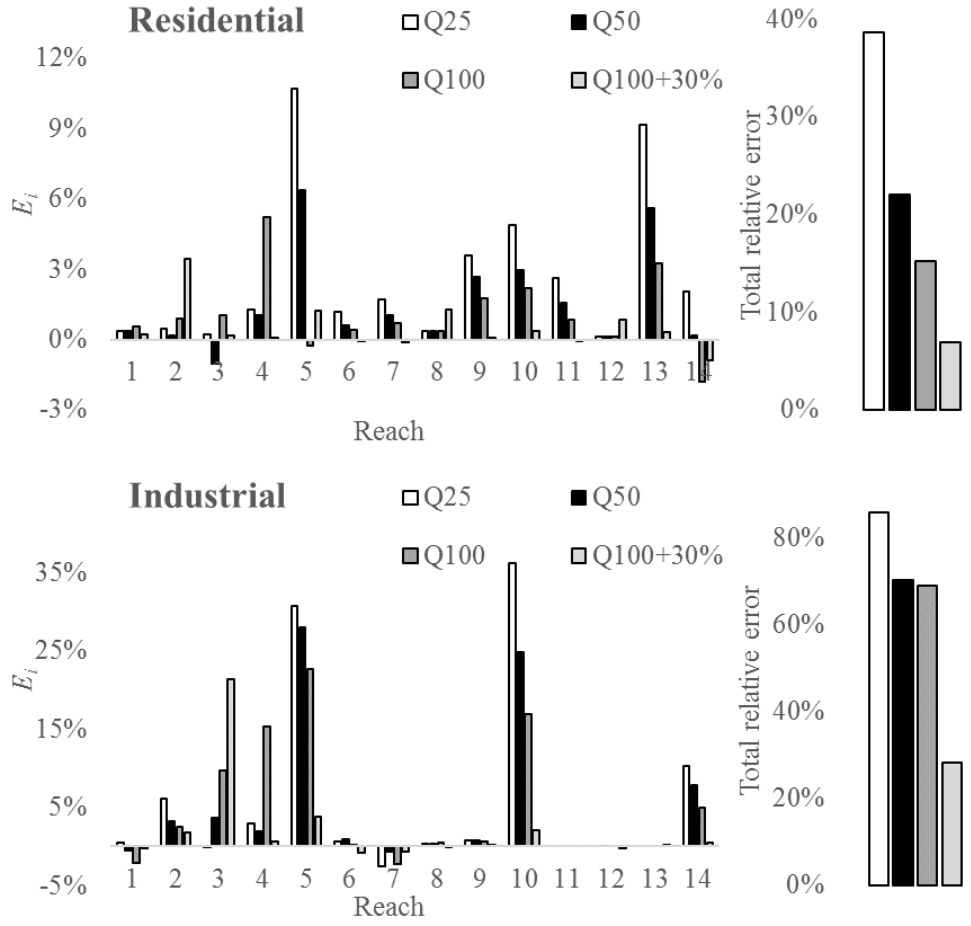

Figure 6-7 : Relative difference E_i on the computed flood discharge with the meso-scale land use data for residential and industrial buildings.

6.3.3. Influence of the source of land use information

Here, the flood damage computed with the land use map of this study are compared to those obtained with a land use registry database giving the location and geometry of land use parcels (Table 6-7), as used by Beckers et al. (2013).

	Land registry database	Land use map of this study
Resolution	1 :10.000	100 × 100 m^2
Type	Vector	Raster
Information	Land registry parcel	Building density class for the residential and industrial categories

Table 6-7: Comparison between different sources of land use information.

The monetary values were calibrated in section 6.2.4 to reproduce values close to those computed by Beckers et al. (2013) for the 100-year flood scenario. For this reason, the difference between

the flood damage computed with the two land use sources is very low for Q_{100} (Table 6-8). Also for other flood scenarios, the impact of the source of land use information on the flood damages remains lower than 20%. Comparing to the effect of rasterizing land use data (section 6.3.2), varying the source of the land use information seems here to have a lower influence. This result is consistent with the study of de Moel and Aerts (2011), who concluded that the source of land use information has a relatively modest effect on flood damages compared to other sources of uncertainty.

Flood discharge	Relative difference
Q_{25}	-19%
Q_{50}	-16%
Q_{100}	-1%

Table 6-8: Changes between the total flood damages computed with a land registry database (reference values) and with the land use map of this study.

6.4. Results and discussion

First, the flood damages computed for the baseline scenario are compared between the different sub-basins in section 6.4.1. In section 6.4.2, the influence of the uncertainty of the urbanization scenario on the results of the damage computation is investigated for the 2050 time horizon. Finally, the increase in future flood risk due to urbanization is quantified in section 6.4.3 for time horizons 2030, 2050, 2070 and 2100, and for urbanization scenarios selected based on the analysis of section 6.4.2.

The uncertainty in computed flood damage resulting from the type of land use information and from its limited resolution were shown to be substantial, particularly for moderate events such as flood discharge Q_{25} (sections 6.3.2 and 6.3.3). Although this effect decreases for higher flood discharges, the assessment of the flood damage in absolute monetary values should be interpreted with caution. For this reason, consistently with Moel and Aerts (2011), we prefer to use relative values of flood damage, taken as a percentage of a reference damage value (in the baseline scenario) computed with the same methodology.

6.4.1. Flood damage in the baseline scenario

Figure 6-8 shows the flood damages computed with the 2010 land use map for the Q_{25}, Q_{50} and Q_{100} flood discharges. The damage assigned to the residential category represents around 85% of the overall damage for the three flood discharges. The main results show that:

- the computed flood damages are the highest in the Meuse amont, Meuse aval and Ourthe sub-basins. This is consistent with the high number of sectors which are computed in these sub-basins (Figure 6-9).
- The flood damages in the Vesdre sub-basin are more than twice higher than in the Semois-Chiers, Lesse and Amblève sub-basins, despite a smaller sub-basin area and the existence of large reservoirs in the upper part of the Vesdre catchment. This result may be related to the population density, which is four to six times higher in the Vesdre sub-basin than in the other ones.
- In the Escaut district (Dyle-Gette, Senne, Dendre and Escaut-Lys sub-basins), the computed flood damages are the lowest, as only a limited number of sectors are computed.

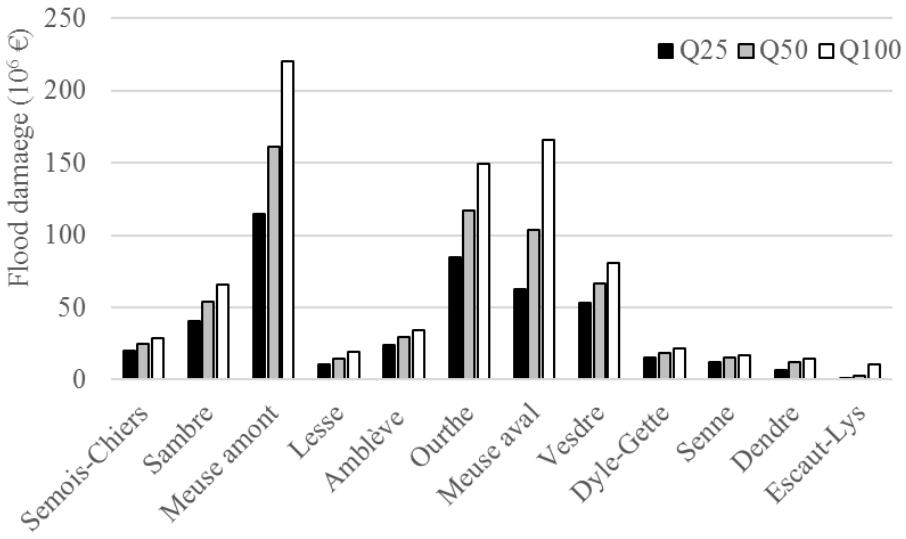

Figure 6-8 : Flood damages computed for the baseline scenario (2010 land use map).

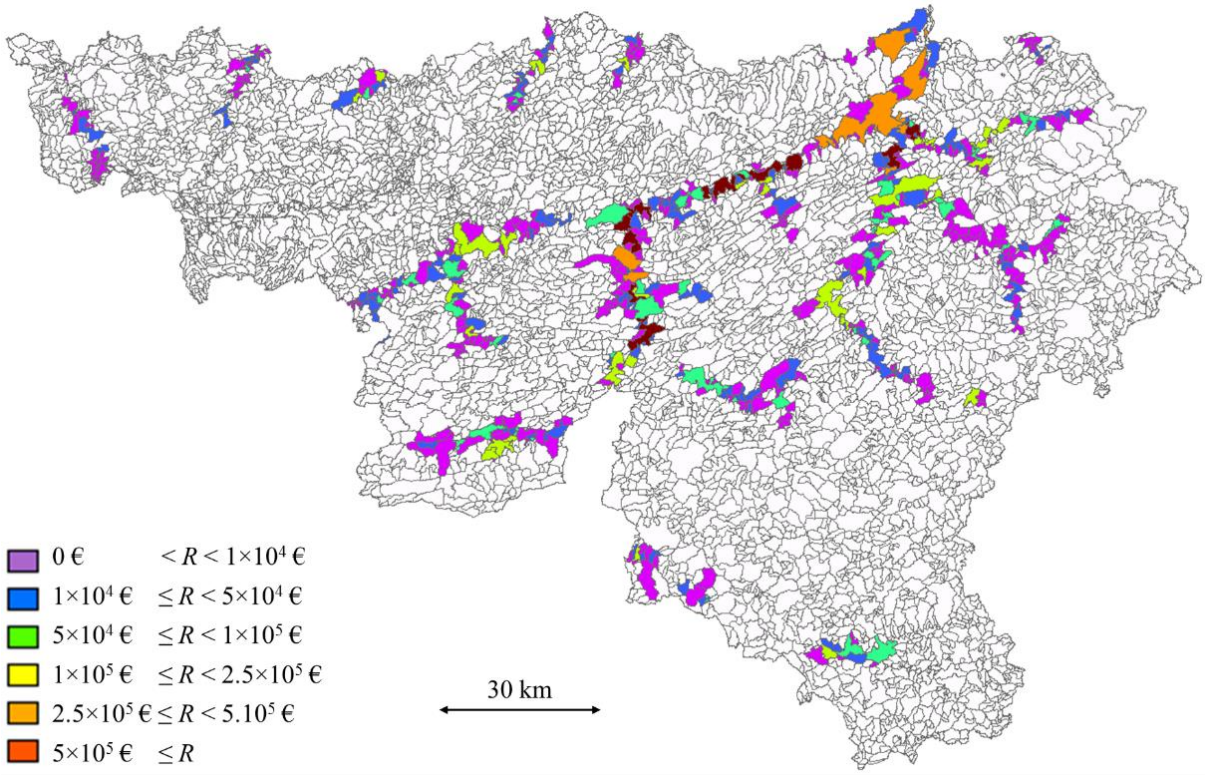

Figure 6-9 : Spatial distribution of flood risk indicator R over the hydrographic sectors for the baseline scenario.

6.4.2. Influence of all urbanization scenarios on future flood damage

In this section, the total flood damage is computed for the 2050 time horizon based on 18 different urbanization scenarios, as defined in section 6.2.2.

Compared to the baseline scenario, the increase in the total flood damage ranges in-between 3% and 49% for the 2050 time horizon (Table 6-9), depending on the urbanization scenario.

This relative increase in flood damage varies weakly with the considered flood discharge, whereas it differs significantly depending on the considered urbanization scenario. Indeed, for a given urbanization scenario, the increase in flood damage varies at most by one percentage point as a function of the computed flood discharge, except in the cases without banning on new developments for which the variations are around five percentage points.

The results show that banning new developments in flood-prone areas has a substantial impact on flood damage. A ban on new developments in flood-prone zones 2 and 3 would limit the increases in flood damage to roughly one fourth of their values obtained without any ban on new developments. Extending the ban to flood-prone zone 1 has a lower impact, but still it contributes to further mitigate the increases in flood damage.

In all cases with some degree of banning on new developments (resp. without banning on new developments), the densification policy leads flood damages from two to four percentage points (resp. from 10 to 16 percentage points) higher than the business as usual policy. The influence of the uncertainty related to the urbanization rate is lower than the effect of the urbanization policy (business as usual or densification). However, its impact remains significant since the increases in flood damage computed based on a low urbanization rate scenario are one to fifteen percentage points lower than those obtained with a high urbanization rate scenario.

	Urbanization rate	High			Medium			Low		
	Ban on new developments in flood-prone areas	Q_{25}	Q_{50}	Q_{100}	Q_{25}	Q_{50}	Q_{100}	Q_{25}	Q_{50}	Q_{100}
Business as usual	None	33%	30%	28%	29%	27%	25%	23%	21%	19%
	In zones 2 and 3	8%	7%	8%	6%	6%	7%	6%	5%	6%
	In all zones	5%	5%	5%	4%	4%	4%	4%	3%	4%
Densification	None	49%	45%	42%	40%	37%	35%	34%	32%	29%
	In zones 2 and 3	12%	11%	12%	10%	10%	11%	9%	8%	9%
	In all zones	9%	9%	8%	8%	8%	7%	7%	6%	6%

Table 6-9: Increase in the total flood damage for the 2050 time horizon based on different urbanization scenarios, compared to the baseline scenario. In grey: the urbanization scenarios used in section 6.4.3.

6.4.3. Impact of selected urbanization scenarios on future flood risk

In section 6.4.2, the range of variation of the increase in flood damage in 2050 was shown to be strongly influenced by the urbanization scenario. In this section, increases in flood risk are computed for the five following urbanization scenarios:

- densification policy (D) with a high urbanization rate (H) and no restriction on urbanization in flood-prone areas (scenario DH);
- business as usual policy (B) with a high urbanization rate and no restriction on urbanization in flood-prone areas (scenario BH);
- business as usual policy with a low urbanization rate (L) and no restriction on urbanization in flood-prone areas (scenario BL);
- business as usual policy with a low urbanization rate and a ban on new developments in flood-prone zones 2 and 3 (scenario BLR-23);
- business as usual policy with a low urbanization rate and a ban on new developments in all flood-prone zones (scenario BLR-123).

The firsts three scenarios (DH, BH and BL) are representative of the range of variation of the computed flood damages without restriction on urbanization in flood-prone areas. The

comparison of the last three scenarios (BL, BLR-23 and BLR-123) enables assessing the effect of restrictions on new developments in flood-prone areas.

Again, the results indicate a very high sensitivity of the computed changes in flood risk as a function of the urbanization scenario (Figure 6-10). The total increase in the flood risk indicator ranges respectively in-between 0-25%, 5-45%, 5-65% and 10-100% for the time horizons 2030, 2050, 2070 and 2100 depending on the urbanization scenario.

Without ban on new developments in flood-prone areas, the total flood risk indicator increases in-between 10-25%, 20-45%, 35-65% and 50-100% for respectively 2030, 2050, 2070 and 2100. Over all the time horizons, the increase in *total* flood risk is around twice higher for scenario DH than for BL. However, the distribution of the increases in flood risk in-between the different sub-basins varies substantially between the DH and BH scenarios, which correspond to the same urbanization rate, and with scenario BL.

For the densification scenario (DH), the changes in flood risk are higher in the sub-basins of the Meuse district than in the Escaut district. The Semois-Chiers, Lesse and Amblève sub-basins, weakly affected by floods in the baseline scenario (Figure 6-8) and characterized by a limited urbanization (Table 6-1), show high relative increases in flood risk as a result of urbanization. On contrary, the relative increases in flood risk are lower in the more densely urbanized Meuse aval and Vesdre sub-basins, already more affected by floods in the baseline scenario. In the Ourthe sub-basin, the results show both high flood risk in the baseline scenario and substantial increases as a result of urbanization. This may be a consequence of the relatively low population density in this sub-basin combined with the V-shape of the Ourthe valley, which tends to promote developments in the floodplains of the river Ourthe. In contrast, for the business as usual scenarios (BH and BL), the changes in flood risk are distinctively higher in the Escaut district than in the Meuse district.

For all sub-basins, restrictions on urbanization in flood-prone areas can be instrumental in mitigating the increases in flood risk due to urbanization. Banning new developments in flood-prone zones 2 and 3 (BLR-23) reduces the increases in flood risk by a factors in-between 3.5 and 4.3 compared to the scenario without restriction. Extending the ban to zone 1 also (BLR-123) leads to a reduction factor around 5.3-6.4. Most of the reduction in the future flood risk is obtained with a ban in flood-prone zones 2 and 3 (minus 36 percentage points on the total increase in flood risk for the 2100 time horizon compared to an extra reduction of just three percentage points when the ban is extended to flood-prone zone 1). The maximum increases in the flood risk

indicator over all the sub-basins are respectively 17% (6%), 22% (8%), 29% (11%) and 38% (17%) in 2030, 2050, 2070 and 2100 for the BLR-23 (BLR-123) scenario.

Along the Meuse river, Beckers et al. (2013) evaluated the increase in flood damage due to urbanization in-between 1 and 40% for a 100-year flood. In this study, the range of the increases in flood damage for Q_{100} is 5-30% for the business as usual scenarios, while a maximum increase by 75% is computed for the densification scenario (DH).

In addition to this discussion at the sub-basin level, the spatial distribution of the changes in flood risk for the PARIS sectors are displayed in Appendix H for the DH and BL scenarios (time horizons 2050 and 2100).

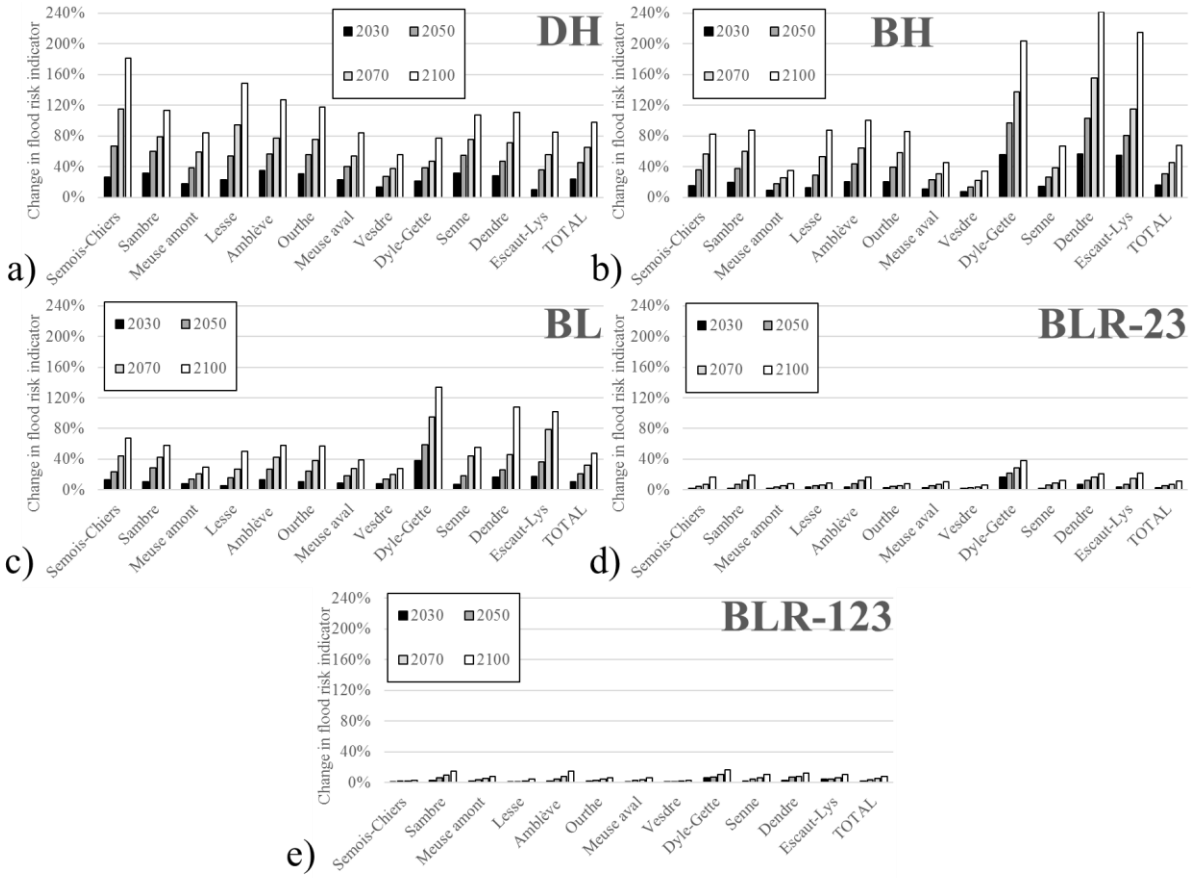

Figure 6-10 : Changes in flood risk indicator compared to baseline values for the (a) DH, (b) BH, (c) BL, (d) BLR-23 and (e) BLR-123 urbanization scenarios.

6.5. Conclusion

In this chapter, we investigate the influence of urbanization on future flood damage for several hundreds of kilometres of rivers throughout the Walloon Region, in Belgium, for flood discharges corresponding to return periods of 25, 50 and 100 years.

Future urbanization maps were generated using an original agent-based model considering topological (elevation, slope), neighbourhood (distance to roads, railway stations, cities and other buildings), land use policies and socio-economic (employment rate and wealth index) driving factors. The resulting maps give the spatial distribution of different building density classes for residential and industrial categories. Various scenarios were defined depending on the urbanization rate, on the type of urbanization considered (business as usual or densification) and on building regulation in flood-prone zones.

By means of sensitivity analysis, we showed the added-value of having land use maps containing subgrid information about the building density, and not just a binary information (urbanized vs. not urbanized).

The high uncertainty related to future urbanization has a strong influence on the computed flood damages and on their spatial distribution. Without considering any ban on urbanization in flood-prone areas, the increase in total flood damage varies by a factor of approximately two depending on the urbanization scenario. The sensitivity of the computed flood damage to the urbanization policy (business as usual vs. densification) is shown to be higher than to the urbanization rate itself. This highlights than spatial planning may have a substantial influence on future flood damage, even for a fixed urbanization rate.

For the time horizons 2030, 2050, 2070 and 2100, the increase in flood damage is evaluated to around, respectively, 10-20%, 20-45%, 30-65% and 50-100%. Banning new developments in flood-prone areas would enable a strong reduction of these increases: they would be reduced by a factor in-between 3.5 and 6.4 depending on the scenario.

Overall, the Meuse and Vesdre sub-basins show lower increases in flood damage compared to the relatively weakly urbanized Lesse, Amblève, Ourthe and Semois-Chier sub-basins in the baseline scenario, as well as in the Escaut district.

Finally, we acknowledge that the coarse resolution of the land use maps (100×100 m^2) and the assumption that flow characteristics does not change with the urbanization are two strong limitations of this study. Nonetheless, we believe that the main findings of this research are

contributions of significant relevance for sustainable flood risk management and that they pave the way for more flood-proof and resilient spatial planning.

CONCLUSION

World urban population will grow substantially over the coming decades. From 54% in 2014, the United Nations (2014) evaluate to around 66% the proportion of people living in urban areas in 2050. Among other consequences, this urbanization rate will result in increased flood risk. In this context, the overall objective of this research is a contribution to the evaluation of the influence of urbanization on future flood characteristics and flood damage.

Future urbanization affects inundation in many aspects and at different scales. For instance, while the impacts of the increase of the exposure of buildings to floods can be studied at a typical scale of 10^1-10^2 m, the modification of the flow field due to new buildings should consider the detailed location of these buildings. Additionally, a high level of uncertainty is related to the estimation of future urbanization. While the wide range of uncertainty can be taken into account by the analysis of a large number of future urban scenarios, the consideration of the modification of inundation flow for all the scenarios is challenging due to the computational cost of standard inundation models.

In section a, we summarize the different contributions and findings of this research. In section b, we acknowledge some limitations of this research and give perspectives for future works.

a. Contributions and findings

We developed an original porosity-based hydraulic model which enables a significant reduction of the computational cost for urban flood modelling (section a.1). This model makes possible the systematic analysis of the influence of building layouts on inundation flow through the computation of the flow variables for a wide range of urban geometries (section a.2). Finally, the impact of urbanization on future flood damage is analysed for the Walloon Region (section a.3).

a.1. Porosity-based hydraulic model

Different approaches exist to reduce the computational time of hydraulic models including parallelization, simplification of the mathematical model and coarsening of the mesh. Approaches involving subgrid models take advantage of the coarsening of the mesh in terms of computational efficiency while preserving the detailed geometric data to some extent. Among them, porosity-

based models preserve the fine scale topographic information by the use of porosity parameters reflecting their impacts on the computed variables at a coarser scale.

In section 1, we compare the different existing porosity-based models as well as their underlying assumptions, applicability ranges and definitions of the porosity parameters. The respective strengths and limitations are highlighted to identify the porosity-based model which is the most relevant for this research. Based on analysis of idealized and real-world urban networks, we show the added value of using anisotropic porosities to distinguish the impacts of obstacles on the reduction of the storage capacity in computational cells (storage porosity), from the alteration of flow conveyance along the cell edges (conveyance porosity). Additionally, the computation of the porosity parameters should be conducted at the grid-scale to reproduce more accurately the detailed topographic information, although it makes these parameters mesh-dependent.

An anisotropic porosity model was implemented in the existing model Wolf2D. In this context, additional developments were required to make this porosity model consistent with the specific flux-vector splitting method and the Cartesian grid of the existing model. Therefore, we discuss in section 2 the most appropriate formulations of pressure and bed slope terms so that their discretization complies with requirements arising from the flux-vector splitting technique of the model Wolf2D. In particular, we highlight the benefit of the divergence formulation of the bed slope term for the porosity model. Based on theoretical and numerical analyses for a wide range of flow conditions, an optimal discretization of this divergence formulation was found to minimize the numerical variations of specific energy. The methodology used for this study is of high practical relevance for the design of other numerical schemes.

Additionally; the impact of conveyance porosities in terms of energy balance is investigated theoretically in section 3 for a five cells numerical domain with sub-critical flow. The results show, for the first time, that the conveyance porosity parameters induce an overall numerical dissipation of specific energy. This loss of specific energy is higher for small conveyance porosities and high Froude numbers. While the dissipation of specific energy remains marginal for most flow conditions, it rises rapidly if the acceleration of the flow due to the conveyance porosity leads to a Froude number close to unity.

In section 4, we present the advanced anisotropic porosity-based model developed during this research. With his model, we made three main original contributions. First, we introduce a merging technique to deal with cells with low storage porosity values and save computational time. Second, we distinguish between two modelling scales depending on the size of the computational cells compared to the characteristic size of obstacles and flow ways. If the cell size

is lower than the urban characteristic size (meso-scale modelling), the conveyance porosity should be evaluated directly along the edges while, at the macro-scale modelling, the presence of nearby obstacles must also be considered. Third, we investigate the potential benefit of distinguishing the porosity parameters used in each term of the shallow-water equations. It was shown for an idealized urban network that benefits could indeed be obtained even if the estimation of all porosity parameters remains challenging in practice. The model was validated against four test cases covering a wide range of configurations and type of reference results (theoretical, numerical and experimental). Finally, the capacity of the porosity model to compute inundation flows at a coarse scale while maintaining a high degree of accuracy is shown in two applications: one at meso-scale and one at macro-scale. Compared to standard models computing inundation flows at a high resolution, the porosity-based model gives typical speedup values ranging in-between 10 and 100, depending on the relative sizes between the coarse and the fine scale, while the errors on water depths remain around few percent.

a.2. Influence of building layout on inundation flow

While a large number of existing studies analysed the influence of urbanization on inundations, the impact of the building layout of urbanized areas on the modification of the flow field is generally disregarded. The porosity-based model developed in this research offers a useful tool to explore this influence since it makes the computational time compatible with the computation of urban floods for a large number of urban patterns.

A unique set of 2,000 synthetics urban patterns covering a wide range of building layouts was generated with an urban procedural model by A. Mustafa in the context of the FloodLand project. Considering identical hydraulic conditions for each urban pattern, steady inundation flows were computed with the porosity-based model. This enabled for the first time a systematic analysis of the influence of several urban characteristics (street width, building coverage, distance between adjacent building, etc.) on inundation characteristics.

The results show that while the building coverage plays logically a major role regarding the inundation depths, the urban characteristics controlling the conveyance of the flow, like the distance in-between the buildings and the spatial distribution of the buildings, have also a significant impact. This suggests that the impact of future urbanization on the augmentation of inundation water depths could be effectively mitigated by the choice of a suitable building layout.

Besides the analysis performed in terms of urban characteristics directly relevant for urban stakeholders, we elaborated a conceptual model predicting the influence of urban layout on

inundation water depths from hydraulically-based characteristics. Consistently with the use of porosity parameters in porosity-based models to reproduce the detailed description of obstacles at a coarse scale, we found out that the augmentation of water depths can be accurately predicted from storage and conveyance porosity parameters evaluated at the scale of the urban district.

The findings of this first systematic analysis on the influence of building layout on inundation flow paves the way for more flood-proof urban design.

a.3. Influence of urbanization on future flood damage

In the context of the FloodLand project, an urban expansion model was developed by A. Mustafa. This model generates maps of future urbanization throughout the Walloon region, in Belgium, for time horizons up to 2100. At a mesh resolution of 100×100 m^2, these maps give the spatial distribution of several classes of building density, for residential and industrial buildings. The uncertainties on future urbanization is handled through the consideration of different urbanization scenarios.

These land use maps are used in combination with existing inundation maps in a flood damage model to study the impact of urbanization on future flood damage for several hundreds of kilometres of rivers in the Walloon region and for flood events corresponding to return periods of 25, 50 and 100 years. First, we demonstrated the benefit of defining different building density classes as subgrid land use information for the computation of flood damage. Then, the results show the high impact of the uncertainty in future urbanization on the computed flood damages and their spatial distributions. Indeed, the increase in total flood damages can vary by a factor around 2 depending on the urbanization scenario. Without any building regulation in flood-prone areas, the flood damages are expected to increase in-between 20-45% for 2050 and 50-100% in 2100 compared to the current situation. Banning new developments in flood-prone areas enables a strong mitigation of these increases in flood damage. Finally, this research investigates for the first time the spatial distribution of the increase in flood damage throughout the Walloon region. This spatially distributed information could be used by stakeholders to guide future flood-proof urbanization.

b. Limitations and perspectives

Four years is definitively not enough to tackle all urgent questions on the topic of the thesis without leaving behind some limitations or perspectives of future work.

The main limitations and perspectives of the conducted research are presented in the following sections. While some of them could be addressed in the near-future, others are more fundamental since they are related to a lack of data or to the present research possibilities.

b.1. Porosity-based hydraulic model

We identify five main limitations and perspectives for improvements in the porosity-based hydraulic model developed during this research.

First, we used depth-independent porosity parameters. This requires the treatment of the topographic information to identify the obstacles sufficiently high for not being overtopped by the flood. Özgen et al. (2016a, 2016b) derived recently a porosity model with depth-dependent porosity parameters but they only used their model to compute flows over low-level obstacles (micro-topography). It is of high interest to explore the possibility to reproduce the submersion of higher level obstacles like buildings with such depth-dependent porosity model.

Although we highlight the potential benefit of distinguishing different porosity parameters for each term of the governing equations to reproduce optimally the impacts of the obstacles, it misses today a generalization of this approach for real-world application. To fill that gap, further work is needed to analyse the complex impact of the fine-scale obstacles on the coarse-scale flow field. The recent contribution by Guinot et al. (2017) paves the way in this direction, by distinguishing different porosity parameters for the advective terms of the governing equations in its dual integral porosity model.

Third, while the computation of inundation flow at a macro-scale was shown to reproduce the inundation water depths with a good level of accuracy, the complex distribution of the dynamic variables is poorly represented at this scale. This is more a limitation of the porosity model than a perspective for future improvements. Similarly, more knowledge on the anisotropic porosity models could be gained through a deeper analysis of the energy conservation properties of the numerical schemes in the presence of spatially-varying porosity parameters. This would also lead to the design of enhanced energy-balanced numerical techniques for discretizing the anisotropic porosity model.

Fourthly, the porosity model presented in this manuscript does not enable multiple flow paths within a single computational cell. A promising technique was introduced by Chen et al. (2012b) to consider such complex flow fields with a multi-layered grid approach; but it was tested only for applications in urban hydrology (rain-fed flow conditions).

Finally, we acknowledge that we mainly used the porosity-based model for flows in subcritical flow regimes. Additional tests should be done to assess the porosity model in a wider range of applications, including fast transients.

b.2. Influence of building layout on inundation flow

In this research, we investigated the influence of building layout on inundation flows for one specific configuration with (*i*) a steady flow, (*ii*) in subcritical regime, (*iii*) on a horizontal bottom and (*iv*) for a single flood discharge. This has several consequences.

- The findings of the study are only valid for long-duration floods typical of lowland rivers (e.g. Rhine, Meuse, etc.). Additional work should be conducted to assess the influence of urban geometry under unsteady flows like flash-floods or short duration floods. This requires generally a higher computational time and a methodology for analysing the time-varying computed flow variables.
- Most long-duration floods are sub-critical in lowland rivers. However, the influence of building layout on flood could be investigated for floodplains with steep slopes for which super-critical flow occur. The findings are expected to differ substantially (e.g., effect of street orientation and curvature).
- The validity of our conclusions should be confirmed by testing a wider range of flood discharges.

Moreover, some improvements of the models would enable considering additional processes.

- In this research, we do not consider the transient impact of the water entering in the buildings which are normally not impervious to water. This could be taken into account in the porosity-based models by an introduction of a storage capacity collecting water during the flood rising limb and releasing it during the receding period.
- Different land use categories like parks, garden, etc. could be distinguished in the urban procedural model. In this way, a spatial distribution of roughness coefficients and coefficients of infiltration would improve the representation of urban areas.
- While it could be reasonably assumed that the capacity of the drainage system is full for long-duration flows, this should be reconsidered for unsteady flows.

b.3. Influence of urbanization on future flood damage

The major limitations of this study are (*i*) the coarse size of the land use maps (100 × 100 m^2) which exacerbates the uncertainties related to the computed flood damages and (*ii*) the assumption that the flow characteristics do not evolve with the urbanization.

The first limitation arises from the uncertainty related to future urbanization which does not enable generating future land use maps up to 2100 at a more detailed spatial scale with an acceptable level of reliability.

The second limitation is intrinsically linked to the first one since inundation characteristics are dependent on detailed topographic data at the scale of few meters. An option could be to take benefit from the relationships derived in section 5 between the building-coverage and the augmentation of inundation water depths. However, the conveyance characteristics of the urban areas are not provided by the urbanization model while they were shown to have a significant influence on the inundation water depths.

The outcomes of this basic research pave the way for more policy-oriented analyses, which are particularly timely and of high societal relevance since local, regional and national policies have generally a more direct influence on spatial planning than they have on global climate evolution.

BIBLIOGRAPHY

Alcrudo, S. F. Soares-Frazão. 1999. Conclusions from the 1st CADAM meeting - Wallingford UK. Concerted Action on Dam-Break Modeling – Proc. CADAM meeting, Wallingford, United Kingdom 2 and 3 March 1998, European Commission, Brussels.

An, H., S. Yu, G. Lee, and Y. Kim. 2015. Analysis of an open source quadtree grid shallow water flow solver for flood simulation. Quaternary International 384:118–128.

Araud, Q. 2012. Simulation des écoulements en milieu urbain lors d'un événement pluvieux extrême [in French]. . Université de Strasbourg.

Arrault, A., P. Finaud-Guyot, P. Archambeau, M. Bruwier, S. Erpicum, M. Pirotton, and B. Dewals. 2016. Hydrodynamics of long-duration urban floods: Experiments and numerical modelling. Natural Hazards and Earth System Sciences 16:1413–1429.

Aureli, F., A. Maranzoni, and P. Mignosa. 2014. A semi-analytical method for predicting the outflow hydrograph due to dam-break in natural valleys. Advances in Water Resources 63:38–44.

Aureli, F., A. Maranzoni, P. Mignosa, and C. Ziveri. 2008. A weighted surface-depth gradient method for the numerical integration of the 2D shallow water equations with topography. Advances in Water Resources 31:962–974.

Bates, P. D. 2000. Development and testing of a subgrid-scale model for moving-boundary hydrodynamic problems in shallow water. Hydrological Processes 14:2073–2088.

Bates, P. D., M. S. Horritt, and T. J. Fewtrell. 2010. A simple inertial formulation of the shallow water equations for efficient two-dimensional flood inundation modelling. Journal of Hydrology 387:33–45.

Bates, P. D., K. J. Marks, and M. S. Horritt. 2003. Optimal use of high-resolution topographic data in flood inundation models. Hydrological Processes 17:537–557.

Bazin, P.-H. 2013. Flows during floods in urban areas : influence of the detailed topography and exchanges with the sewer system. . Université Claude Bernard - Lyon I.

Bazin, P.-H., E. Mignot, and A. Paquier. 2016. Computing flooding of crossroads with obstacles using a 2D numerical model. Journal of Hydraulic Research:1–13.

Bear, J. 2013. Dynamics of Fluids in Porous Media. . Courier Corporation.

Beckers, A., B. Dewals, S. Erpicum, S. Dujardin, S. Detrembleur, J. Teller, M. Pirotton, and P. Archambeau. 2013. Contribution of land use changes to future flood damage along the river Meuse in the Walloon region. Natural Hazards and Earth System Sciences 13:2301–2318.

Begnudelli, L., and B. F. Sanders. 2006. Unstructured grid finite-volume algorithm for shallow-water flow and scalar transport with wetting and drying. Journal of Hydraulic Engineering 132:371–384.

Bermúdez, A., A. Dervieux, J.-A. Desideri, and M. E. Vázquez. 1998. Upwind schemes for the two-dimensional shallow water equations with variable depth using unstructured meshes. Computer Methods in Applied Mechanics and Engineering 155:49–72.

Bettaieb, M. B., O. Débordes, A. Dogui, and L. Dûchene. 2012. Averaging properties for periodic homogenization and large deformation. International Journal for Multiscale Computational Engineering 10:281–293.

Brodtkorb, A. R., M. L. Sætra, and M. Altinakar. 2012. Efficient shallow water simulations on GPUs: Implementation, visualization, verification, and validation. Computers and Fluids 55:1–12.

Bruwier, M., P. Archambeau, S. Erpicum, M. Pirotton, and B. Dewals. 2016. Discretization of the divergence formulation of the bed slope term in the shallow-water equations and consequences in terms of energy balance. Applied Mathematical Modelling 40:7532–7544.

Bruwier, M., P. Archambeau, S. Erpicum, M. Pirotton, and B. Dewals. 2017a. Shallow-water models with anisotropic porosity and merging for flood modelling on Cartesian grids. Journal of Hydrology.

Bruwier, M., S. Erpicum, P. Archambeau, M. Pirotton, and B. Dewals. 2014. Mathematical formulation of shallow water models with porosity for urban flood modelling. Proceeding of the ICHE 2014 Conference, Hamburg, Germany, 28 September - 2 October.

Bruwier, M., S. Erpicum, P. Archambeau, M. Pirotton, and B. Dewals. 2017b. Discussion of "Computing flooding of crossroads with obstacles using a 2D numerical model" by P.-H. Bazin, E. Mignot and A. Paquier. Journal of Hydraulic Research.

Bruwier, M., S. Erpicum, M. Pirotton, P. Archambeau, and B. J. Dewals. 2015. Assessing the operation rules of a reservoir system based on a detailed modelling chain. Natural Hazards and Earth System Sciences 15:365–379.

Bruwier, M., A. Mustafa, D. G. Aliaga, S. Erpicum, P. Archambeau, G. Nishida, X. Zhang, M. Pirotton, and B. Dewals. 2017c. Influence of urban patterns of flooding. Proceeding of the 37th IAHR World Congress, Kuala Lumpur, Malaysia, August 13 - 18.

Cammerer, H., A. H. Thieken, and P. H. Verburg. 2013. Spatio-temporal dynamics in the flood exposure due to land use changes in the Alpine Lech Valley in Tyrol (Austria). Natural Hazards 68:1243–1270.

Camnasio, E., S. Erpicum, P. Archambeau, M. Pirotton, and B. Dewals. 2014. Prediction of mean and turbulent kinetic energy in rectangular shallow reservoirs. Engineering Applications of Computational Fluid Mechanics 8:586–597.

Canelas, R., J. Murillo, and R. M. L. Ferreira. 2013. Two-dimensional depth-averaged modelling of dam-break flows over mobile beds. Journal of Hydraulic Research 51:392–407.

Castro-Orgaz, O., J. V. Giráldez, and J. L. Ayuso. 2008. Energy and momentum under critical flow conditions. Journal of Hydraulic Research 46:844–848.

Causon, D. M., D. . Ingram, and C. G. Mingham. 2001. A Cartesian cut cell method for shallow water flows with moving boundaries. Advances in Water Resources 24:899–911.

Causon, D. M., D. M. Ingram, C. G. Mingham, G. Yang, and R. V. Pearson. 2000. Calculation of shallow water flows using a Cartesian cut cell approach. Advances in Water Resources 23:545–562.

Cea, L., M. Garrido, and J. Puertas. 2010. Experimental validation of two-dimensional depth-averaged models for forecasting rainfall-runoff from precipitation data in urban areas. Journal of Hydrology 382:88–102.

Cea, L., and M. E. Vázquez-Cendón. 2010. Unstructured finite volume discretization of two-dimensional depth-averaged shallow water equations with porosity. International Journal for Numerical Methods in Fluids 63:903–930.

Chanson, H. 2009. Application of the method of characteristics to the dam break wave problem. Journal of Hydraulic Research 47:41–49.

Chaudhry, H. 1993. Open-channel flow. . Englewood Cliffs, NJ: Prentice Hall.

Chen, A. S., B. Evans, S. Djordjević, and D. A. Savić. 2012a. A coarse-grid approach to representing building blockage effects in 2D urban flood modelling. Journal of Hydrology 426–427:1–16.

Chen, A. S., B. Evans, S. Djordjević, and D. A. Savić. 2012b. Multi-layered coarse grid modelling in 2D urban flood simulations. Journal of Hydrology 470–471:1–11.

Chen, Y., H. Zhou, H. Zhang, G. Du, and J. Zhou. 2015. Urban flood risk warning under rapid urbanization. Environmental Research 139:3–10.

Choi, S.-U., and M. H. Garcia. 2002. k-ε turbulence modeling of density currents developing two dimensionally on a slope. Journal of Hydraulic Engineering 128:55–63.

Costabile, P., and F. Macchione. 2015. Enhancing river model set-up for 2-D dynamic flood modelling. Environmental Modelling and Software 67:89–107.

Costanza-Robinson, M. S., B. D. Estabrook, and D. F. Fouhey. 2011. Representative elementary volume estimation for porosity, moisture saturation, and air-water interfacial areas in unsaturated porous media: Data quality implications. Water Resources Research 47.

Defina, A. 2000. Two-dimensional shallow flow equations for partially dry areas. Water Resources Research 36:3251–3264.

Delestre, O., S. Cordier, F. Darboux, and F. James. 2012. A limitation of the hydrostatic reconstruction technique for Shallow Water equations. Comptes Rendus Mathematique 350:677–681.

Detrembleur, S., F. Stilmant, B. Dewals, S. Erpicum, P. Archambeau, and M. Pirotton. 2015. Impacts of climate change on future flood damage on the river Meuse, with a distributed uncertainty analysis. Natural Hazards 77:1533–1549.

Dewals, B. J., S. A. Kantoush, S. Erpicum, M. Pirotton, and A. J. Schleiss. 2008. Experimental and numerical analysis of flow instabilities in rectangular shallow basins. Environmental Fluid Mechanics 8:31–54.

DGO3, S. 2015a. District hydrographique international de l'Escaut : Projet de Plan de Gestion des Risques d'Inondation en Wallonie [in French]. . Ministère de la Région Wallone.

DGO3, S. 2015b. Rapport d'incidences environnementales du Plan de Gestion des Risques d'Inondation en Wallonie (PGRI) du district hydrographique international de la Meuse [in French]. . Ministère de la Région Wallone.

Dottori, F., G. Di Baldassarre, and E. Todini. 2013. Detailed data is welcome, but with a pinch of salt: Accuracy, precision, and uncertainty in flood inundation modeling. Water Resources Research 49:6079–6085.

Drogue, G., L. Pfister, T. Leviandier, A. El Idrissi, J.-F. Iffly, P. Matgen, J. Humbert, and L. Hoffmann. 2004. Simulating the spatio-temporal variability of streamflow response to climate change scenarios in a mesoscale basin. Journal of Hydrology 293:255–269.

Drugan, W. J., and J. R. Willis. 1996. A micromechanics-based nonlocal constitutive equation and estimates of representative volume element size for elastic composites. Journal of the Mechanics and Physics of Solids 44:497–524.

Eaton, T. T. 2006. On the importance of geological heterogeneity for flow simulation. Sedimentary Geology 184:187–201.

El Kadi Abderrezzak, K., A. Paquier, and B. Gay. 2008. One-dimensional numerical modelling of dam-break waves over movable beds: Application to experimental and field cases. Environmental Fluid Mechanics 8:169–198.

El Kadi Abderrezzak, K., A. Paquier, and E. Mignot. 2009. Modelling flash flood propagation in urban areas using a two-dimensional numerical model. Natural Hazards 50:433–460.

Elmer, F., J. Hoymann, D. Düthmann, S. Vorogushyn, and H. Kreibich. 2012. Drivers of flood risk change in residential areas. Natural Hazards and Earth System Science 12:1641–1657.

Ernst, J., B. J. Dewals, S. Detrembleur, P. Archambeau, S. Erpicum, and M. Pirotton. 2010. Micro-scale flood risk analysis based on detailed 2D hydraulic modelling and high resolution geographic data. Natural Hazards 55:181–209.

Erpicum, S. 2006. Optimisation objective de paramètres en écoulements turbulents à surface libre sur maillage multibloc. . University of Liege (ULG), Belgium.

Erpicum, S., P. Archambeau, B. Dewals, S. Detrembleur, and M. Pirotton. 2006. Fluid-structure interaction modeling with a coupled 1D-2D free surface flow solver. Proceedings of Riverflow 2006.

Erpicum, S., B. Dewals, P. Archambeau, and M. Pirotton. 2010a. Dam-break flow computation based on an efficient flux-vector splitting. Journal of Computational and Applied Mathematics 234:2143–2151.

Erpicum, S., B. J. Dewals, P. Archambeau, S. Detrembleur, and M. Pirotton. 2010b. Detailed inundation modelling using high resolution DEMs. Engineering Applications of Computational Fluid Mechanics 4:196–208.

Field, W. G., M. F. Lambert, and B. J. Williams. 1998. Energy and momentum in one dimensional open channel flow. Journal of Hydraulic Research 36:29–42.

Finaud-Guyot, P., C. Delenne, J. Lhomme, V. Guinot, and C. Llovel. 2010. An approximate-state Riemann solver for the two-dimensional shallow water equations with porosity. International Journal for Numerical Methods in Fluids 62:1299–1331.

Gaines, J. M. 2016. Flooding: Water potential. Nature 531:S54–S55.

Garcia-Navarro, P., and M. E. Vazquez-Cendon. 2000. On numerical treatment of the source terms in the shallow water equations. Computers and Fluids 29:951–979.

Ghostine, R., I. Hoteit, J. Vazquez, A. Terfous, A. Ghenaim, and R. Mose. 2015. Comparison between a coupled 1D-2D model and a fully 2D model for supercritical flow simulation in crossroads. Journal of Hydraulic Research 53:274–281.

Gray, W. G., and S. M. Hassanizadeh. 1989. Averaging theorems and averaged equations for transport of interface properties in multiphase systems. International Journal of Multiphase Flow 15:81–95.

Guinot, V. 2012. Multiple porosity shallow water models for macroscopic modelling of urban floods. Advances in Water Resources 37:40–72.

Guinot, V., B. F. Sanders, and J. E. Schubert. 2017. Dual integral porosity shallow water model for urban flood modelling. Advances in Water Resources 103:16–31.

Guinot, V., and S. Soares-Frazão. 2006. Flux and source term discretization in two-dimensional shallow water models with porosity on unstructured grids. International Journal for Numerical Methods in Fluids 50:309–345.

Haaland, S. E. 1983. Simple and explicit formulas for the friction factor in turbulent flow. Journal of Fluids Engineering, Transactions of the ASME 105:89–90.

Hager, W. H. 2010. Wastewater hydraulics: Theory and practice: Second edition. Pages 1–652 Wastewater Hydraulics: Theory and Practice: Second Edition. . Heidelberg: Springer.

Han, Y., and H. Jia. 2017. Simulating the spatial dynamics of urban growth with an integrated modeling approach: A case study of Foshan, China. Ecological Modelling 353:107–116.

Hannaford, J., and T. J. Marsh. 2008. High-flow and flood trends in a network of undisturbed catchments in the UK. International Journal of Climatology 28:1325–1338.

Haque, M. I. 2015. Mechanics of groundwater in porous media. (T. & F. Group, Ed.). . CRC Press.

Hervouet, J.-M. 2003. Hydrodynamique des écoulements à surface libre. . Presses de l'Ecole Nationale des Ponts et Chaussees, Paris, France.

Hervouet, J.-M., R. Samie, and B. Moreau. 2000. Modelling urban areas in dam-break flood-wave numerical simulations. Proceedings of the International Seminar and Workshop on Rescue Actions Based on Dam-Break Flood Analysis 1st–16th October 2000, Seinajoki, Finland.

Hou, J., Q. Liang, F. Simons, and R. Hinkelmann. 2013a. A 2D well-balanced shallow flow model for unstructured grids with novel slope source term treatment. Advances in Water Resources 52:107–131.

Hou, J., F. Simons, M. Mahgoub, and R. Hinkelmann. 2013b. A robust well-balanced model on unstructured grids for shallow water flows with wetting and drying over complex topography. Computer Methods in Applied Mechanics and Engineering 257:126–149.

Hsu, H.-C., A. Torres-Freyermuth, T.-J. Hsu, H.-H. Hwung, and P.-C. Kuo. 2014. On dam-break wave propagation and its implication to sediment erosion. Journal of Hydraulic Research 52:205–218.

Huang, C.-J., M.-H. Hsu, W.-H. Teng, and Y.-H. Wang. 2014. The impact of building coverage in the metropolitan area on the flow calculation. Water (Switzerland) 6:2449–2466.

Hubbard, M. E. 1999. Multidimensional Slope Limiters for MUSCL-Type Finite Volume Schemes on Unstructured Grids. Journal of Computational Physics 155:54–74.

Jenks, G. F., and F. C. Caspall. 1971. Error on Choroplethic Maps: Definition, Measurement, Reduction. Annals of the American Association of Geographers 61:217–244.

Kanit, T., S. Forest, I. Galliet, V. Mounoury, and D. Jeulin. 2003. Determination of the size of the representative volume element for random composites: Statistical and numerical approach. International Journal of Solids and Structures 40:3647–3679.

Kesserwani, G. 2013. Topography discretization techniques for Godunov-type shallow water numerical models: A comparative study. Journal of Hydraulic Research 51:351–367.

Kim, B., B. F. Sanders, J. S. Famiglietti, and V. Guinot. 2015. Urban flood modeling with porous shallow-water equations: A case study of model errors in the presence of anisotropic porosity. Journal of Hydrology 523:680–692.

Kim, B., B. F. Sanders, J. E. Schubert, and J. S. Famiglietti. 2014. Mesh type tradeoffs in 2D hydrodynamic modeling of flooding with a Godunov-based flow solver. Advances in Water Resources 68:42–61.

Kim, H.-J., and Y.-S. Cho. 2011. Numerical model for flood routing with a Cartesian cut-cell domain. Journal of Hydraulic Research 49:205–212.

Kreibich, H., J. C. J. M. Van Den Bergh, L. M. Bouwer, P. Bubeck, P. Ciavola, C. Green, S. Hallegatte, I. Logar, V. Meyer, R. Schwarze, and A. H. Thieken. 2014. Costing natural hazards. Nature Climate Change 4:303–306.

Kreibich, H., I. Seifert, B. Merz, and A. H. Thieken. 2010. Development of FLEMOcs - a new model for the estimation of flood losses in the commercial sector [Développement de FLEMOcs - un nouveau modèle pour l'estimation des dommages dus aux inondations dans le secteur commercial]. Hydrological Sciences Journal 55:1302–1314.

Kundzewicz, Z. W., U. Ulbrich, T. Brücher, D. Graczyk, A. Krüger, G. C. Leckebusch, L. Menzel, I. Pińskwar, M. Radziejewski, and M. Szwed. 2005. Summer floods in Central Europe - Climate change track? Natural Hazards 36:165–189.

Lauber, G., and W. H. Hager. 1998a. Experiments to dambreak wave: Horizontal channel. Journal of Hydraulic Research 36:291–306.

Lauber, G., and W. H. Hager. 1998b. Experiments to dambreak wave: Sloping channel. Journal of Hydraulic Research 36:761–772.

Lehmann, J., D. Coumou, and K. Frieler. 2015. Increased record-breaking precipitation events under global warming. Climatic Change 132:501–515.

LeVeque, R. J. 1998. Balancing Source Terms and Flux Gradients in High-Resolution Godunov Methods: The Quasi-Steady Wave-Propagation Algorithm. Journal of Computational Physics 146:346–365.

Lhomme, J. 2006. Modélisation des inondations en milieu urbain: approches unidimensionnelle, bidimensionnelle et macroscopique. . Université de Montpellier II.

Liang, Q., and F. Marche. 2009. Numerical resolution of well-balanced shallow water equations with complex source terms. Advances in Water Resources 32:873–884.

Lin, E., K. Shaad, and C. Girot. 2016. Developing river rehabilitation scenarios by integrating landscape and hydrodynamic modeling for the Ciliwung River in Jakarta, Indonesia. Sustainable Cities and Society 20:180–198.

Liu, D. 2016. Water supply: China's sponge cities to soak up rainwater. Nature 537:307.

Long, Y., H. Han, S.-K. Lai, and Q. Mao. 2013. Urban growth boundaries of the Beijing Metropolitan Area: Comparison of simulation and artwork. Cities 31.

Mallakpour, I., and G. Villarini. 2015. The changing nature of flooding across the central United States. Nature Climate Change 5:250–254.

McMillan, H. K., and J. Brasington. 2007. Reduced complexity strategies for modelling urban floodplain inundation. Geomorphology 90:226–243.

Merz, B., A. H. Thieken, and M. Gocht. 2007. Flood Risk Mapping At The Local Scale: Concepts and Challenges. Pages 231–251 *in* S. Begum, M. J. F. Stive, and J. W. Hall, editors. Flood Risk Management in Europe: Innovation in Policy and Practice. . Springer Netherlands, Dordrecht.

Messner, F., E. C. Pennning Rowsell, C. Green, M. V., T. S.M., and van der Veen A. 2007. Evaluating flood damages: guidance and recommendations on principles and practices. Pages 1–178. . FLOODsite.

Mignot, E., and R. Cienfuegos. 2009. On the application of a Boussinesq model to river flows including shocks. Coastal Engineering 56:23–31.

Mignot, E., A. Paquier, and S. Haider. 2006. Modeling floods in a dense urban area using 2D shallow water equations. Journal of Hydrology 327:186–199.

Mignot, E., C. Zeng, G. Dominguez, C.-W. Li, N. Rivière, and P.-H. Bazin. 2013. Impact of topographic obstacles on the discharge distribution in open-channel bifurcations. Journal of Hydrology 494:10–19.

Moel, H., and J. C. J. H. Aerts. 2011. Effect of uncertainty in land use, damage models and inundation depth on flood damage estimates. Natural Hazards 58:407–425.

Mohamed, K. 2014. A finite volume method for numerical simulation of shallow water models with porosity. Computers and Fluids 104:9–19.

Munich Re. 2010. Topics Geo, Natural catastrophes 2009: analyses, assessments, positions. . Munich: Munich Reinsurance Company.

Munson, B. R., D. F. Young, and T. H. Okiishi. 2006. Fundamentals of Fluid Mechanics, 5th edition. John Wiley & Sons.

Murillo, J., and P. García-Navarro. 2013. Energy balance numerical schemes for shallow water equations with discontinuous topography. Journal of Computational Physics 236:119–142.

Murillo, J., and P. García-Navarro. 2014. Accurate numerical modeling of 1D flow in channels with arbitrary shape. Application of the energy balanced property. Journal of Computational Physics 260:222–248.

Mustafa, A., M. Bruwier, J. Teller, P. Archambeau, S. Erpicum, M. Pirotton, and B. Dewals. 2016. Impacts of urban expansion on future flood damage: A case study in the River Meuse basin, Belgium. Sustainable Hydraulics in the Era of Global Change: Proceedings of the 4th IAHR Europe Congress. . CRC Press.

Nujić, M. 1995. Efficient implementation of non-oscillatory schemes for the computation of free-surface flows [Développement de schémas numériques performants non oscillatoires pour les écoulements à surface libre]. Journal of Hydraulic Research 33:101–111.

Oertel, M., and D. B. Bung. 2012. Initial stage of two-dimensional dam-break waves: Laboratory versus VOF. Journal of Hydraulic Research 50:89–97.

Özgen, I., D. Liang, and R. Hinkelmann. 2016a. Shallow water equations with depth-dependent anisotropic porosity for subgrid-scale topography. Applied Mathematical Modelling 40:7447–7473.

Özgen, I., J. Zhao, D. Liang, and R. Hinkelmann. 2016b. Urban flood modeling using shallow water equations with depth-dependent anisotropic porosity. Journal of Hydrology 541:1165–1184.

Parish, Y. I. H., and P. Müller. 2001. Procedural modeling of cities. Proceedings of the 28th Annual Conference on Computer Graphics and Interactive Techniques,:301–308.

Poelmans, L., A. V. Rompaey, V. Ntegeka, and P. Willems. 2011. The relative impact of climate change and urban expansion on peak flows: A case study in central Belgium. Hydrological Processes 25:2846–2858.

Poelmans, L., A. Van Rompaey, and O. Batelaan. 2010. Coupling urban expansion models and hydrological models: How important are spatial patterns? Land use Policy 27:965–975.

Potter, K. K. M.C. Wiggert D.C. Hondzo M. Shih T.I.-P. Chaudhry. 2010. Mechanics of fluids (3rd ed.). . Stamford, CT: Cengage Learning.

Prusinkiewicz, P., and A. Lindenmayer. 1990. Modeling of cellular layers. The Algorithmic Beauty of Plants:145–174.

Rand, W., D. Brown, R. Riolo, and D. Robinson. 2005. Toward a Graphical ABM Toolkit with GIS Integration. Proceedings of the Agent 2005 Conference on Generative Social Processes, Models and Mechanisms:27–41.

Rhee, H. K., R. Aris, and N. R. Amundson. 1986. First order partial differential equations. Theory and applications of single equations, 1. . Englewood Cliffs, NJ: Prentice-Hall.

Ritter, A. 1892. Die Fortpflanzung von Wasserwellen [The propagation of water waves]. Zeitschrift Verein Deutscher Ingenieure 36:947–954.

Robson, A. J. 2002. Evidence for trends in UK flooding. Philosophical Transactions of the Royal Society A: Mathematical, Physical and Engineering Sciences 360:1327–1343.

Rulot, F., B. J. Dewals, S. Erpicum, P. Archambeau, and M. Pirotton. 2012. Modelling sediment transport over partially non-erodible bottoms. International Journal for Numerical Methods in Fluids 70:186–199.

Sanders, B. F., J. E. Schubert, and H. A. Gallegos. 2008. Integral formulation of shallow-water equations with anisotropic porosity for urban flood modeling. Journal of Hydrology 362:19–38.

Schubert, J. E., and B. F. Sanders. 2012. Building treatments for urban flood inundation models and implications for predictive skill and modeling efficiency. Advances in Water Resources 41:49–64.

Soares-Frazão, S., J. Lhomme, V. Guinot, and Y. Zech. 2008. Two-dimensional shallow-water model with porosity for urban flood modelling. Journal of Hydraulic Research 46:45–64.

Stelling, G. S. 2012. Quadtree flood simulations with sub-grid digital elevation models. Proceedings of the Institution of Civil Engineers: Water Management 165:567–580.

Stelling, G. S., and S. P. A. Duinmeijer. 2003. A staggered conservative scheme for every Froude number in rapidly varied shallow water flows. International Journal for Numerical Methods in Fluids 43:1329–1354.

Stilmant, F., M. Pirotton, P. Archambeau, S. Erpicum, and B. Dewals. 2015. Can the collapse of a fly ash heap develop into an air-fluidized flow? - Reanalysis of the Jupille accident (1961). Geomorphology 228:746–755.

Stilmant, F., M. Pirotton, P. Archambeau, S. Roger, S. Erpicum, and B. Dewals. 2013. Dike-break induced flows: A simplified model. Environmental Fluid Mechanics 13:89–100.

Sturm, T. W. 2010. Open channel hydraulics (2nd ed.). . Boston, MA: McGraw-Hill.

Tannier, C., and I. Thomas. 2013. Defining and characterizing urban boundaries: A fractal analysis of theoretical cities and Belgian cities. Computers, Environment and Urban Systems 41:234–248.

UNISDR. 2009. 2009 UNISDR Terminology on Disaster Risk Reduction. . United Nations International Strategy for Disaster Reduction (UNISDR).

UNISDR. 2011. Global Assessment Report on Disaster Risk Reduction. Revealing Risk, Redefining Development. . Geneva: United Nations International Strategy for Disaster Reduction Secretariat.

United Nations. 2014. World Urbanization Prospects: The 2014 Revision, Highlights. . United Nations, Department of Economic and Social Affairs, Population Division.

Vafai, K., and C. L. Tien. 1981. Boundary and inertia effects on flow and heat transfer in porous media. International Journal of Heat and Mass Transfer 24:195–203.

Valiani, A., and L. Begnudelli. 2006. Divergence form for bed slope source term in shallow water equations. Journal of Hydraulic Engineering 132:652–665.

Valiani, A., and L. Begnudelli. 2008. Closure to "divergence form for bed slope source term in shallow water equations" by Alessandro Valiani and Lorenzo Begnudelli. Journal of Hydraulic Engineering 134:680–682.

Valiani, A., V. Caleffi, and A. Zanni. 2002. Case study: Malpasset dam-break simulation using a two-dimensional finite volume method. Journal of Hydraulic Engineering 128:460–472.

Vanegas, C. A., D. G. Aliaga, B. Beneš, and P. A. Waddell. 2009. Interactive design of urban spaces using geometrical and behavioral modeling. ACM Transactions on Graphics 28:111:1–111:9.

Vansteenkiste, T., M. Tavakoli, V. Ntegeka, P. Willems, F. De Smedt, and O. Batelaan. 2013. Climate change impact on river flows and catchment hydrology: A comparison of two spatially distributed models. Hydrological Processes 27:3649–3662.

Vázquez-Cendón, M. E. 1999. Improved Treatment of Source Terms in Upwind Schemes for the Shallow Water Equations in Channels with Irregular Geometry. Journal of Computational Physics 148:497–526.

Veldkamp, A., and E. F. Lambin. 2001. Predicting land-use change. Agriculture, Ecosystems & Environment 85:1–6.

Velickovic, M., Y. Zech, and S. Soares-Frazão. 2017. Steady-flow experiments in urban areas and anisotropic porosity model. Journal of Hydraulic Research 55:85–100.

Vojinovic, Z., S. Seyoum, M. H. Salum, R. K. Price, A. K. Fikri, and Y. Abebe. 2013. Modelling floods in urban areas and representation of buildings with a method based on adjusted conveyance and storage characteristics. Journal of Hydroinformatics 15:1150–1168.

Vollmer, D., D. Costa, E. S. Lin, Y. Ninsalam, K. Shaad, M. F. Prescott, S. Gurusamy, F. Remondi, R. Padawangi, P. Burlando, C. Girot, A. Grêt-Regamey, and J. Rekittke. 2015. Changing the Course of Rivers in an Asian City: Linking Landscapes to Human Benefits through Iterative Modeling and Design. Journal of the American Water Resources Association 51:672–688.

Volp, N. D., B. C. Van Prooijen, and G. S. Stelling. 2013. A finite volume approach for shallow water flow accounting for high-resolution bathymetry and roughness data. Water Resources Research 49:4126–4135.

Wang, H., S. He, X. Liu, L. Dai, P. Pan, S. Hong, and W. Zhang. 2013. Simulating urban expansion using a cloud-based cellular automata model: A case study of Jiangxia, Wuhan, China. Landscape and Urban Planning 110:99–112.

Ward, P. J., H. Renssen, J. C. J. H. Aerts, and P. H. Verburg. 2011. Sensitivity of discharge and flood frequency to twenty-first century and late Holocene changes in climate and land use (River Meuse, northwest Europe). Climatic Change 106:179–202.

Whitaker, S. 1967. Diffusion and dispersion in porous media. AIChe Journal 13:420–427.

White, F. 2008. Fluid mechanics (6th ed.). . Boston, MA: McGraw-Hill.

Wiacek, J., M. Molenda, J. Y. Ooi, and J. Favier. 2012. Experimental and numerical determination of representative elementary volume for granular plant materials. Granular Matter 14:449–456.

Wind, H. G., T. M. Nierop, C. J. De Blois, and J. L. De Kok. 1999. Analysis of flood damages from the 1993 and 1995 Meuse floods. Water Resources Research 35:3459–3465.

Wood, E. F., M. Sivapalan, K. Beven, and L. Band. 1988. Effects of spatial variability and scale with implications to hydrologic modeling. Journal of Hydrology 102:29–47.

Wright, N. 2014. Advances in flood modelling helping to reduce flood risk. Proceedings of the Institution of Civil Engineers: Civil Engineering 167:52.

Wu, W. 2008. Computational river dynamics. . London: Taylor & Francis.

Yoon, K. 2007. Experimental Study on Flood Inundation Considering Urban Characteristics (FFC06-05). . Urban Flood Disaster Management Research Center, Seoul.

Yu, D., and S. N. Lane. 2006a. Urban fluvial flood modelling using a two-dimensional diffusion-wave treatment, part 2: Development of a sub-grid-scale treatment. Hydrological Processes 20:1567–1583.

Yu, D., and S. N. Lane. 2006b. Urban fluvial flood modelling using a two-dimensional diffusion-wave treatment, part 1: Mesh resolution effects. Hydrological Processes 20:1541–1565.

Zhou, J. G., D. M. Causon, C. G. Mingham, and D. M. Ingram. 2001. The Surface Gradient Method for the Treatment of Source Terms in the Shallow-Water Equations. Journal of Computational Physics 168:1–25.

APPENDICES

A. Supplemental data to section 1: Classification of porosity concepts used for urban flood modelling

A.1. Representative Elementary Volume

Idealized urban network

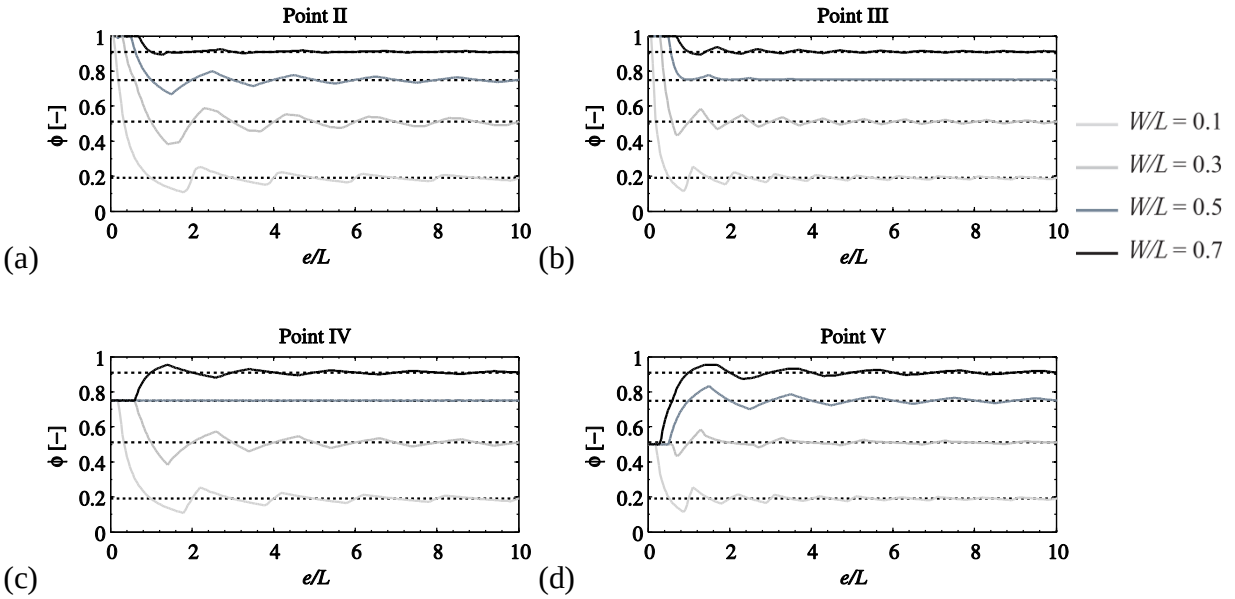

Figure A-1: Evolution of the storage porosity ϕ for different sizes e/L of the CV and locations II to V of the point around which the considered CV are located.

Real-world urban area

At point B (Figure A-3), the CV reaches the river Meuse in the east and the side of the valley in the west for a size of the CV close to 600 m, i.e. the CV reaches the limit of the QHA I (Figure 1-4b). The influence of the river results mainly in an increase in porosity for the lowest levels because the surface available for water storage increases. The effect of the side of the valley is a decrease in porosity for the higher levels since the rise in topography levels reduces the space available for water storage. For relatively small CVs, the absence of buildings in the boulevard where point B is located induces porosities equal to one for the highest levels (z > 62 m).

At point C (Figure A-4), the porosities are highly variable because the CV spreads over three QHA once its size exceeds 200 m (Figure 1-5c).

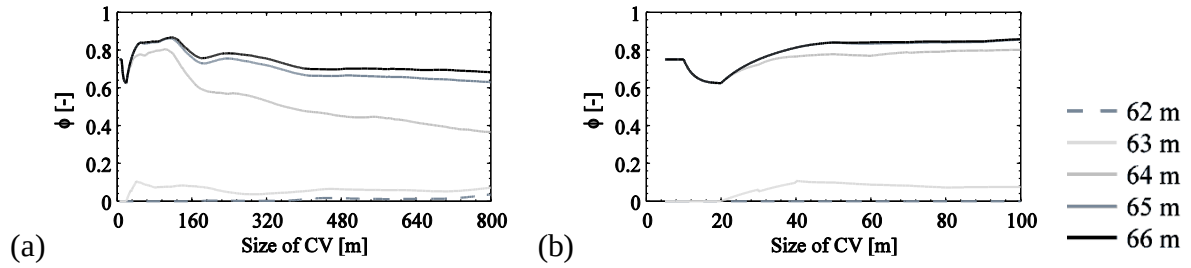

Figure A-2: Evolution of the depth-dependent areal storage porosity ϕ as a function of the size of the CV at point A and for different levels.

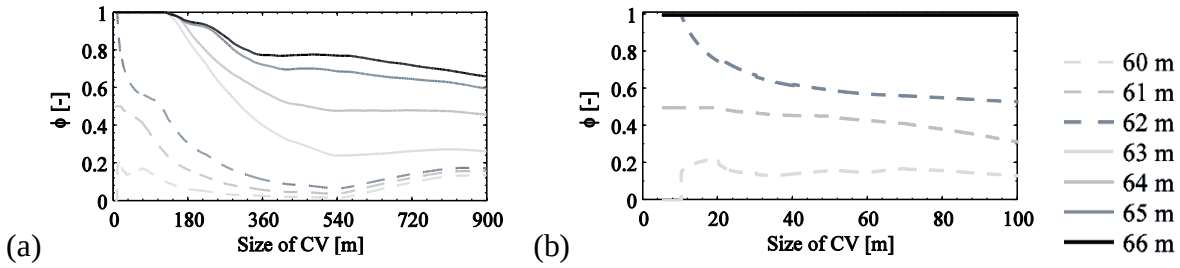

Figure A-3: Evolution of the depth-dependent areal storage porosity ϕ as a function of the size of the CV at point B and for different levels.

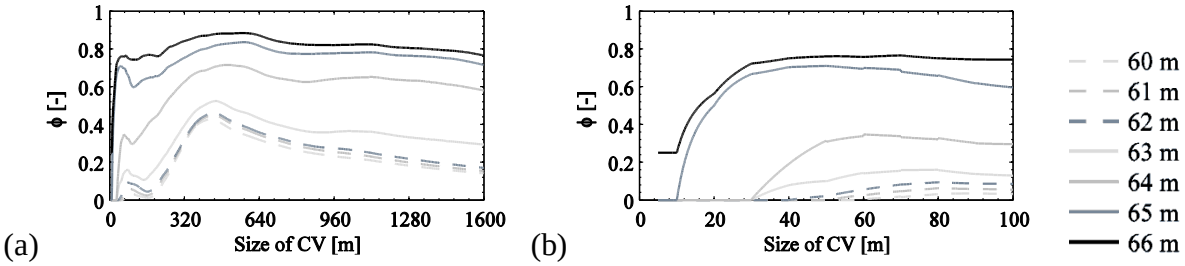

Figure A-4: Evolution of the depth-dependent areal storage porosity ϕ as a function of the size of the CV at point C and for different levels.

A.2. Spatial variability of porosity

For the idealized urban network and different CV sizes (e/L), the storage porosity ϕ was computed considering centres of the CV distributed continuously in-between points III (x/L = 0) and VI (x/L = 1). The streets and obstacles widths were equal (W/L = 0.5). As shown in Figure A-5, the porosity shows substantial variations at x/L = 0.25 and x/L = 0.75 for the smallest CVs, which are much smaller than the REV. When the size of the CV increases, the spatial variations

in the storage porosity decrease because the porosity value converges towards the asymptotic value ϕ_{as}.

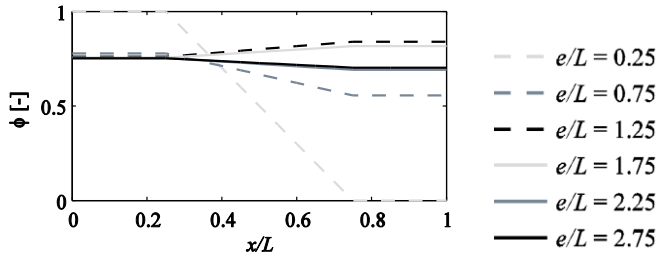

Figure A-5: Spatial variation of the storage porosity ϕ considering centres of the CV distributed continuously in-between points III and VI for different CV sizes.

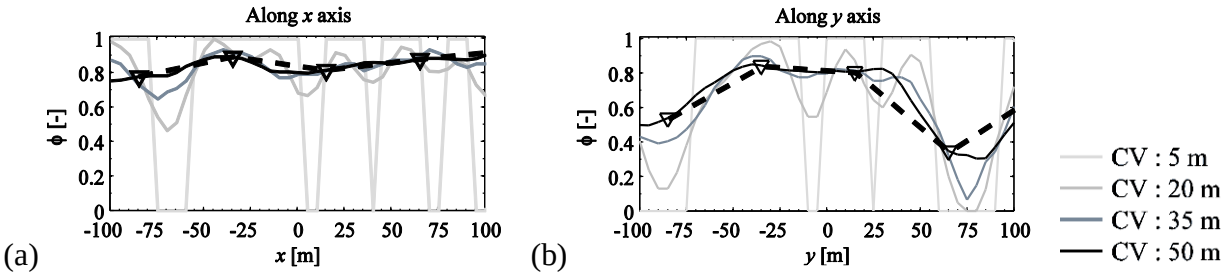

Figure A-6: Spatial variation of the areal storage porosity ϕ at z = 64.5 m around point A.

A.3. Isotropic vs anisotropic porosities

We consider first the idealized urban network with two different geometric configurations: $W/L = 0.1$ and $W/L = 0.5$. The storage and conveyance porosities were computed for CVs of different sizes centred around a point situated in the middle of an obstacle (Point VI). As shown in Figure A-7, the conveyance porosity ψ is highly discontinuous and fluctuates around the asymptotic porosity ϕ_{as} without converging, even for very large sizes of the CV.

Since Lhomme (2006) defined the conveyance porosity at a REV scale, we also evaluated the mean conveyance porosity $\overline{\psi}$ for a given CV centred around a given point and for a given direction as the average of all conveyance porosities ψ computed for smaller CVs centred around the same point, in this direction. This mean conveyance porosity converges slowly towards the asymptotic porosity ϕ_{as} when the size of the CV increases, thanks to the homogeneity of the network. Nonetheless, for equal street and obstacle widths ($W/L = 0.5$), the mean conveyance porosity remains about 7% higher than the asymptotic porosity when the size of the CV reaches the size of the REV related to the storage porosity. For the ratio $W/L = 0.1$, the maximum difference reaches around 30%. So, even at the scale of the REV relative to the storage porosity,

replacing the mean conveyance porosity by the storage porosity remains questionable. In other terms, the REV relative to the mean conveyance porosity appears to be systematically larger than the REV relative to the storage porosity.

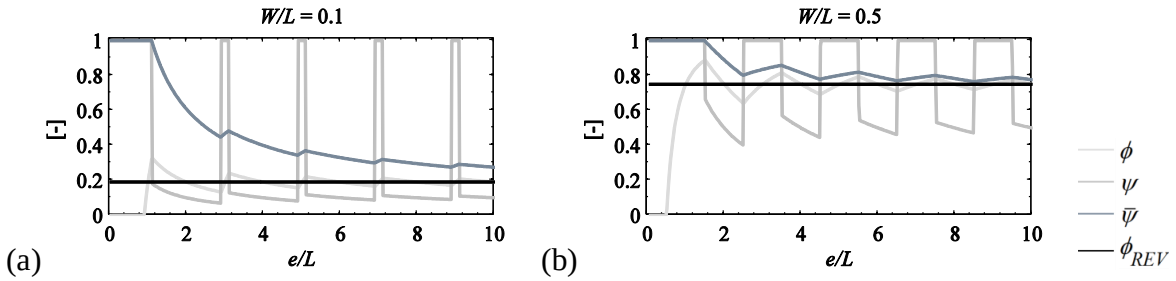

Figure A-7: Evolution of storage ϕ, conveyance ψ and mean conveyance $\overline{\psi}$ porosities as a function of the size e/L of the CV for a point situated in the centre of gravity of an obstacle block (Point VI).

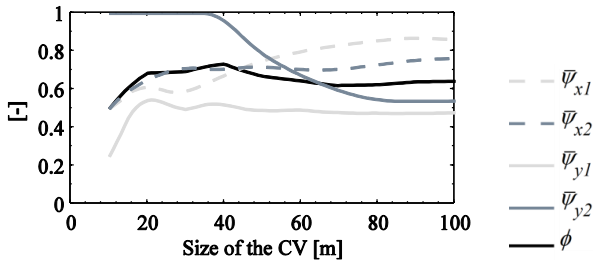

Figure A-8: Evolution of areal storage ϕ and mean linear conveyance $\overline{\psi}$ porosities as a function of the size of the CV around point D at an altitude of 63 m.

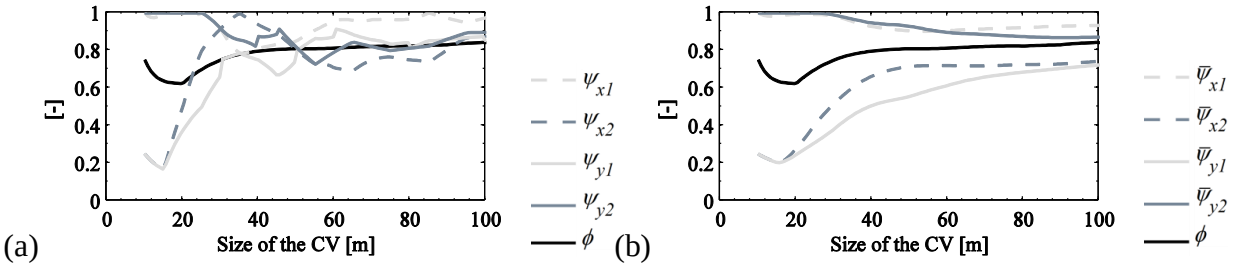

Figure A-9: Evolution of areal storage ϕ and linear conveyance ψ porosities (a) and evolution of areal storage ϕ and mean linear conveyance $\overline{\psi}$ porosities (b) as a function of the size of the CV around point A at an altitude of 64.5 m.

The mean linear conveyance porosities $\overline{\psi}$ were also evaluated (Figure A-8 and Figure A-9b). Their variations with the size of the CV become lower as the size of the considered CVs increases. However, the mean conveyance porosities remain different from one border to the other and are not equal to the storage porosity, thereby confirming the anisotropy of the urban area even for large CVs (Figure A-10).

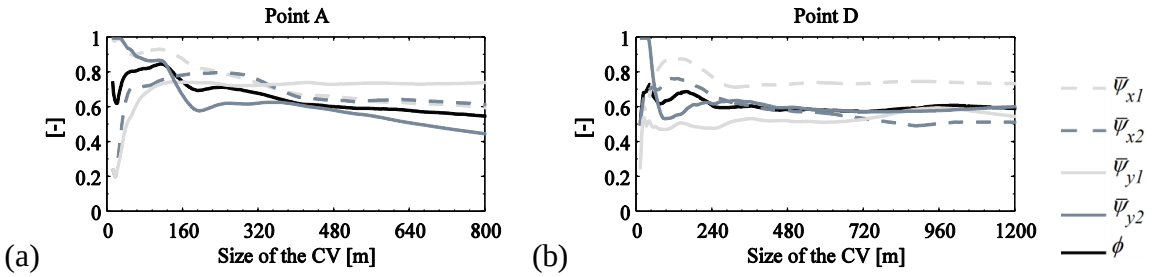

Figure A-10: Evolution of areal storage ϕ and mean linear conveyance $\overline{\psi}$ porosities as a function of the size of the CV around points A (a) and D (b) at an altitude of, respectively, 64.5 m and 63 m.

B. Supplementary material: Bruwier et al. 2016, Applied Mathematical Modelling

Following a similar approach as detailed by Murillo and Garcia-Navarro (2013), we derive here the value of η_0 which would lead to an energy balance discretization of the DFB. We show however that the corresponding expression for η_0 may become singular and is substantially more complex than the approach considered in the paper.

The discretized formulations of Eqs (2-13) and (2-14) write respectively:

$$\begin{aligned}&\left[hu^2\right]_{i+\frac{1}{2}}-\left[hu^2\right]_{i-\frac{1}{2}}+\frac{g}{2}\left(h_{i+\frac{1}{2}}^2-h_{i-\frac{1}{2}}^2\right)\\&=\frac{g}{2}\left[\left(\left[\eta_0\right]-z_{i+\frac{1}{2}}\right)^2-\left(\left[\eta_0\right]-z_{i-\frac{1}{2}}\right)^2\right]\end{aligned} \tag{B-1}$$

$$\frac{u_{i+\frac{1}{2}}^2}{2g}-\frac{u_{i-\frac{1}{2}}^2}{2g}+z_{i+\frac{1}{2}}-z_{i-\frac{1}{2}}+h_{i+\frac{1}{2}}-h_{i-\frac{1}{2}}=0 \tag{B-2}$$

The momentum equation can be reformulated as follows:

$$\left[hu^2\right]_{i+\frac{1}{2}}-\left[hu^2\right]_{i-\frac{1}{2}}+g\frac{h_{i+\frac{1}{2}}+h_{i-\frac{1}{2}}}{2}\left(h_{i+\frac{1}{2}}-h_{i-\frac{1}{2}}\right)=-g\left(z_{i+\frac{1}{2}}-z_{i-\frac{1}{2}}\right)\left(\left[\eta_0\right]-\frac{z_{i+\frac{1}{2}}+z_{i-\frac{1}{2}}}{2}\right) \tag{B-3}$$

Adding the same term g ($z_{i+1/2}$ - $z_{i-1/2}$) ($h_{i+1/2}$ + $h_{i-1/2}$) / 2 on both sides of the momentum equation (B-3), it can be rewritten as follows:

$$\left[hu^2\right]_{i+\frac{1}{2}}-\left[hu^2\right]_{i-\frac{1}{2}}+g\frac{h_{i+\frac{1}{2}}+h_{i-\frac{1}{2}}}{2}\left(\eta_{i+\frac{1}{2}}-\eta_{i-\frac{1}{2}}\right)=-g\left(z_{i+\frac{1}{2}}-z_{i-\frac{1}{2}}\right)\left(\left[\eta_0\right]-\frac{\eta_{i+\frac{1}{2}}+\eta_{i-\frac{1}{2}}}{2}\right) \tag{B-4}$$

Multiplying the energy equation (B-2) by the average depth ($h_{i+1/2}$ + $h_{i-1/2}$) / 2, it becomes:

$$\frac{h_{i+\frac{1}{2}}+h_{i-\frac{1}{2}}}{2}\left(\frac{u_{i+\frac{1}{2}}^2}{2}-\frac{u_{i-\frac{1}{2}}^2}{2}\right)+g\frac{h_{i+\frac{1}{2}}+h_{i-\frac{1}{2}}}{2}\left(\eta_{i+\frac{1}{2}}-\eta_{i-\frac{1}{2}}\right)=0 \tag{B-5}$$

Equations (B-4) and (B-5) are equivalent under the following condition, obtained by subtracting Eq. (B-5) from Eq. (B-4):

$$\left[hu^2\right]_{i+\frac{1}{2}}-\left[hu^2\right]_{i-\frac{1}{2}}-\frac{h_{i+\frac{1}{2}}+h_{i-\frac{1}{2}}}{2}\left(\frac{u_{i+\frac{1}{2}}^2}{2}-\frac{u_{i-\frac{1}{2}}^2}{2}\right)=-g\left(z_{i+\frac{1}{2}}-z_{i-\frac{1}{2}}\right)\left(\left[\eta_0\right]-\frac{\eta_{i+\frac{1}{2}}+\eta_{i-\frac{1}{2}}}{2}\right) \tag{B-6}$$

Solving for $[\eta_0]$, one obtains:

$$[\eta_0] = \frac{\eta_{i+\frac{1}{2}} + \eta_{i-\frac{1}{2}}}{2} - \frac{\left[hu^2\right]_{i+\frac{1}{2}} - \left[hu^2\right]_{i-\frac{1}{2}} - \frac{h_{i+\frac{1}{2}} + h_{i-\frac{1}{2}}}{2}\left(\frac{u^2_{i+\frac{1}{2}}}{2} - \frac{u^2_{i-\frac{1}{2}}}{2}\right)}{g\left(z_{i+\frac{1}{2}} - z_{i-\frac{1}{2}}\right)} \tag{B-7}$$

Substituting result (B-7) into the source term in Eq. (B-1) leads to:

$$\begin{aligned} &\frac{g}{2}\left[\left([\eta_0] - z_{i+\frac{1}{2}}\right)^2 - \left([\eta_0] - z_{i-\frac{1}{2}}\right)^2\right] \\ &= \frac{g}{2}\left[\left(\frac{\eta_{i+\frac{1}{2}} + \eta_{i-\frac{1}{2}}}{2} - \frac{\mathcal{A}}{g\left(z_{i+\frac{1}{2}} - z_{i-\frac{1}{2}}\right)} - z_{i+\frac{1}{2}}\right)^2 - \left(\frac{\eta_{i+\frac{1}{2}} + \eta_{i-\frac{1}{2}}}{2} - \frac{\mathcal{A}}{g\left(z_{i+\frac{1}{2}} - z_{i-\frac{1}{2}}\right)} - z_{i-\frac{1}{2}}\right)^2\right] \end{aligned} \tag{B-8}$$

with

$$\mathcal{A} = \left[hu^2\right]_{i+\frac{1}{2}} - \left[hu^2\right]_{i-\frac{1}{2}} - \frac{h_{i+\frac{1}{2}} + h_{i-\frac{1}{2}}}{2}\left(\frac{u^2_{i+\frac{1}{2}}}{2} - \frac{u^2_{i-\frac{1}{2}}}{2}\right) \tag{B-9}$$

Equation (B-9) leads however to a far more intricate evaluation of the free surface elevation η_0 compared to a simple weighted-average of the free surface elevations $\eta_{i+1/2}$ and $\eta_{i-1/2}$. In addition, the correction term in Eq. (B-9) becomes singular when the bottom is flat, since $z_{i+1/2} = z_{i-1/2}$ while $\mathcal{A}$ does not necessarily tend towards zero.

C. Energy conservation properties of Ritter solution for idealized dam break flow

This section is based on the technical note "*Energy conservation properties of Ritter solution for idealized dam break flow*" by B. Dewals, **M. Bruwier**, S. Erpicum, M. Pirotton, and P. Archambeau, published in 2016 in *Journal of Hydraulic Research*. The PhD candidate was involved in all conceptual and mathematical derivations presented in the note.

ABSTRACT: We examine different aspects of energy conservation in the case of the analytical solution of Ritter for idealized dam break flow in a horizontal frictionless and dry channel. We detail the application of the unsteady Bernoulli equation in this case and highlight that the inertial effects cancel out when averaged over the whole flow region. We also show that the potential and kinetic contributions to the total mechanical energy in the flow region have a distinct and constant relative importance: potential energy accounts for 60 %, and kinetic energy for 40 % of the total mechanical energy. These properties of Ritter solution are rarely emphasized while they may be of practical relevance, particularly for the verification of numerical schemes with respect to their ability to ensure energy conservation.

C.1. Introduction

We consider here the case of an idealized dam break flow occurring in a flat and frictionless prismatic channel, with an upstream reservoir of infinite length. The cross-section is rectangular and the initial water depth in the reservoir is noted h_0 (Figure C-1). This idealized configuration also schematizes sudden flow releases resulting from sluice gate operation or hydroelectric load acceptance in a headrace (Sturm 2010). It was widely used to verify numerical schemes (e.g., Begnudelli and Sanders, 2006; Canelas et al., 2013; Mignot and Cienfuegos, 2009; Oertel and Bung, 2012; Wu, 2008), to compare with experimental data (e.g., El Kadi Abderrezzak et al., 2008; Hsu et al., 2014; Lauber and Hager, 1998a; Lauber and Hager, 1998b; Oertel and Bung, 2012) and to derive more advanced analytical solutions, accounting for flow resistance, initial water depth downstream or bed slope (e.g., Aureli et al., 2014; Chanson, 2009).

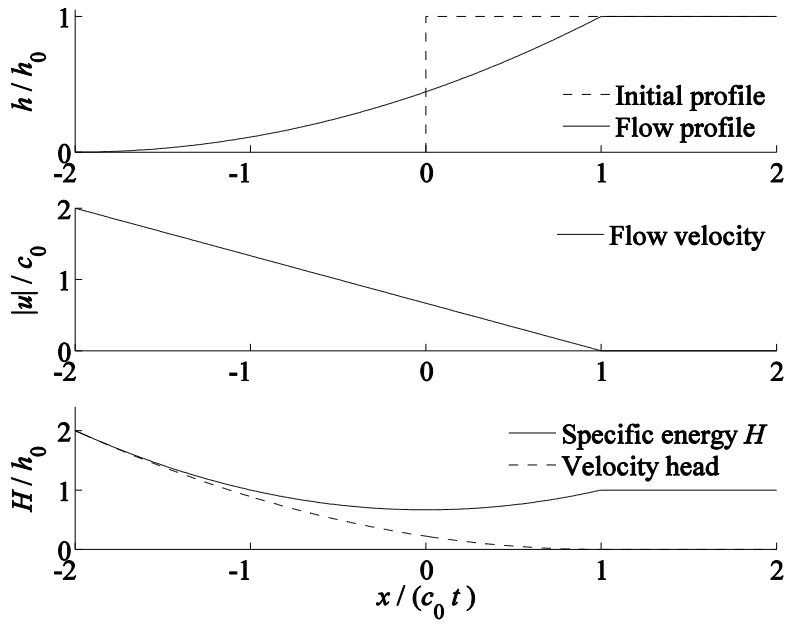

Figure C-1: Water depth h, flow velocity u and specific energy H in Ritter solution, normalized using the initial water depth h_0 in the reservoir and the corresponding wave celerity $c_0 = (g\ h_0)^{0.5}$. Flow from right to left.

Assuming a uniform velocity profile over the flow depth and considering that the pressure distribution is hydrostatic, Ritter (1892) developed an analytical solution based on the theory of characteristics applied to simple wave problems. As shown in Figure C-1, it corresponds to a rarefaction wave (e.g., Rhee et al., 1986) travelling towards upstream in the reservoir, at the velocity $c_0 = (g\ h_0)^{0.5}$, and towards downstream at the velocity $-2\ c_0$, where g is the gravity acceleration. In the flow region (i.e. $-2\ c_0\ t \le x \le c_0\ t$), the water depth h and the depth-averaged flow velocity u may be expressed as a function of time $t > 0$ and position x as (Ritter 1892):

$$h = \frac{1}{9} h_0 \left(\frac{x}{c_0 t} + 2 \right)^2 \qquad \text{(C-1)}$$

$$u = \frac{2}{3} c_0 \left(\frac{x}{c_0 t} - 1 \right) \qquad \text{(C-2)}$$

At the initial location of the dam ($x = 0$), the water depth is constant ($4/9\ h_0$) and the flow is critical (i.e. $F = 1$, with $F = |u|/(gh)^{0.5}$).

As the bottom is assumed frictionless and the flow is continuous, no head losses are encountered in such a flow. We detail here how the conservation of energy can be formulated for this idealized dam break flow configuration. In section C.2, we focus on the specific energy, while the conservation of mechanical energy in the flow is examined in section C.3.

C.2. Specific energy

In general, the *energy head* (or *total head*) E is defined as the sum of the elevation z (representing the *potential head*), the *pressure head* $p / (\rho g)$ and the *velocity head* $u^2 / (2 g)$: $E = z + p / (\rho g) + u^2 / (2 g)$, with p the pressure and ρ the fluid density (Chaudhry 1993, Sturm 2010). Since the pressure is assumed hydrostatic and the channel bottom is horizontal ($z = 0$), the sum of potential and pressure heads yields simply the flow depth h, which represents here the *piezometric head*. Hence, the energy head is also equal to the *specific energy* $H = h + u^2 / (2 g)$ (Hager 2010, Sturm 2010).

From Eqs (C-1) and (C-2), the *specific energy* H of the flow may be evaluated as a function of position x and time t:

$$H = h + \frac{u^2}{2g} = h_0 \frac{1}{3}\left[\left(\frac{x}{c_0 t}\right)^2 + 2\right] \qquad \text{(C-3)}$$

Although the flow does not lead to *head losses*, the specific energy is obviously neither constant nor uniform. This results from the transient nature of the flow. In particular, H is found minimum ($H = 2/3\ h_0$) at the initial location of the dam ($x = 0$), where the flow is critical (Figure C-1).

The equation of motion for unsteady flow (e.g., Eq. 7.15 in Sturm, 2010) writes:

$$\frac{1}{g}\frac{\partial u}{\partial t} + \frac{\partial}{\partial x}\left(\frac{u^2}{2g} + h\right) = 0 \qquad \text{(C-4)}$$

in which the non-homogeneous terms (bottom and friction slopes) were omitted since a flat and frictionless bottom is assumed. By integrating Eq. (C-4) between two arbitrary positions x_A and x_B in the flow region, one obtains:

$$H_A = H_B + \int_{x_A}^{x_B} \frac{1}{g}\frac{\partial u}{\partial t}\,\mathrm{d}x \qquad \text{(C-5)}$$

which is one formulation of the unsteady Bernoulli equation.

Given Eq. (C-2), the inertial term in Eq. (C-5) becomes:

$$\int_{x_A}^{x_B} \frac{1}{g}\frac{\partial u}{\partial t}\,\mathrm{d}x = -\frac{2}{3}h_0 \int_{x_A/(c_0 t)}^{x_B/(c_0 t)} \xi\,\mathrm{d}\xi = \frac{1}{3}h_0\left[\left(\frac{x_A}{c_0 t}\right)^2 - \left(\frac{x_B}{c_0 t}\right)^2\right] \qquad \text{(C-6)}$$

Introducing Eqs (C-3) and (C-6) into Eq. (C-5) confirms that both sides of Eq. (C-5) are equal, which follows simply from the fact that the unsteady Bernoulli equation holds for Ritter solution.

This is consistent with the absence of head losses under such frictionless and continuous flow conditions.

Integrating the inertial term (C-6) between the upstream ($x = c_0\,t$) and downstream ($x = -\,2\,c_0\,t$) ends of the flow region, considering $x_A = c_0\,t$ (upstream limit of the flow region), leads to:

$$\int_{-2c_0t}^{c_0t} \frac{1}{3} h_0 \left[\left(\frac{c_0 t}{c_0 t} \right)^2 - \left(\frac{x}{c_0 t} \right)^2 \right] \mathrm{d}x = \frac{1}{3} h_0 c_0 t \int_{-2}^{1} \left(1 - \xi^2 \right) \mathrm{d}\xi = 0 \qquad \text{(C-7)}$$

This confirms that the effect of inertia over the whole flow region is to spatially redistribute the specific energy. This contrasts with a standard head loss term, the integral of which would be non-zero.

Consequently, integrating the specific energy over the whole flow domain and up to a finite abscissa L_R in the undisturbed part of the upstream reservoir ($L_R \geq c_0 t$) yields:

$$\int_{-\infty}^{L_R} \left(h + \frac{u^2}{2g} \right) \mathrm{d}x = \underbrace{\int_{-2c_0t}^{c_0t} h \,\mathrm{d}x}_{①} + \underbrace{\int_{-2c_0t}^{c_0t} \frac{u^2}{2g} \mathrm{d}x}_{②} + h_0 \left(L_R - c_0 t \right) = h_0 \left(2c_0 t + L_R \right) \qquad \text{(C-8)}$$

which simply equals the length of the flow domain times the initial specific energy h_0. This is consistent with the fact that inertial effects cancel *in average*. In Eq. (C-8), term ① represents the streamwise-integration over the flow region of the combination of pressure and potential heads (i.e. piezometric head), while term ② corresponds to the streamwise integration of the velocity head. Their respective values are:

$$① = \int_{-2c_0t}^{c_0t} h \,\mathrm{d}x = h_0 c_0 t \frac{1}{9} \int_{-2}^{1} \left(\xi + 2 \right)^2 \mathrm{d}\xi = h_0 c_0 t \qquad \text{(C-9)}$$

$$② = \int_{-2c_0t}^{c_0t} \frac{u^2}{2g} \mathrm{d}x = h_0 c_0 t \frac{1}{2} \frac{4}{9} \int_{-2}^{1} \left(\xi - 1 \right)^2 \mathrm{d}\xi = 2\, h_0 c_0 t \qquad \text{(C-10)}$$

which shows that the piezometric head accounts for 1 / 3 of the streamwise-integrated specific energy over the flow region ($3\, h_0\, c_0\, t$), while the velocity head contributes for 2 / 3. This ratio remains constant over time as a result of the self-similar nature of Ritter solution.

Since Eq. (C-4) is derived from the principle of *momentum* conservation, Eq. (C-8) is not a direct expression of the conservation of the mechanical *energy*. This is discussed in the next section.

C.3. Mechanical energy

The mechanical energy e per unit mass of a flowing fluid can be expressed as the sum of the *kinetic energy* $v^2 / 2$ and the *potential energy* $g\,z$, both per unit mass (White 2008, Potter 2010):

$$e = \frac{v^2}{2} + gz \tag{C-11}$$

with $v = (\boldsymbol{v} \bullet \boldsymbol{v})^{0.5}$, $\boldsymbol{v}$ the fluid velocity vector, measured with respect to a fixed reference frame, and z the vertical elevation above the horizontal channel bottom. Other types of energy, including internal energy, are not considered here as we focus on the motion of an incompressible and inviscid fluid without thermal effects. Under these assumptions, the conservation equation for mechanical energy over an *arbitrary* control volume Ω bounded by a closed surface S writes (Potter 2010):

$$\frac{\partial}{\partial t}\int_{\Omega} \rho\left(gz + \frac{v^2}{2}\right) \mathrm{d}\Omega + \int_{S} \rho\left(gz + \frac{v^2}{2}\right)(\mathrm{v} - \mathrm{v_I}) \cdot \mathrm{n}\, \mathrm{d}S = \int_{S} -p(\mathrm{v} \cdot \mathrm{n})\, \mathrm{d}S \tag{C-12}$$

with $\boldsymbol{n}$ the unit vector normal to S pointing outwards and $\boldsymbol{v_I}$ the local velocity of the closed surface S. The shear stress tensor was neglected in Eq. (C-12) as the fluid is assumed inviscid. The right-hand-side of Eq. (C-12) represents the power developed by the pressure forces.

Consistently with Ritter solution, we consider a one-dimensional flow domain of unit width, in which only the x-component of the fluid velocity is non-zero, i.e. $\boldsymbol{v} = [\, u \;\; 0 \;\; 0 \,]^{\mathrm{T}}$. Since the velocity distribution is assumed uniform and the pressure is hydrostatic, Eq. (C-12) reduces to:

$$\begin{aligned}
&\frac{\partial}{\partial t}\int_{x_A}^{x_B} \rho\left(g\frac{h^2}{2} + h\frac{u^2}{2}\right) \mathrm{d}x \\
&+\rho\left(g\frac{h^2}{2} + h\frac{u^2}{2}\right)_{x=x_B} \left[u(x_B,t) - v_B(t)\right] \\
&-\rho\left(g\frac{h^2}{2} + h\frac{u^2}{2}\right)_{x=x_A} \left[u(x_A,t) - v_A(t)\right] \\
&= -\rho g\left[\left(\frac{h^2}{2}\right)_{x=x_B} u(x_B,t) - \left(\frac{h^2}{2}\right)_{x=x_A} u(x_A,t)\right]
\end{aligned} \tag{C-13}$$

where the abscissa x_A and x_B define the positions of two arbitrary cross-sections A and B in the flow domain. These cross-sections A and B may be mobile, at velocities v_A and v_B respectively. We examine hereafter the application of Eq. (C-13), first to the flow *region*, next to the whole flow *domain*.

Let us consider first a deforming control volume which expands over time to match the flow region (- 2 $c_0\,t \le x \le c_0\,t$). The first term of the left-hand side in Eq. (C-13) becomes:

$$\begin{aligned}
&\int_{-2c_0t}^{c_0t} \rho\left(g\frac{h^2}{2}+h\frac{u^2}{2}\right)\mathrm{d}x \\
&= \rho g \frac{h_0^2}{2} c_0 t \underbrace{\frac{1}{81}\int_{-2}^{1}(\xi+2)^4\,\mathrm{d}\xi}_{①} \\
&+\rho g \frac{h_0^2}{2} c_0 t \underbrace{\frac{4}{81}\int_{-2}^{1}(\xi+2)^2(\xi-1)^2\,\mathrm{d}\xi}_{②} \\
&= \rho g \frac{h_0^2}{2} c_0 t
\end{aligned} \qquad \text{(C-14)}$$

This confirms that, at any time $t > 0$, the total mechanical energy contained within the flow region is equal to the mean potential energy per unit mass $\rho g\, h_0 / 2$ times the volume $h_0\, c_0\, t$ of the undisturbed fluid initially present in the flow region (i.e. between the location of the dam and the upstream position of the rarefaction wave at current time t). In addition, the integrals ① and ② in Eq. (C-14) are respectively equal to 3 / 5 and 2 / 5. This reveals that the relative contributions of the potential energy and the kinetic energy remain distinctively constant over time, corresponding respectively to 60 % and 40 % of the total energy contained in the flow region. This independence from time results also from the self-similar nature of Ritter solution over time. This is also shown in Figure C-2, which represents the distribution of both contributions over the flow region. The part of the flow region situated downstream of the reservoir (i.e. $x < 0$) contributes predominantly with kinetic energy, while the potential energy dominates within the reservoir (i.e. $x > 0$).

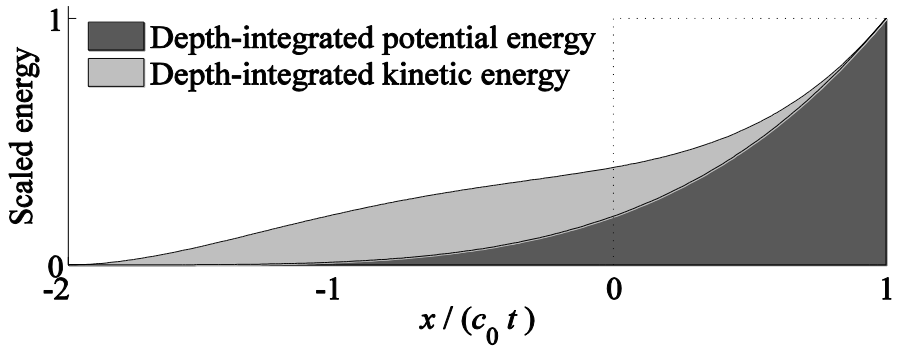

Figure C-2: Streamwise distribution of the depth-integrated potential and kinetic energy per unit mass, scaled by the corresponding value $\rho g\, h_0^2 / 2$ in the undisturbed part of the reservoir.

Considering x_A = - 2 $c_0\, t$ and $x_B = c_0\, t$, the right-hand side of Eq. (C-13) vanishes since $u(x_B,t) = 0$ and $h(x_A,t) = 0$. Given that $v_A(t) = u(x_A,t)$ and taking into account Eq. (C-14), Eq. (C-13) yields:

$$\frac{\partial}{\partial t}\left(\rho g\frac{h_0^2}{2}c_0 t\right)+\rho g\frac{h_0^2}{2}\left(-c_0\right)=0 \qquad \text{(C-15)}$$

which is indeed verified as the conservation of energy applies for the smooth and continuous flow conditions considered here. Equation (C-15) expresses that the rate of change of the total energy contained within the flow region is equal to the potential energy per unit length in the undisturbed part of the reservoir times the celerity c_0 of the rarefaction wave in the reservoir.

Let us consider now a fixed control volume which extends beyond the flow region, from - ∞ up to an arbitrary abscissa $L_R \geq c_0\, t$ upstream in the reservoir. Using Eqs (C-1) and (C-2), the volume integral in Eq. (C-13) may be evaluated as follows:

$$\begin{aligned}&\int_{-\infty}^{L_R}\rho\left(g\frac{h^2}{2}+h\frac{u^2}{2}\right)\mathrm{d}x\\&=\rho g\frac{h_0^2}{2}c_0 t\int_{-2}^{1}\left[\left(\frac{h}{h_0}\right)^2+\frac{h}{h_0}\frac{u^2}{gh_0}\right]\mathrm{d}\left(\frac{x}{c_0 t}\right)+\rho g\frac{h_0^2}{2}\left(L_R-c_0 t\right) \qquad \text{(C-16)}\\&=\rho g\frac{h_0^2}{2}L_R\end{aligned}$$

This simply results from the fact that, at any time, the total mechanical energy in the flow domain remains equal to the potential energy initially present in the reservoir at rest. Equation (C-16) is a simple and practical relation which may be used to verify the energy conservation in the discrete solution provided by numerical schemes. Equation (C-13) holds also for the fixed control volume considered here, since in this case all terms, including the time derivative, are equal to zero.

C.4. Conclusion

By examining the formulation of energy conservation in the well-known Ritter solution for idealized dam break flow, we highlighted several distinctive properties which are rarely emphasized. The unsteady Bernoulli equation holds with a substantial influence of the inertial term, which nonetheless is zero in average over the *flow length* as inertial effects merely redistribute specific energy. The conservation of mechanical energy in the whole flow domain was also examined. It remains constant over time and equal to its initial value, since the flow is frictionless and continuous. Within the flow region, the relative importance of potential and kinetic energy remains constant over time and takes distinctive values: respectively 60 % and 40 % of the total mechanical energy. Relationships derived here, such as Eq. (C-16), may prove useful in practice for benchmarking numerical methods in terms of energy conservation.

D. Supplemental data to section 3

D.1. Domain with four cells and a local obstruction over an edge

Let us solve equations (3-5) and (3-6) for the smallest possible numerical grid which enables a suitable resolution of the problem accounting properly for the typical boundary conditions and for the presence of a local obstruction over a single edge. Hence, the domain is discretized with four cells (Figure D-1), numbered from $i = 1$ (upstream) to $i = 4$ (downstream) with the following conveyance porosities:

$$\begin{aligned} \psi_{1/2} = \psi_{3/2} = \psi_{9/2} = \psi_{11/2} = 1 \\ 0 < \psi_{5/2} = \psi_{7/2} = \psi \leq 1 \end{aligned} \qquad \text{(D-1)}$$

where the edge k between cells i and i+1 is numbered $k = i$+1/2.

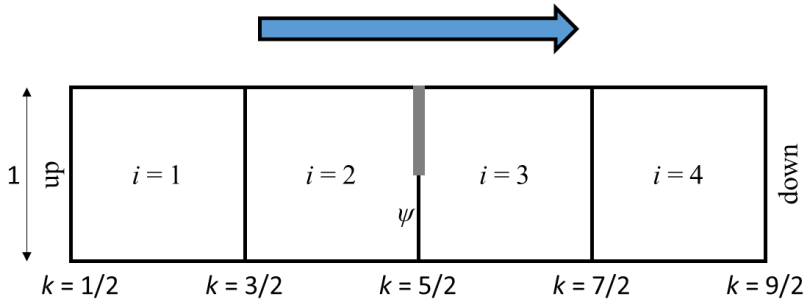

Figure D-1 : Numerical domain with four cells and a local obstruction over an edge.

Establishment of the equations

Applying the equations of the mass and momentum conservations for the four cells in a subcritical flow leads to the same equations than the ones in Table 3-1 for the upstream border and the cells 1 and 2 of the numerical domain with a contraction-expansion zone. For cells 3 and 4, the equations give:

- Cell 3:

$$u_3 = \frac{q}{h_3}$$

$$\left(u^2h\right)_3 - \psi\left(u^2h\right)_2 + \frac{g}{2}\left(h_4^2 - \psi h_3^2\right) = \frac{g}{2}\left(1-\psi\right)\left(\frac{h_4+h_3}{2}\right)^2 \qquad \text{(D-2)}$$

$$\Leftrightarrow \quad h_4^2\left(1+\frac{\left(\psi-1\right)}{4}\right) + \left(\psi-1\right)\left(\frac{h_3h_4}{2}\right) - h_3^2\left(\psi - \frac{\left(\psi-1\right)}{4}\right) + \frac{2q^2}{\psi g}\left(\frac{\psi}{h_3} - \frac{1}{h_2}\right) = 0$$

- Cell 4:

$$u_4 = \frac{q}{h_4}$$

$$\left(u^2h\right)_4 - \left(u^2h\right)_3 + \frac{g}{2}\left(h_{down}^2 - h_4^2\right) = 0 \qquad \text{(D-3)}$$

$$\Leftrightarrow \quad h_{down}^2 = h_4^2 - \frac{2q^2}{g}\left(\frac{1}{h_4} - \frac{1}{h_3}\right)$$

Based on the non-dimensional variables of Eq. (3-8), the non-dimensional formulation write:

$$h_{up}^* = h_1^* = h_2^* = 1 \qquad \text{(D-4)}$$

$$h_3^{*2}\frac{1+3\psi}{4} + h_3^*\left(1-\psi\right)\frac{1}{2} + \frac{2\mathrm{Fr}_{up}^2}{\psi}\left(1-\psi\right) - \frac{1}{4}\left(\psi+3\right) = 0 \qquad \text{(D-5)}$$

$$h_4^{*2}\left(1+\frac{\left(\psi-1\right)}{4}\right) + \left(\psi-1\right)\left(\frac{h_4^*h_3^*}{2}\right) - h_3^{*2}\left(\psi - \frac{\left(\psi-1\right)}{4}\right) + \frac{2\mathrm{Fr}_{up}^2}{\psi}\left(\psi h_3^{*-1} - h_2^{*-1}\right) = 0 \qquad \text{(D-6)}$$

$$h_{down}^{2*} = h_4^{2*} - 2\mathrm{Fr}_{up}^2\left(\frac{1}{h_4^*} - \frac{1}{h_3^*}\right) \qquad \text{(D-7)}$$

Results

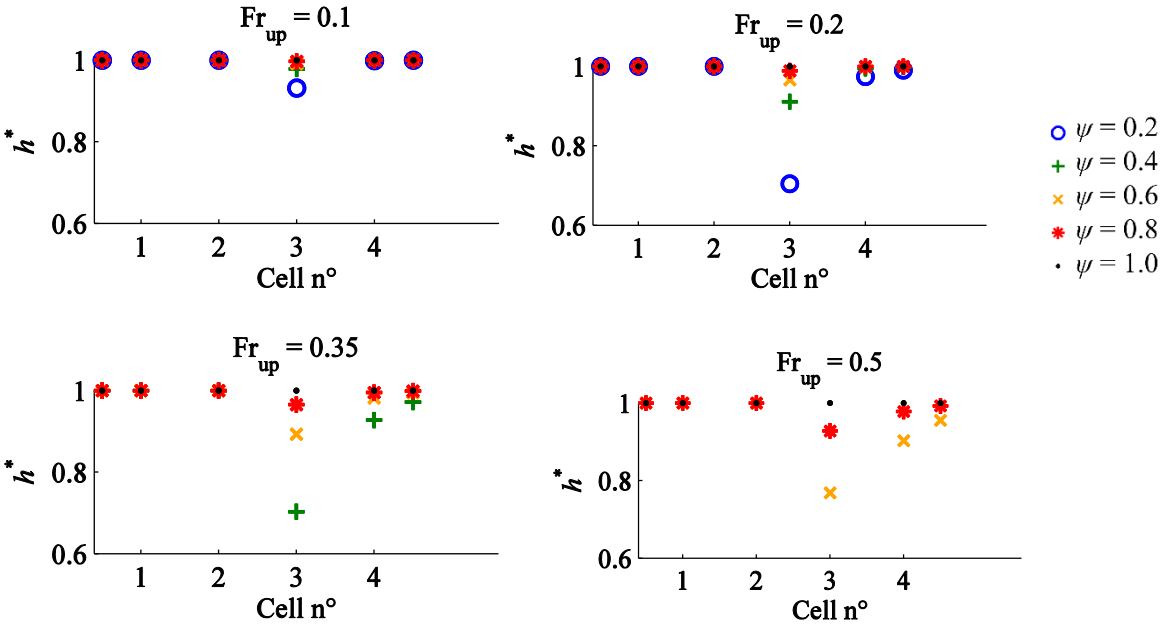

Figure D-2 : Water depth profiles for different upstream Froude numbers Fr_{up} and conveyance porosities ψ .

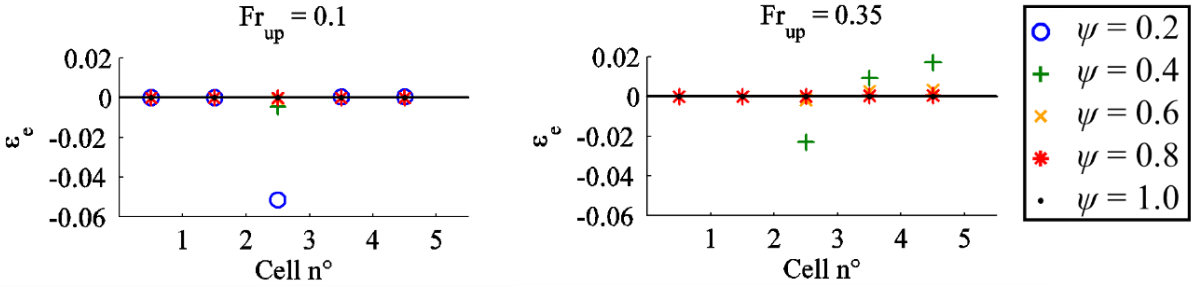

Figure D-3 : Loss of specific energy for different upstream Froude numbers Fr_{up} and conveyance porosities ψ .

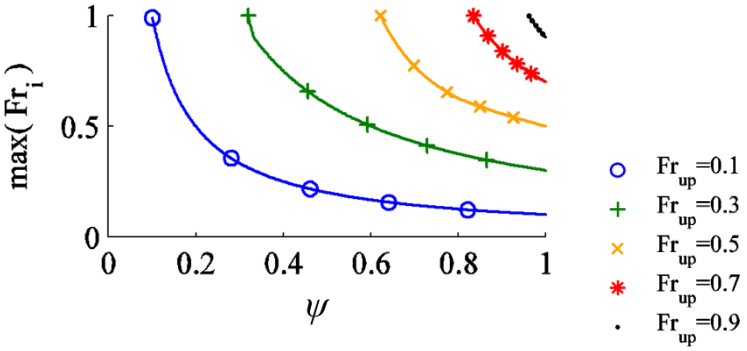

Figure D-4 : Maximum Froude number over the five cells for different upstream Froude numbers as a function of the conveyance porosity.

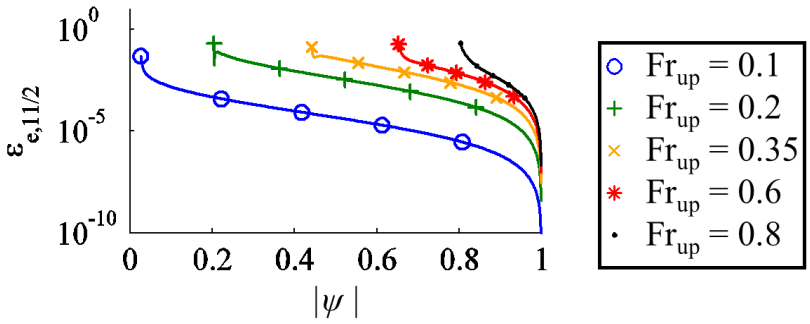

Figure D-5 : Overall variation of specific energy for different upstream Froude numbers as a function of the conveyance porosity.

D.2. Details on the derivation of the equations of section 3.2.2

Applying the equations of the mass and momentum conservations in a subcritical flow for the cells of the computation domains with a contraction zone (Figure 3-1a), an expansion zone (Figure 3-1b) and a contraction-expansion zone (Figure 3-1c) leads to:

Contraction zone

- Cell 1:

$$h_1 u_1 = [hu]_{up}$$
$$h_1 u_1^2 - \frac{[hu]_{up}^2}{h_1} + \frac{1}{2} g \left(h_2^2 - h_1^2 \right) = 0 \qquad \Rightarrow \qquad h_2 = h_1 \tag{D-8}$$

- Cell 2:

$$\psi h_2 u_2 = [hu]_{up}$$
$$\frac{[hu]_{up}^2}{h_1} \left(\frac{1}{\psi} - 1 \right) + \frac{g}{2} \left(\psi h_3^2 - h_1^2 \right) = \frac{g}{2} (\psi - 1) \left(\frac{h_1 + h_3}{2} \right)^2 \tag{D-9}$$

- Cell 3:

$$h_3 u_3 = h_2 u_2 = \frac{[hu]_{up}}{\psi}$$
$$\frac{[hu]_{up}^2}{\psi^2} \left(\frac{1}{h_3} - \frac{1}{h_1} \right) + \frac{1}{2} g \left(h_4^2 - h_3^2 \right) = 0 \quad \Rightarrow \quad h_4^2 = h_3^2 + \frac{2[hu]_{up}^2}{g\psi^2} \left(\frac{1}{h_1} - \frac{1}{h_3} \right) \tag{D-10}$$

- Cell 4:

$$h_4 u_4 = h_3 u_3 = \frac{[hu]_{up}}{\psi}$$
$$\frac{[hu]_{up}^2}{\psi^2}\left(\frac{1}{h_4}-\frac{1}{h_3}\right)+\frac{g}{2}\left([h]_{down}^2-h_4^2\right)=0 \Rightarrow \qquad h_4^2=[h]_{down}^2+\frac{2[hu]_{up}^2}{g\psi^2}\left(\frac{1}{h_4}-\frac{1}{h_3}\right) \tag{D-11}$$

Expansion zone

- Cell 1:

$$h_1 u_1 = [hu]_{up}$$
$$h_2 = h_1 \tag{D-12}$$

- Cell 2:

$$h_2 u_2 = [hu]_{up}$$
$$\frac{[hu]_{up}^2}{h_2}-\frac{[hu]_{up}^2}{h_1}+\frac{1}{2}g\left(h_3^2-h_2^2\right)=0 \qquad \Rightarrow \qquad h_3 = h_2 \tag{D-13}$$

- Cell 3:

$$h_3 u_3 = \psi [hu]_{up}$$
$$(\psi-1)\frac{\psi[hu]_{up}^2}{h_1}+\frac{1}{2}g\left(h_4^2-\psi h_1^2\right)=\frac{1}{2}g(1-\psi)\left(\frac{h_1+h_4}{2}\right)^2 \tag{D-14}$$

- Cell 4:

$$h_4 u_4 = h_3 u_3 = \psi [hu]_{up}$$
$$h_4^2 = [h]_{down}^2+\frac{2\psi^2[hu]_{up}^2}{g}\left(\frac{1}{h_4}-\frac{1}{h_1}\right) \tag{D-15}$$

Contraction-expansion zone

- Cell 1:

$$h_1 u_1 = [hu]_{up}$$
$$h_2 = h_1 \tag{D-16}$$

- Cell 2:

$$\psi h_2 u_2 = \left[hu\right]_{\text{up}}$$

$$\frac{\left[hu\right]_{\text{up}}^2}{h_1}\left(\frac{1}{\psi}-1\right)+\frac{g}{2}\left(\psi h_3^2-h_1^2\right)=\frac{g}{2}\left(\psi-1\right)\left(\frac{h_1+h_3}{2}\right)^2 \qquad \text{(D-17)}$$

- Cell 3:

$$h_3 u_3 = h_2 u_2 = \frac{\left[hu\right]_{\text{up}}}{\psi}$$

$$\frac{\left[hu\right]_{\text{up}}^2}{\psi^2}\left(\frac{1}{h_3}-\frac{1}{h_1}\right)+\frac{1}{2}g\left(h_4^2-h_3^2\right)=0 \quad \Rightarrow \quad h_4^2=h_3^2+\frac{2\left[hu\right]_{\text{up}}^2}{\psi^2 g h_1}\left(1-\frac{h_1}{h_3}\right) \qquad \text{(D-18)}$$

- Cell 4:

$$h_4 u_4 = \psi h_3 u_3 = \left[hu\right]_{\text{up}}$$

$$\left[hu\right]_{\text{up}}^2\left(\frac{1}{h_4}-\frac{1}{\psi h_3}\right)+\frac{1}{2}g\left(h_5^2-\psi h_4^2\right)=\frac{g}{2}\left(1-\psi\right)\left(\frac{h_4+h_5}{2}\right)^2 \qquad \text{(D-19)}$$

- Cell 5:

$$h_5 u_5 = h_4 u_4 = \left[hu\right]_{\text{up}}$$

$$\left[hu\right]_{\text{up}}^2\left(\frac{1}{h_5}-\frac{1}{h_4}\right)+\frac{g}{2}\left(\left[h\right]_{\text{down}}^2-h_5^2\right)=0 \qquad \text{(D-20)}$$

E. Derivation of the eigenvalues of the porosity-based governing equations

Considering an infinitesimal control volume, a horizontal and frictionless bottom and applying the classical divergence theorem for continuous and differentiable solutions, the governing equations are rewritten in a differentiable formulation for a one-directional flow (Guinot et al. 2017):

$$\partial_t\left(\phi\begin{bmatrix} h \\ uh \\ vh \end{bmatrix}\right)+\partial_x\left(\begin{bmatrix} \psi_c uh \\ (1-\mu)\left(\psi_{mA_1}u^2h+\psi_{mP}\dfrac{gh^2}{2}\right) \\ (1-\mu)\psi_{mA_2}uvh \end{bmatrix}\right)=0 \tag{E-1}$$

The corresponding Jacobian matrix **A** is:

$$\mathbf{A}=\frac{1}{\phi}\begin{bmatrix} 0 & \psi_c & 0 \\ (1-\mu)\left(\psi_{mP}c^2-\psi_{mA_1}u^2\right) & 2(1-\mu)\psi_{mA_1}u & 0 \\ -(1-\mu)\psi_{mA_2}uv & (1-\mu)\psi_{mA_2}v & (1-\mu)\psi_{mA_2}u \end{bmatrix} \tag{E-2}$$

with $c=\sqrt{gh}$.

The eigenvalues for the one-directional case are:

$$\begin{aligned} \lambda_1&=(1-\mu)\frac{\psi_{mA_1}}{\phi}u-c' \\ \lambda_2&=(1-\mu)\frac{\psi_{mA_2}}{\phi}u \\ \lambda_3&=(1-\mu)\frac{\psi_{mA_1}}{\phi}u+c' \end{aligned} \tag{E-3}$$

with $c'=\sqrt{(1-\mu)\left(\frac{\psi_{mA_1}}{\phi^2}u^2\left[(1-\mu)\psi_{mA_1}-\psi_c\right]+\frac{\psi_c\psi_{mP}}{\phi^2}c^2\right)}$.

If the values of the edge porosity parameters are replaced by the corresponding values according to Table 4-1 for model PS-A-1-D (i.e. DIP model, with $\psi_{mA_1}=\psi_{mA_2}=\phi^2/\psi$; $\psi_c=\phi$, and $\psi_{mP}=\psi$,), the same eigenvalues as computed by Guinot et al. (2017) are retrieved.

To ensure the existence of the eigenvalues in Eq. (E-3), configurations leading to $\psi_c > (1-\mu)\psi_{mA_1}$ should be excluded. For steady and quasi-steady flows (μ being set to zero), the hyperbolicity of the system is hence ensured when $\psi_{mA_1} \geq \psi_c$.

F. Supplemental data to the test cases of section 4

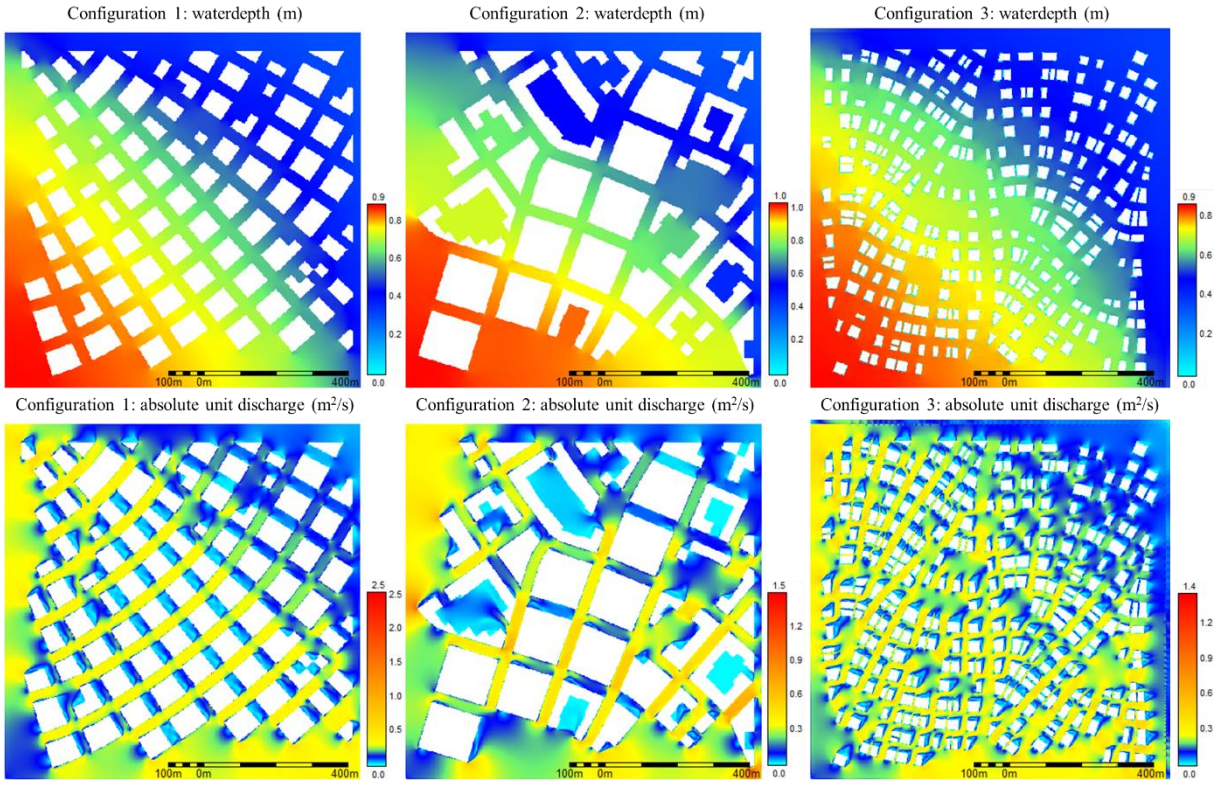

Figure F-1 : Waterdepths (m) and magnitude of unit discharges (m^2/s) resulting from the micro-scale computation with the CS model and a grid size of 1 m (CS-1m).

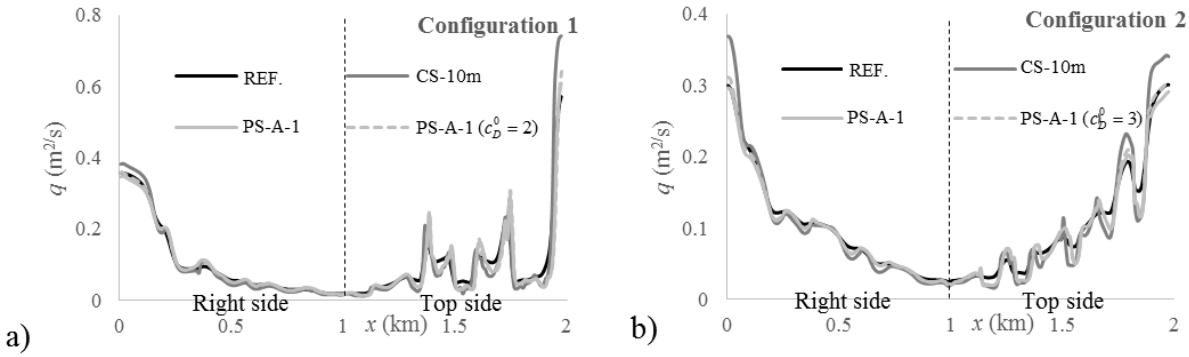

Figure F-2 : Normal unit discharge profiles from the top-left corner to the bottom-right corner along the downstream borders for configurations 1 (a) and 2 (b).

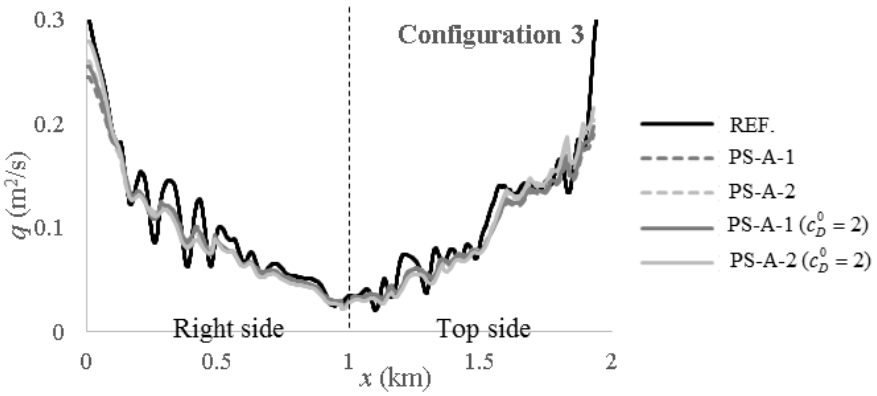

Figure F-3 : Normal unit discharge profiles from the top-left corner to the bottom-right corner along the downstream borders for configuration 3.

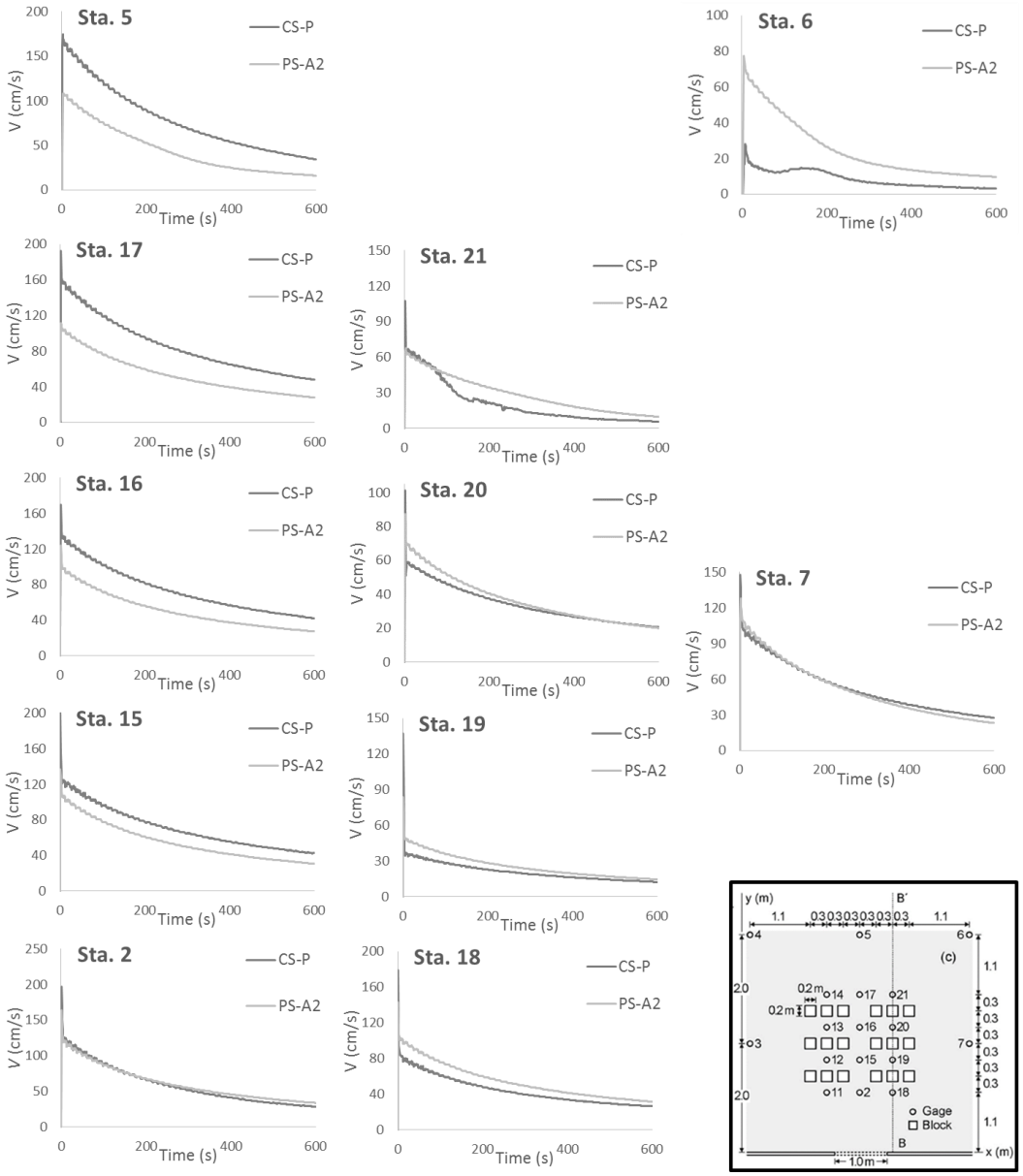

Figure F-4 : Comparison of velocity magnitudes: CS-P predictions and computations with the PS-A-2 model using the optimal value of $c_D^0 = 2$ for velocity magnitude.

G. Supplemental material: Bruwier et al. 2016, Journal of Hydraulic Research

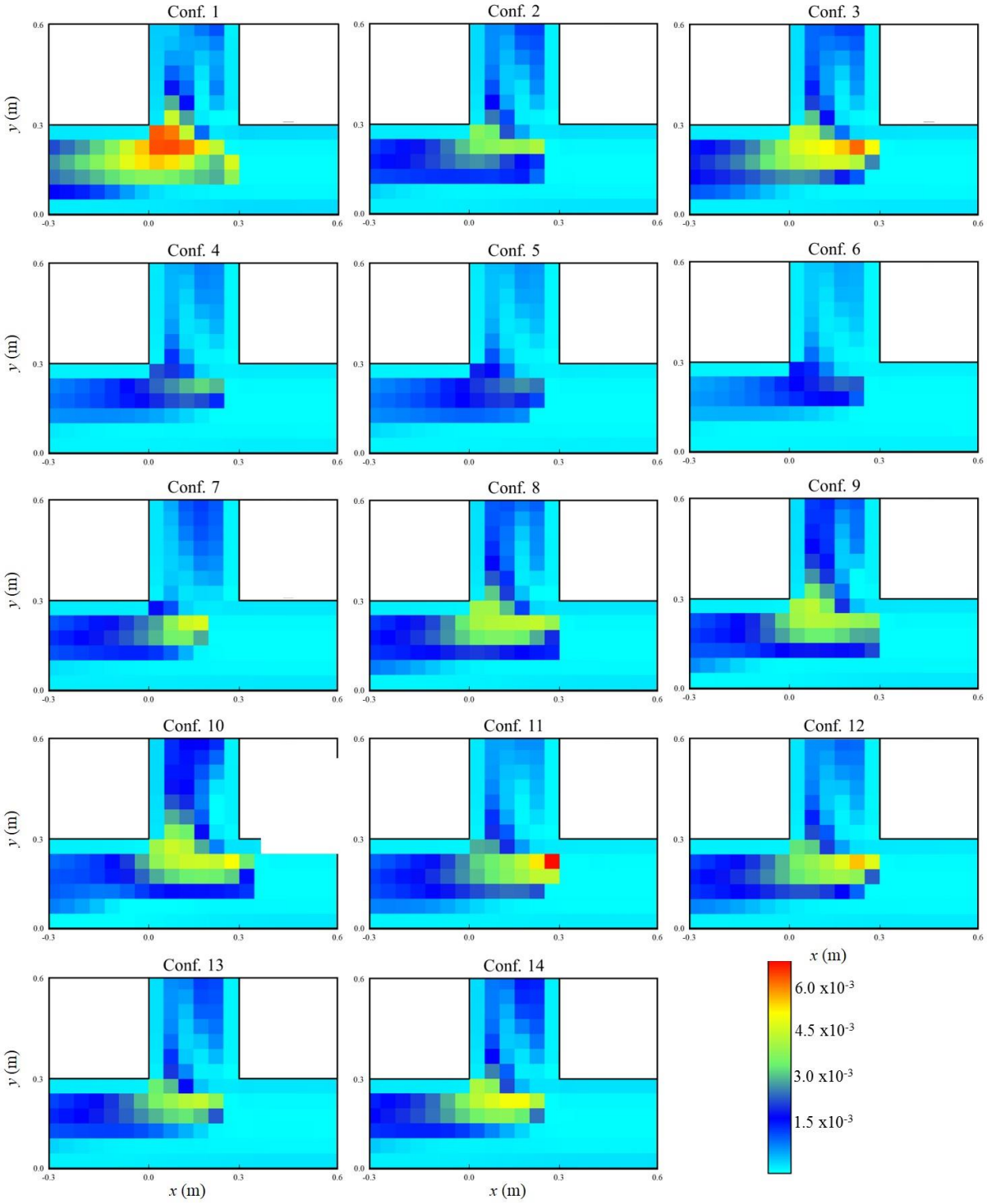

Figure G-1: Computed maps of eddy viscosity for simulations without obstacles.

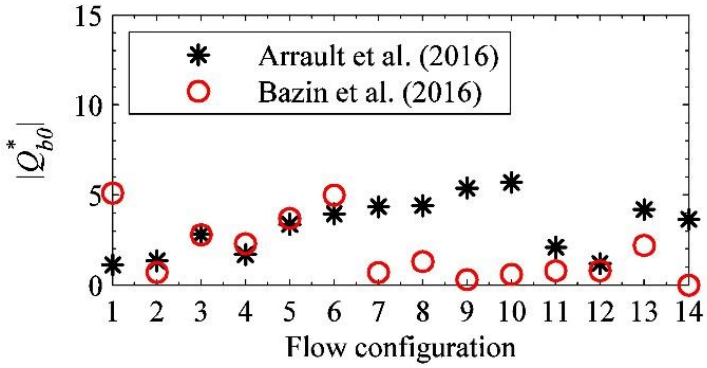

Figure G-2: Absolute values of the relative errors of the lateral discharge Q^*_{b0} for simulations without obstacles.

H. Supplemental data to section 6.4.3: flood risk for the PARIS sectors

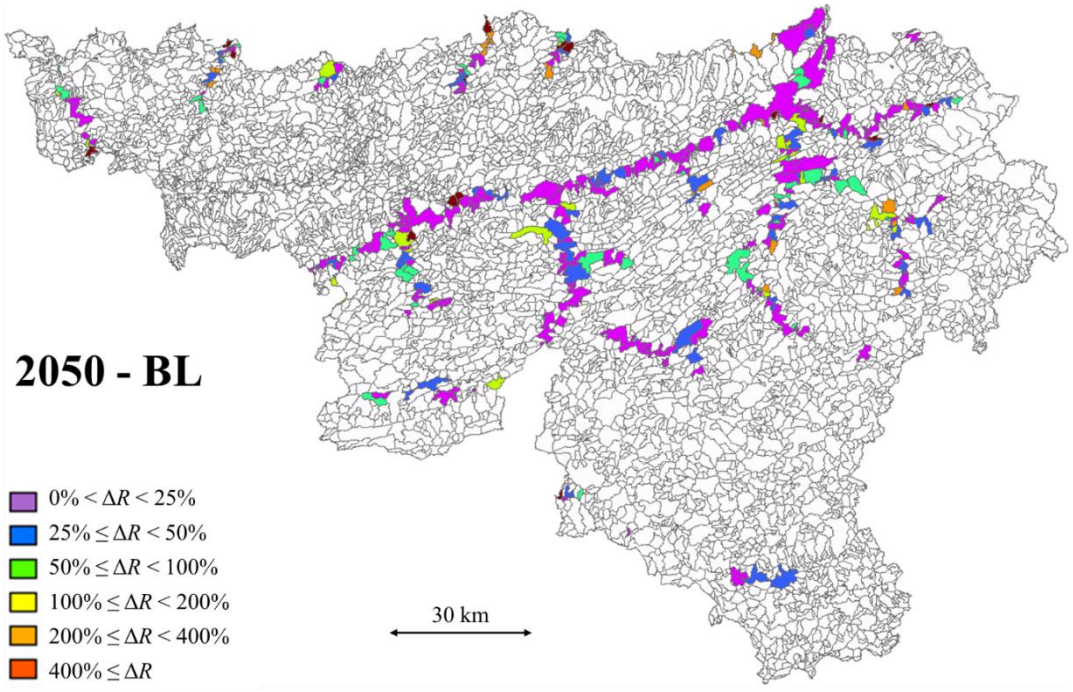

Figure H-1 : Changes in flood risk indicator compared to the current value in 2050 for the BL scenario.

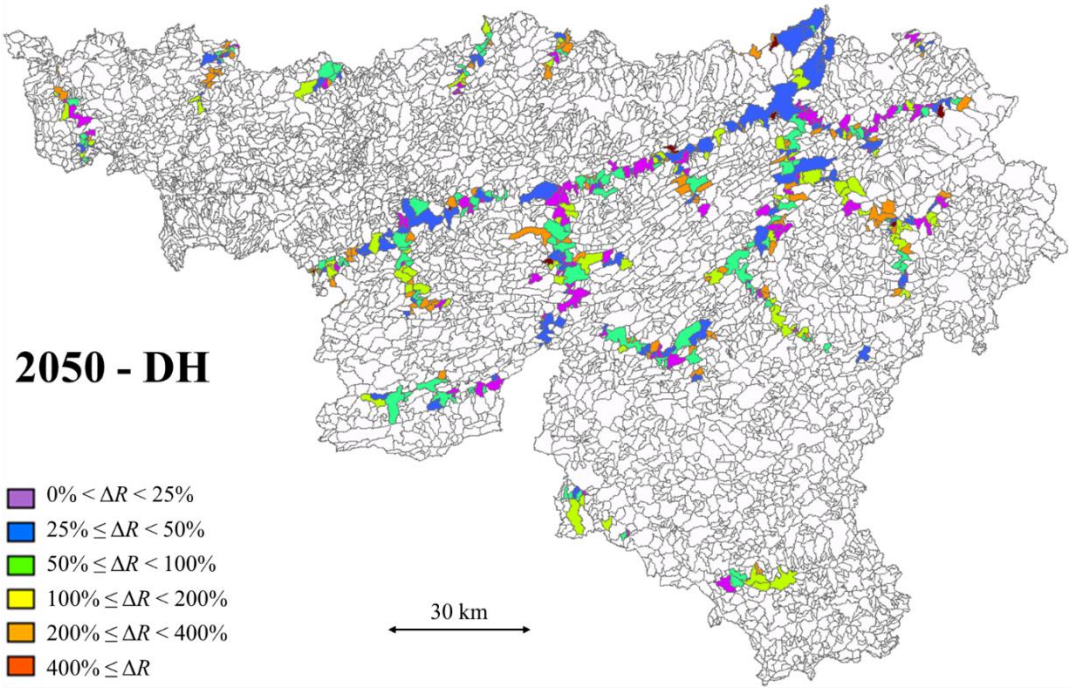

Figure H-2 : Changes in flood risk indicator compared to the current value in 2050 for the LH scenario.

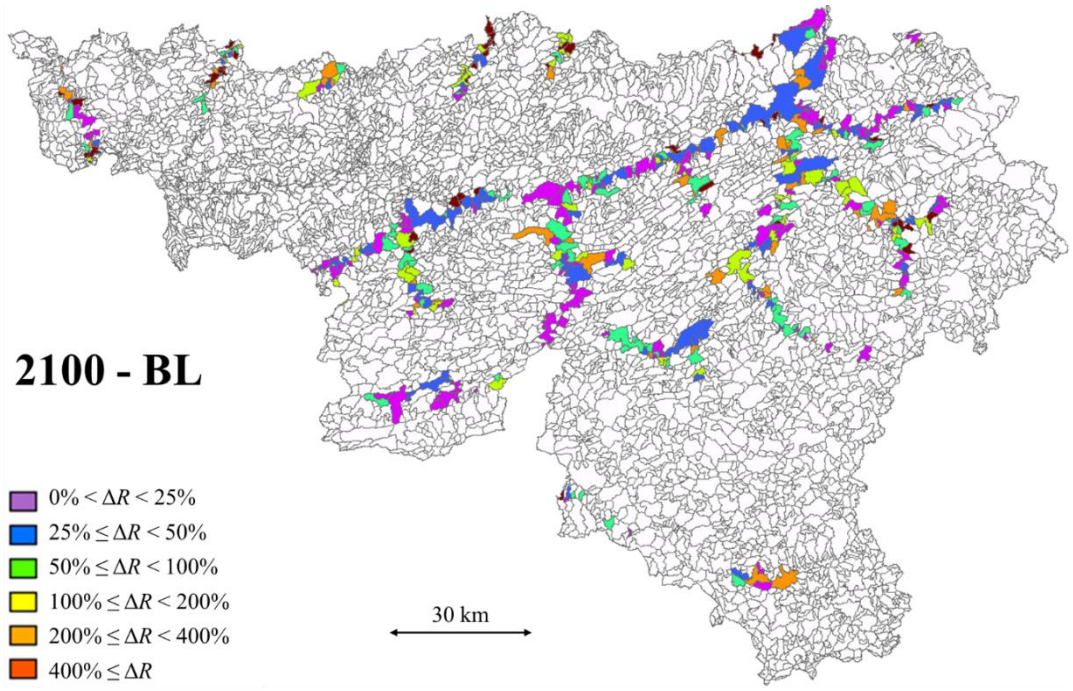

Figure H-3 : Changes in flood risk indicator compared to the current value in 2100 for the BL scenario.

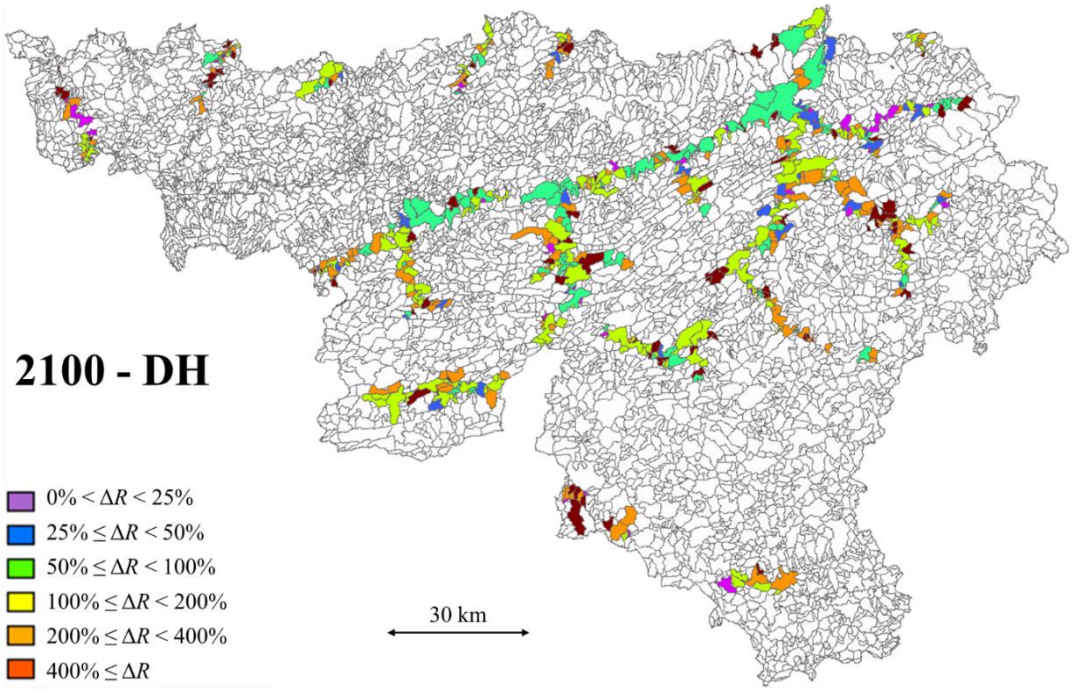

Figure H-4 : Changes in flood risk indicator compared to the current value in 2100 for the LH scenario.